

X 89. 36005

X 89-36005

NASA Technical Memorandum 4100

The NASA Langley
Laminar-Flow-Control
Experiment on a Swept
Supercritical Airfoil

Basic Results for Slotted Configuration

Charles D. Harris, Cuyler W. Brooks, Jr.,
Patricia G. Clukey, and John P. Stack

JUNE 1989

NASA

NASA Technical Memorandum 4100

The NASA Langley
Laminar-Flow-Control
Experiment on a Swept
Supercritical Airfoil

Basic Results for Slotted Configuration

Charles D. Harris, Cuyler W. Brooks, Jr.,
Patricia G. Clukey, and John P. Stack
*Langley Research Center
Hampton, Virginia*



National Aeronautics and
Space Administration
Office of Management
Scientific and Technical
Information Division

1989

Summary

The effects of Mach number and Reynolds number on the experimental pressure distributions and transition patterns for a slotted, laminar-flow-control (LFC), swept supercritical airfoil in the Langley 8-Foot Transonic Pressure Tunnel are presented and discussed. Mach number was varied from 0.40 to 0.82 at chord Reynolds numbers of 10×10^6 and 20×10^6 , and Reynolds number was varied from 10×10^6 to 20×10^6 at operational design conditions. Results show that full-chord laminar flow was achieved on both upper and lower surfaces at the design Mach number for the lower Reynolds numbers. The design pressure distributions for the model and the contoured test section wall liner were generally achieved, although agreement between design theory and experiment was better at a Reynolds number of 10×10^6 than at the design Reynolds number of 20×10^6 . Drag was substantially lower than that experienced on conventional or supercritical turbulent airfoils. Interactions between the model and the liner were found to be present and produced velocities on the upper surface of the model which were higher and more uneven than design, and caused the supersonic bubble on the upper surface at design Mach number to collapse rapidly toward the leading edge when Mach number was reduced by a very small increment.

Introduction

Large decreases in friction drag can be realized on airfoils if a laminar boundary layer can be maintained either by passive natural laminar flow (NLF), which is controlled through geometric shaping, or by active laminar flow control (LFC), which combines shaping and local mass transfer through the surface. A large-chord, 13-percent-thick, 23° swept LFC airfoil has been tested in the Langley 8-Foot Transonic Pressure Tunnel (8-ft TPT) to evaluate the compatibility of active LFC suction systems incorporating various surface suction concepts with current supercritical airfoil technology. The experiment was conducted in three general phases. The results of the first phase—evaluation of spanwise slots on both upper and lower surfaces—are reported herein. The second phase involved the evaluation of a perforated upper surface in combination with the slotted lower surface of the first phase. Free-stream design conditions for the first two phases, typical of high-performance transport aircraft, included a Mach number of 0.82, a section lift coefficient of 0.47, and a chord Reynolds number of 20×10^6 . A third phase combined a perforated suction surface over the forward 26 percent of the upper surface with a passive, nonsuction, laminar flow surface over the remainder of the upper surface

and the slotted lower surface of the first and second phases. Free-stream design conditions of this hybrid configuration (Mach number of 0.815, lift coefficient of 0.47, and chord Reynolds number of 17.7×10^6) were slightly different from those of the first two configurations.

Special requirements for the experiment included modifications to the wind tunnel to achieve the necessary test section flow quality and contouring of the test section walls to simulate free airflow about an infinite swept model at transonic speeds. An overview of the slotted experiment is reported in reference 1; the design concepts incorporated into the supercritical LFC airfoil are discussed in reference 2; the design of the contoured test section liner is discussed in reference 3; and the modifications to the tunnel are described in reference 4.

This report documents the effects of variations in Mach number and Reynolds number on the pressure distributions and transition patterns of the slotted configuration. Also included is a discussion of the influence of interactions between the model and the liner on model pressure distributions. Results are presented for Mach numbers from 0.40 to 0.82 at two chord Reynolds numbers, 10×10^6 and 20×10^6 , and over a range of Reynolds numbers from 10×10^6 to 20×10^6 at the operational design Mach number.

Symbols

b	model reference span, distance along swept span between upper and lower surfaces of liner substructure, 91.146 in.
C_p	pressure coefficient, $\frac{p - p_\infty}{q_\infty}$
$C_{p, \text{sonic}}$	pressure coefficient corresponding to local Mach number of 1.0
C_Q	coefficient of suction, $\frac{\rho_w w_w}{\rho_\infty U_\infty}$
c	model chord parallel to free-stream direction, 7.07 ft
c_d	section drag coefficient
$c_{d,s}$	section suction drag coefficient
$c_{d,t}$	section total drag coefficient, $c_{d,w} + c_{d,s}$
$c_{d,w}$	section wake drag coefficient
c_l	section lift coefficient

$c_{l,N}$	section lift coefficient normal to leading edge
L	laminar (see fig. 40)
M	Mach number
p	pressure, psf
q	dynamic pressure, psf
R_c	Reynolds number based on free-stream conditions and streamwise chord
$R_{c,N}$	Reynolds number based on flow conditions and chord normal to leading edge
T	turbulent (see fig. 40)
t/c	model thickness-to-chord ratio
U_∞	free-stream velocity
w	velocity component in z -direction
x	distance along model chord from leading edge (positive toward trailing edge)
y	distance along model span from centerline of test section (positive toward top of test section)
z	distance perpendicular to model chord plane (positive toward model upper surface)
α	angle of attack, deg
δ	flap angle, deg
Λ	leading-edge sweep angle, deg
ρ	density
Subscripts:	
c	central flap
i, b	intermediate, bottom flap
i, t	intermediate, top flap
ℓ	lower surface
N	normal to wing leading edge
o, b	outer, bottom flap
o, t	outer, top flap
t	stagnation conditions

u	upper surface
w	wall conditions at suction surface
∞	free-stream property

Abbreviations:

cfm	cubic feet per minute
LFC	laminar flow control
NLF	natural laminar flow
psf	pounds per square foot
rpm	revolutions per minute
TPT	Transonic Pressure Tunnel
2-D, 3-D	two- and three-dimensional

List of Figures

For the convenience of the reader, a list of the figures, including both pictorial and graphic results, is given as follows:

	Figure
Experimental test setup for LFC, swept supercritical airfoil in 8-Foot Transonic Pressure Tunnel	1
Photographs of installed liner and model	2
Airfoil design parameters	3
Theoretical pressure distribution and sonic lines (Korn-Garabedian calculations) for "near final" shock-free design normal to leading edge	4
"Final" theoretical pressure distribution (combining Korn-Garabedian and Eppler calculations) for shock-free design normal to leading edge	5
Sketches of LFC airfoil normal to leading edge	6
Laminar "test" zones and turbulent wedges	7
Scaled illustration of relative size of LFC airfoil model, 3-D supersonic flow regions, and liner shape	8
Sketches of LFC model normal to leading edge	9
Effect of simulated loading on deviation of upper surface from template along centerline without shims	10
Effect of shims on deviation of upper surface from template along centerline	11
Deviation of upper surface from template for model with shims, with and without simulated load	12
Sketch of adjustable choke plate	13

Photograph of slotted suction surface	14
Sketches and photographs of segments of suction system	15
Theoretical suction requirements	16
Photographs of airfoil suction ducts and nozzles	17
Photograph of installed variable sonic nozzles	18
Liner suction collar	19
Sketches of slotted LFC model showing actual locations of pressure orifices	20
Sketches of slotted LFC model showing actual locations of thin films	21
Pressure orifice locations over four walls of liner	22
Sketches and photographs of profile drag rake	23
Sensitivity of flow near midspan (station 8) to small variations in M_∞ near $M_{\infty, \text{design}}$ at $R_c = 10 \times 10^6$	24
Sensitivity of upper-surface spanwise pressure distribution to small variations in M_∞ near $M_{\infty, \text{design}}$ at $R_c = 10 \times 10^6$	25
Effect on experimental chordwise pressure distribution near midspan (station 8) of varying M_∞ at $R_c = 10 \times 10^6$	26
Effect on experimental upper-surface spanwise pressure distribution of varying M_∞ at $R_c = 10 \times 10^6$	27
Variation of drag with M_∞ at $R_c = 10 \times 10^6$	28
Sensitivity of flow near midspan (station 8) to small variations in M_∞ near $M_{\infty, \text{design}}$ at $R_c = 20 \times 10^6$	29
Sensitivity of upper-surface spanwise pressure distribution to small variations in M_∞ near $M_{\infty, \text{design}}$ at $R_c = 20 \times 10^6$	30
Experimental pressure distributions near midspan (station 8) at operational design conditions	31
Transition patterns at operational design conditions	32
Local Mach number distributions on vertical test section liner walls opposite model upper and lower surfaces. $R_c = 10 \times 10^6$	33
Local Mach number distributions on vertical test section liner walls opposite model upper and lower surfaces. $R_c = 20 \times 10^6$	34
Comparison of theoretical and experimental suction distributions at operational design conditions	35
Variation of transition patterns with Reynolds number at operational design Mach number within boundaries of design laminar "test" zones	36

Effect on experimental chordwise pressure distribution near midspan (station 8) of varying Reynolds number at operational design Mach number	37
Effect on experimental upper-surface spanwise pressure distribution of varying Reynolds number at operational design Mach number	38
Variation of transition location with Reynolds number at operational design Mach numbers	39
Example thin film signals and corresponding locations on upper surface	40
Variation of drag with Reynolds number at operational design Mach number	41

Test Apparatus

Schematics of the overall LFC experimental setup in the 8-ft TPT are shown in figure 1 along with facility modifications. Major components consisted of a large-chord, swept, supercritical, LFC airfoil model that spanned the full test section height, a contoured test section liner, facility disturbance suppression devices, and a model suction system. Photographs of the installed liner and model are shown in figure 2.

The following sections provide brief descriptions of the major components of the experiment. More detailed descriptions are presented in reference 1.

Airfoil

Airfoil design. Reference 2 describes the approaches used in combining an active LFC suction system with current supercritical airfoil technology. This reference places emphasis on a high design Mach number with shock-free flow, includes features to minimize the growth of boundary-layer disturbances, and outlines suction control requirements. Airfoil design parameters are shown in figure 3.

The "near final" shock-free design pressure distribution and sonic lines normal to the leading edge for the resultant airfoil (as calculated by the airfoil analysis code of ref. 5) are shown in figure 4. Various types of boundary-layer instabilities considered during the design process are also indicated.

The airfoil analysis code of reference 5 did not include provisions for a laminar boundary layer; and, in view of the extremely thin laminar boundary layer expected with suction, the flow was treated inviscidly assuming zero displacement thickness up to the point of specified transition. Transition was specified during design to occur near the end of the suction regions—96-percent chord on the upper surface and 84-percent chord on the lower surface.

The upper-surface pressure distribution (discussed in ref. 2) was characterized by a steep acceleration around the leading edge (because of the relatively sharp and specially designed leading edge) followed by a gradual and progressively slower deceleration to about 40-percent chord. Over the mid-chord region, the pressure gradient was near zero. Downstream of the 70-percent chord, the flow decelerated through a steep subsonic pressure rise toward the trailing edge in a manner similar to a Stratford-type pressure recovery. The supersonic zone on the upper surface thus extended over about 80 percent of the chord of the airfoil, and the maximum local Mach number reached was about 1.11.

On the lower surface, the flow accelerated rapidly around the small leading edge toward the concave region at high static pressure with a local deceleration at about 10-percent chord. The flow then accelerated rapidly in a second acceleration to sonic velocity in the midchord region. The small pocket of supersonic flow in the midchord region was followed by a Stratford-type rear pressure recovery to high static pressures in the rear concave-curvature region. The flow finally accelerated to the trailing-edge static pressure.

The feasibility of the LFC airfoil lower surface depended on the ability to maintain laminar flow in the concave-curvature regions where centrifugal Taylor-Görtler (T-G) type of boundary-layer instabilities dominate (ref. 2). One technique for minimizing the growth of T-G instabilities was to turn the flow through a given angle over the shortest possible chordwise distance in the concave-curvature region at one or more "corner" locations instead of using a gradual turn over a longer chordwise distance. As a result, the two concave regions on the lower surface had local regions of high curvature, and two dips, labeled "Taylor-Görtler" instabilities, appear in the pressure distribution of figure 4.

To provide suitable computational resolution to analyze spikes in the pressure distributions at such "corners," the incompressible Eppler code (ref. 6) was used with extra grid points in the low-speed flow of the forward and aft concave regions of the lower surface. These corners and the resulting pressure spikes were then superimposed on the "near final" calculations of figure 4, and the "final" composite design pressure distribution is shown in figure 5. The resulting airfoil profile is shown in figure 6, and the coordinates are presented in table I. As described in reference 7, there were two concave corners in the forward region and two in the aft region where boundary-layer suction was provided to prevent laminar separation. There were four additional concave corners in the region downstream of where the suction ended. Ref-

erence 7 also compares the "final" configuration with earlier configurations and describes the detailed geometry of the lower surface corners.

Wind-tunnel model. The 23° swept model had a streamwise chord length of 7.07 ft, was mounted vertically, and extended through the test section liner from ceiling to floor about 10 ft forward of the regular test section (figs. 1 and 7). It was displaced from the tunnel centerline toward the lower surface by approximately 15-percent chord (fig. 8). The model location was chosen to minimize viscous blockage, diffuser losses, and tunnel-wall boundary-layer radiated noise and to allow unrestricted development of the supersonic zone in the flow field above the upper surface.

A large chord was chosen so that the flight conditions could be simulated at relatively low unit Reynolds numbers, thereby reducing background disturbance levels and increasing the probability of maintaining laminar flow. Other important considerations were fabrication constraints on slot-duct construction and surface tolerances. The leading-edge sweep was chosen to simulate flight cross-flow Reynolds numbers on transport aircraft with the moderately swept high-aspect-ratio wings envisioned for LFC application.

The model was assembled with an aluminum wing-box (fig. 9) to which six individual aluminum panels (three upper surface and three lower surface) were attached. The upper-surface suction panels were assembled using splice joints and bolted to the wing box from the underside to minimize steps or gaps on the upper surface. The three lower-surface panels were bolted directly to the wing box from the outside, and the bolt heads were covered by narrow cover plates. Suction ducts were machined into the panel and suction slots were cut into a 0.032-in-thick external aluminum skin bonded to the outer surface of each panel. After assembly in the tunnel, joints and cover plates were hand polished until judged to be aerodynamically smooth.

The upper- and lower-surface forward panels were cantilevered off the leading edge of the wing box and were bolted together from the underside where they contacted along a spanwise mating surface at the leading edge. The upper- and lower-surface aft panels were cantilevered off the trailing edge of the wing box and were bolted together from the underside where they contacted along a spanwise mating surface near the 77-percent-chord station and at the trailing edge of the panels. The contours of the vertically mounted upper surface were checked after installation by measuring the gap between the surface and a female template. The template was mounted in the streamwise direction at various spanwise

stations and moved toward the surface until contact was made in at least two places. The gap was then measured at slot locations with feeler gauges to an accuracy of about 0.001 in. Since there was no way to determine the absolute surface deviations, the measured gaps were translated and rotated assuming that the deviation was zero (assuming that the contours were correct) at the "hard points" where the panels were bolted to the wing box ($x/c = 0.262$ and 0.591) immediately downstream of the panel joints. The measurements, shown in figure 10 for the midspan region with the model unloaded, indicate that the forward panel was up about 0.008 in. ($z/c \approx 0.00009$) at the leading edge and that there was some unevenness over the chord. Under simulated loading conditions for a midrange test Reynolds number of about 15×10^6 (8000 lb), using hydraulic load cells and loading pads in the lower-surface cusp regions, the measured gap data of figure 10 indicate that the cantilevered forward panels deflected upward under load to about 0.019 in. ($z/c \approx 0.00022$) at the leading edge. The cantilevered aft panels deformed in a peaky fashion and resulted in a bump about 0.023 in. ($z/c = 0.00027$) high near the 77-percent-chord station. This bump occurred where the panels were bolted together and formed a carry-through structure to transfer some of the lower-surface loading to the upper surface.

An attempt was made to rotate the cantilevered forward and aft panels downward so that under load they would deform to near the design contours. This was accomplished by inserting thin spanwise shims between the lower-surface forward and aft panels and the wing box on one side of the bolts holding the lower-surface forward and aft panels to the wing box. These shims beneath the lower-surface panels (0.008 in. beneath the forward panel and 0.005 in. beneath the aft panel) rotated the leading and trailing edges downward by an amount shown in figure 11 for both unloaded and loaded conditions. Figure 11(b) indicates that the upper surface of the shimmed forward panels deformed under simulated load to very near the design contour. The deformation over the aft panel was reduced but retained the bump near $x/c = 0.77$. Figure 12 summarizes the effects of the shims for unloaded and loaded conditions for three spanwise positions: along the centerline, and 24 in. above and below the centerline. Figure 12(a) indicates that the shims overcorrected toward the top end of the model.

There was also a lateral translation of the model toward the vertical test section wall opposite the upper surface because of a bowing of the wing box under simulated loading conditions. This translation was measured to be approximately 0.015 in. along the

model midspan but does not appear in the template gap measurements of model deformation. Since, as discussed in a later section, deformation of the model combined with the proximity of the test section wall opposite the upper surface to produce an apparent supersonic channeling effect in the flow above the model, this lateral translation would have to be considered when analyzing the pressure distributions on the model.

All three upper-surface panels and the forward lower-surface panel were protected by infusing the aluminum surface with polymeric particles (TUFRAM¹ coating), thus forming a hardened surface that minimized corrosion and damage during installation and testing. The surfaces of the mid and aft lower-surface panels were not hardened because they were not considered so critical to surface erosion as the forward lower-surface and three upper-surface panels.

The trailing edge of the model consisted of a 10.9-percent-chord, manually adjustable, five-segment flap. This five-segment flap system (fig. 7) included a central laminar suction flap with a 13.6-in. span and two separate nonsuction flaps on either side of the central flap. Segmentation of the flap compensated for decambering of the airfoil due to viscous effects along the span associated with the turbulent wedges originating from the junctures of the model leading edge and the liner.

Wind-Tunnel Liner

The conventional slotted test section was reshaped with a contoured, solid wall liner (fig. 1) to account for wall interference associated with the large-chord model. The liner was 54 ft long and extended from the tunnel contraction region (the 24-ft tunnel station) through the test section and into the diffuser (the 78-ft tunnel station).

All four walls were contoured in order to produce a transonic wind-tunnel flow which simulated unbounded, free-air flow around an infinite swept wing. The shape of the contoured liner conformed to the computed streamline flow field around the wing at design conditions ($M_\infty = 0.82$, $c_l = 0.47$, $\alpha = 0.51^\circ$, and $R_c = 20 \times 10^6$) and was corrected for the growth of the tunnel wall boundary layer throughout the test section and diffuser. Measurements with surveying equipment indicated that installed liner contours were generally within about 0.040 in. of design values. Photographs of the finished liner are shown in figure 2.

¹ TUFRAM: Registered trademark of General Magnaplate Corporation.

Facility Disturbance-Suppression Devices

The success of the LFC experiment depended to a large extent on environmental disturbance levels since the ability to maintain laminar boundary layers in wind tunnels depends on the characteristic disturbance levels in the flow. Levels of stream turbulence and acoustic noise should approach those of free-air flight conditions so that the suction required to maintain laminar flow on the model is representative of that required in flight.

Sonic throat. To prevent facility-generated pressure disturbances in the diffuser from feeding forward into the test section, an adjustable sonic throat consisting of two-dimensional, bell-crank-operated plates (fig. 13) positioned on the liner along opposing tunnel sidewalls was included as part of the liner design. These sonic choke devices were located about 1 chord length downstream of the model trailing edge between the test section and the diffuser. The test section was vented to the plenum chamber surrounding the test section through porous strips in the surface of the choke plates downstream of the maximum deflection point to equalize pressures across the liner during transients due to changes in operating conditions.

Screens and honeycomb. Downstream propagating disturbances such as pressure and vorticity fluctuations were reduced by installing a honeycomb and five screens in the settling chamber upstream of the test section (fig. 1).

Suction System

Laminar flow control by boundary-layer removal was achieved with suction through closely spaced slots (fig. 14) extending spanwise on the airfoil surface. After passing through the slots and small underlying plenums, the air passed through appropriately spaced metering holes and was collected by spanwise ducts with suction nozzles located at the ends. Air from the nozzles passed through model evacuation lines, through airflow control boxes that controlled the amount of suction to the individual duct suction nozzles, through sonic nozzles, through hoses to a collector manifold, and, finally, to a 10 000-ft³/min (cfm) compressor with a 4.5:1 compression ratio which supplied the suction.

A schematic of the overall suction system is included in figure 1 and sketches and photographs of some of the individual elements of the suction system are shown in figure 15.

Design suction distribution. Figure 16 shows the theoretical chordwise suction distributions over the upper and lower surfaces in terms of the suction

coefficient C_Q for $R_c = 10 \times 10^6$ and 20×10^6 . Suction in the laminar test region extended in the chordwise direction from 2.5- to 96.2-percent chord in the upper-surface central flap region and from 5.0- to 84.1-percent chord on the lower surface. In the spanwise regions of the intermediate and outer flaps there were no slots beyond the flap hinge line.

Because of the turbulent wedges sweeping across the ends of the model, spanwise variations in suction were required with more suction toward the ends of the model, and separate suction controls were designed for the laminar and turbulent test zones. This was accomplished with bulkheads in the spanwise suction ducts (fig. 15(e)) located to approximate the turbulent wedge boundaries and separate the laminar regions on both surfaces from the turbulent regions. Figure 16(c) shows the spanwise design suction distributions for the upper and lower surfaces at several chordwise stations. Design values of suction in the turbulent zones are shown as multiples of the suction values in corresponding laminar zones. In general, the suction levels in the laminar zones extended the full span to about 60-percent chord on the upper surface and to about 15-percent chord on the lower surface before increased suction in the turbulent zones was required. On both surfaces, laminar suction levels extended into the turbulent zone before increasing rapidly to the turbulent level. The asymmetry in the suction gradients for the turbulent ducts at the floor and ceiling of the model (fig. 16(c)) is because the turbulent ducts at corresponding chordwise locations on the floor and ceiling were not the same length.

Slots, plenums, metering holes. The spanwise running slots varied in width from 0.0020 to 0.0063 in. Slot width and spacing are presented in table II. The higher suction levels required in the upper-aft pressure-rise region, in the decelerated-flow zone of the lower-surface concave region, and in the turbulent wedge zones near the ends of the model were achieved with more closely spaced slots and metering holes, as well as duct and nozzle arrangement and sizing.

Two spanwise rows of metering holes were located on opposite sides of the shallow plenum beneath each slot with diameter less than 0.020 in. and spaced 0.50 in. or less apart. Such a plenum metering-hole configuration resulted in more uniform spanwise suction and was less sensitive to internal duct noise and chordwise displacement of the holes than single rows of holes aligned with the slots.

Ducts, nozzles, evacuation lines. Figures 15 and 17 show sketches and photographs of various elements of the airflow suction system. In some

laminar ducts, where the predicted C_Q levels were high, a nozzle was placed at each end to ensure that low velocities were maintained in the duct. Typical connecting suction hoses and couplings that extended from each nozzle exit through either the test section floor or the ceiling to the airflow suction-control boxes are shown in figure 15.

As previously mentioned, individual laminar test region suction ducts were separated from their corresponding turbulent zones by chordwise bulkheads which followed the turbulent wedge boundaries. Penetration holes were drilled through the bulkheads and the ends of the ducts for nozzle extensions, connector hoses, pressure orifice tubes, and electrical leads. The penetration holes were sealed around the connector hoses to prevent leakage.

Airflow control boxes. Suction levels in individual ducts were designed to be controlled by airflow control boxes (figs. 1 and 15(g)) that were connected by hoses to the suction nozzles inside the model. Each control box contained 27 remotely operated, motor-driven needle valves for individual control of the mass flow from each model suction duct.

Variable sonic nozzle. Figure 18 is a photograph of the sonic nozzles that were located downstream of the individual airflow control boxes. The sonic nozzles provided control of the flow from the suction compressor and blocked feedback noise through the system. In general, design of the sonic nozzles was based on the sonic plug principle and included a motor-driven needle assembly very similar to those in the airflow control boxes. Sonic flow at the contraction was achieved by longitudinal adjustment of the needle with varying flow rates.

The initial design of the suction control system called for a variable sonic nozzle for each of the five airflow control boxes. However, it was found during the experiment that, to attain the required suction levels, it was necessary to eliminate all but the two largest sonic nozzles on the boxes controlling the laminar region suction. These two remaining sonic nozzles were adjusted to have a shock pressure drop in the range of 0.5–1.0 psi.

Liner suction collar. Suction was applied through slots in collar ducts in the liner around the ends of the model (fig. 19) to prevent the turbulent boundary layer on the liner from separating in the vicinity of the model-liner juncture. The plenums, metering holes, ducting, suction nozzles, and evacuation hoses were similar to those of the model suction system discussed above. The collar suction slots, approximately 0.025-in. wide, were wider than those on the model.

Measurements and Instrumentation

Conventional measurement techniques and instrumentation were used to measure tunnel reference temperature and pressures, model and liner surface pressures, variations of stagnation and static pressures across the wake rake, and pressures and temperatures in the various elements of the suction system. These measurement techniques and instrumentation are described in reference 1.

Drag Measurements

Total drag for the LFC model is defined as the sum of the suction drag associated with the energy expended in the suction system and the wake drag associated with momentum losses in the wake.

$$C_{d,\text{total}} = C_{d,\text{suction}} + C_{d,\text{wake}}$$

The suction drag is derived from considerations relating to the power required to create suction through the model surface. It is not a physical drag which opposes the motion of the wing through the air, but a drag computed from suction power requirements. The wake drag is a physical drag that can be approximated by integrating momentum deficits across the wake as computed from measured wake rake pressures. The development of equations for the calculation of both types of drag is given in reference 8.

Aerodynamic Measurements

Surface static-pressure measurements. There were 270 static-pressure orifices distributed along 12 upper-surface rows and 12 lower-surface rows oriented along theoretically determined surface streamlines as shown in figure 20. The orifices were staggered about theoretical streamlines to prevent wedges of orifice-generated disturbances shed by forward orifices from reinforcing each other so that orifice-induced transition would occur at a more rearward orifice. The orifices were generally centered between suction slots and were most concentrated in regions where shock waves were most likely to occur.

For bookkeeping purposes, each upper-surface chordwise row of orifices, and its corresponding lower-surface row, was identified by a station number. Figure 20(c) is a sketch of the trailing edge of the model looking upstream and showing the spanwise location at which orifice rows crossed the trailing edge. As may be seen from figures 20(a) and (b), corresponding upper- and lower-surface rows followed different streamline paths but arrived at the same spanwise location at the trailing edge. The $2y/b$ values noted in figures 20(a) and (b) are the spanwise locations of the last orifice in each row. Although there

are orifice rows identified as stations 13 and 14 on the lower surface (fig. 20(b)), there were only 12 rows on the lower surface. The two lower-surface rows toward the ceiling corresponding to upper-surface rows 1 and 2 would have been covered by the liner and therefore not installed. Similarly, there were no station 13 or 14 rows on the upper surface (fig. 20(a)) corresponding to lower-surface rows 13 and 14.

The primary and most dense upper-surface row of orifices, station 8, was slightly below the midspan and followed a streamline that crossed the trailing edge at about $2y/b = 0.06$ below the centerline of the test section. A slightly less dense row, station 6, followed a streamline that crossed the trailing edge at about $2y/b = 0.23$ above the centerline. The remaining rows were less dense and were principally used to measure spanwise pressure gradients.

Boundary-layer thin-film gauges. Forty-five flush-mounted thin-film gauges were distributed over the upper and lower surfaces (fig. 21) to measure local surface heat transfer rates as indicators of whether the boundary layer was laminar, transitional, or turbulent.

Liner and choke. Approximately 700 static-pressure orifices were located along computed streamlines distributed over the four walls of the liner (fig. 22) from the 24-ft tunnel station at the upstream end of the contraction region to the 53-ft station immediately upstream of the movable choke plates. Approximately 240 more static-pressure orifices were located on 14 streamwise rows distributed around the test section between the 53-ft and 59-ft stations in the vicinity of the choke plates. Starting at the 60-ft station and extending to the 78-ft station downstream of the choke, approximately 70 static-pressure orifices were located on 4 streamwise rows near the vertical and horizontal centerline planes of the tunnel.

Wake rake. Wake drag was determined from variations of stagnation and static pressures measured across the wake of the model with a conventional wake rake shown in figure 23. The rake was cantilevered off the vertical test section wall opposite the model lower surface in the center of the laminar-zone flap and approximately 8 in. behind the model trailing edge. It had 47 total pressure orifices and six static-pressure orifices spread across a 6-in. span. The ends of the stagnation pressure tubes were flattened and spaced closely together in the region of the wake associated with skin-friction boundary-layer losses. In addition, some of the stagnation pressure tubes in this closely spaced region were staggered 1/4 in. off the horizontal plane of symmetry of the rake to permit closer spacing across the wake. The ends of the staggered tubes were not in a vertical

plane: the ones below the horizontal plane of symmetry were shortened about 0.1 in. and the ones above the plane of symmetry were longer by about 0.1 in. such that all the total pressure tubes on the rake were at the same streamline distance from the wing trailing edge. That is, the plane defined by the tips of the total pressure tubes was parallel to the line of the swept trailing edge.

No attempt was made to set the wake rake so as to compensate for the cross flow on the swept wing. The plane of the wake rake was parallel to the horizontal plane through the tunnel centerline.

Modifications to Test Setup During Experiment

Three modifications were made to the test setup during the slotted model phase of the experiment. One was the installation of two 8-ft-long area strips (one on the ceiling and another on the floor of the test section) that extended streamwise from the 51.13-ft tunnel station to the 59.13-ft tunnel station (fig. 2(d)). The maximum cross-sectional area of each strip was 40 in² at the 55.13-ft station, which corresponded to the tunnel station at which maximum movement of the flexible chokes occurred. These strips were installed to act as "fixed chokes" and to minimize movement of the flexible choke plates into the flow. The intent was to reduce the possibility of choke vibration affecting the stability of the model boundary layer, although no conclusive evidence of such vibration was established.

The second modification was the installation of a single streamwise area strip along the floor near the juncture of the airfoil upper surface and the liner; it extended from the airfoil leading edge to the trailing edge (fig. 2(e)). This strip, identified as Floor Area Strip No. 6, had a maximum cross-sectional area of 5.3 in² near the model 60-percent-chord station. The floor area strip was effective in forcing the upper-surface shock wave, which tended to be more forward near the floor than toward the ceiling, to a more rearward position, thereby improving the two-dimensional character of the upper-surface pressure distribution.

The third modification involved the installation of vortex generators (fig. 2(f)) on the tunnel walls at two locations downstream of the choke to energize the wall boundary layer in the corners, thus delaying and reducing separation in the diffuser. One array, consisting of eight vortex generators (two in each corner), was located at the 59-ft, 6-in. tunnel station, immediately downstream of the sonic wall choke. The second array, also consisting of eight vortex generators (two in each corner), was located at the

71-ft, 3-in. tunnel station, immediately downstream of the test section access door.

Discussion

The experimental data presented and discussed herein are based on free-stream conditions rather than flow characteristics normal to the leading edge. The theoretical pressure distribution normal to the leading edge shown in figure 5 has, therefore, been adjusted for sweep effects by the cosine squared of the sweep angle so that it may be compared directly with the experimental data.

Because of the proximity of the model to the vertical liner wall opposite the upper surface, deformation of the aft panel under load, and impingement of the supersonic bubble above the upper surface on the liner wall (discussed in more detail later), the upstream influence of flap deflection was blocked and small changes in flap deflections were generally ineffectual in changing the upper-surface pressure distribution.

A study of the effects of various combinations of flap deflection indicated that, at the design angle of attack of 0.51° , pressure distributions closest to design were obtained with flap deflections of approximately $\delta_{o,t} = 2.3^\circ$, $\delta_{i,t} = 0.5^\circ$, $\delta_c = 0.1^\circ$, $\delta_{i,b} = 0.6^\circ$, and $\delta_{o,b} = 2.8^\circ$. Such deflections are close to what would be predicted by two-dimensional theory and all experimental data presented herein were measured with these settings.

Establishing Minimum Test Reynolds Number

For the lower test Reynolds numbers, the tunnel circuit had to be evacuated to very low stagnation pressures. For example, for $R_c = 10 \times 10^6$ and $M_\infty = 0.82$, stagnation pressure was about $1/3$ atm. The pressure on the model upper surface was even lower since the local static pressure at design conditions ($M_{\text{local}} > 1.0$ in supersonic bubble) was approximately one-half the stagnation pressure (i.e., $p_{\text{local}}/p_{\text{stagnation}} = 0.528$ for $M_{\text{local}} = 1.0$). The 4.5:1 compression ratio, 10 000 cfm compressor was therefore exhausted to the stagnation pressure of the tunnel circuit (fig. 1) rather than to outside ambient conditions.

In the normal operation of the tunnel, the 10 000 cfm compressor exhaust would be vented to the atmosphere through an automatic modulating valve to maintain a constant stagnation pressure (constant Reynolds number) against piping and access hatch leaks. It was impossible in this experiment, however, to do this and simultaneously satisfy the suction requirements for the reasons outlined above. Therefore, an auxiliary 2000 cfm compressor

was installed midway through the experiment to balance the tunnel stagnation pressure against leaks.

While bringing the tunnel on line, the 10 000 cfm compressor was used to evacuate the tunnel circuit to a minimum of about $1/4$ atm. Fan speed, which controls Mach number, was kept below about 200 rpm to reduce loads across the model outer skin, since, while being used to evacuate the tunnel, the 10 000 cfm compressor was not available to apply suction to the model. Once the minimum stagnation pressure was reached, the 10 000 cfm compressor was switched over to apply model suction and exhausted to tunnel stagnation pressure through hollow turning vanes at the end of the diffuser. As the fan speed was then increased to that required for the design Mach number, it followed that stagnation pressure, and consequently Reynolds number, was forced to increase since the 10 000 cfm compressor was no longer available to maintain constant stagnation pressure. The auxiliary 2000 cfm compressor, which was used primarily to maintain stagnation pressure against leaks, was not capable of maintaining constant stagnation pressure against rapid Mach number increases. By the time that the design Mach number of 0.82 was reached, the Reynolds number had drifted up to near $R_c = 10 \times 10^6$ (depending on how fast rpm was increased) and this was the minimum Reynolds number which could be stabilized.

Channel Flow Between Model and Wall

As shown and discussed in subsequent sections, the local Mach number on the vertical liner wall opposite the model upper surface approached 1.0 at design conditions and the supersonic bubble above the upper surface extended outward very nearly to the wall. Thus, the flow region between the model upper surface and wall acted as a supersonic channel. When the model side of this supersonic channel deformed under load with a predominant bump near 77-percent chord (fig. 12) it caused an effective supersonic "throat" in the channel. This throat corresponded to the location on the model where the upper-surface shock formed and tended to remain stationary. Not until the Mach number was reduced far enough for the supersonic flow in the channel to nearly disappear did the shock wave move significantly forward. Once this occurred, the shock moved rapidly forward and appeared to collapse toward the leading edge for a very small incremental reduction in Mach number.

Operational Design Mach Number

Because of the tendency for the supersonic bubble on the upper surface to apparently collapse and the

shock wave to move very rapidly toward the leading edge with small changes in Mach number, it was not possible to set experimental conditions at the predetermined "theoretical design Mach number" of $M_\infty = 0.82$ and get the desired pressure distribution. The resulting "operational design Mach number" was a Mach number high enough to force the supersonic zone to the rear of the airfoil, but low enough to cause the shock wave at the end of the supersonic zone to be as weak and as close to the shock-free theoretical curve as possible before it collapsed to near the leading edge. Consequently, the operational design Mach number varied slightly from run to run depending on small variations in model and test conditions. It also depended to some extent on the subjective judgment of the test engineer as to how low the Mach number could be decreased and the flow over the model remain stable during a data recording cycle. A data cycle lasted just for a few seconds if only an electroscanning pressure system was used to acquire model data. When liner data were acquired using a mechanical stepping valve system, however, a data cycle required that the flow remain steady for almost a minute.

Effects of Varying Mach Number

Figure 24 shows the change in pressure distribution near the midspan as the Mach number was reduced in very small increments by moving the adjustable chokes into the flow near the design Mach number at $R_c = 10 \times 10^6$. Figure 25 presents the corresponding spanwise pressure distributions. The chordwise orifice row with its last orifice located at $2y/b = -0.06$ and identified as station 8 corresponds to the midspan distributions of figure 24. Figures 26 and 27 show similar pressure distributions for $R_c = 10 \times 10^6$, but over a wider Mach number range.

The absolute precision of the tunnel reference pressure instrumentation (sonar manometers) was ± 0.2 psf, checked daily by comparing the stagnation-pressure sonar manometer to the static-pressure sonar manometer and having the manometers readjusted if they differed by more than 0.2 psf. This level of precision in the reference pressures would lead to a level of precision in the computed Mach number of ± 0.0007 , at the design Mach number of 0.82 and $R_c = 20 \times 10^6$ ($p_t = 1456$ psf), assuming a worst-case condition of maximum errors of opposite sign occurring in the two manometers simultaneously. However, even though it is not possible to maintain the manometers to precisions better than ± 0.2 psf, they can be read to ± 0.03 psf (0.03 being the electronic noise level jump in the display). Pressure errors of ± 0.03 psf yield, in the worst-case conditions defined

above, a Mach number error of ± 0.0001 ; for this reason, real-time data displayed Mach number to four decimal places. It was believed that for small changes in pressure associated with choke plate adjustment, any change greater than the 0.03 psf was meaningful in a relative sense. When experience showed that Mach number changes in the fourth decimal place could be consistently associated with changes in the wing pressure distribution, the decision was made to retain the fourth decimal place in the published Mach number, even though absolute precision levels would only justify three decimal places. Figure 24, in particular, would be meaningless without the fourth decimal place in the Mach number.

Note that the preceding analysis of the free-stream Mach number precision based on the capability of the primary pressure standards of the 8-ft TPT is not a statistical analysis. The flow-off discrepancy of as much as ± 0.2 psf between the primary pressure standards (which gives the Mach number error of ± 0.0007) is a systematic error that varies from day to day but not during a given run and therefore is not susceptible to statistical analysis. Thus this Mach number error of ± 0.0007 is the worst case based on the floating systematic error of the primary pressure standards. On the other hand, the Mach number error of ± 0.0001 derived from the ± 0.03 psf electronic noise error of the primary pressure standard is the smallest Mach number error that could be computed from these pressure standards, because no pressure data variation can be obtained within the jump level; that is, there is no way to choose between, for example, a pressure of 1456.03 psf and a pressure of 1456.06 psf when the instrumentation cannot measure any intermediate pressure.

The effect of reducing Mach number from 0.8225 (fig. 24(a)) through small increments to about 0.8215 (fig. 24(f)) was to reduce the region of reacceleration around 75-percent chord and force the pressure distribution closer to the theoretical, shock-free curve. Figure 24(e) is considered to be the closest pressure distribution to design conditions and is referred to as the "operational design" conditions for $R_c = 10 \times 10^6$. The experimental pressure distribution shown in figure 24(e) indicated a smooth, essentially shockless, recovery. With further decrease in Mach number to 0.8214 (fig. 24(g)), a plateau developed in the pressure distribution at about 80-percent chord as a precursor that the flow in the supersonic channel over the upper surface had become unstable and the shock was about to collapse (fig. 24(h)) toward the leading edge—usually without further movement of the chokes by the tunnel operator. This collapse of the supersonic bubble and the rapid movement of the shock wave toward the leading edge did not follow a

smooth progression as might be expected from airfoil theory but was consistent with what would be expected in supersonic channel flow.

The spanwise pressure distributions (fig. 25) for $R_c = 10 \times 10^6$ show that at "operational design" conditions (fig. 25(e)) the leading-edge peaks were lower toward the ceiling than toward the floor. Even though there were not as many pressure orifices toward the ends of the model, there seemed to be a progression from a wavy, uneven chordwise pressure distribution toward the ceiling to a more saddleback distribution near the floor. The shock wave location was nearly two-dimensional across the span with a slight forward movement near the floor. In addition, the shock appeared to be somewhat stronger on the lower half of the model.

As the Mach number was decreased below design, the spanwise pressure distributions (fig. 27) became less two-dimensional in character with a much higher leading-edge peak toward the ceiling than toward the floor. In addition, the pressure gradient over the mid-chord region changed from positive near the ceiling to negative toward the floor. In the midspan region, the pressure distribution over the midchord region was more saddleback in character at the intermediate off-design Mach numbers between about 0.80 and 0.70. As the Mach number was reduced further to $M_\infty = 0.60$ and 0.40, the pressure distribution over the midspan, midchord region tended to flatten out.

Figure 28(a) shows how total drag (upper- and lower-surface drag combined) varied over the wide Mach number range corresponding to the Mach numbers of figure 26 for $R_c = 10 \times 10^6$. Suction drag $c_{d,s}$ remained relatively constant for these conditions. The total drag at $M_\infty = 0.40$ and 0.82 with full-chord laminar flow is seen to be about 31 counts ($c_{d,t} = 0.0031$). This represents an approximately 60-percent drag reduction as compared with an equivalent turbulent airfoil drag level of about 80 to 90 counts. The increase in wake drag level for Mach numbers just below the operational design Mach number was associated with the formation of a weak shock wake near the leading edge as the supersonic bubble began to develop. As the bubble developed, full-chord laminar flow was present but periodic turbulent bursts shedding downstream over the upper surface from the developing shock wave caused an increase in the wake drag. As the Mach number increased to the shock-free operational Mach number, the supersonic bubble spread rapidly toward the rear of the model, the turbulent bursts over the upper surface disappeared, and the wake drag returned to the subsonic level.

Figure 28(b) presents in more detail how the drag varied on the upper surface for Mach num-

bers close to the operational design Mach number ($M_\infty = 0.8216$) at $R_c = 10 \times 10^6$ and shows that the upper-surface wake drag increased on either side of 0.8216. The division of suction drag between the upper and lower surfaces was possible since the suction drag was computed duct by duct and integrated over each surface independently. The wake drag was separated into upper- and lower-surface components on the basis of the assumption that the wake could be divided between the upper and lower surfaces at the point on the wake rake where the stagnation pressure deficit was the greatest. As Mach number was decreased below 0.8216, the supersonic bubble collapsed toward the leading edge (fig. 24(h)), turbulent boundary-layer bursts propagated downstream over the upper surface from the recompression around 20-percent chord, and the wake drag increased. As Mach number was increased beyond the operational design Mach number, the reacceleration around 75-percent chord became more pronounced (fig. 24(a)), a shock wave began to form, and wake drag increased.

Although the operational design Mach number could be approached smoothly from above, there was a hysteresis effect which prevented it from being reached smoothly from below. When approached from below, the flexible choke plates had to be moved so far into the flow that a strong shock wave formed near 77-percent chord. As mentioned previously, the channel between the model upper surface and vertical test section liner wall effectively acted as a supersonic throat, wherein the supersonic flow over the model reached all the way to the wall and a strong shock formed at the minimum cross-sectional area of the channel. This minimum cross-sectional area corresponded to the location of the deformation bump on the aft panel. As the Mach number was then slowly reduced, the supersonic bubble pulled far enough away from the wall so that the shock strength could be smoothly reduced to a minimum before moving rapidly forward.

The effects on the midspan chordwise pressure distribution of varying Mach number in small increments near design Mach number at $R_c = 20 \times 10^6$ are shown in figure 29. Corresponding spanwise distributions are shown in figure 30. The pressure distribution shown in figure 29(c), $M_\infty = 0.8226$, is considered to be the closest to shockless design conditions and is referred to as the operational Mach number for $R_c = 20 \times 10^6$. The flow on the lower surface was separated in the rear cusp and a weak shock had developed on the upper surface near 70- to 75-percent chord, but the collapse of the supersonic zone was not quite as abrupt as observed at $R_c = 10 \times 10^6$.

Operational Design Characteristics

Figure 31 shows a comparison of the measured and theoretical chordwise pressure distributions at the operational design Mach numbers for $R_c = 10 \times 10^6$ and 20×10^6 . The measured pressure distribution at the lower Reynolds number was very close to the design distribution. The upper surface was essentially shock free, the lower surface forward and aft cusp regions agreed very well with design, and there was full-chord laminar flow (as evidenced by the surface thin-film gauges used for transition detection) on both upper and lower surfaces (figs. 32(a) and (b)). The films at the bottom end of the model upper surface indicate that the turbulent wedge extended farther up on the model than design. The small wedge of turbulent flow immediately ahead of the flap and above the centerline was attributed to a concentrated cluster of pressure orifices (fig. 20(a)) installed in that area to provide detailed pressure measurements in the vicinity of a slot. The spanwise pressure distribution (fig. 25(e)) indicates that the flow was generally two-dimensional with a slightly more forward shock location near the floor of the test section.

The fairings connecting thin films that were determined to be either fully laminar or fully turbulent in figures 32 and 36 are intuitive interpretations of transition patterns for the reader's convenience. Although actual transition patterns may vary somewhat from those shown, the conclusions reached on the basis of these patterns will not change. Attempts to define transition patterns in more detail by using various flow visualization techniques were not successful since the liquids and sprays normally used would not adhere to the TUFRAM coatings.

Figure 33 shows that the local Mach number distribution along the liner wall opposite the upper surface of the model agreed well with design for $R_c = 10 \times 10^6$. These local wall Mach numbers indicate, however, that the supersonic bubble on the airfoil was slightly larger than design and extended practically to the wall. Design liner characteristics predicted maximum local Mach numbers to be about 0.96, but the experimental measurements indicate that the maximum local Mach numbers in this region approached 1.0. The larger bubble was believed to be due to the inability to completely account for three-dimensional boundary-layer displacement thickness effects in the design analysis of the contoured liner wall and model deformation which effectively reshaped the channel above the upper surface.

The overall slightly higher velocities (more negative pressure coefficients) and the deviations from

a smooth pressure distribution on the upper surface (fig. 31) were at first attributed simply to "wall interference," since some suppression or distortion of the supersonic bubble would be expected because of the proximity of the wall. Measurements (figs. 10 to 12) of model deformation under simulated aerodynamic loading conditions, however, suggested trends that were in the right direction to have caused the uneven upper-surface pressure distributions and provided an explanation for the observed Mach number effects on the upper-surface pressure distributions.

Attempts to compensate for these deformations by the use of shims (discussed above), as well as preliminary data (not presented) from tests on the perforated model with identical upper-surface contour and similar deformation characteristics, led to the conclusion that the behavior of the flow on the upper surface was dominated by interactions between the model and the liner and the resultant supersonic channeling effects as a result of the model deforming under load.

Under normal conditions, velocities on the upper surface could have been reduced by reducing the angle of attack. Since the angle of attack was adjusted by rotating the model about $x/c = 0.24$, decreasing the angle of attack moved the trailing edge of the model toward the liner wall, thus reducing the area of the channel between the model and the wall and strengthening the shock wave on the upper surface. This channeling effect was amplified by the deformation of the model since, under load, the rear panel of the model, which was cantilevered off the trailing edge of the wing box, moved closer to the wall (fig. 12).

At $R_c = 20 \times 10^6$, upper-surface transition had moved forward to the pattern shown in figures 32(c) and (d) and a weak shock had developed at about 72-percent chord near the rear of the supersonic bubble (fig. 31). The weak shock was located slightly ahead of the peaky aft panel deformation (fig. 12), which would have yielded a region of relatively high curvature on the upper surface. On the lower surface, transition had moved to near the leading edge (fig. 32(d)) and the flow had separated in the rear cusp region. The local Mach number distributions on the vertical test section wall opposite the upper surface (fig. 34) for $R_c = 20 \times 10^6$ are very similar to those discussed above for $R_c = 10 \times 10^6$.

The measured and theoretical suction distributions corresponding to the two operational design pressure distributions shown in figure 31 are presented in figure 35. The measured suction was higher than that theoretically required and generally represents the maximum suction capability of the system. There was, of course, an infinite combination of

individual duct suction levels and overall suction distribution possibilities. The distributions shown were near optimum, that is, the level of suction that gave the greatest chordwise extent of laminar flow. In general, this corresponded to the maximum suction capability of each suction duct combined with the maximum suction capacity of the compressor system used to provide suction to the model. Small local variations may be permissible within these overall distributions without an adverse effect on the extent of laminar flow as determined to within the resolution permitted by the rather sparse chordwise spacing of thin films. Reductions in the overall levels of the suction distributions (by varying compressor controls in amounts large enough to be measured in the sum of the suction drag over the entire upper surface) generally resulted in either a detrimental effect on the laminar flow pattern or an increase in wake drag.

Effects of Varying Reynolds Number at Operational Design Mach Number

Figure 36 shows how the transition patterns on the upper and lower surfaces changed as R_c was increased from 10×10^6 to 20×10^6 at operational design Mach numbers. Figures 37 and 38 show corresponding chordwise pressure distributions near the midspan and the spanwise variation of pressure across the span, respectively. Figure 39 is a summary of the transition patterns on the upper and lower surfaces over the Reynolds number range. The lower line on figures 39(a) and (b) is the locus of the x/c location of the most rearward thin film that was fully laminar regardless of its spanwise location. Similarly, the upper line is the locus of the x/c location of the most forward thin film that was fully turbulent at the same spanwise location. Transition occurred in the transition zone between the two lines. For this analysis, films were judged to be fully laminar when their output indicated 20 percent or less turbulent bursts, and fully turbulent when 80 percent or more turbulent bursts were present. Figure 40 shows traces of thin-film voltage output for various levels of transition. Full-chord laminar flow was indicated on both upper and lower surfaces at $R_c = 10 \times 10^6$ (fig. 36(a)). As Reynolds number increased, transition moved gradually forward on the upper surface and rapidly forward on the lower surface until at $R_c = 20 \times 10^6$ the transition was as shown in figure 36(i). When the Reynolds number reached about $R_c = 14 \times 10^6$ (figs. 36(e) and 37(e)), the boundary layer on the lower surface was unable to withstand the adverse pressure gradient leading into the trailing-edge cusp region, and there was evidence of onset of separation in the aft lower surface concave, or cusp, region. This may be seen

as a slight increase in the pressure coefficient in the negative direction at about 80-percent chord in figure 37(e). At $R_c = 15 \times 10^6$ (fig. 37(f)) separation in the cusp had become more pronounced, the lift coefficient dropped from about $c_l = 0.52$ to about 0.50, and transition (fig. 36(f)) moved forward to around 30-percent chord. With decreasing extent of laminar boundary layer and the appearance of separation on the lower surface, the local effective area distribution of the test section changed, resulting in higher free-stream Mach numbers being required to achieve the design plateau pressure distribution as Reynolds number increased.

Analysis of spanwise pressure distributions (fig. 38) and transition patterns (fig. 36) showed that the flow was nearly two-dimensional but that the leading-edge peak pressure coefficient tended to increase along the span between the ceiling and floor. Transition, however, tended to move forward with increasing Reynolds number in a somewhat non-two-dimensional fashion. In general, transition moved forward more rapidly toward the floor where leading-edge peaks were greater and more slowly toward the ceiling where leading-edge peaks were lower.

It was uncertain whether or not the forward movement of transition on the upper surface with increasing Reynolds number was due to the global effect of the separation on the lower surface strengthening the upper-surface shock, forcing transition at the shock; increased interactions between the model and the liner; the upper-surface shock strength increasing as a natural consequence of increasing Reynolds number; or there simply not being enough suction to maintain laminar flow through the shock region after the flow had passed through the local pressure variations ahead of the shock. Nevertheless, in spite of all the adverse factors and nonideal conditions, laminar flow was maintained over a large supercritical zone on a swept LFC airfoil at high lift, which was the primary goal of the experiment.

It should be reemphasized that the suction system was operating at full capacity to overcome nonideal conditions. It was believed that had additional suction capacity been available, forward movement of transition could have been delayed to higher Reynolds numbers. More importantly, it was believed that the same results could have been achieved with less suction had it not been for the interactions between the model and the liner and the associated supersonic channeling effect of the flow over the upper surface. In addition, laminar flow could more likely have been maintained over a wider range of test conditions had it not been for these interactions between the model and the liner.

Drag Characteristics

Figure 41(a) shows how the contribution of suction and wake drag to the total drag varied for the operational design Mach number over the Reynolds number range from 10×10^6 to 20×10^6 . Figure 41(b) presents a further breakdown of the suction and wake drag for the upper and lower surfaces. Since suction had to be set at its maximum system levels at the lower Reynolds number, suction drag coefficient remained essentially constant with increases in Reynolds number. There was, however, a substantial increase in wake drag associated with the rapid forward movement of transition and separation on the lower surface at fairly low Reynolds numbers, particularly noticeable between $R_c \approx 14 \times 10^6$ and 15×10^6 . The relatively small increase in wake drag associated with the upper surface was due to the more gradual forward movement of transition beginning at $R_c \approx 12 \times 10^6$.

At a Reynolds number of 10×10^6 , wake drag was limited to $c_{d,w} = 0.0004$ on the upper surface and on the lower surface, for a total wake drag coefficient of 0.0008. Suction drag, however, was higher than expected because of the higher velocities and wavy pressure distribution on the upper surface and the very sensitive lower surface; $c_{d,s} = 0.0009$ on the upper surface and 0.0014 on the lower surface for a total suction drag coefficient of 0.0023. Total drag at $R_c = 10 \times 10^6$ was, therefore, $c_{d,t} = 0.0031$.

As discussed in reference 8, the wake drag coefficient of 0.0008 at $R_c = 10 \times 10^6$ was higher than the theoretical wake drag calculated by three different methods. These three methods used theoretical boundary-layer characteristics and yielded, for full-chord laminar flow, wake drag coefficients of about 0.0003. Extensive tuft studies indicated that even though the upper-surface flow along the centerline of the tunnel immediately ahead of the drag rake was laminar (as indicated by the most rearward thin film at 94-percent chord being fully laminar in fig. 36(a)), the flow right at the trailing edge turned downward very nearly parallel to the trailing edge, so that the flow at the wake rake was probably contaminated to some extent by flow from the small wedge of turbulent flow further up on the wing. In addition, the laminar flow pattern on the lower surface immediately ahead of the centerline wake rake in figure 36(a) indicates that transitional flow was present ahead of the rake. The wake drag measurement of 0.0008 is, therefore, considered to be a conservative value for fully laminar conditions.

As Reynolds number increased, upper-surface transition moved gradually forward and upper-surface wake drag increased to 0.0013 at $R_c =$

20×10^6 . Combined with the upper-surface suction drag coefficient of 0.0009, which remained constant as Reynolds number increased, total upper-surface drag coefficient at $R_c = 20 \times 10^6$ was only 0.0022. On the lower surface, transition moved rapidly forward, the rear cusp region separated, and the lower-surface wake drag increased rapidly to $c_{d,w} = 0.0029$ at $R_c = 20 \times 10^6$. Lower-surface suction drag remained fairly constant but did drift upwards to about $c_{d,s} = 0.0015$ at $R_c = 20 \times 10^6$ because of more efficient compressor operation at higher stagnation pressures. This resulted in a total lower-surface drag of $c_{d,t} = 0.0044$ at $R_c = 20 \times 10^6$. Total airfoil drag at $R_c = 20 \times 10^6$ was, therefore, $c_{d,t} = 0.0066$.

Concluding Remarks

Pressure distributions and transition patterns showing the effects of varying free-stream Mach number and Reynolds number on a slotted, laminar-flow-control (LFC), swept supercritical airfoil in the Langley 8-Foot Transonic Pressure Tunnel have been presented. Results were obtained for variations of Mach number from 0.40 to 0.82 for chord Reynolds numbers of 10×10^6 and 20×10^5 , and for variations of Reynolds number from 10×10^6 to 20×10^6 for the design Mach number of 0.82. Full-chord laminar flow was maintained through a large supersonic zone at $R_c = 10 \times 10^6$ at high lift. The model and liner designs were very successful in achieving the design pressure distribution on the airfoil model, although agreement between design and experiment was better at a Reynolds number of 10×10^6 than at the design Reynolds number of 20×10^6 . Interactions between the model and the liner resulted in (1) velocities on the upper surface being faster and more uneven than design, and (2) the supersonic bubble on the upper surface at design Mach number collapsing rapidly toward the leading edge with only a very small reduction in Mach number.

NASA Langley Research Center
Hampton, VA 23665-5225
March 30, 1989

References

1. Harris, Charles D.; Harvey, William D.; and Brooks, Cuyler W., Jr.: *The NASA Langley Laminar-Flow-Control Experiment on a Swept, Supercritical Airfoil—Design Overview*. NASA TP-2809, 1988.
2. Pfenninger, W.; Reed, Helen L.; and Dagenhart, J. R.: *Design Considerations of Advanced Supercritical Low Drag Suction Airfoils. Viscous Flow Drag Reduction*, Gary R. Hough, ed., American Inst. of Aeronautics and Astronautics, c.1980, pp. 249-271.

3. Newman, Perry A.; Anderson, E. Clay; and Peterson, John B., Jr.: *Aerodynamic Design of the Contoured Wind-Tunnel Liner for the NASA Supercritical, Laminar-Flow-Control, Swept-Wing Experiment*. NASA TP-2335, 1984.
4. Harris, Charles D.; and Brooks, Cuyler W., Jr.: *Modifications to the Langley 8-Foot Transonic Pressure Tunnel for the Laminar Flow Control Experiment*. NASA TM-4032, 1988.
5. Bauer, Frances; Garabedian, Paul; Korn, David; and Jameson, Antony: *Supercritical Wing Sections II. Volume 108 of Lecture Notes in Economics and Mathematical Systems*, M. Beckmann and H. P. Kuenzi, eds., Springer-Verlag, 1975.
6. Eppler, Richard; and Somers, Dan M.: *A Computer Program for the Design and Analysis of Low-Speed Airfoils*. NASA TM-80210, 1980.
7. Allison, Dennis O.; and Dagenhart, J. Ray: *Two Experimental Supercritical Laminar-Flow-Control Swept-Wing Airfoils*. NASA TM-89073, 1987.
8. Brooks, Cuyler W., Jr.; Harris, Charles D.; and Harvey, William D.: *The NASA Langley Laminar-Flow-Control Experiment on a Swept, Supercritical Airfoil—Drag Equations*. NASA TM-4096, 1988.

Table I. Theoretical Coordinates of Slotted LFC Supercritical Airfoil
Normal to Leading Edge

$(x/c)_N$	$(z/c_N)_u$	$(x/c)_N$	$(z/c_N)_u$	$(x/c)_N$	$(z/c_N)_u$
0.000000	0.000000	.134371	.037292	.474029	.053239
.000126	.001024	.141029	.038014	.483529	.053238
.000389	.002089	.147817	.038723	.493030	.053215
.000795	.003181	.154734	.039418	.502527	.053170
.001349	.004289	.161778	.040100	.512015	.053104
.002052	.005406	.168950	.040768	.521490	.053015
.002910	.006526	.176244	.041423	.530948	.052903
.003922	.007646	.183656	.042061	.540387	.052769
.005088	.008757	.191183	.042684	.549803	.052613
.006406	.009849	.198823	.043292	.559194	.052435
.007888	.010911	.206572	.043884	.568553	.052235
.009549	.011946	.214430	.044459	.577880	.052012
.011397	.012964	.222392	.045019	.587168	.051766
.013434	.013967	.230455	.045561	.596415	.051498
.015651	.014950	.238617	.046088	.605618	.051207
.018055	.015916	.246871	.046599	.614772	.050892
.020650	.016867	.255218	.047093	.623874	.050553
.023433	.017810	.263652	.047570	.632921	.050191
.026399	.018749	.272172	.048030	.641910	.049806
.029546	.019678	.280774	.048470	.650837	.049395
.032873	.020598	.289453	.048892	.659698	.048960
.036384	.021511	.298206	.049295	.668491	.048501
.040071	.022420	.307031	.049679	.677212	.048018
.043934	.023324	.315924	.050045	.685858	.047511
.047966	.024221	.324881	.050391	.694427	.046979
.052169	.025110	.333900	.050719	.702914	.046424
.056541	.025989	.342975	.051028	.711315	.045842
.061081	.026859	.352105	.051318	.719626	.045233
.065787	.027723	.361284	.051588	.727844	.044595
.070656	.028577	.370509	.051839	.735968	.043930
.075686	.029423	.379778	.052069	.743999	.043238
.080875	.030257	.389086	.052279	.751931	.042519
.086223	.031082	.398431	.052469	.759761	.041771
.091725	.031897	.407807	.052639	.767487	.040996
.097378	.032701	.417210	.052788	.775103	.040192
.103182	.033494	.426639	.052917	.782607	.039358
.109136	.034277	.436089	.053025	.789998	.038493
.115235	.035050	.445557	.053111	.797275	.037591
.121473	.035810	.455040	.053175	.804442	.036651
.127851	.036557	.464532	.053218	.811497	.035676

Table I. Continued

$(x/c)_N$	$(z/c_N)_u$	$(x/c)_N$	$(z/c_N)_\ell$	$(x/c)_N$	$(z/c_N)_\ell$
.818442	.034665	0.000000	0.000000	.127835	-.025535
.825269	.033620	.000019	-.000956	.135118	-.028162
.831976	.032537	.000201	-.001824	.140594	-.030138
.838567	.031409	.000574	-.002590	.144554	-.031566
.845049	.030237	.001170	-.003259	.147525	-.032639
.851485	.029011	.002015	-.003848	.150000	-.033538
.856436	.028031	.003121	-.004375	.151980	-.034290
.861386	.027025	.004484	-.004868	.153465	-.034930
.866337	.026004	.006098	-.005328	.154950	-.035668
.871287	.024974	.007967	-.005755	.156436	-.036474
.876238	.023941	.010103	-.006161	.158416	-.037584
.881188	.022906	.012503	-.006569	.160891	-.038982
.886139	.021871	.015157	-.006988	.164067	-.040777
.891089	.020837	.018058	-.007417	.167228	-.042563
.896040	.019802	.021208	-.007857	.170464	-.044392
.900990	.018767	.024596	-.008306	.176424	-.047725
.905941	.017733	.028212	-.008760	.182162	-.050623
.910891	.016698	.032059	-.009223	.187889	-.053088
.915842	.015663	.035891	-.009673	.193737	-.055206
.920792	.014630	.036881	-.009789	.199755	-.057071
.925743	.013597	.038861	-.010021	.205949	-.058755
.930693	.012565	.042822	-.010484	.212309	-.060304
.935644	.011535	.046782	-.010948	.218818	-.061743
.940594	.010505	.050743	-.011411	.225460	-.063084
.945545	.009476	.054703	-.011874	.232232	-.064334
.950495	.008449	.058663	-.012338	.239130	-.065502
.955446	.007422	.062624	-.012801	.246151	-.066598
.960396	.006397	.066584	-.013264	.253282	-.067625
.965347	.005374	.070545	-.013728	.260515	-.068583
.970297	.004353	.074505	-.014191	.267853	-.069479
.975248	.003335	.078465	-.014654	.275295	-.070318
.980198	.002318	.082426	-.015118	.282831	-.071101
.985149	.001303	.086386	-.015581	.290451	-.071830
.990099	.000290	.090347	-.016045	.298158	-.072503
.995050	-.000721	.094307	-.016508	.305950	-.073124
1.000000	-.001730	.098267	-.016971	.313817	-.073693
		.100990	-.017290	.321752	-.074210
		.103465	-.017588	.329758	-.074677
		.105446	-.017869	.337834	-.075096
		.106931	-.018170	.345971	-.075465
		.108416	-.018584	.354164	-.075786
		.110396	-.019250	.362413	-.076060
		.113366	-.020315	.370714	-.076286
		.117327	-.021743	.379061	-.076464
		.121782	-.023350	.387448	-.076593

Table I. Concluded

$(x/c)_N$	$(z/c_N)_\ell$	$(x/c)_N$	$(z/c_N)_\ell$	$(x/c)_N$	$(z/c_N)_\ell$
.395874	-.076674	.783663	-.014176	.899010	.002938
.404340	-.076707	.793564	-.011196	.902970	.003011
.412837	-.076692	.801980	-.008663	.907921	.003101
.421361	-.076628	.807921	-.006876	.914851	.003216
.429910	-.076518	.811961	-.005661	.921782	.003291
.438482	-.076359	.815130	-.004709	.926733	.003289
.447071	-.076151	.817110	-.004114	.930693	.003235
.455672	-.075894	.818694	-.003641	.934653	.003128
.464283	-.075589	.819882	-.003298	.939604	.002929
.472903	-.075234	.821070	-.002997	.946535	.002571
.481526	-.074830	.822258	-.002750	.953465	.002174
.490147	-.074375	.823447	-.002540	.958416	.001882
.498762	-.073868	.825031	-.002280	.962376	.001647
.507372	-.073310	.826724	-.002006	.965347	.001462
.515971	-.072699	.828699	-.001686	.968317	.001263
.524552	-.072036	.830392	-.001412	.970297	.001118
.533115	-.071319	.832085	-.001137	.972277	.000958
.541656	-.070548	.833778	-.000860	.975248	.000699
.550174	-.069721	.835471	-.000582	.980198	.000240
.558658	-.068839	.837447	-.000257	.985149	-.000229
.567107	-.067899	.839140	.000021	.988119	-.000521
.575514	-.066899	.840724	.000277	.990099	-.000732
.583873	-.065836	.841912	.000456	.992079	-.000965
.592180	-.064704	.843100	.000602	.995050	-.001342
.600430	-.063497	.844288	.000701	1.000000	-.001986
.608620	-.062206	.845476	.000766		
.616747	-.060820	.847060	.000839		
.624811	-.059324	.848753	.000911		
.632822	-.057702	.850729	.000993		
.640795	-.055943	.852422	.001063		
.648750	-.054040	.854115	.001135		
.656709	-.051988	.855808	.001207		
.664701	-.049797	.857501	.001280		
.672750	-.047489	.859476	.001367		
.680868	-.045093	.861386	.001452		
.689604	-.042483	.863366	.001542		
.698515	-.039806	.866337	.001675		
.704455	-.038018	.871287	.001898		
.714356	-.035038	.876238	.002121		
.724257	-.032057	.881188	.002344		
.734158	-.029077	.886139	.002565		
.744059	-.026097	.889109	.002691		
.753960	-.023117	.891089	.002763		
.763861	-.020137	.893069	.002818		
.773762	-.017156	.896040	.002881		

Table II. Location and Width of Suction Slots on LFC Supercritical
Airfoil Normal to Leading Edge

(a) Upper surface

Duct	Slot	$(x/c)_N$	Slot width, in.
1	1	0.02475	0.0021
1	2	.04089	.0029
2	3	.05644	.0030
2	4	.07257	.0033
3	5	.08891	.0033
3	6	.10538	.0033
4	7	.12184	.0034
4	8	.13831	.0036
5	9	.15478	.0035
5	10	.17125	.0038
6	11	.18771	.0036
6	12	.20418	.0038
7	13	.22064	.0038
7	14	.23711	.0039
7	15	.25358	.0038
Joint			
8	16	.27005	.0040
8	17	.28651	.0039
8	18	.30298	.0040
8	19	.31945	.0039
9	20	.33591	.0041
9	21	.35239	.0039
9	22	.36885	.0042
9	23	.38532	.0040
10	24	.40178	.0041
10	25	.41825	.0041
10	26	.43471	.0040
10	27	.45119	.0042
11	28	.46765	.0040
11	29	.48412	.0043
11	30	.50058	.0040
11	31	.51705	.0042
12	32	.53351	.0041
12	33	.54999	.0041
12	34	.56646	.0042
12	35	.58292	.0040
Joint			
13	36	.59939	.0046

Duct	Slot	$(x/c)_N$	Slot width, in.
13	37	.61859	.0044
14	38	.63780	.0046
14	39	.65701	.0045
14	40	.67622	.0049
15	41	.69543	.0051
15	42	.71463	.0057
15	43	.73384	.0062
16	44	.74792	.0060
16	45	.75817	.0056
16	46	.76585	.0053
16	47	.77200	.0050
17	48	.77738	.0047
17	49	.78224	.0045
17	50	.78673	.0042
17	51	.79057	.0043
17	52	.79442	.0043
17	53	.79826	.0044
17	54	.80210	.0043
17	55	.80594	.0043
18	56	.80978	.0042
18	57	.81362	.0042
18	58	.81747	.0042
18	59	.82131	.0041
18	60	.82515	.0041
18	61	.82899	.0041
18	62	.83283	.0040
19	63	.83667	.0040
19	64	.84051	.0040
19	65	.84436	.0041
19	66	.84820	.0043
19	67	.85204	.0044
20	68	.85588	.0045
20	69	.85972	.0047
20	70	.86356	.0048
20	71	.86741	.0049
21	72	.87125	.0050
21	73	.87509	.0052
21	74	.87893	.0051

Table II. Continued

(a) Concluded

Duct	Slot	$(x/c)_N$	Slot width, in.
21	75	0.88277	.0049
21	76	.88661	.0054
Joint			
22	77	.89685	.0050
22	78	.90069	.0042
22	79	.90453	.0040
22	80	.90838	.0039
22	81	.91222	.0038
22	82	.91606	.0037
23	83	.91990	.0037
23	84	.92374	.0036
23	85	.92758	.0036
23	86	.93143	.0035
23	87	.93527	.0035
23	88	.93911	.0035
23	89	.94295	.0035
24	90	.94679	.0035
24	91	.95063	.0035
24	92	.95448	.0035
24	93	.95832	.0035
24	94	.96216	.0034

Table II. Continued

(b) Lower surface

Duct	Slot	$(x/c)_N$	Slot width, in.
1	1	0.05050	0.0028
1	2	.06407	.0028
2	3	.07175	.0039
2	4	.07880	.0046
2	5	.08520	.0051
3	6	.09096	.0047
3	7	.09480	.0045
3	8	.09801	.0039
3	9	.10056	.0031
3	10	.10253	.0027
4	11	.10402	.0024
4	12	.10531	.0023
4	13	.10658	.0027
5	14	.13569	.0020
5	15	.14338	.0023
5	16	.14811	.0031
5	17	.15003	.0035
5	18	.15157	.0031
5	19	.15286	.0063
6	20	.15410	.0025
6	21	.15576	.0020
6	22	.15744	.0020
6	23	.15910	.0020
6	24	.16076	.0020
6	25	.16243	.0020
7	26	.20614	.0038
7	27	.22149	.0033
Joint			
8	28	.25683	.0035
8	29	.28050	.0031
8	30	.30098	.0032
8	31	.32019	.0037
8	32	.33862	.0032

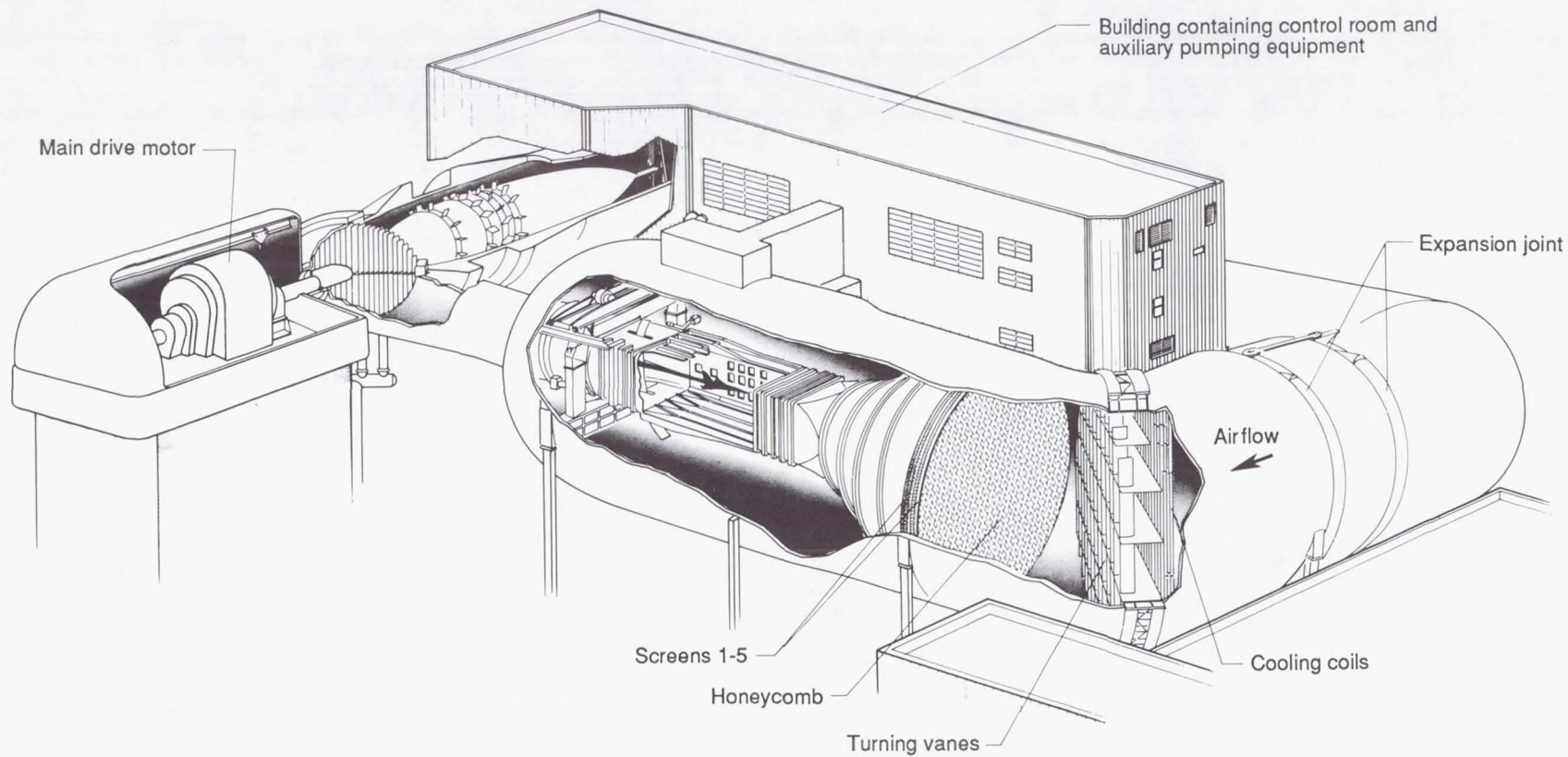
Duct	Slot	$(x/c)_N$	Slot width, in.
9	33	.35783	.0039
9	34	.37448	.0034
9	35	.38984	.0039
9	36	.40419	.0034
9	37	.41852	.0042
10	38	.43287	.0037
10	39	.44619	.0039
10	40	.45950	.0044
10	41	.47282	.0036
10	42	.48511	.0044
11	43	.49741	.0043
11	44	.50893	.0038
11	45	.52046	.0047
11	46	.53134	.0045
11	47	.54158	.0038
11	48	.54894	.0049
Joint			
12	49	.56446	.0043
12	50	.56937	.0042
12	51	.57718	.0046
12	52	.58499	.0046
12	53	.58970	.0044
13	54	.60061	.0046
13	55	.60843	.0053
13	56	.61624	.0051
13	57	.62136	.0050
13	58	.62571	.0052
13	59	.63006	.0048
13	60	.63442	.0048
13	61	.63800	.0048
14	62	.64158	.0047
14	63	.64517	.0045
14	64	.64838	.0043

Table II. Concluded

(b) Concluded

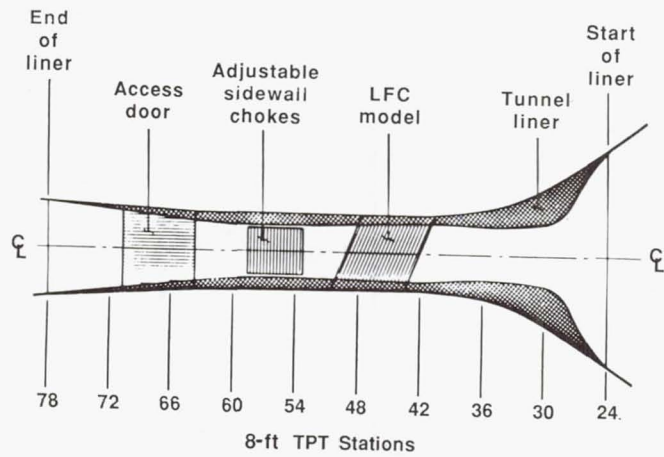
Duct	Slot	$(x/c)_N$	Slot width, in.
14	65	0.65157	0.0042
14	66	.65477	.0040
14	67	.65798	.0039
15	68	.66118	.0038
15	69	.66438	.0037
15	70	.66758	.0037
15	71	.67078	.0036
15	72	.67398	.0036
15	73	.67719	.0036
16	74	.68039	.0036
16	75	.68358	.0035
16	76	.68679	.0034
16	77	.68999	.0034
16	78	.69319	.0033
16	79	.69640	.0033
16	80	.69959	.0032
16	81	.70279	.0032
17	82	.70600	.0032
17	83	.70920	.0032
17	84	.71240	.0032
17	85	.71560	.0032
17	86	.71880	.0031
17	87	.72200	.0031
17	88	.72521	.0031
17	89	.72841	.0030
17	90	.73160	.0030
17	91	.73480	.0030
17	92	.73801	.0030
18	93	.74121	.0031
18	94	.74441	.0033
18	95	.74800	.0033
18	96	.75158	.0032

Duct	Slot	$(x/c)_N$	Slot width, in.
18	97	.75517	.0032
18	98	.75875	.0032
18	99	.76234	.0032
18	100	.76592	.0032
18	101	.76951	.0033
19	102	.77751	.0034
19	103	.78027	.0034
19	104	.78385	.0033
19	105	.78727	.0032
19	106	.79050	.0031
19	107	.79357	.0030
20	108	.79651	.0030
20	109	.79933	.0029
20	110	.80202	.0028
20	111	.80458	.0026
20	112	.80689	.0026
20	113	.80919	.0025
20	114	.81124	.0024
21	115	.81316	.0022
21	116	.81475	.0021
21	117	.81613	.0020
21	118	.81741	.0020
21	119	.81869	.0020
21	120	.81997	.0020
21	121	.83258	.0026
21	122	.83488	.0026
21	123	.83719	.0026
21	124	.83911	.0025
21	125	.84072	.0025

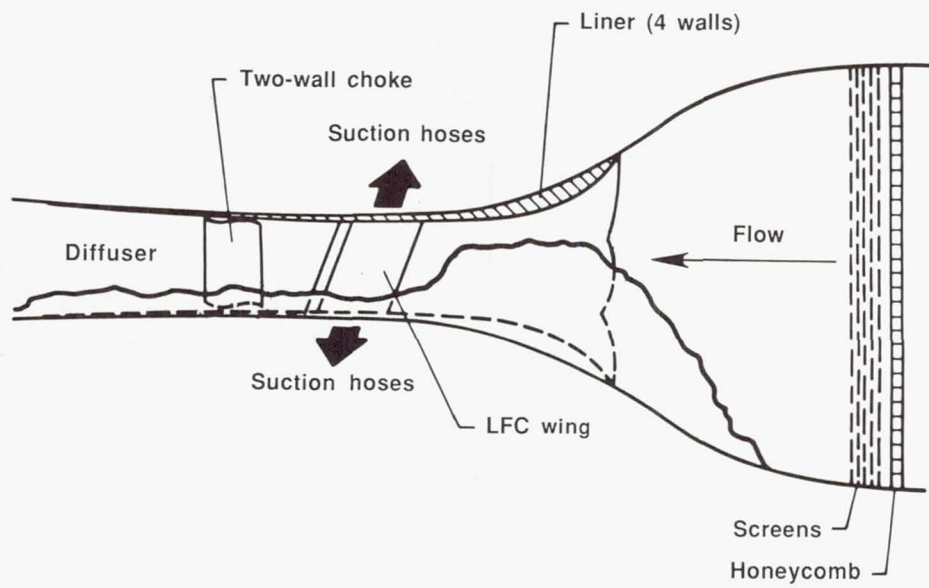


(a) Artist's conception of 8-ft TPT.

Figure 1. Experimental test setup for LFC, swept supercritical airfoil in 8-Foot Transonic Pressure Tunnel.

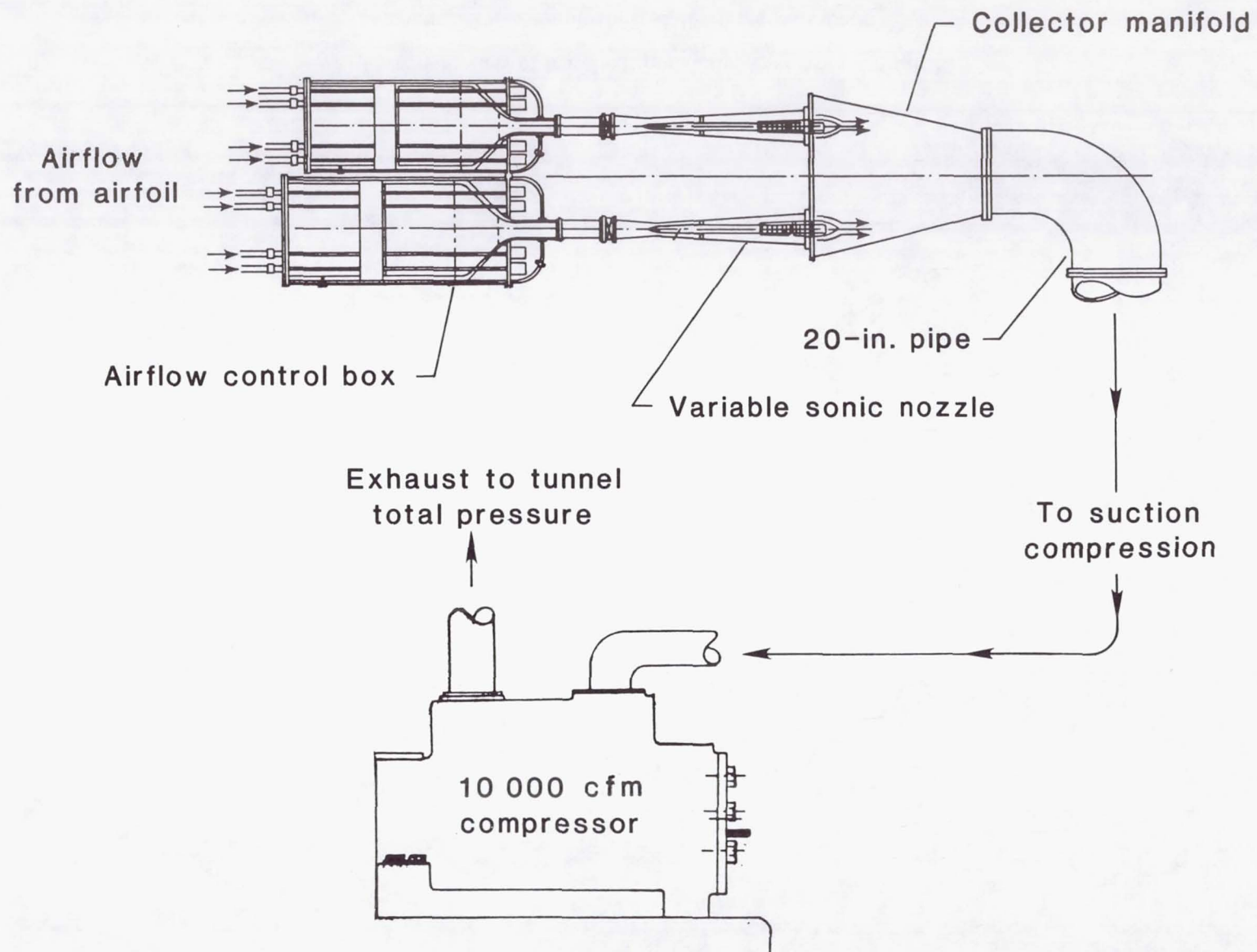


(b) Liner layout.



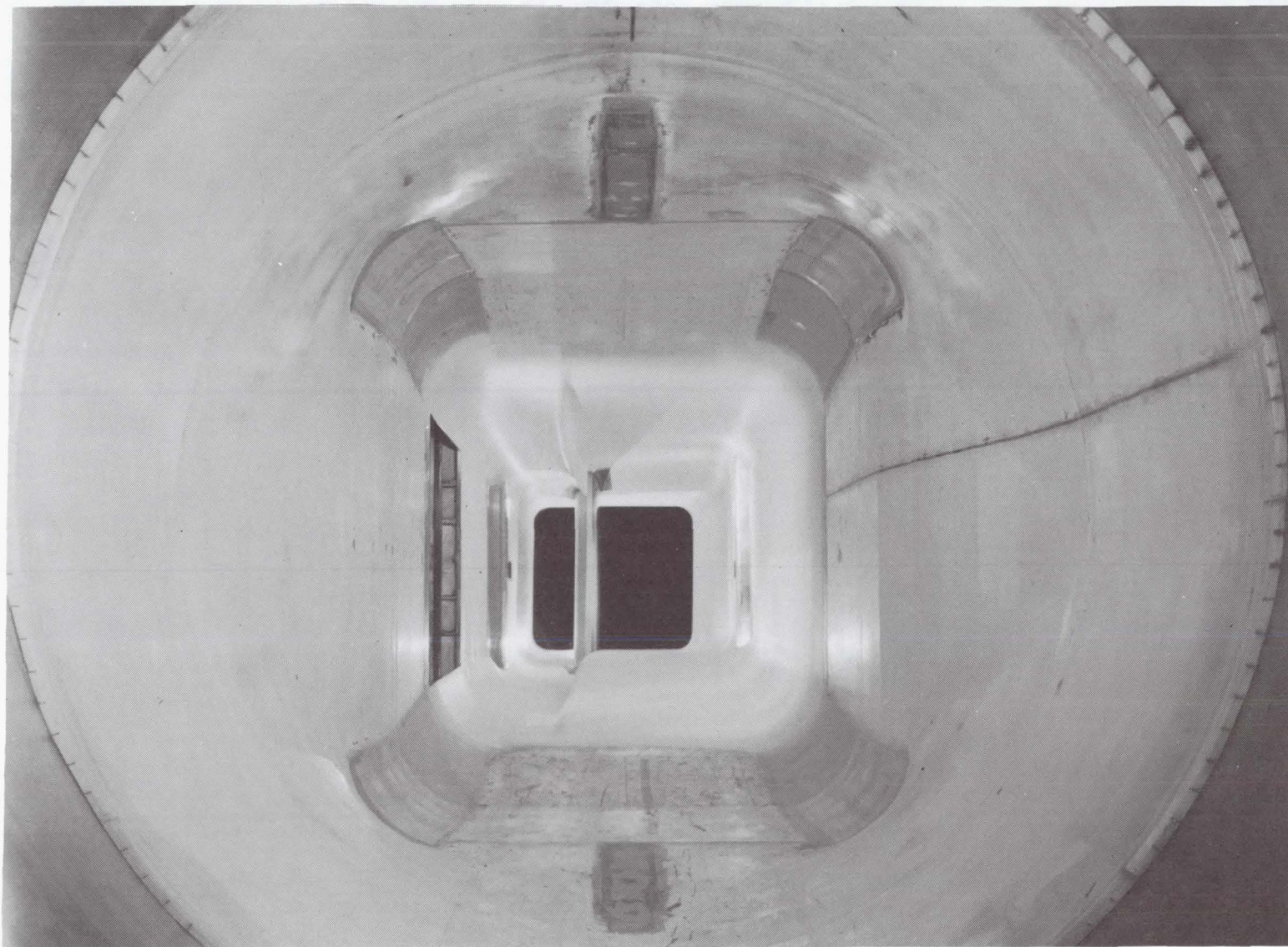
(c) General layout of liner and its location relative to honeycomb and screens.

Figure 1. Continued.



(d) Suction airflow system.

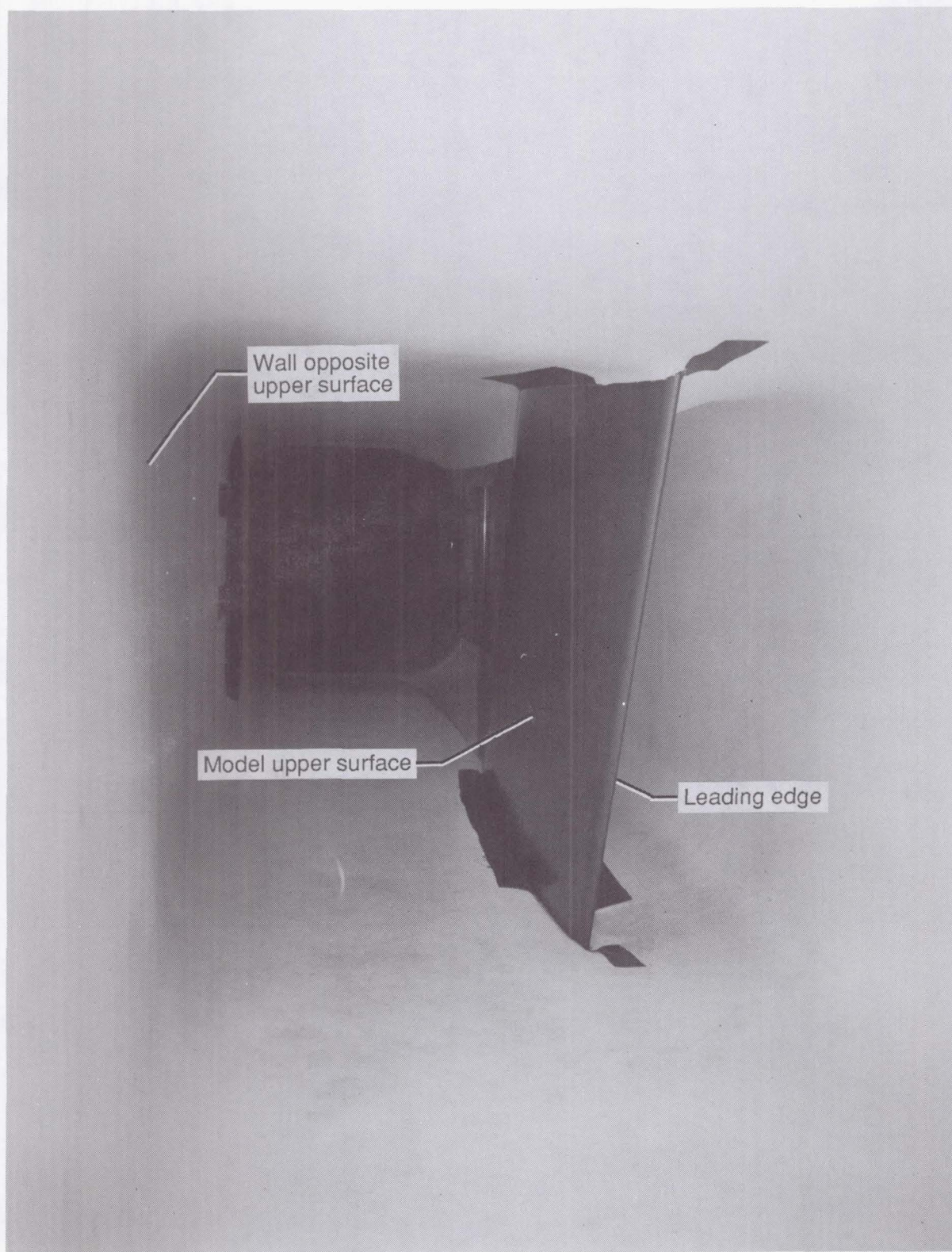
Figure 1. Concluded.



L-82-3066

(a) Upstream view of installed model and liner from diffuser.

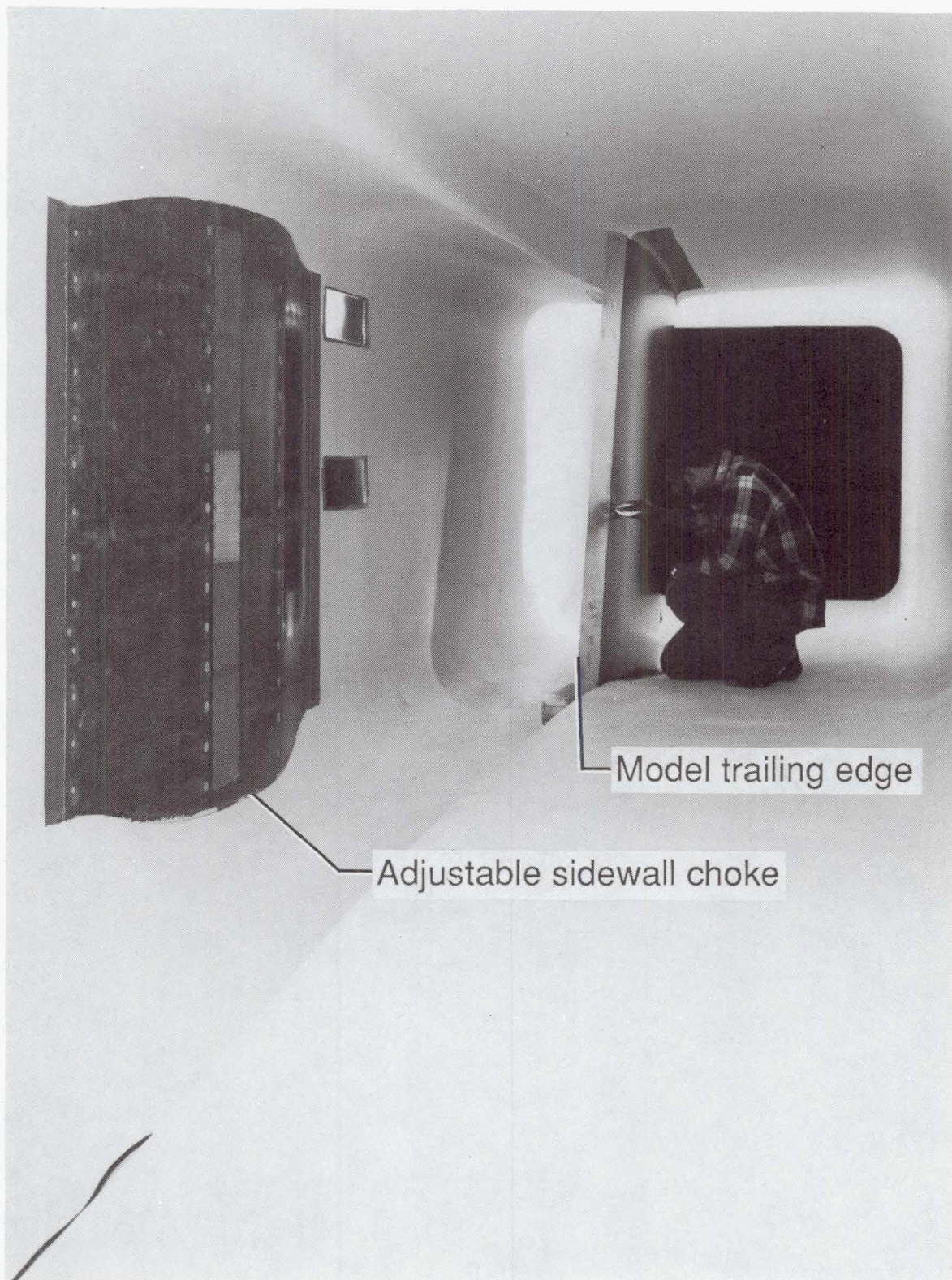
Figure 2. Photographs of installed liner and model.



L-82-3619

(b) Downstream view of model.

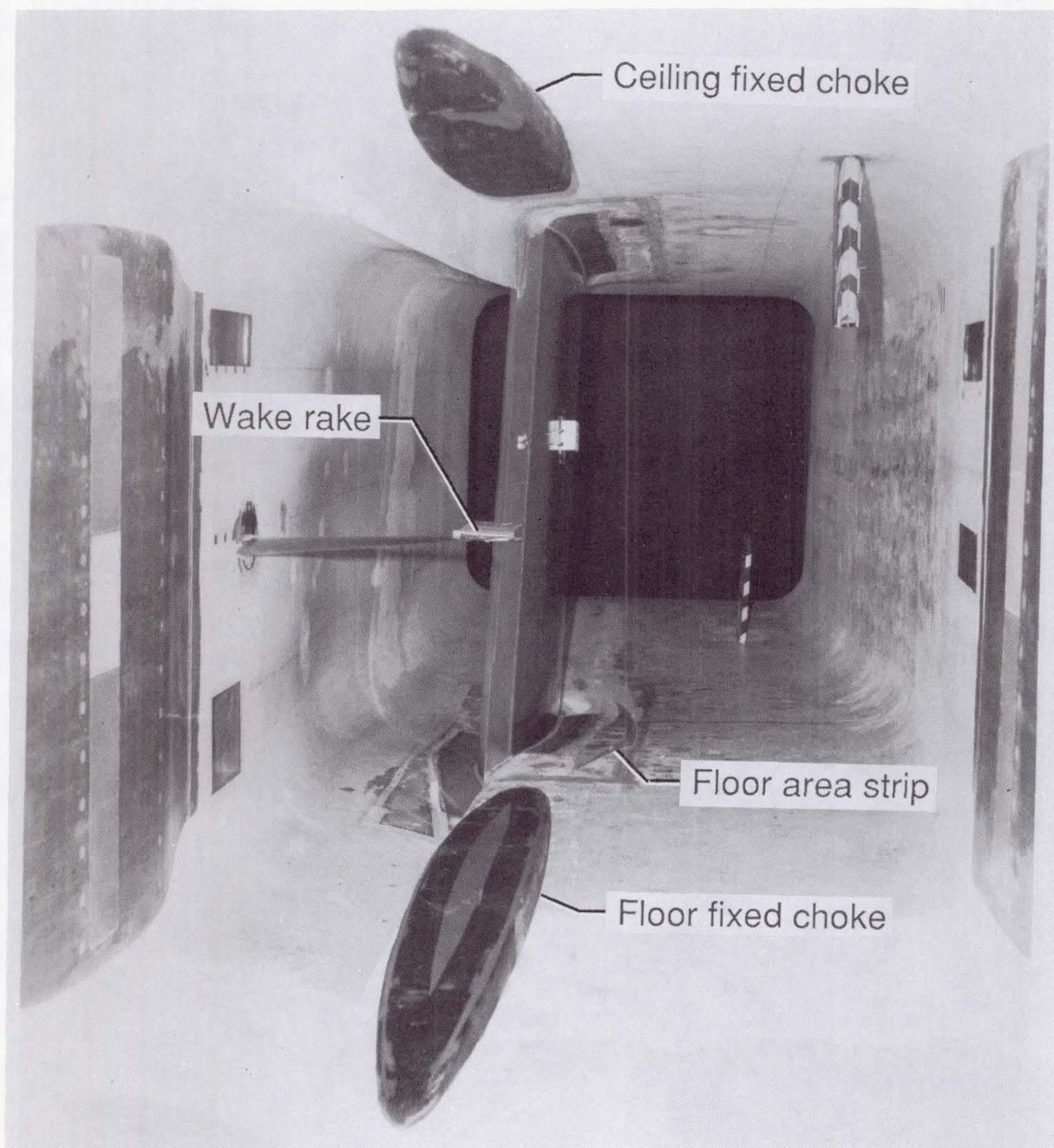
Figure 2. Continued.



L-82-3071

(c) Upstream view of adjustable choke (on wall opposite lower surface) and trailing edge of model.

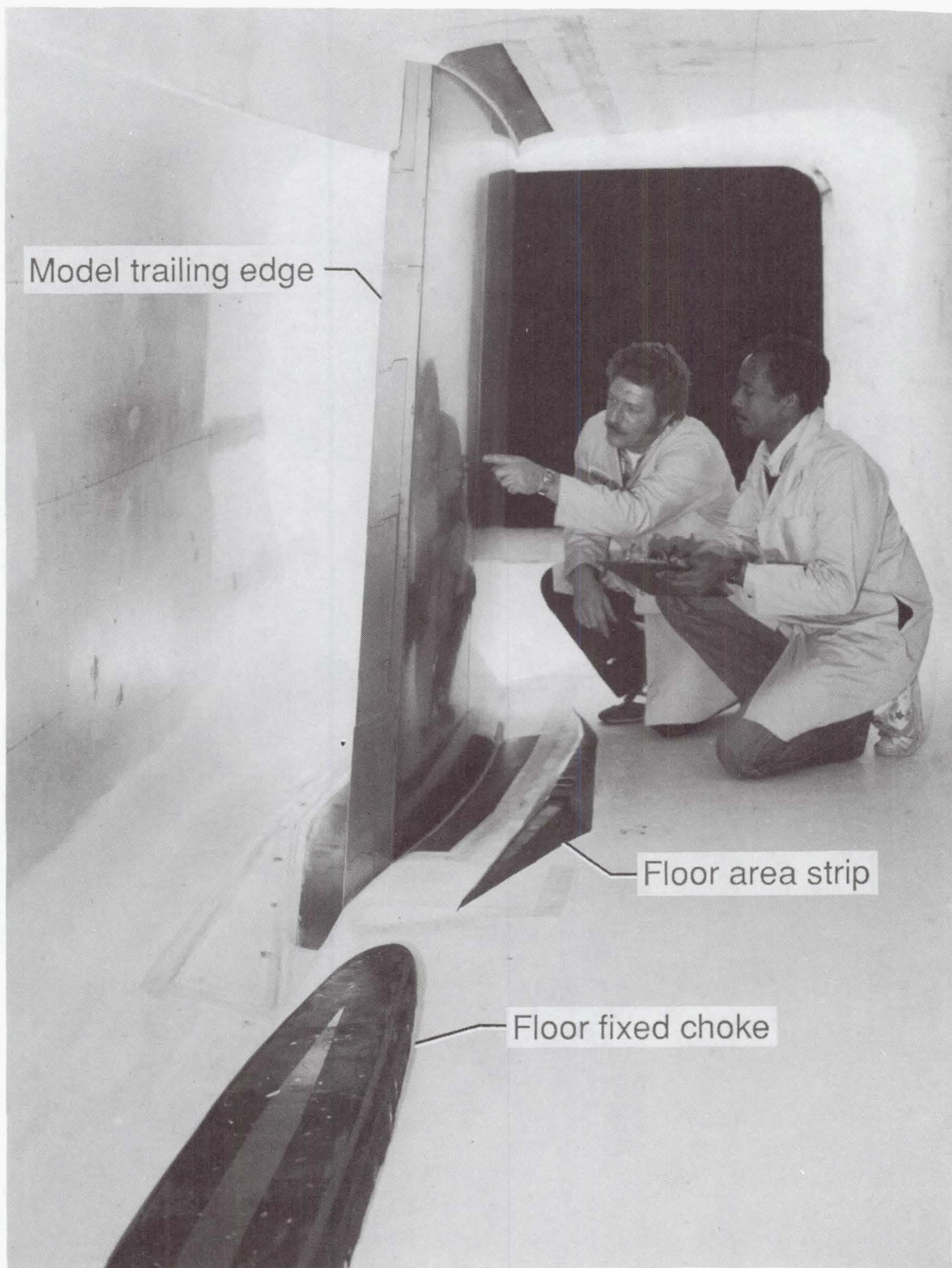
Figure 2. Continued.



L-84-12,369

(d) Upstream view of fixed choke on floor and floor area strip above model upper surface.

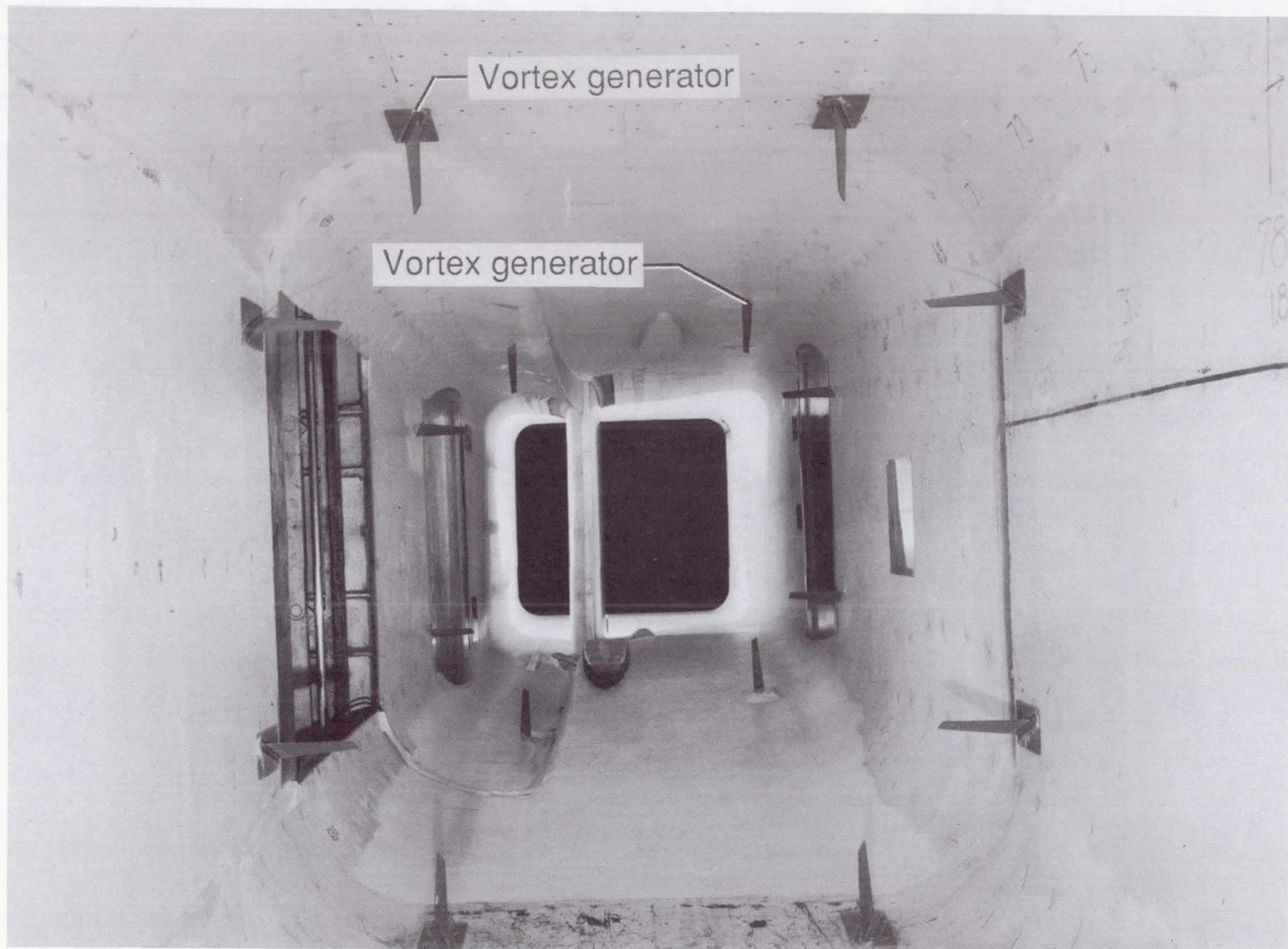
Figure 2. Continued.



L-86-1184

(e) Upstream view of forward portion of fixed choke on floor and floor area strip.

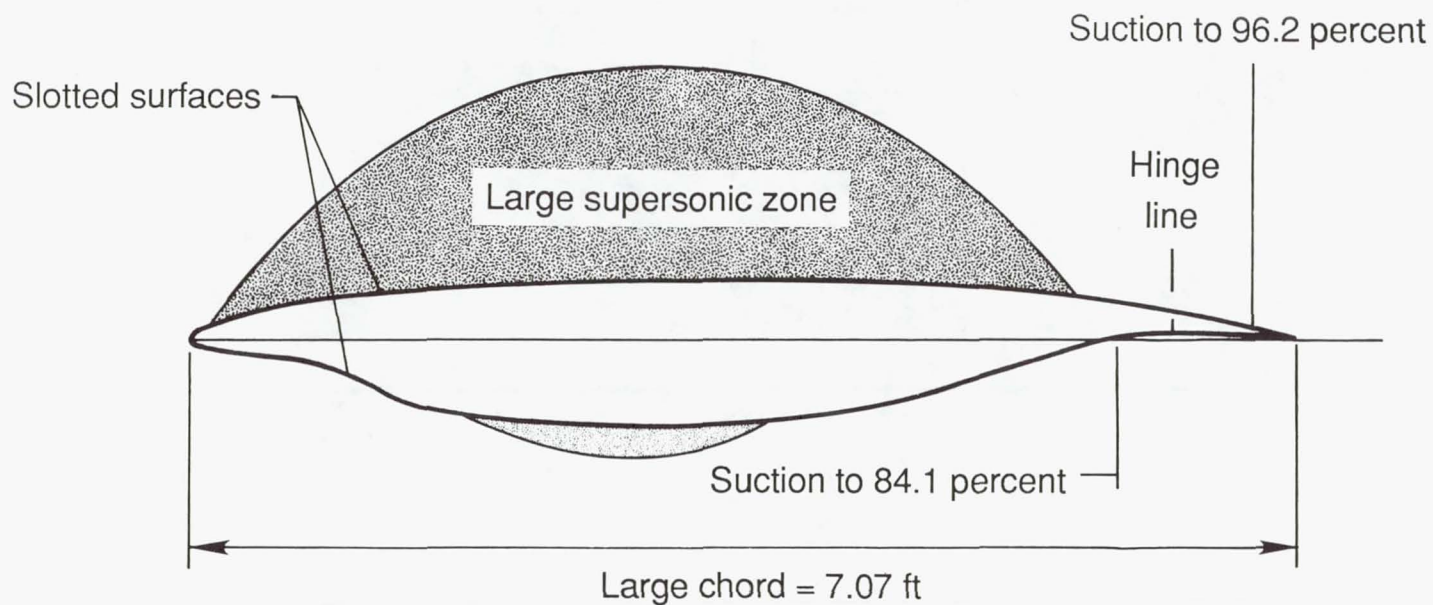
Figure 2. Continued.



L-86-1185

(f) Upstream view of model with vortex generators in corners.

Figure 2. Concluded.



Free-stream design conditions

$$\begin{aligned}
 M_{\infty} &= 0.82 \\
 \Lambda &= 23^{\circ} \\
 c &= 7.07 \text{ ft} \\
 R_C &= 20 \times 10^6 \\
 c_l &= 0.47
 \end{aligned}$$

Design conditions normal to leading edge

$$\begin{aligned}
 M_N &= 0.755 \\
 c_N &= 6.508 \text{ ft} \\
 R_{C,N} &= 16.9 \times 10^6 \\
 (t/c)_N &= 13.0 \text{ percent} \\
 c_{l,N} &= 0.55
 \end{aligned}$$

Figure 3. Airfoil design parameters.

Design

$$M_N = 0.755$$

$$C_{l,N} = 0.55$$

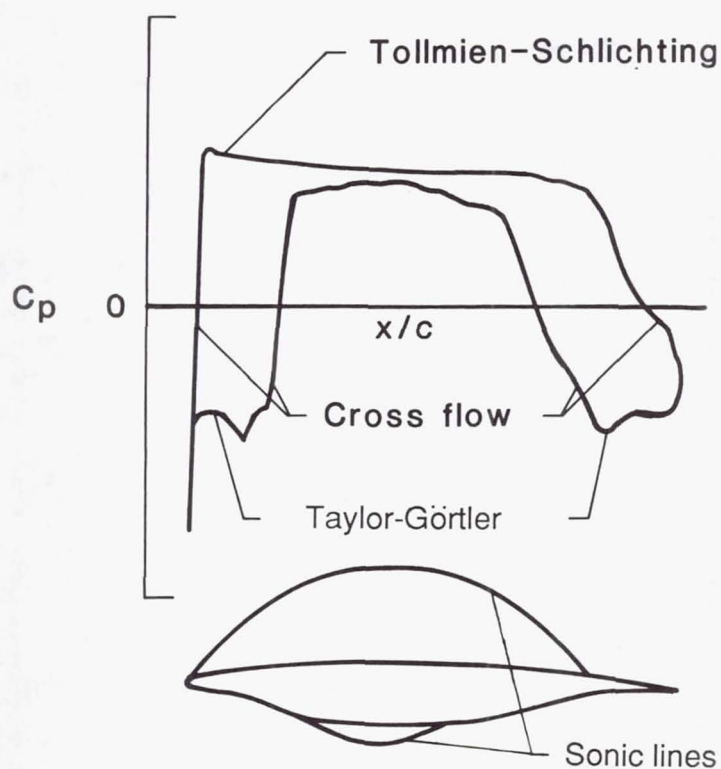


Figure 4. Theoretical pressure distribution and sonic lines (Korn-Garabedian calculations) for "near final" shock-free design normal to leading edge.

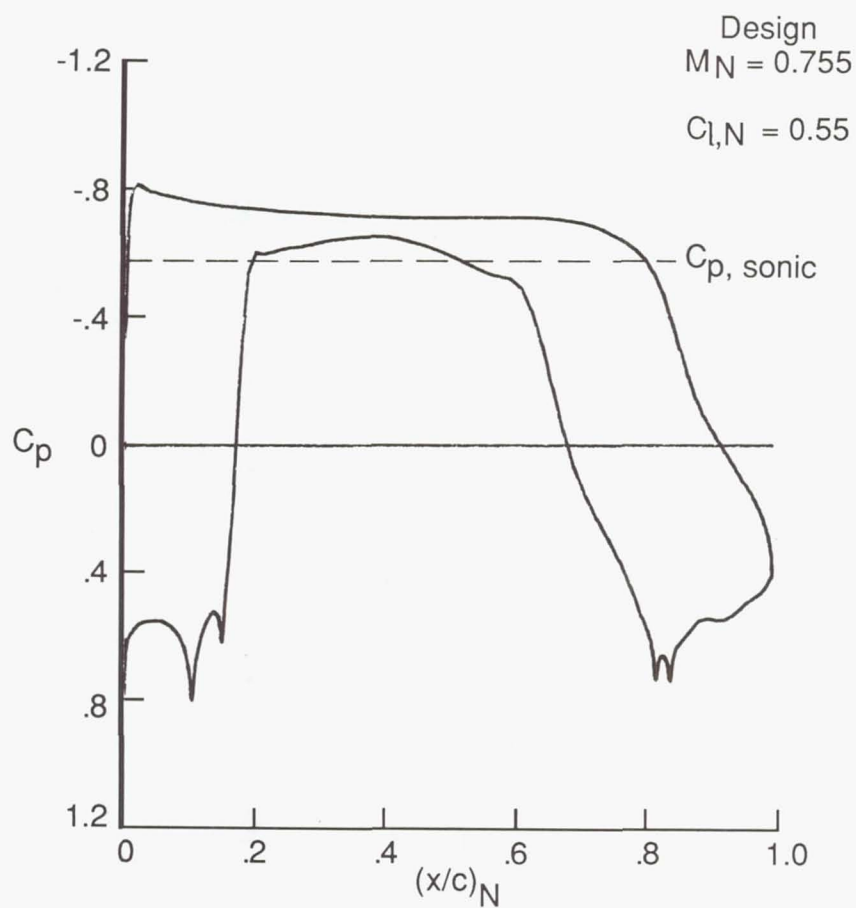
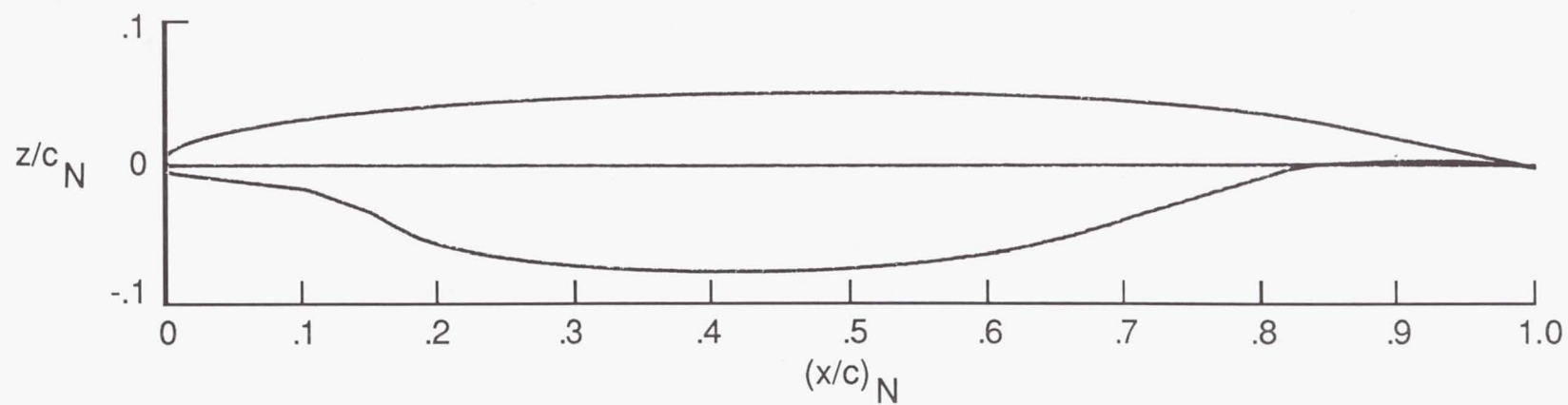
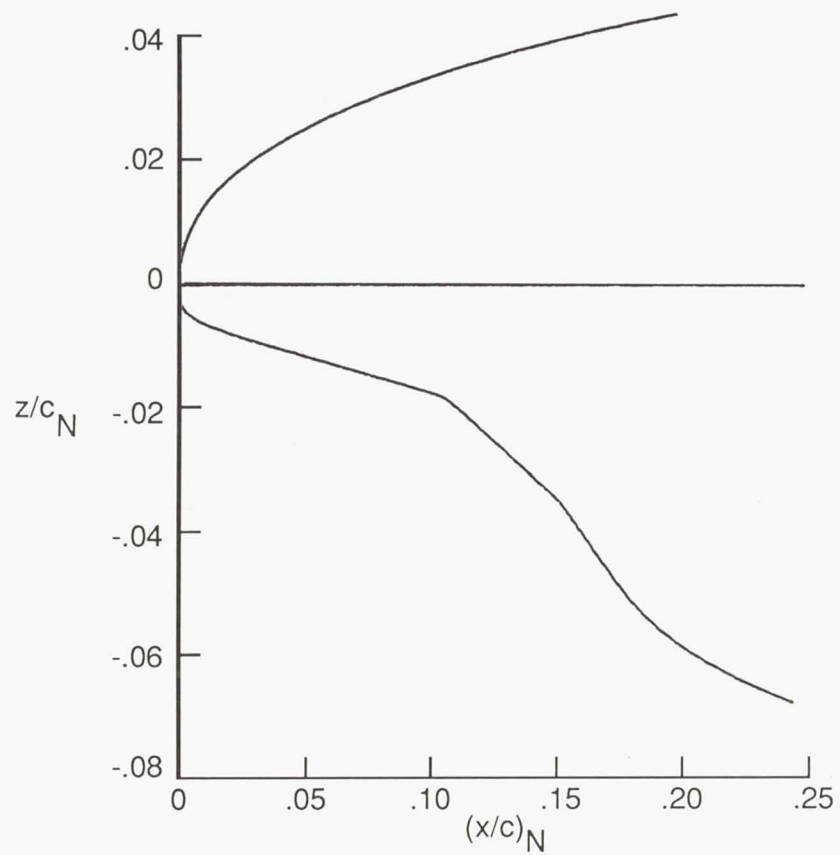


Figure 5. "Final" theoretical pressure distribution (combining Korn-Garabedian and Eppler calculations) for shock-free design normal to leading edge.

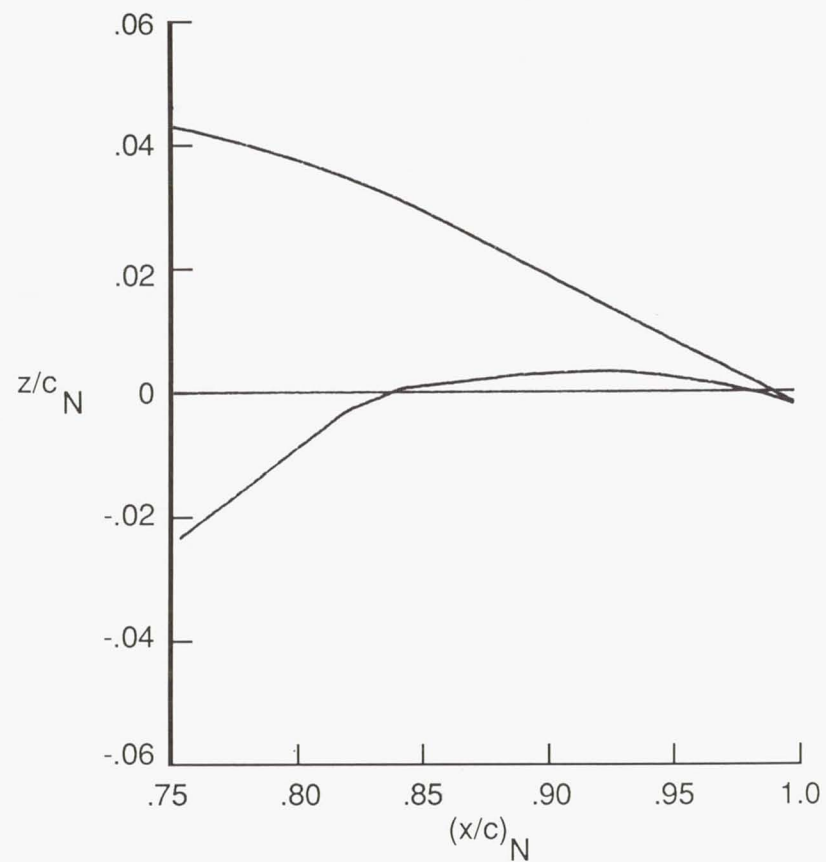


(a) Upper- and lower-surface contours.

Figure 6. Sketches of LFC airfoil normal to leading edge.

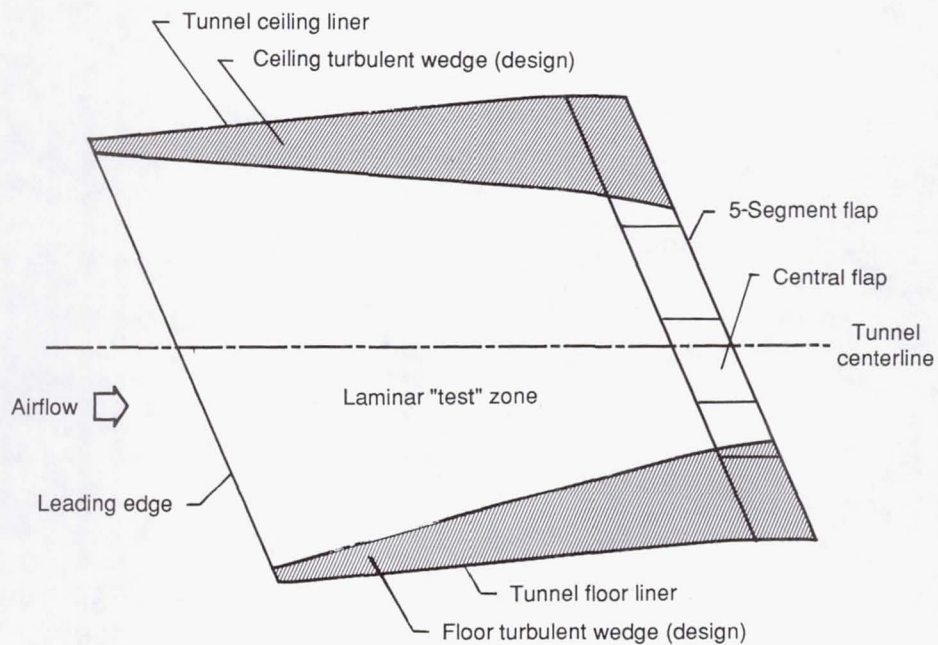


(b) Forward lower surface.

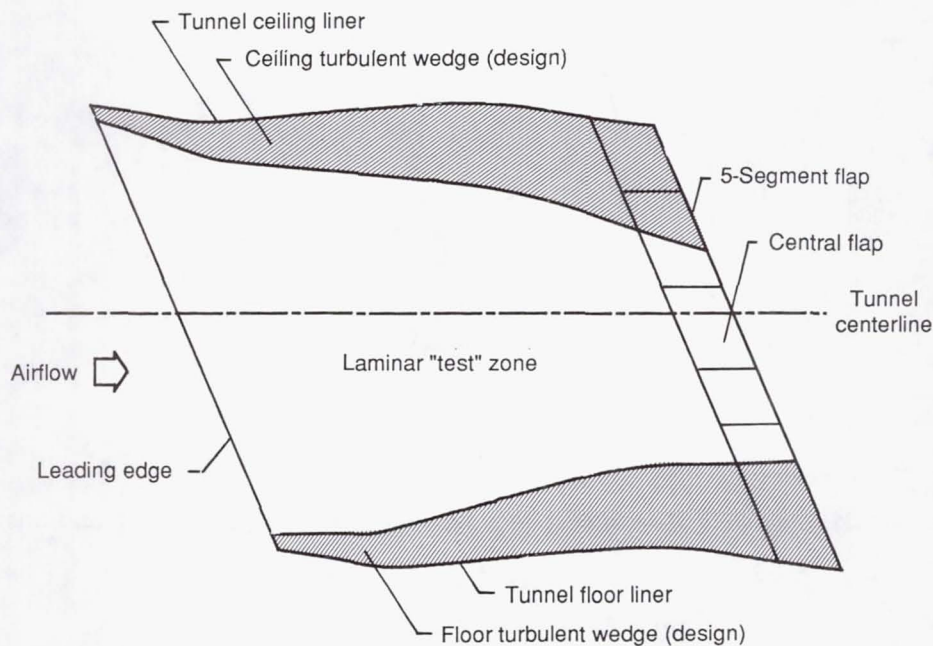


(c) Aft lower surface.

Figure 6. Concluded.

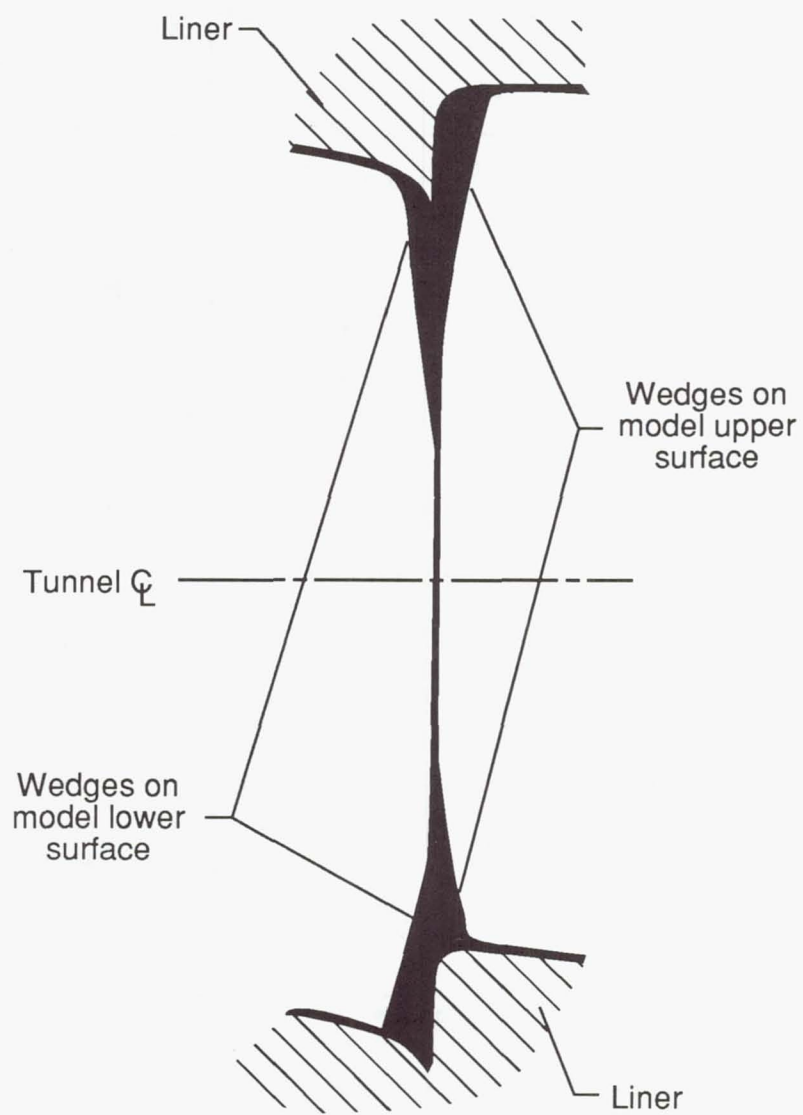


(a) Upper-surface planform as viewed through model from beneath lower surface.



(b) Lower-surface planform as viewed from beneath lower surface.

Figure 7. Laminar "test" zones and turbulent wedges.



(c) Trailing-edge view of turbulent wedges in junctures of model and liner.

Figure 7. Concluded.

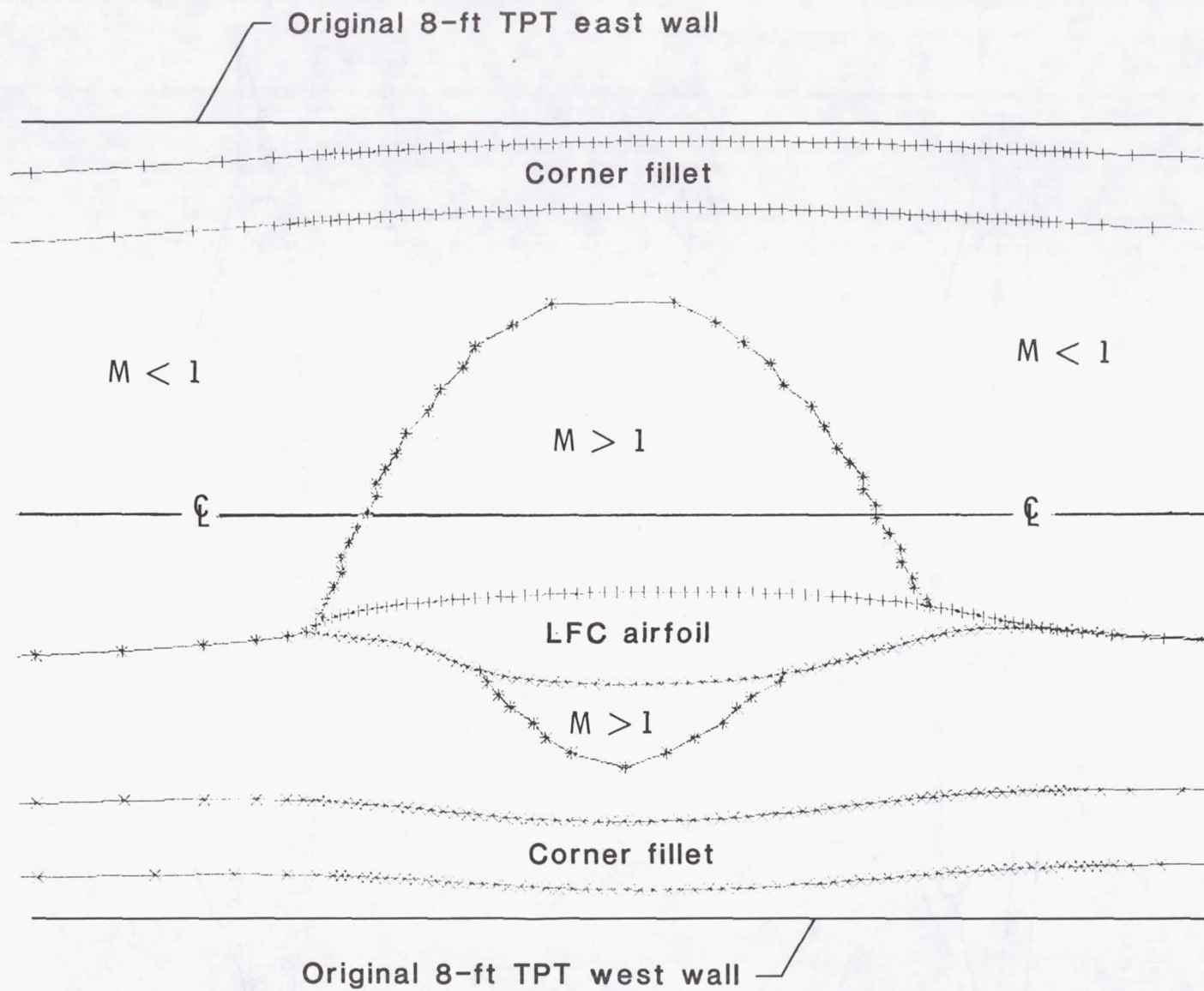
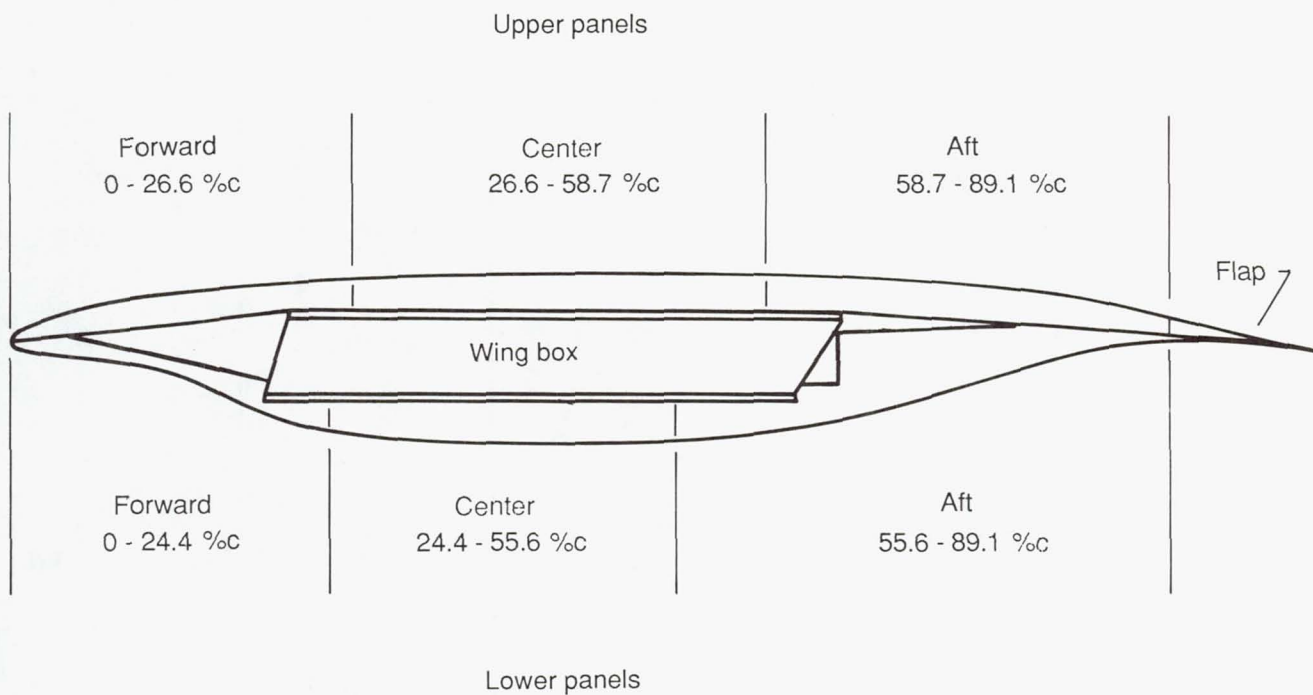
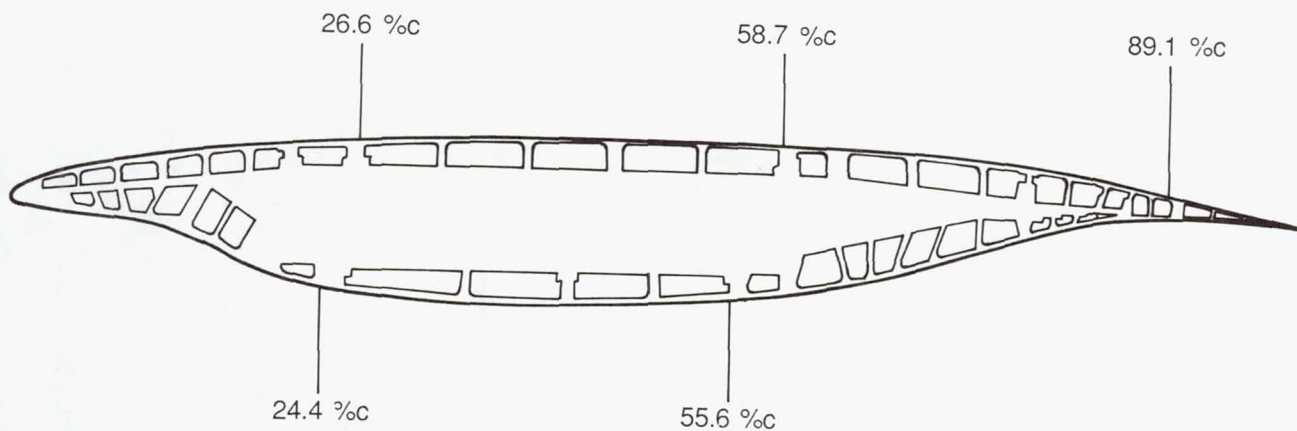


Figure 8. Scaled illustration of relative size of LFC airfoil model, 3-D supersonic flow regions, and liner shape.



(a) Panel arrangement.



(b) Duct arrangement.

Figure 9. Sketches of LFC model normal to leading edge.

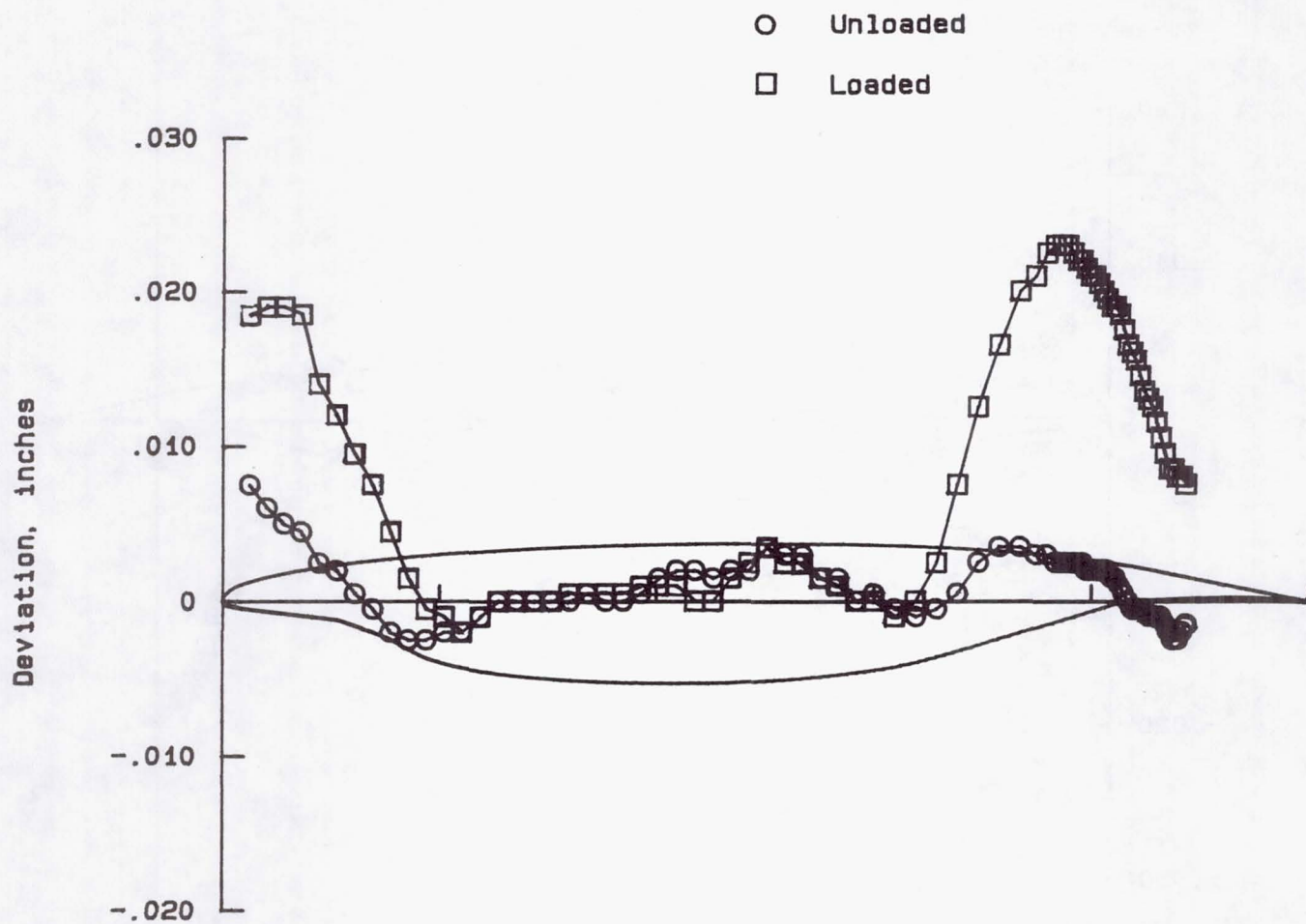
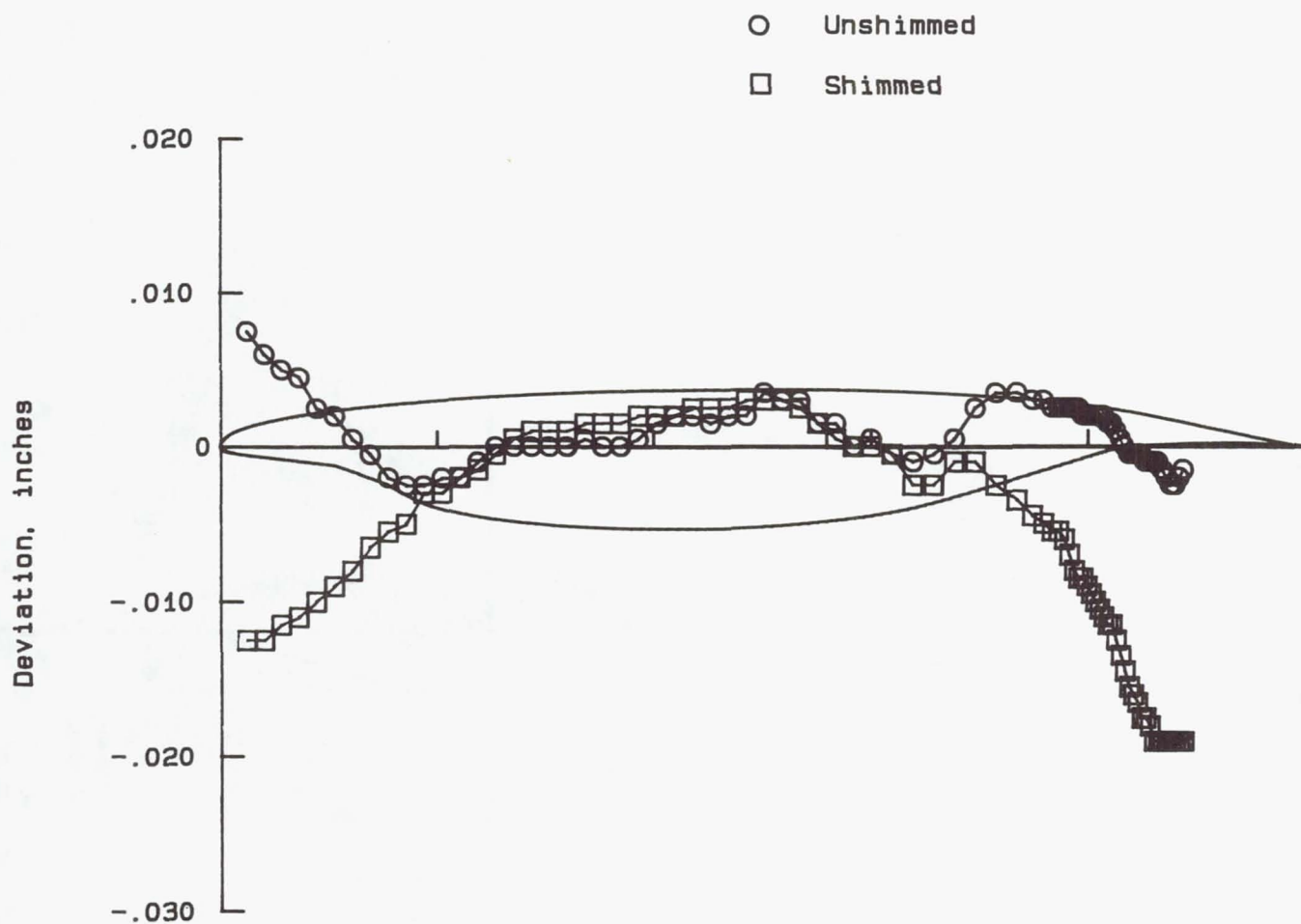
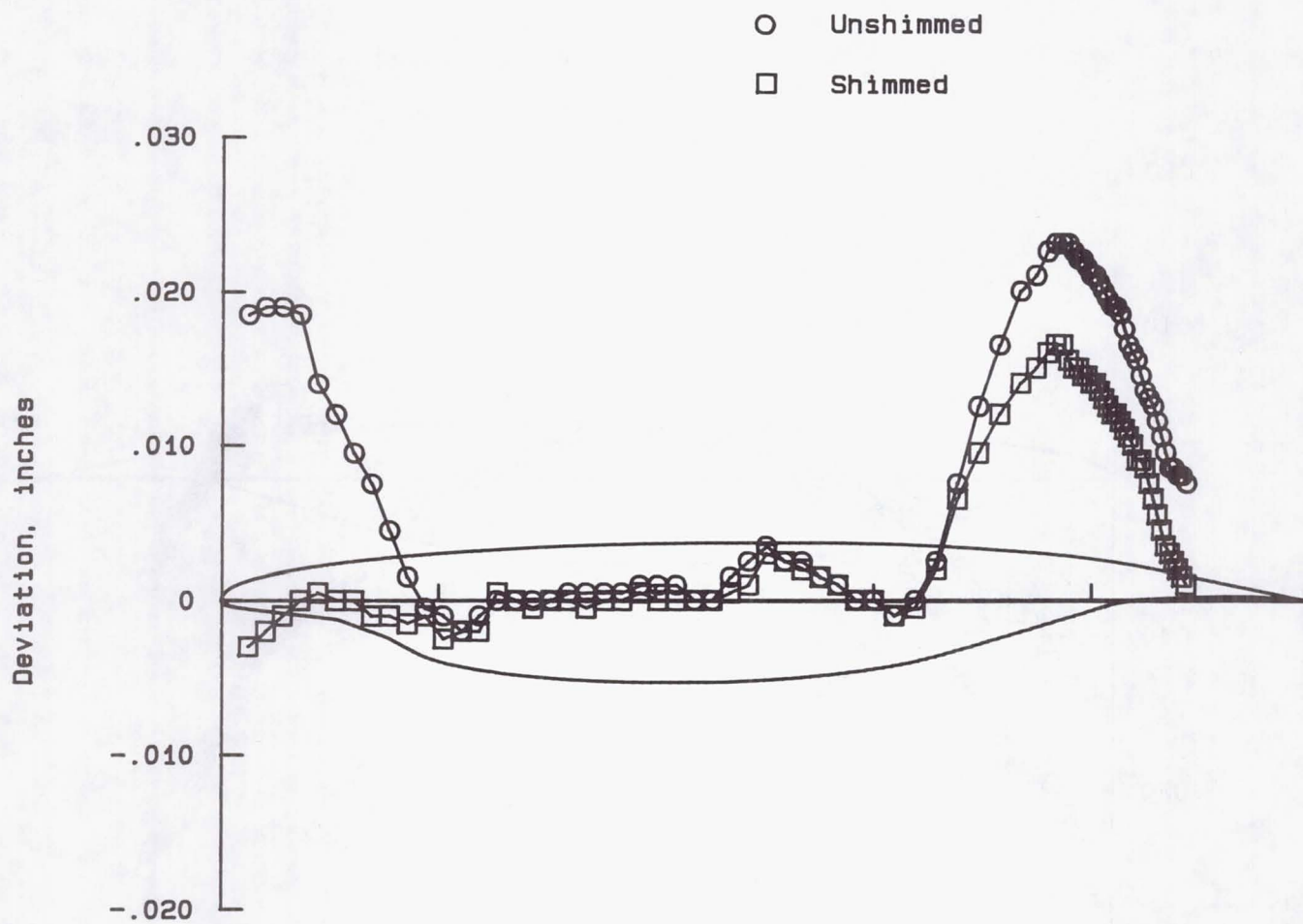


Figure 10. Effect of simulated loading on deviation of upper surface from template along centerline without shims.



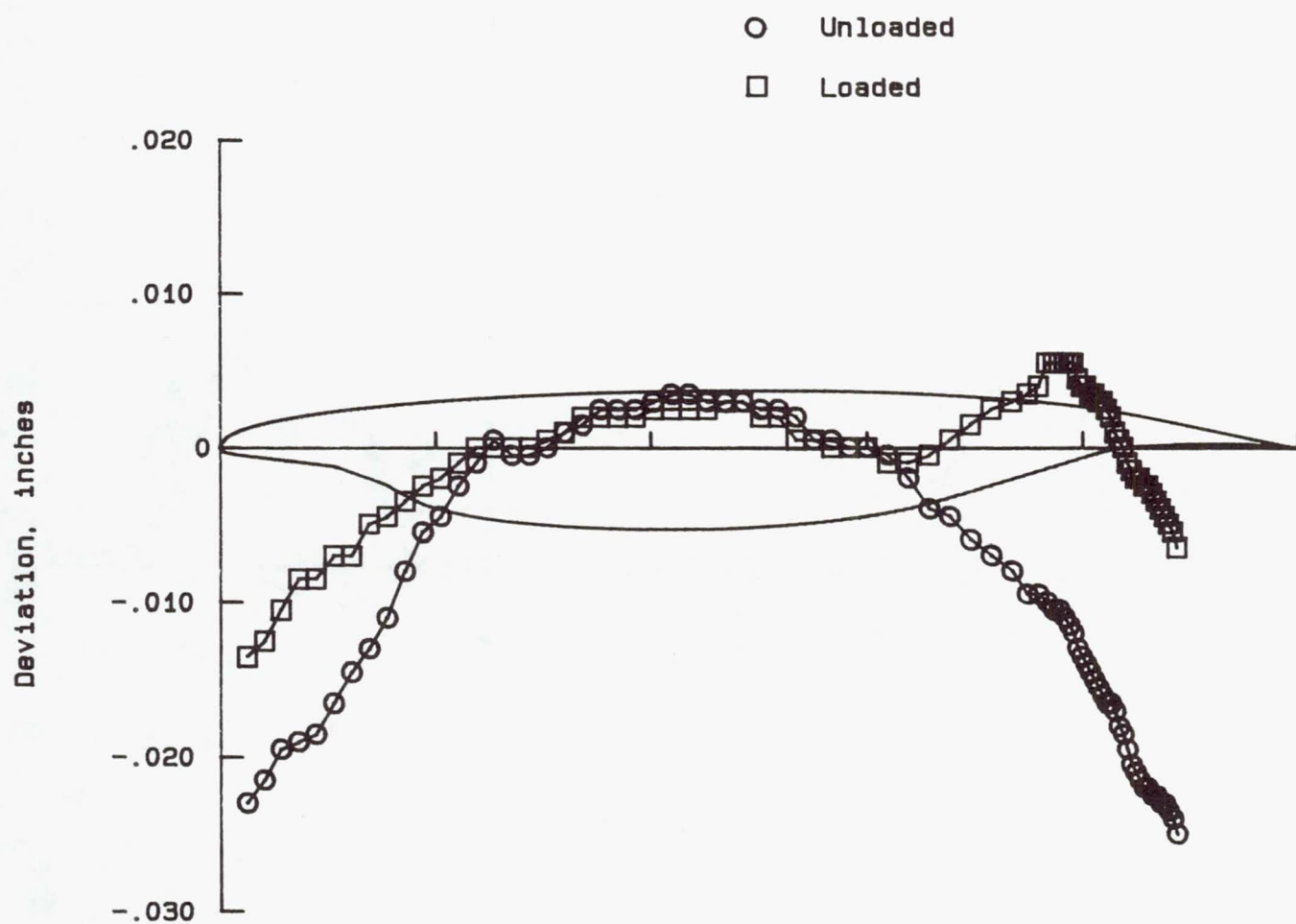
(a) Unloaded.

Figure 11. Effect of shims on deviation of upper surface from template along centerline.



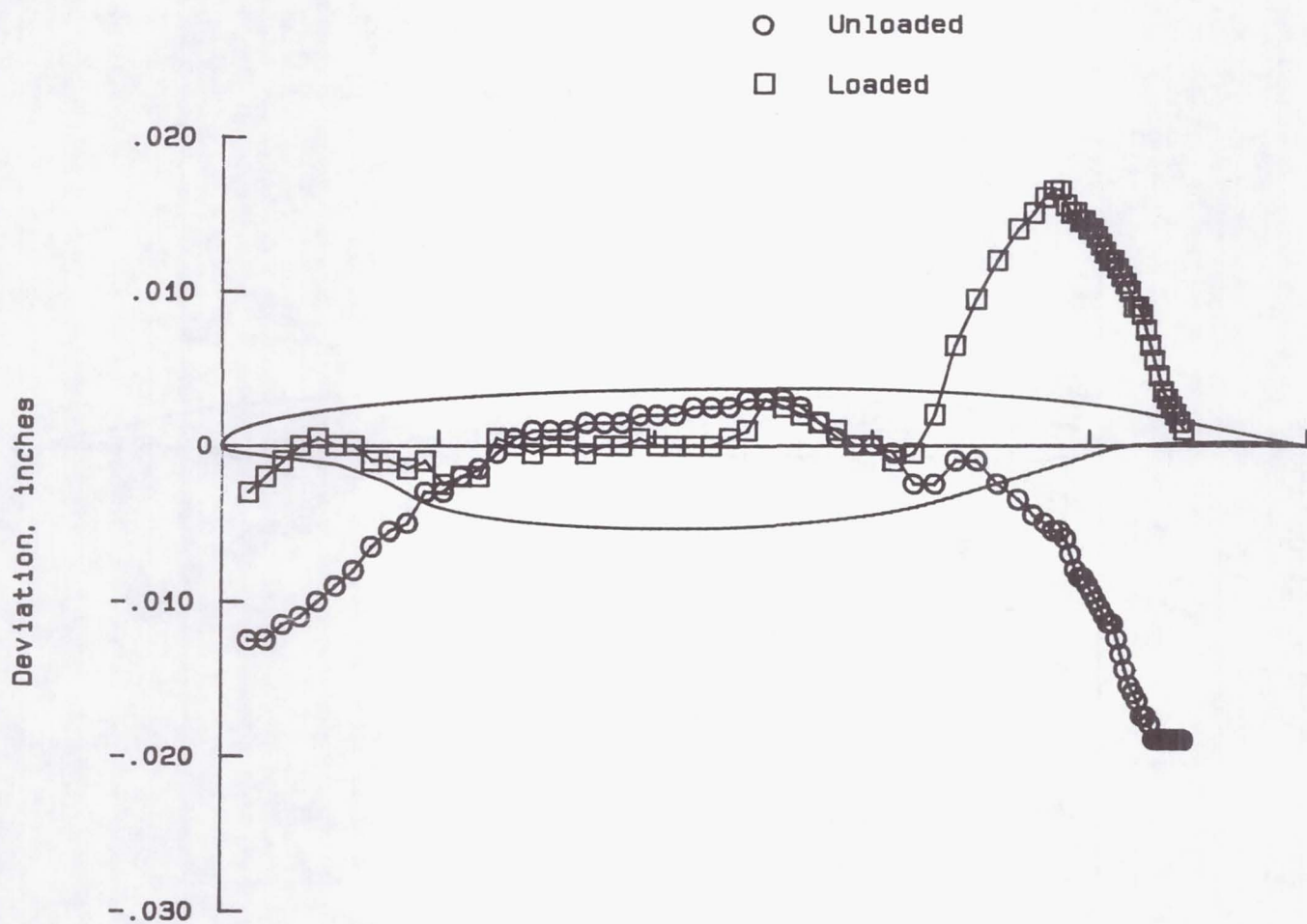
(b) Loaded.

Figure 11. Concluded.



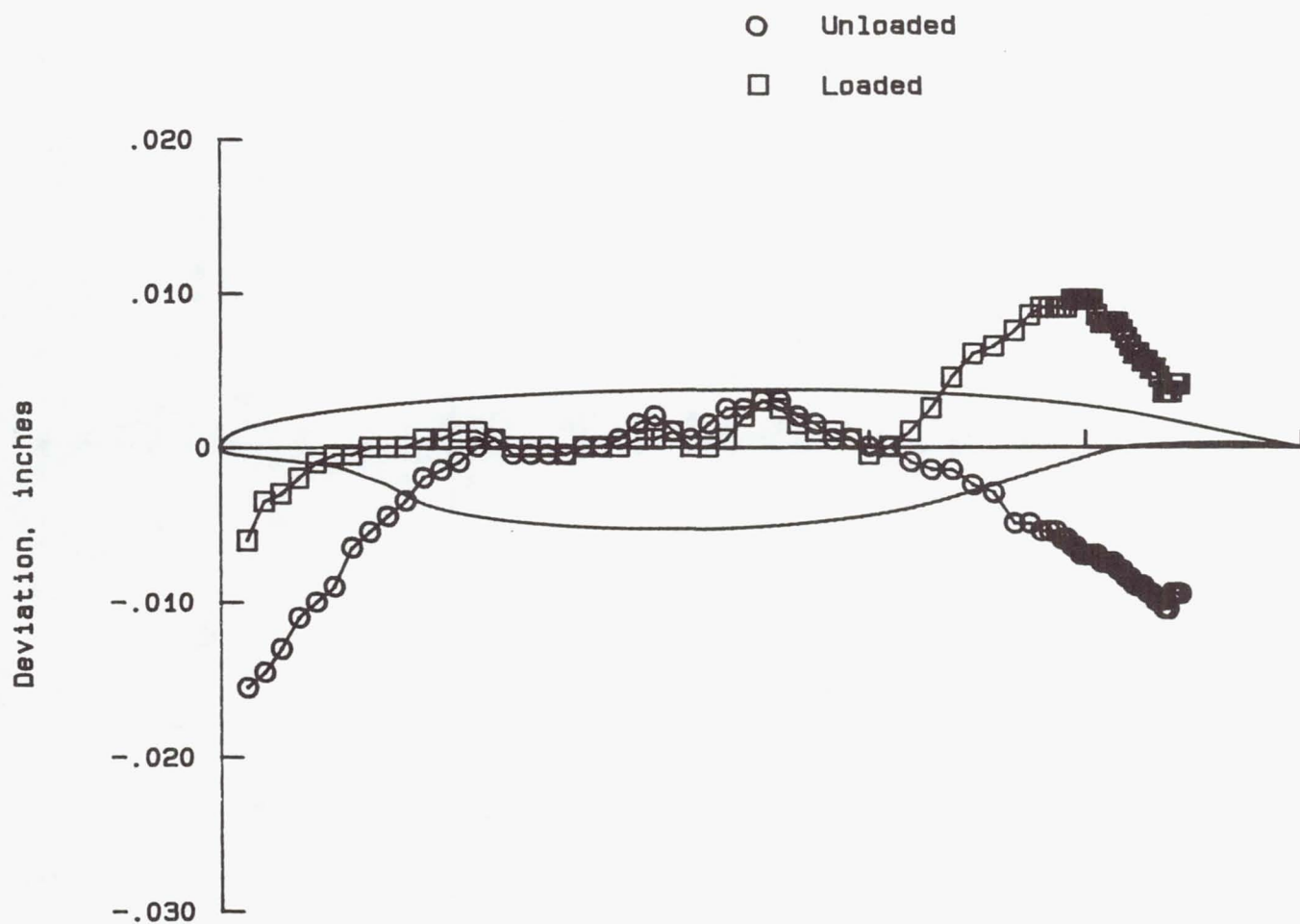
(a) 24 in. above centerline.

Figure 12. Deviation of upper surface from template for model with shims, with and without simulated load.



(b) Along centerline.

Figure 12. Continued.



(c) 24 in. below centerline.

Figure 12. Concluded.

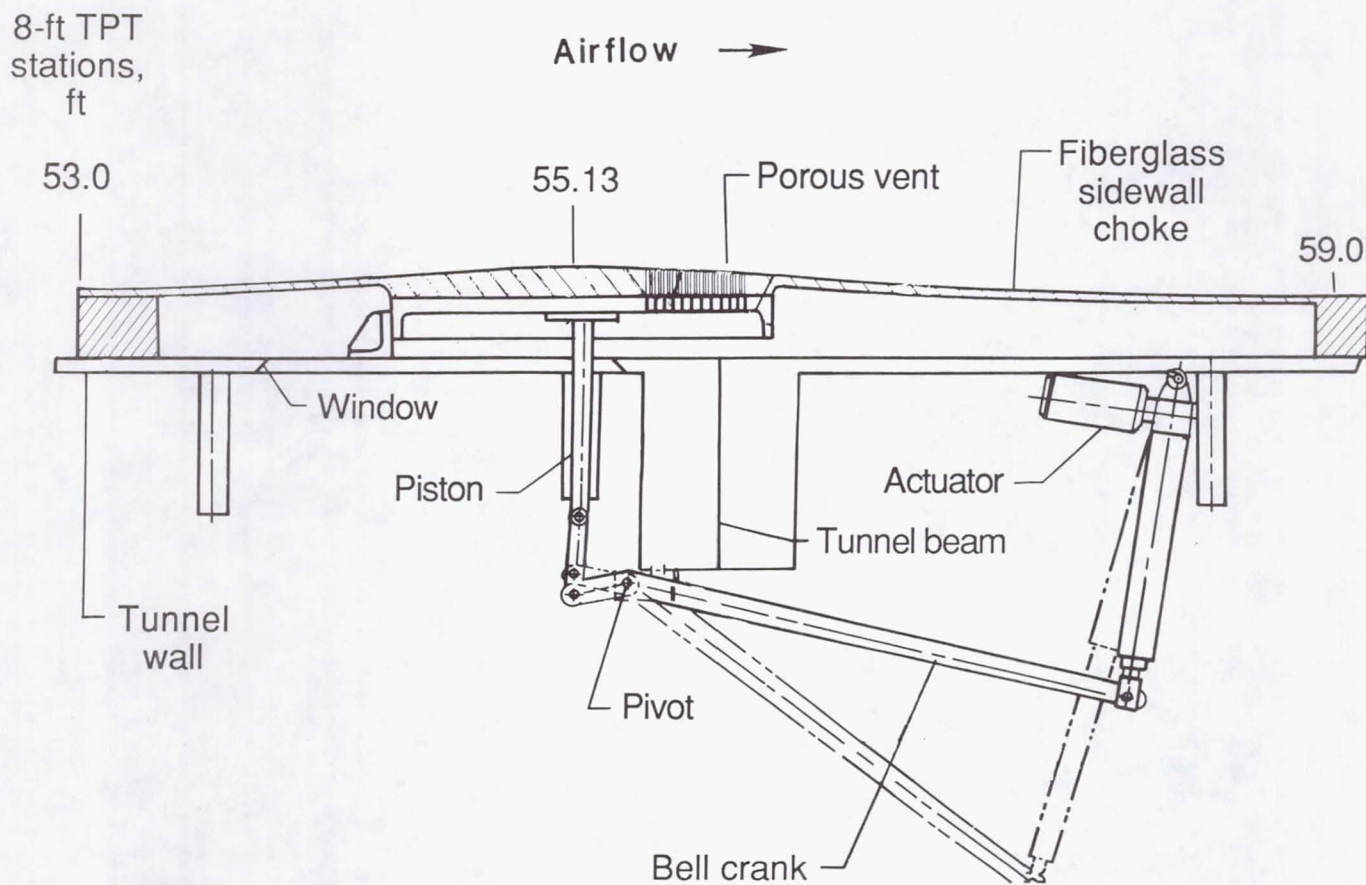
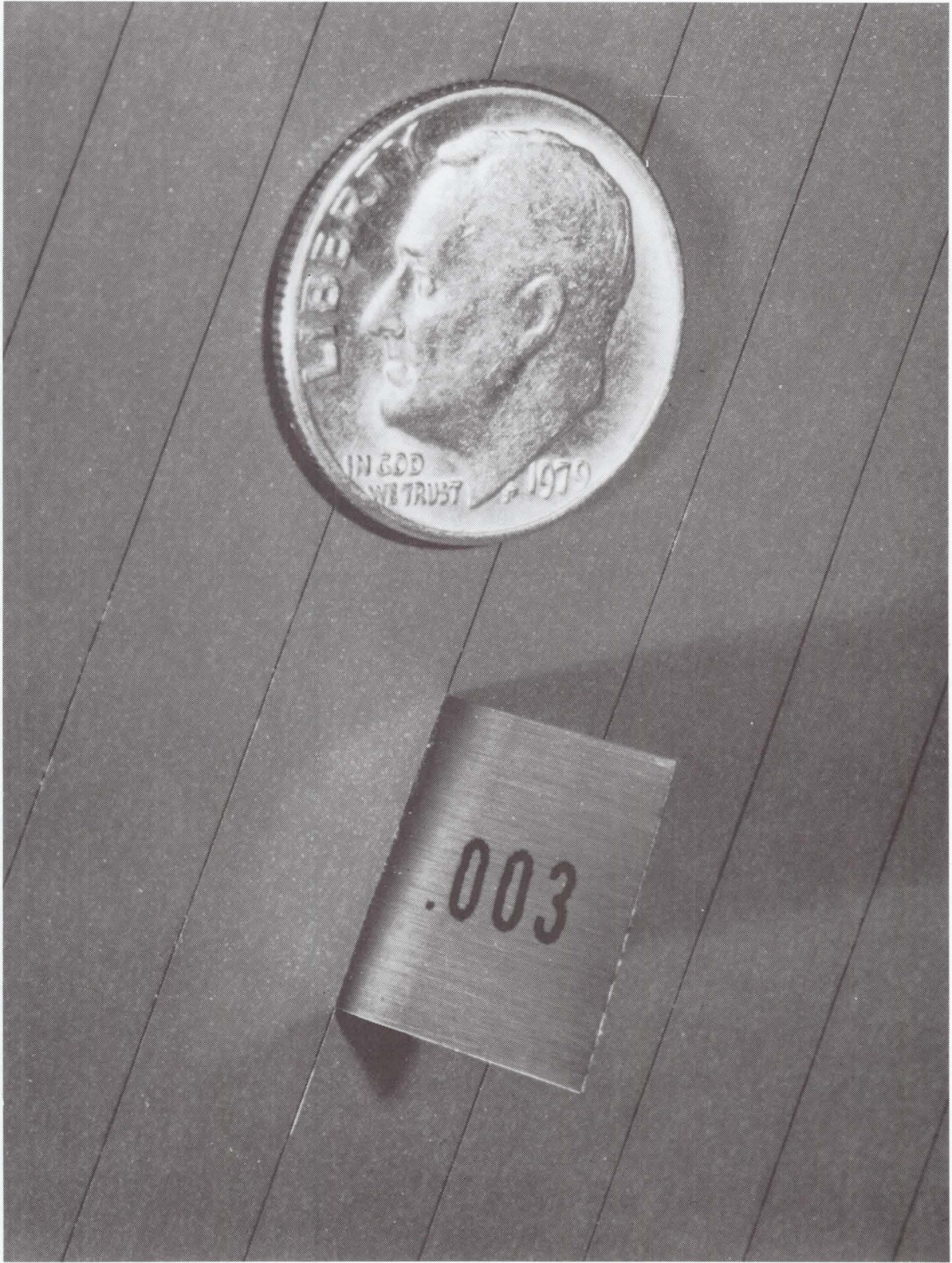
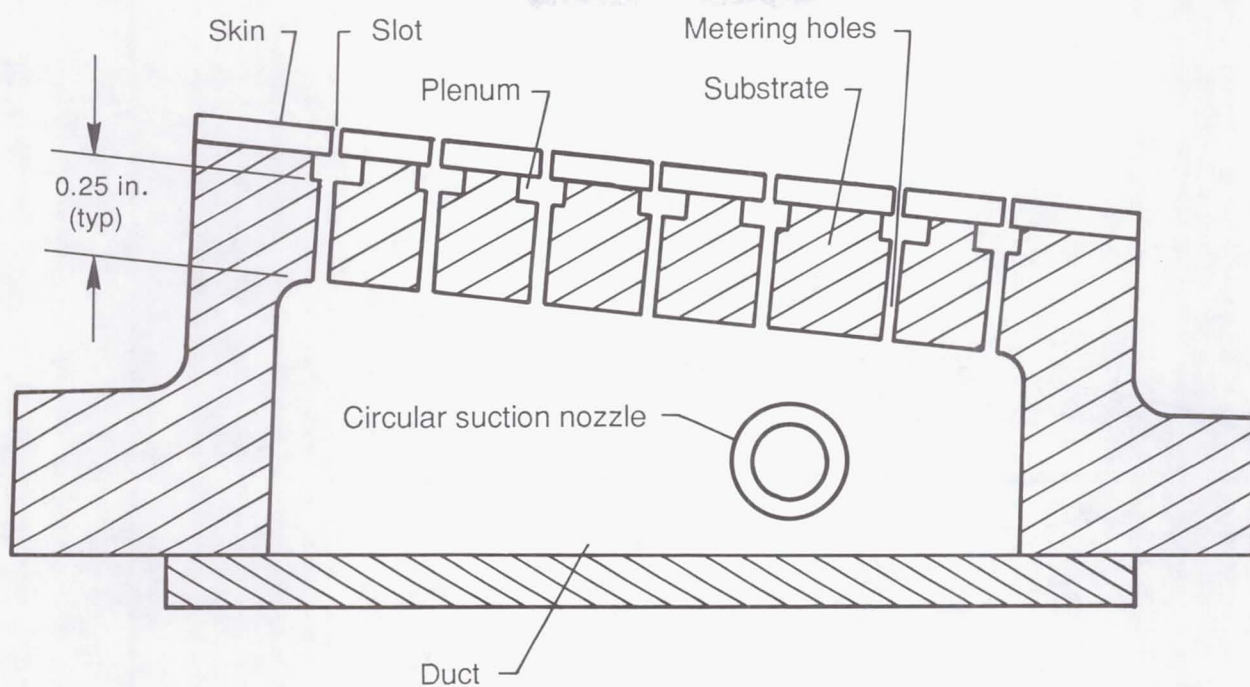


Figure 13. Sketch of adjustable choke plate.

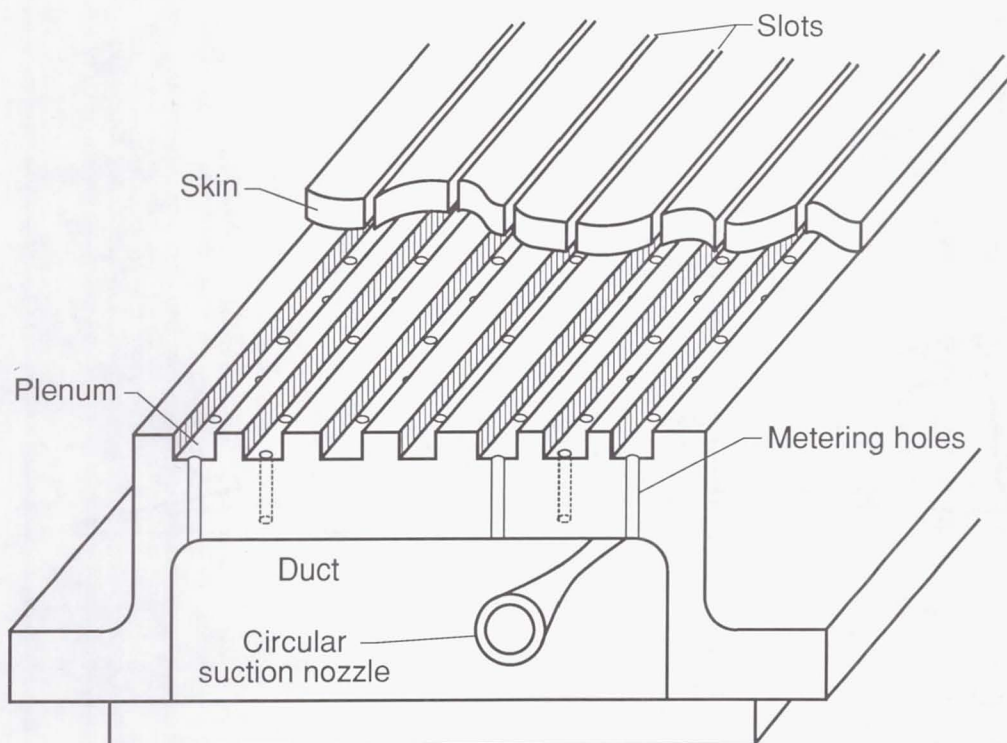


L-83-3975

Figure 14. Photograph of slotted suction surface.

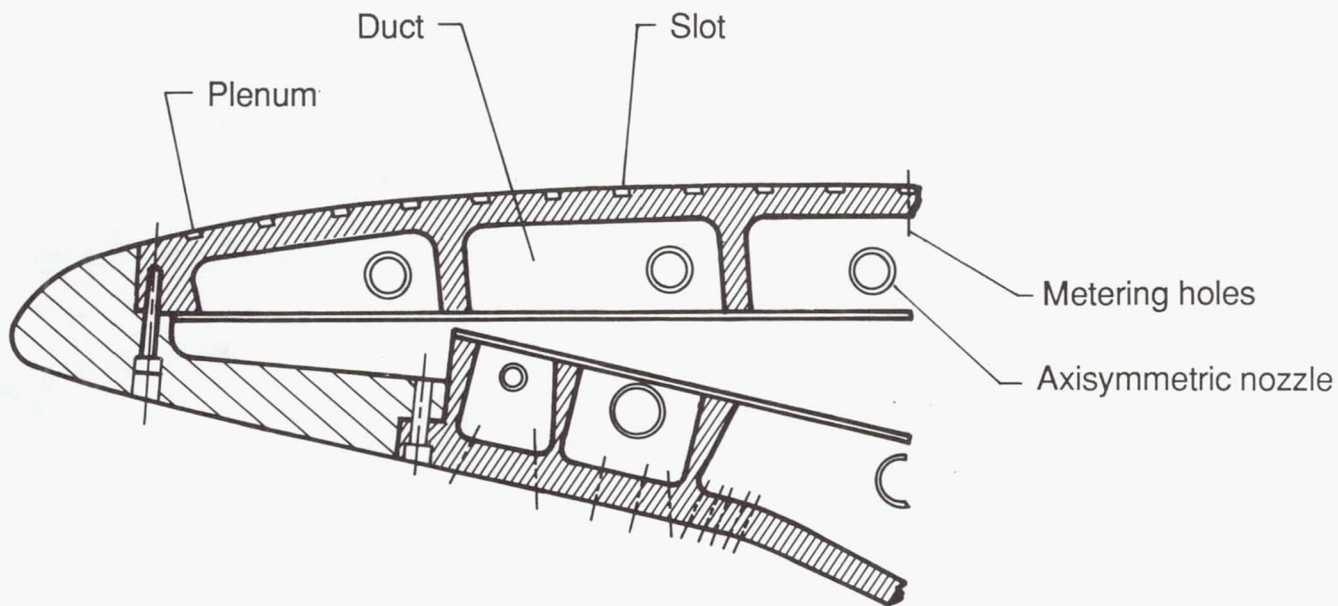


(a) Cross section sketch of suction duct.

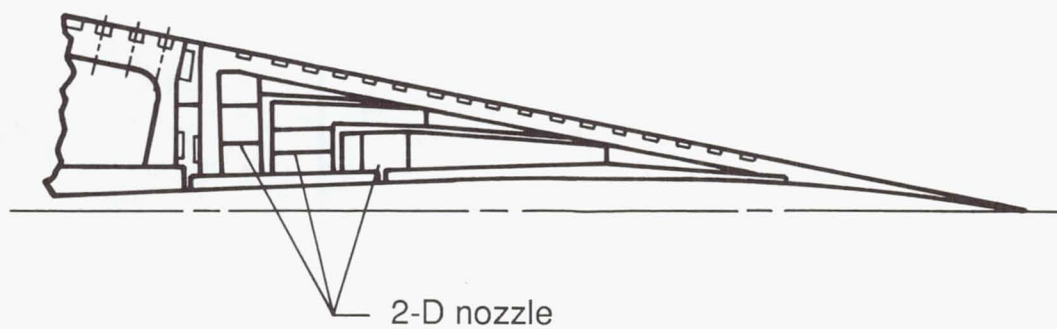


(b) Isometric sketch of suction duct.

Figure 15. Sketches and photographs of segments of suction system.



(c) Airfoil leading-edge region.



(d) Airfoil flap region.

Figure 15. Continued.

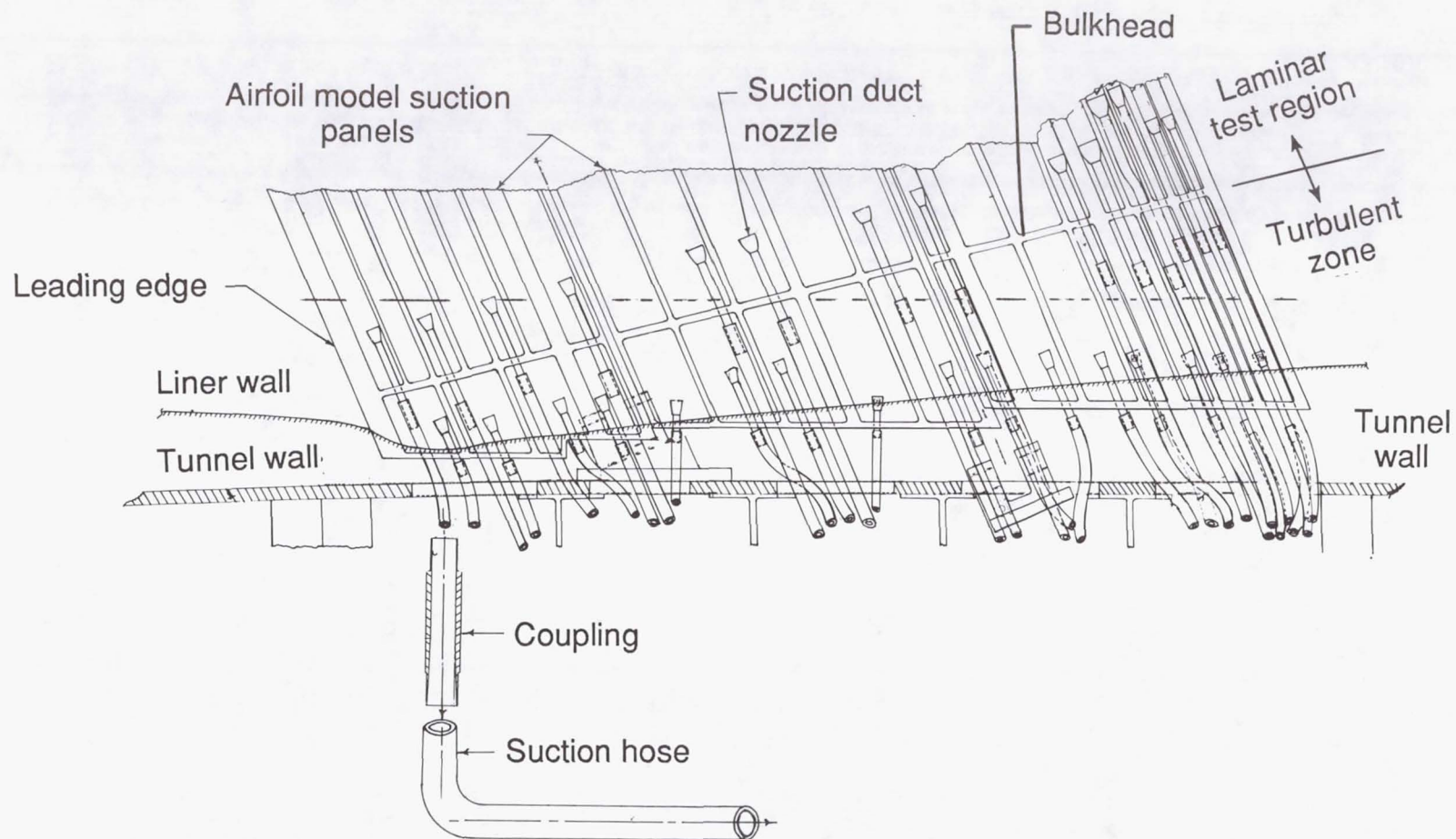
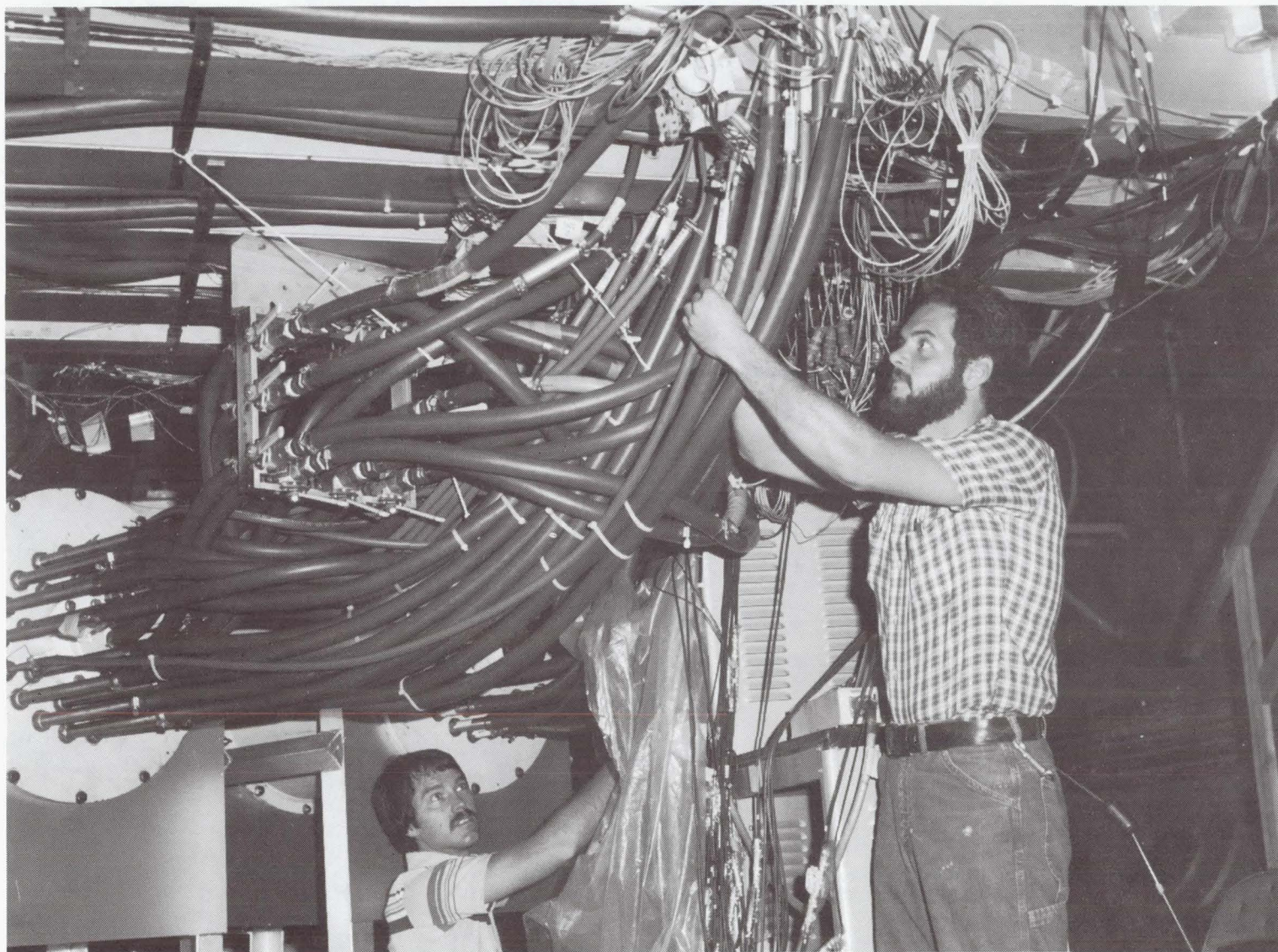


Figure 15. Continued.

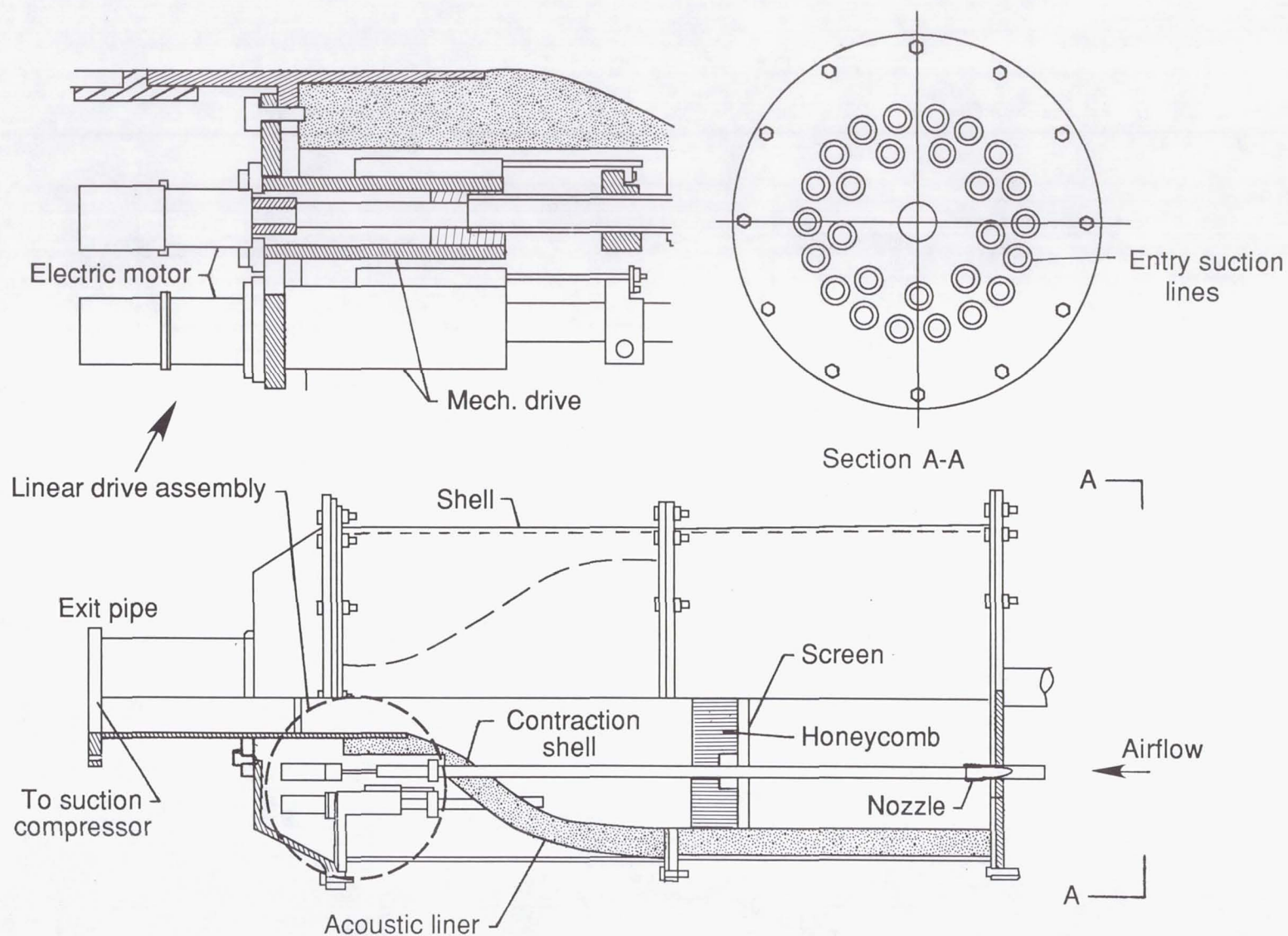
(e) Sketch of end of model nearest test section floor.



L-82-7940

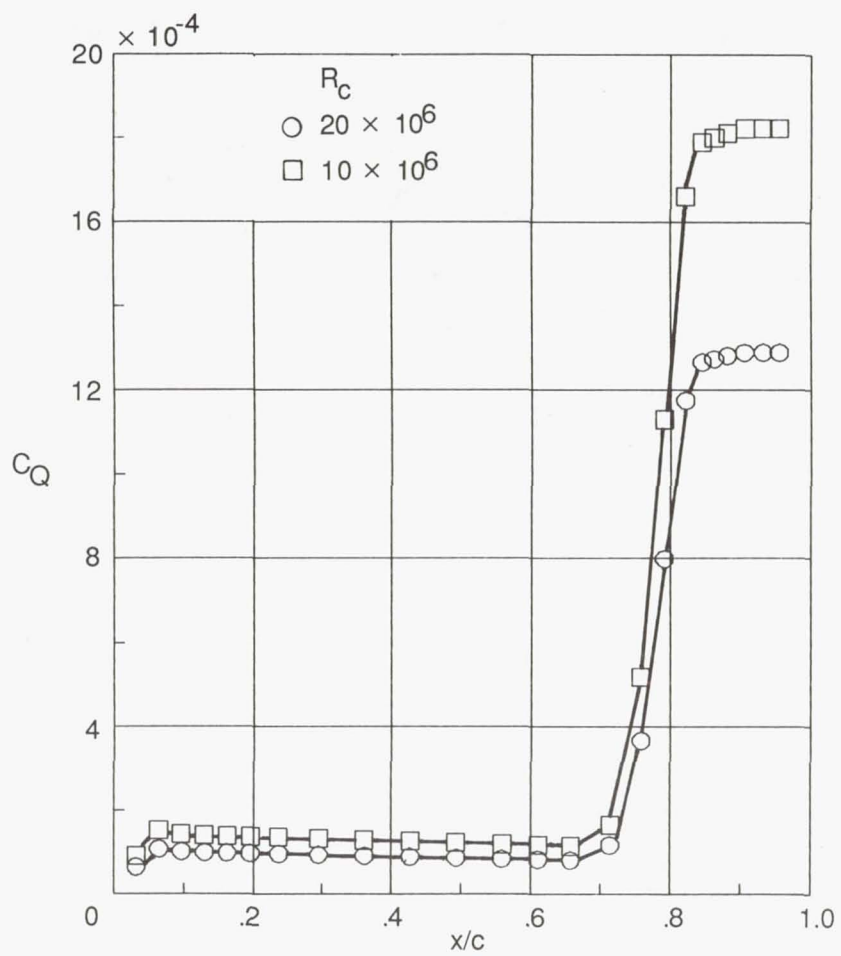
(f) Photograph of external connector hoses between end of model nearest test section floor and airflow control boxes.

Figure 15. Continued.

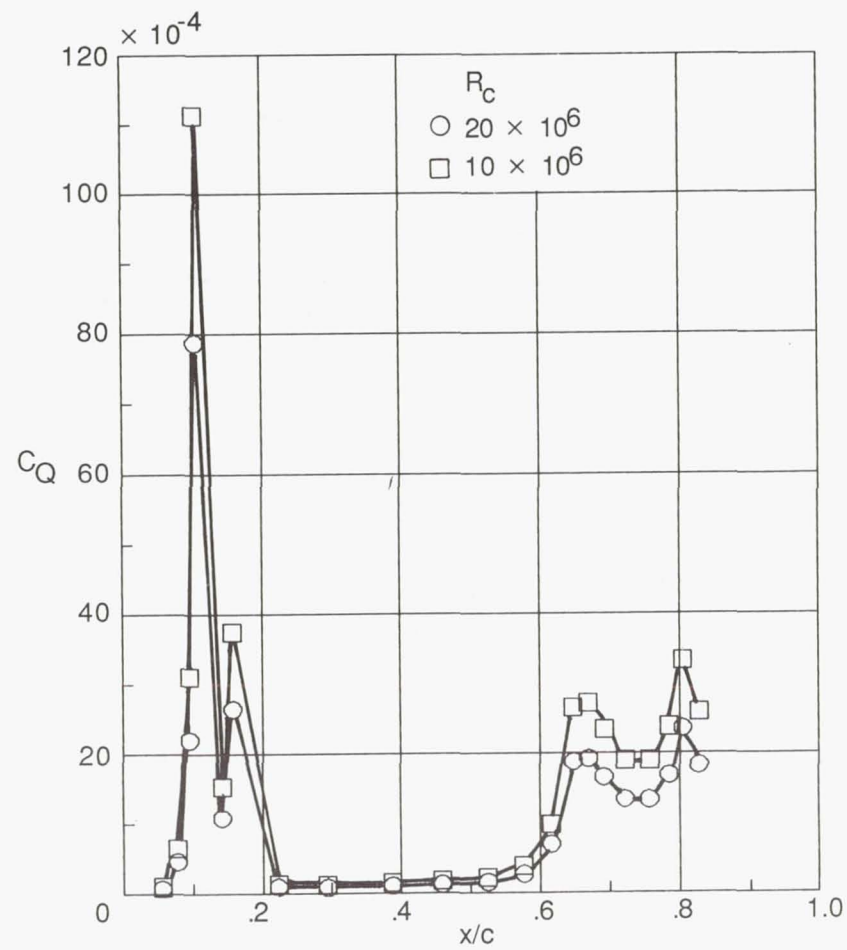


(g) Airflow control box.

Figure 15. Concluded.

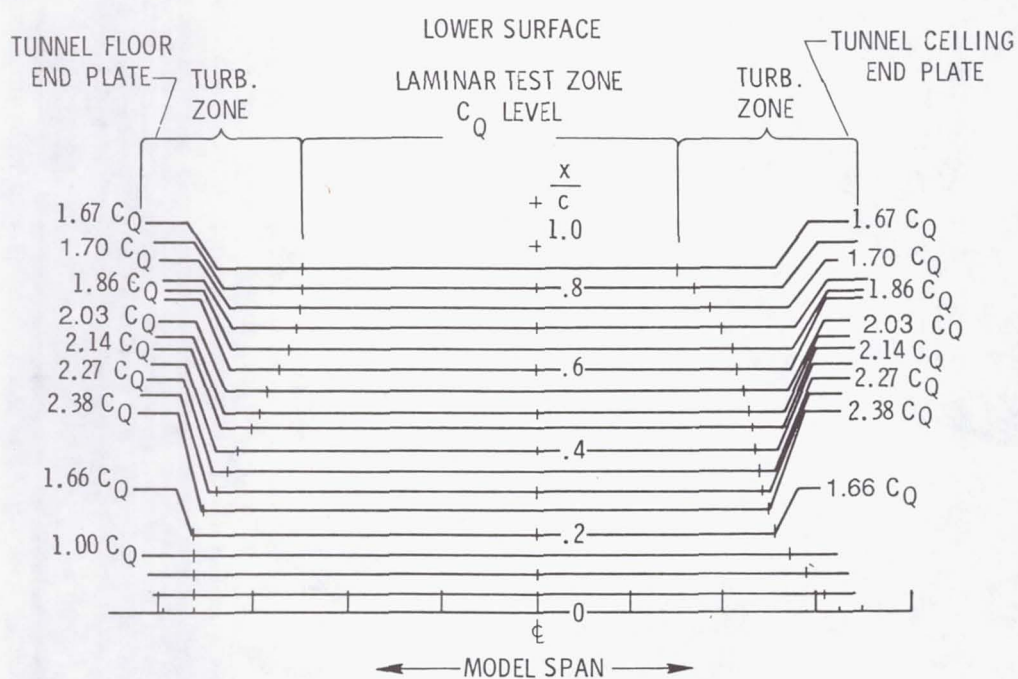
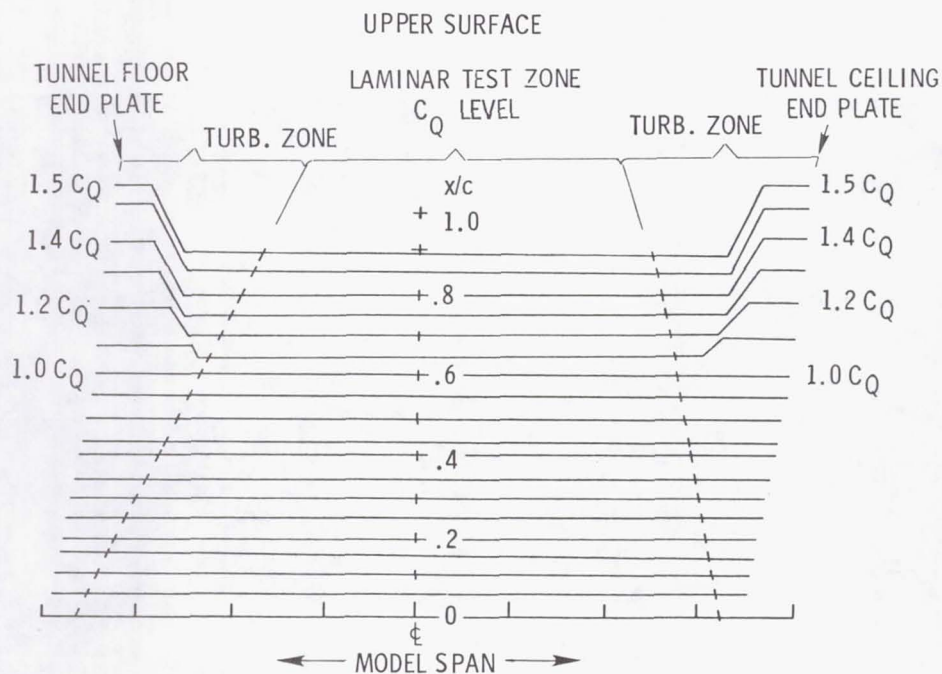


(a) Upper surface.



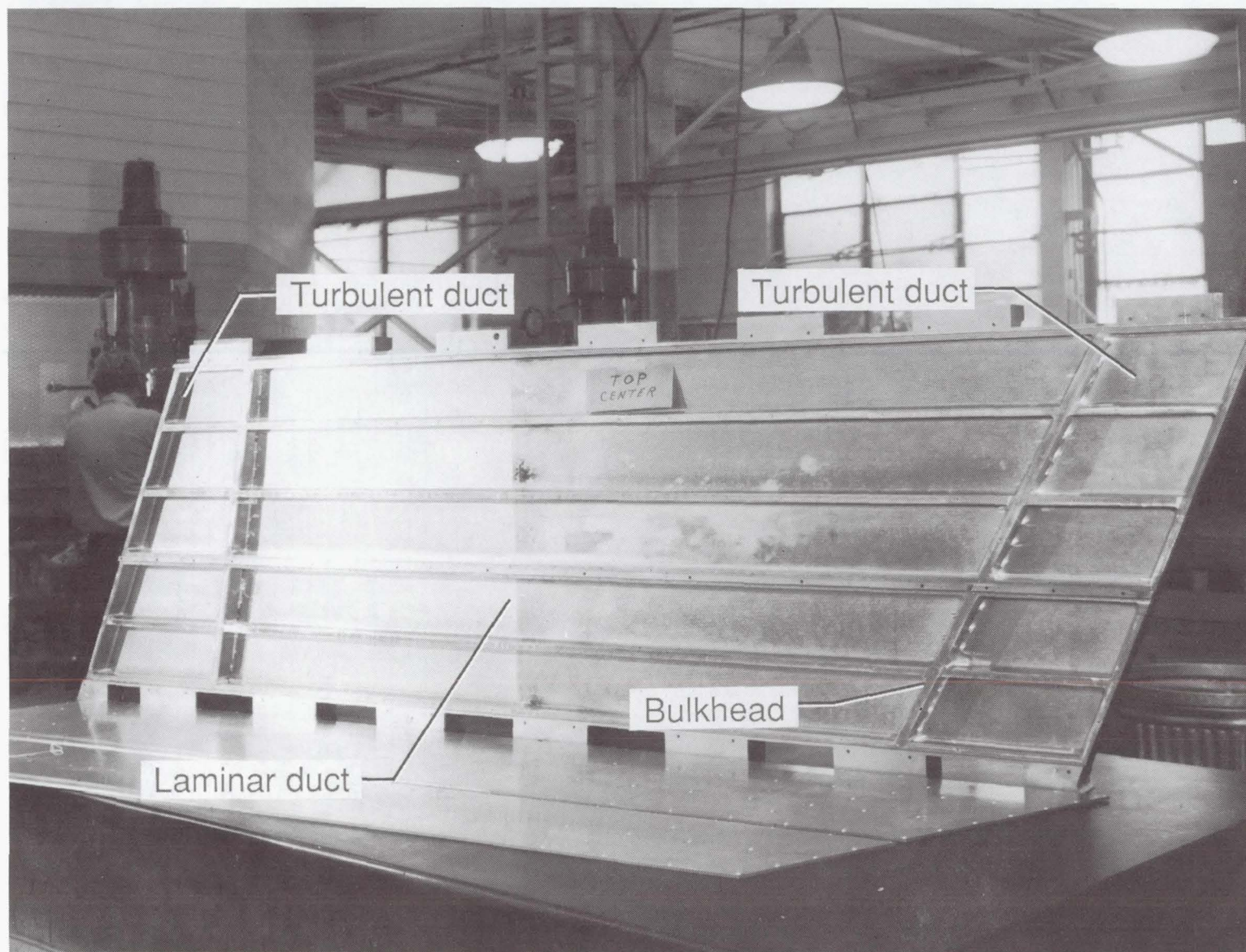
(b) Lower surface.

Figure 16. Theoretical suction requirements.



(c) Spanwise variation of design suction distribution ($R_c = 20 \times 10^6$).

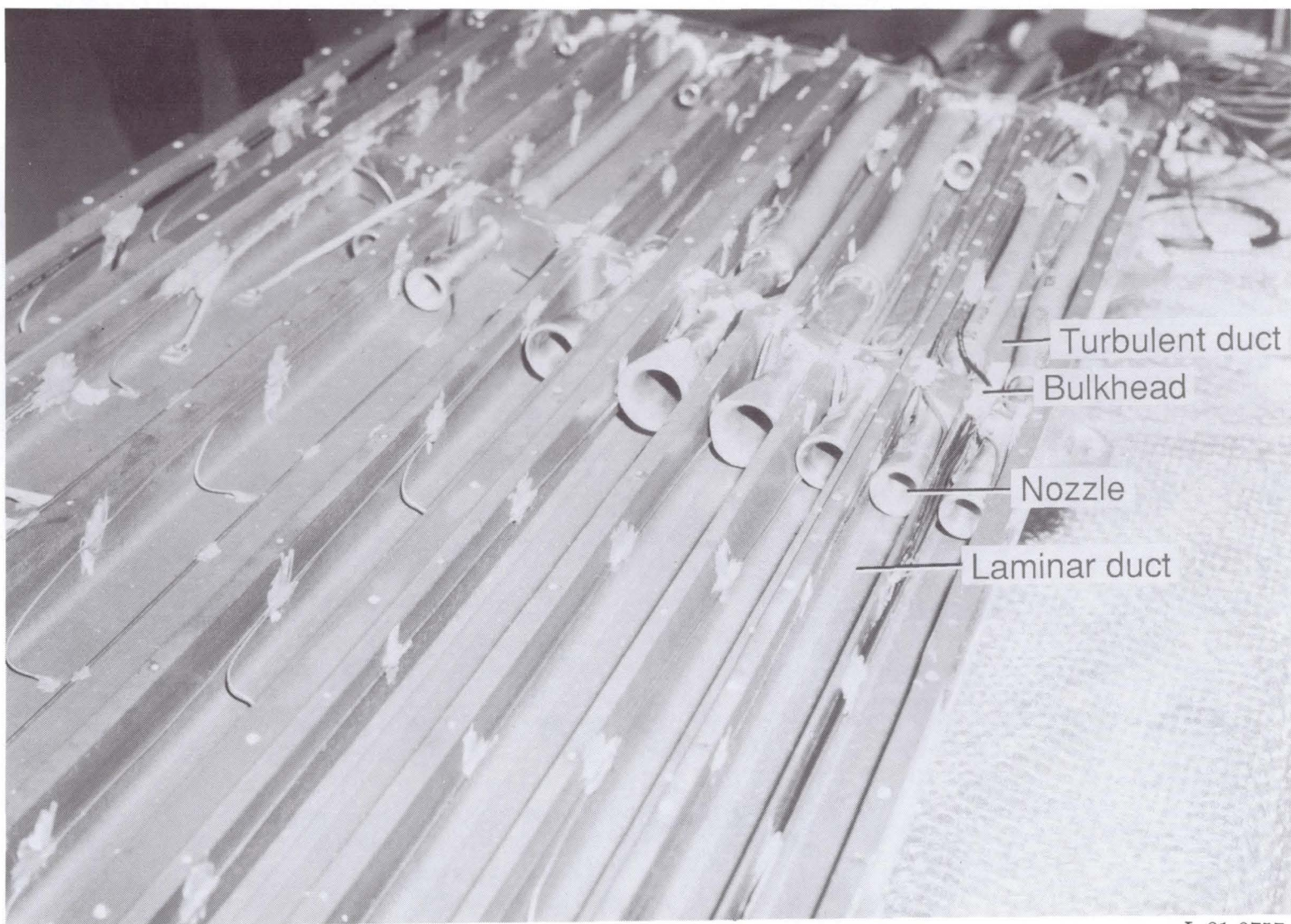
Figure 16. Concluded.



L-79-5436

(a) Photograph of ducts machined in upper surface middle panel.

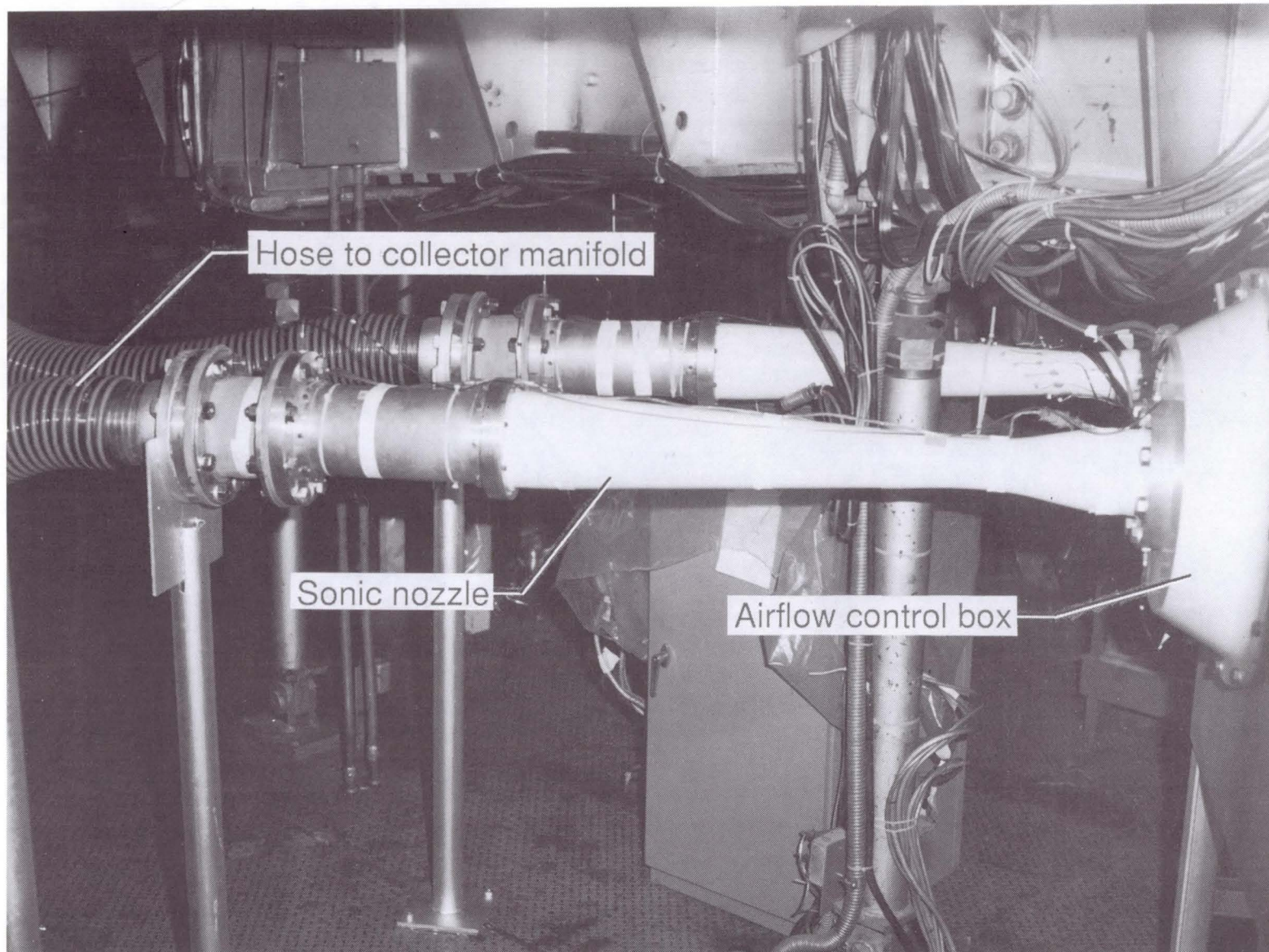
Figure 17. Photographs of airfoil suction ducts and nozzles.



L-81-8757

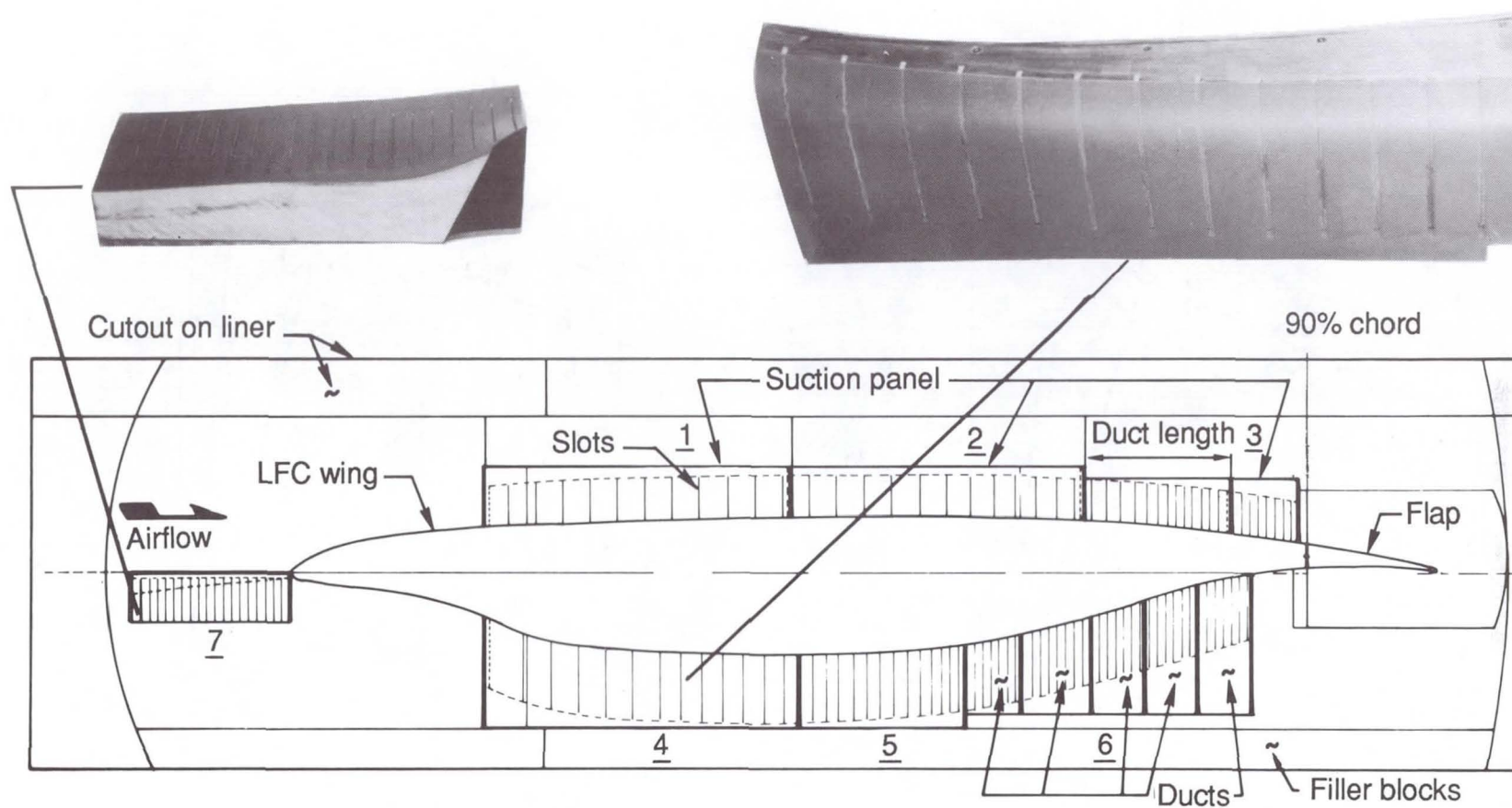
(b) Upper surface aft panel.

Figure 17. Concluded.



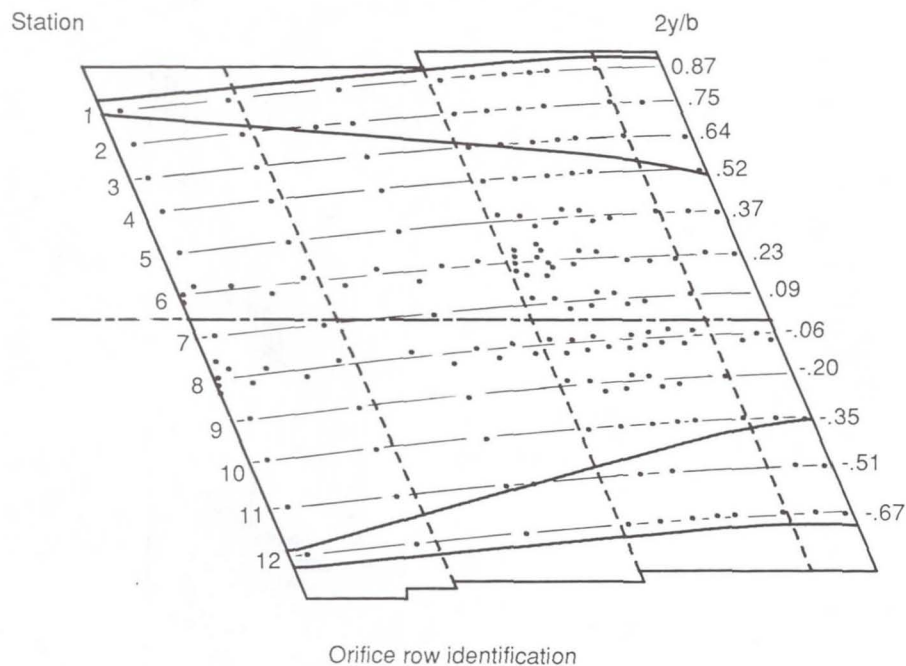
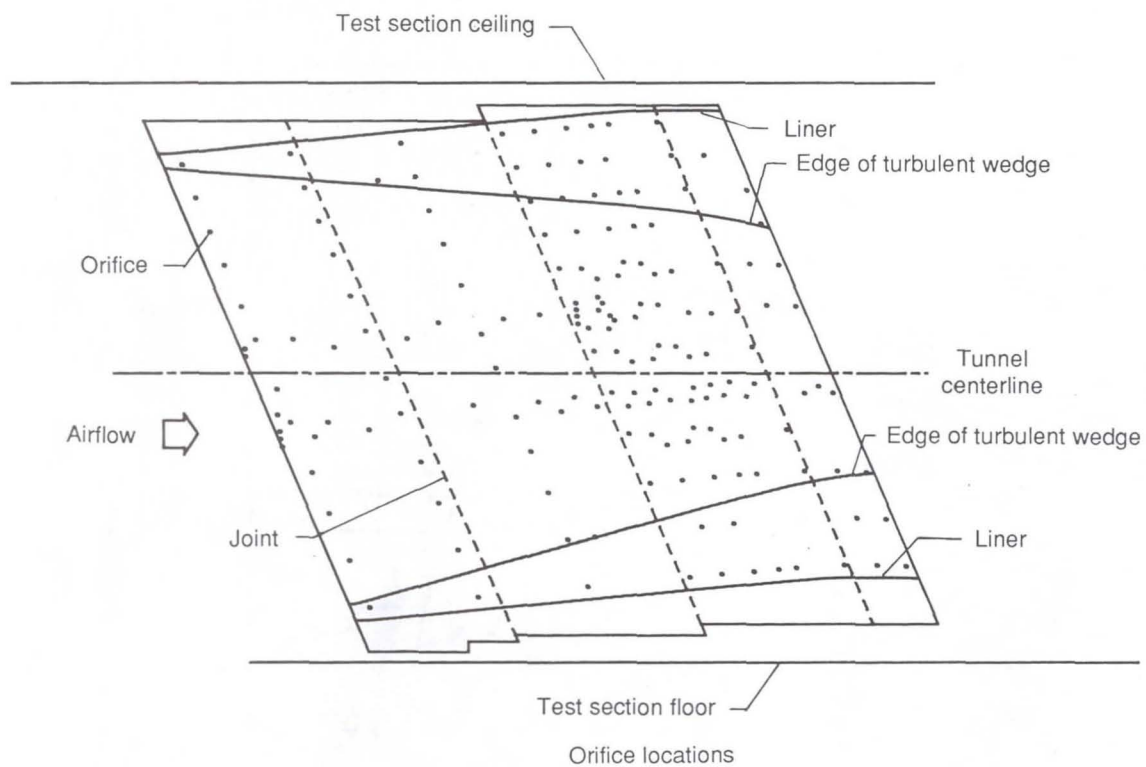
L-82-7944

Figure 18. Photograph of installed variable sonic nozzles.



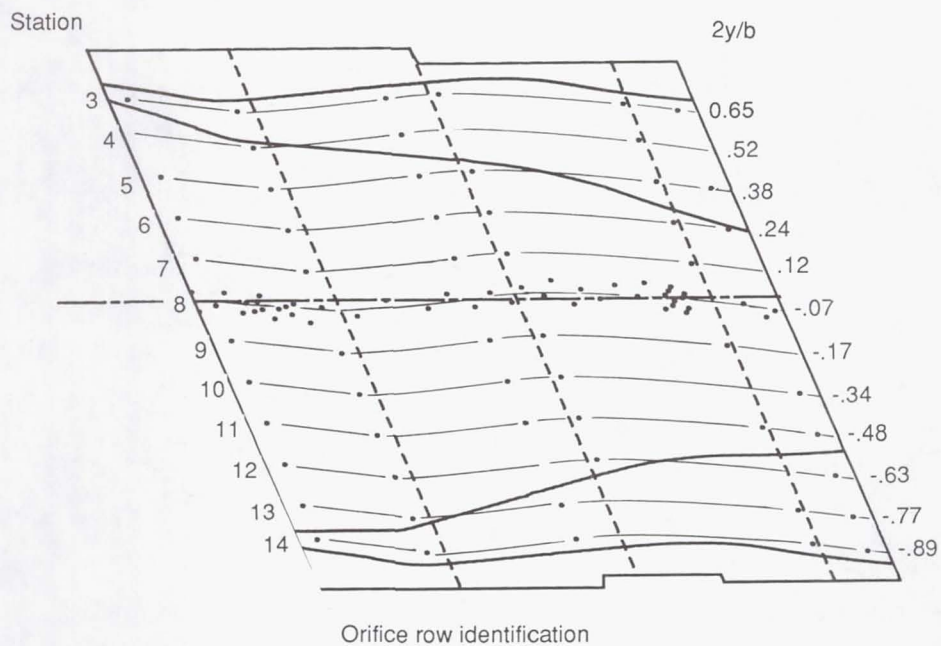
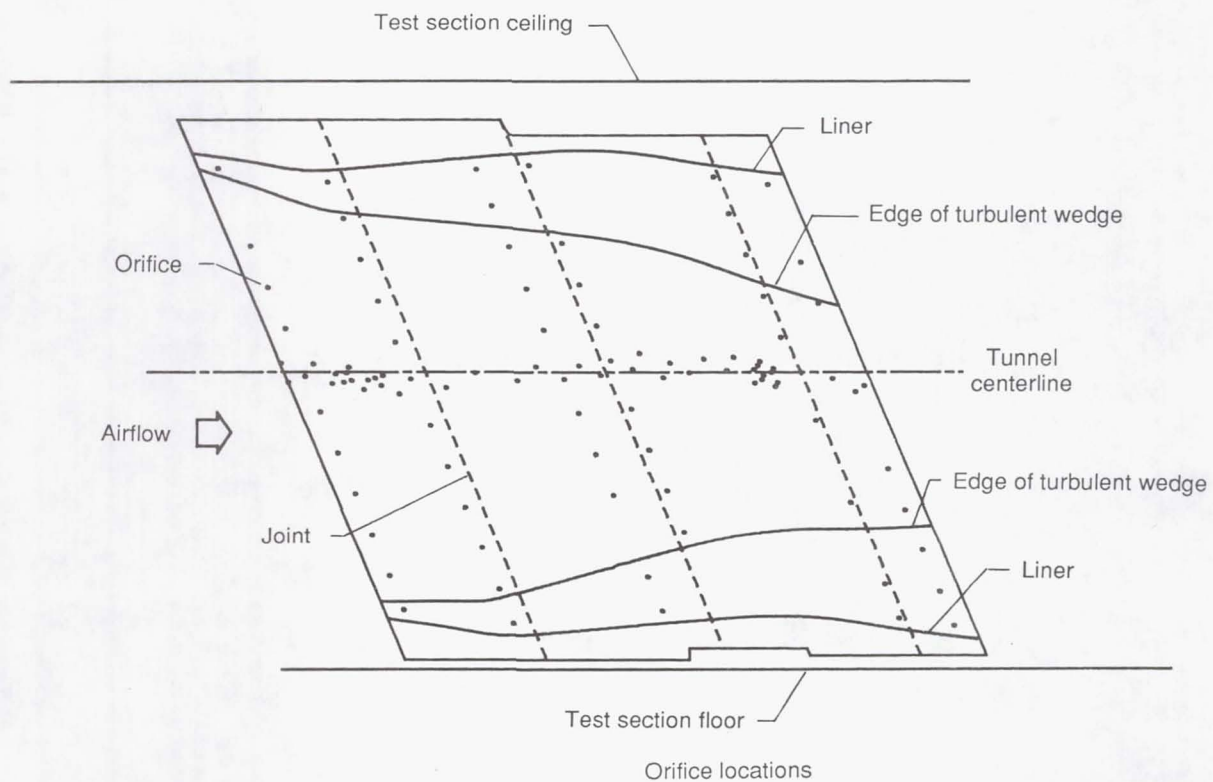
End plate view

Figure 19. Liner suction collar.



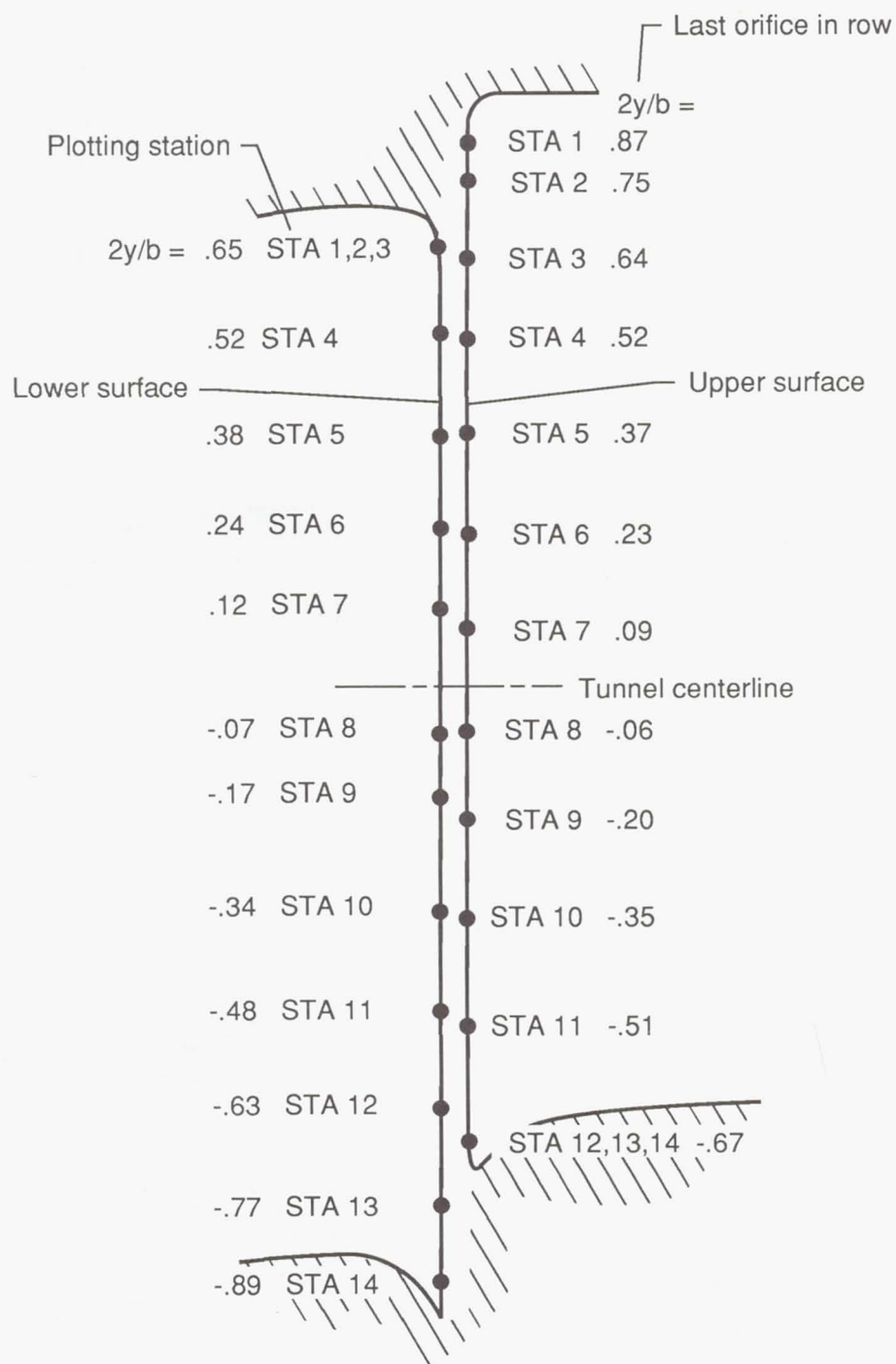
(a) Upper-surface planform.

Figure 20. Sketches of slotted LFC model showing actual locations of pressure orifices.



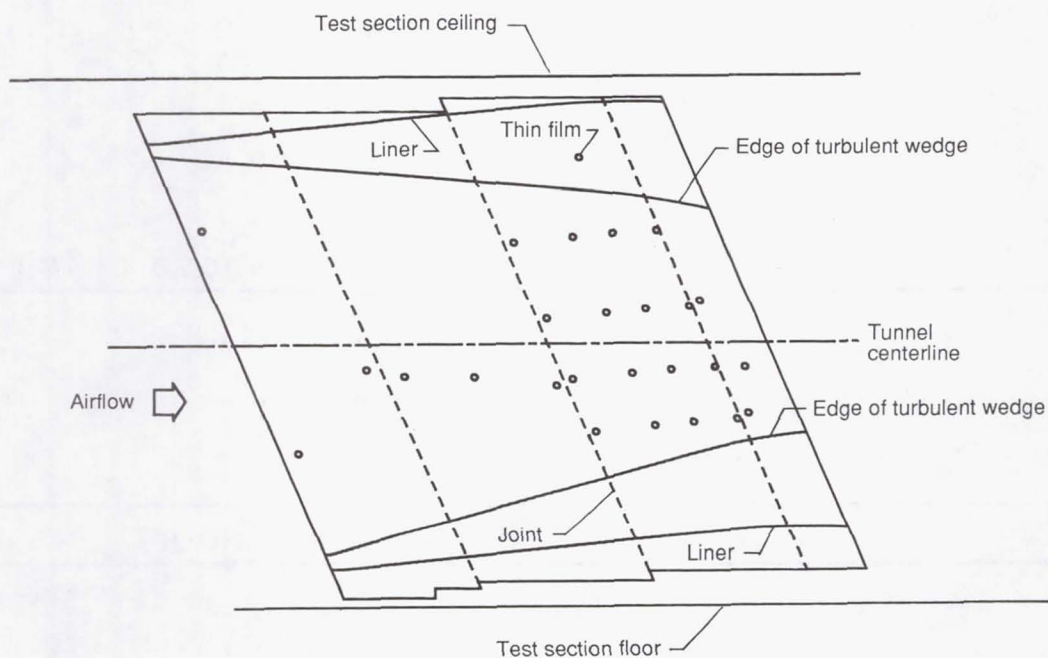
(b) Lower-surface planform.

Figure 20. Continued.

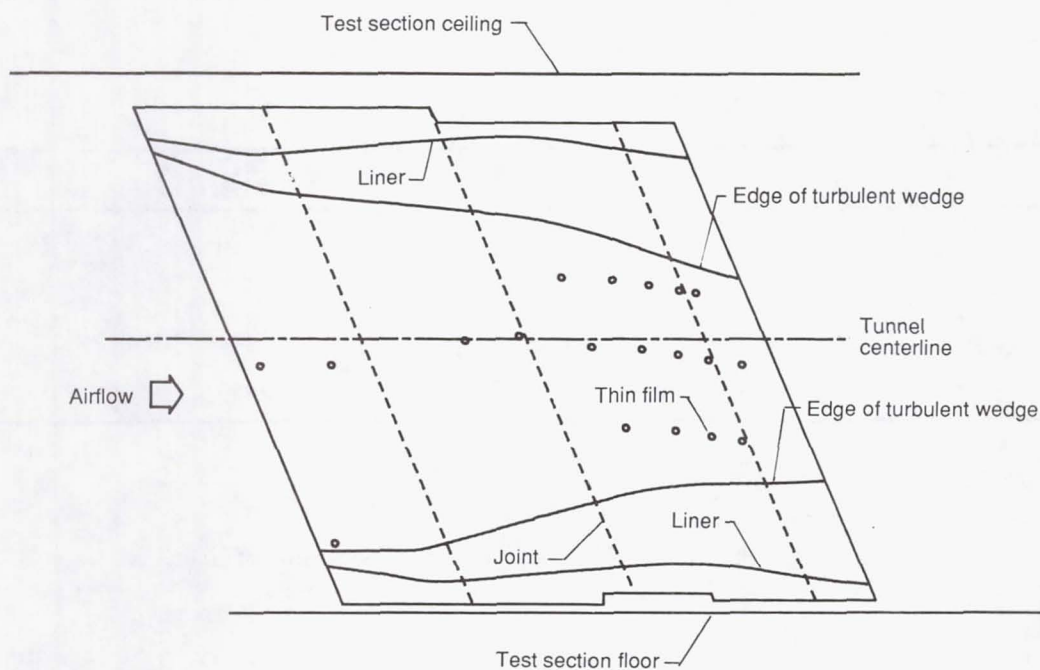


(c) Upstream view of trailing edge showing spanwise locations of last orifice in each row.

Figure 20. Concluded.

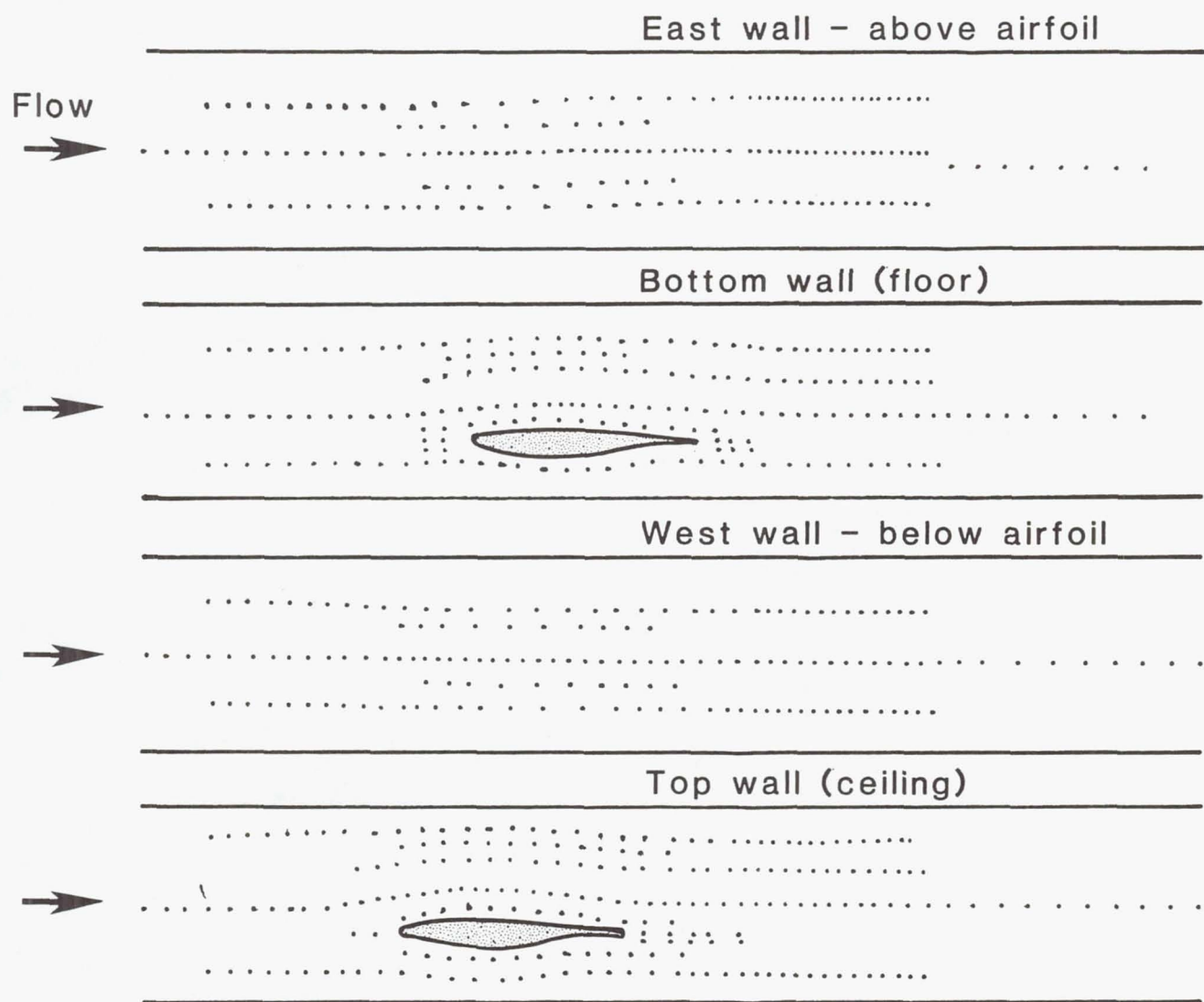


(a) Upper-surface planform as viewed through model from beneath lower surface.



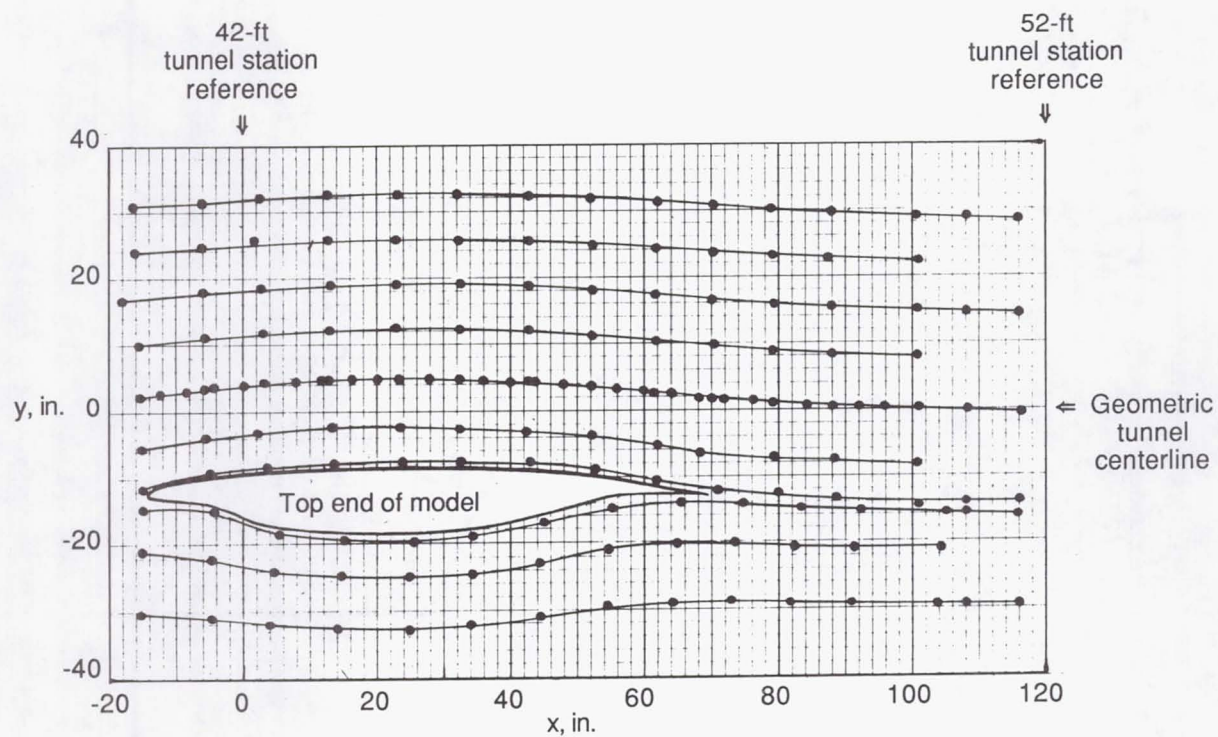
(b) Lower-surface planform as viewed from beneath lower surface.

Figure 21. Sketches of slotted LFC model showing actual locations of thin films.

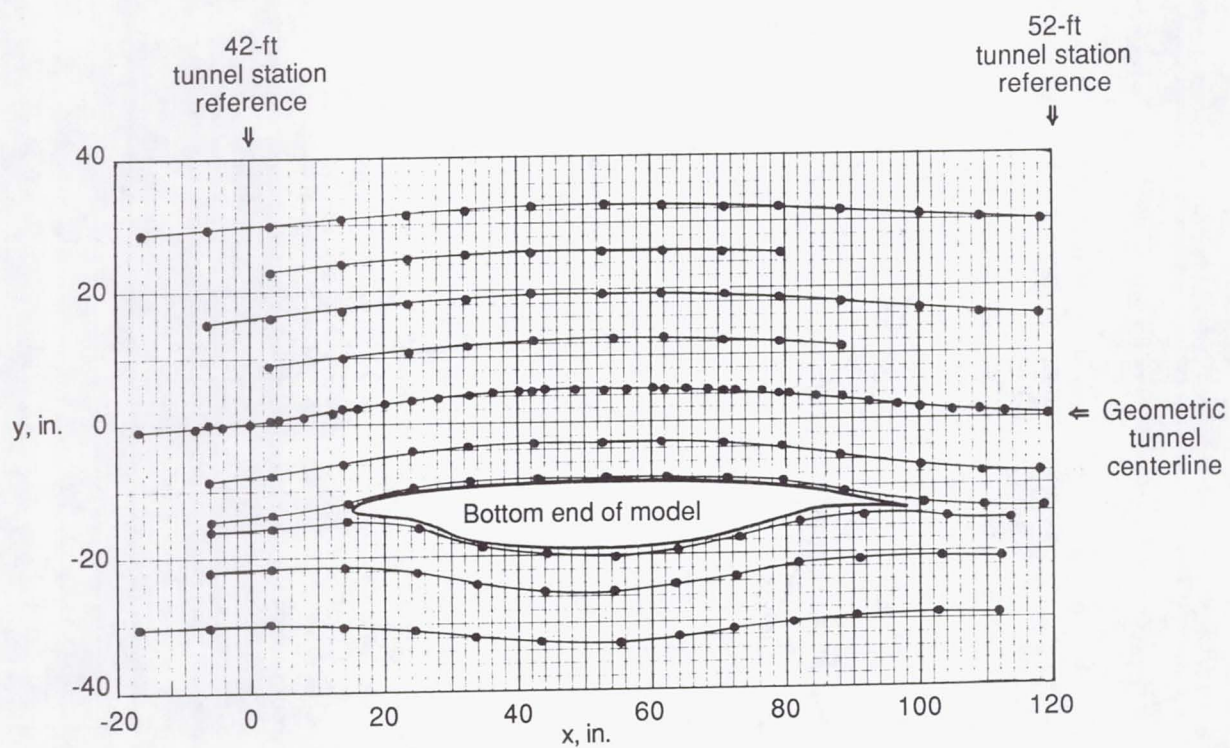


(a) Overall locations.

Figure 22. Pressure orifice locations over four walls of liner.

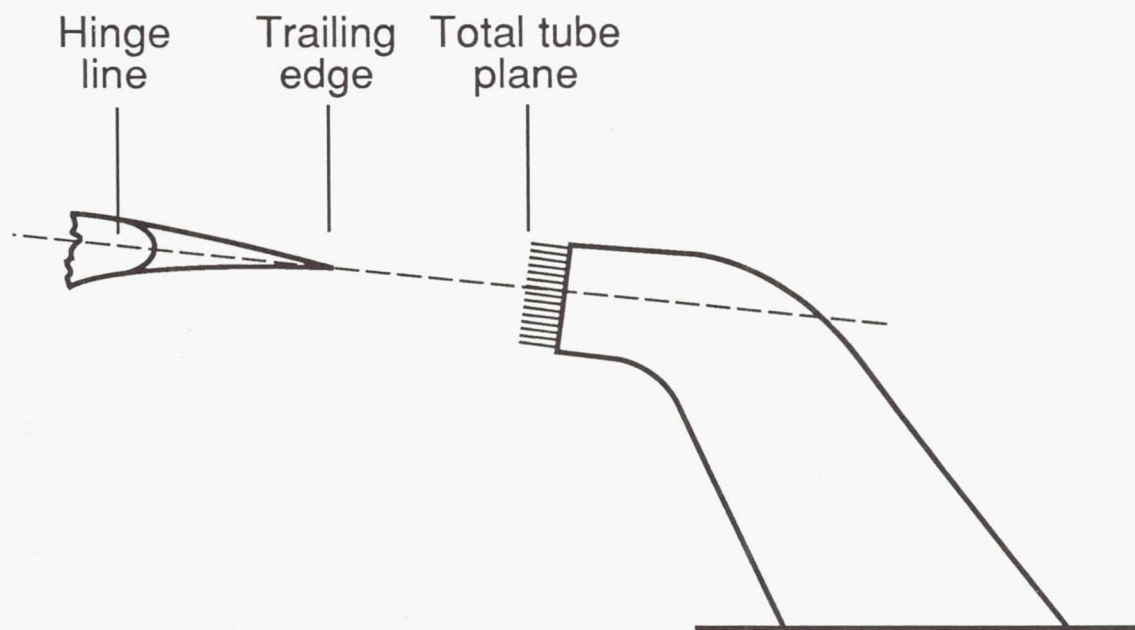


(b) Orifices around model on ceiling of test section.

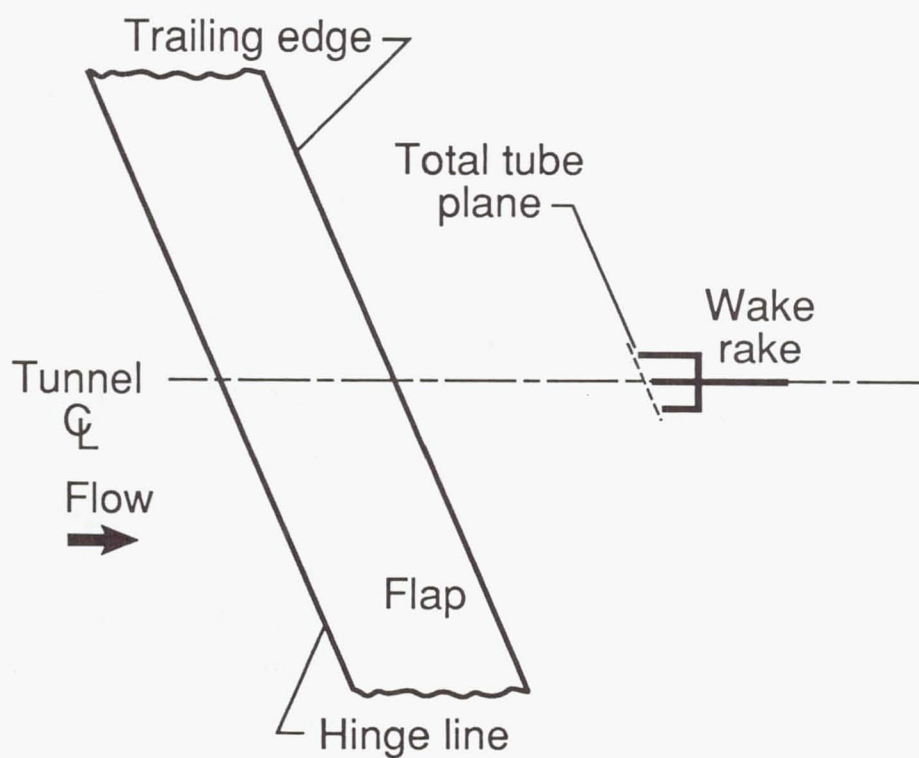


(c) Orifices around model on floor of test section.

Figure 22. Concluded.

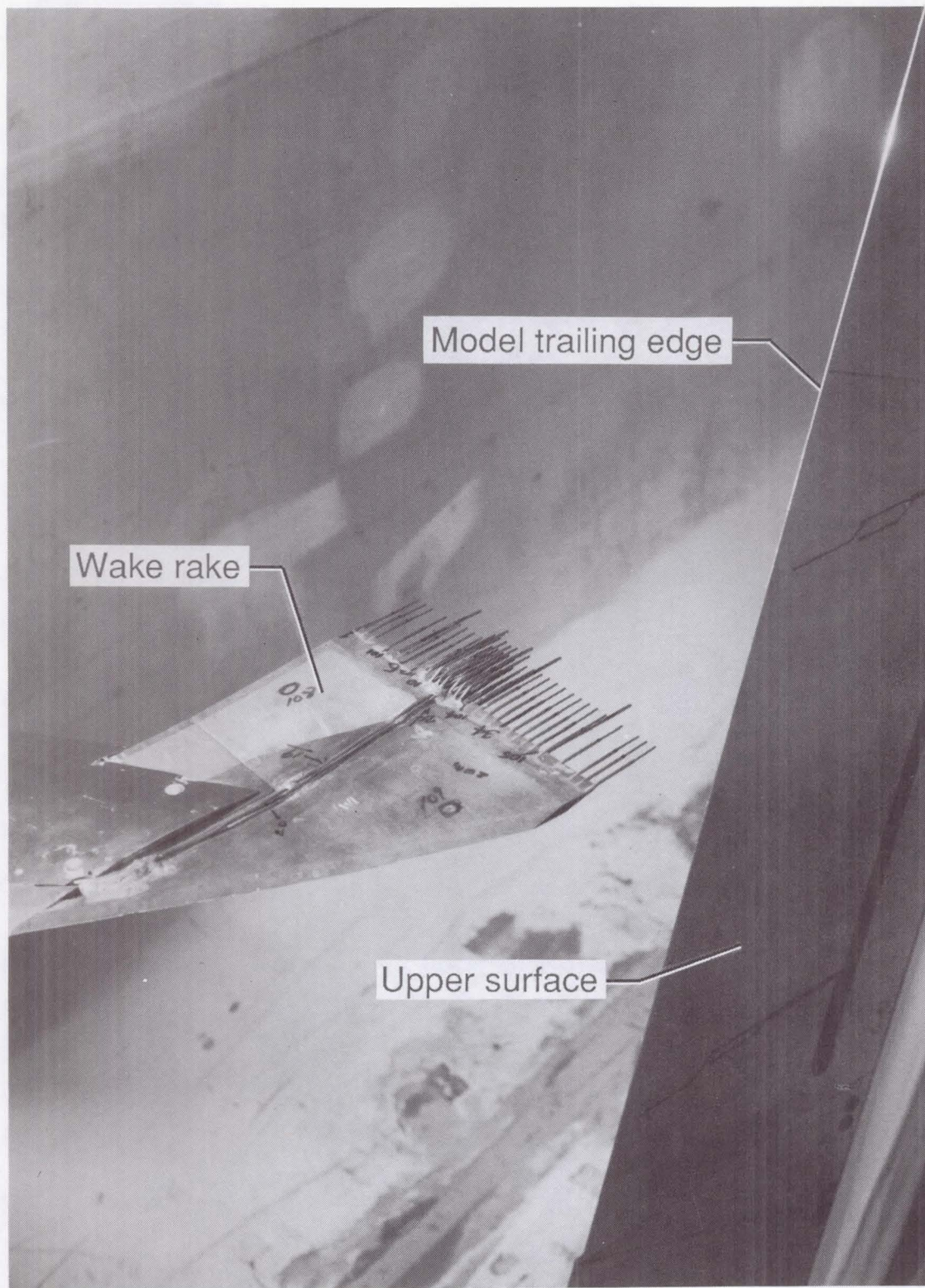


(a) Top view.



(b) Side view from wing lower-surface side of tunnel.

Figure 23. Sketches and photographs of profile drag rake.



L-86-6134

(c) Photograph of profile rake behind trailing edge of model.

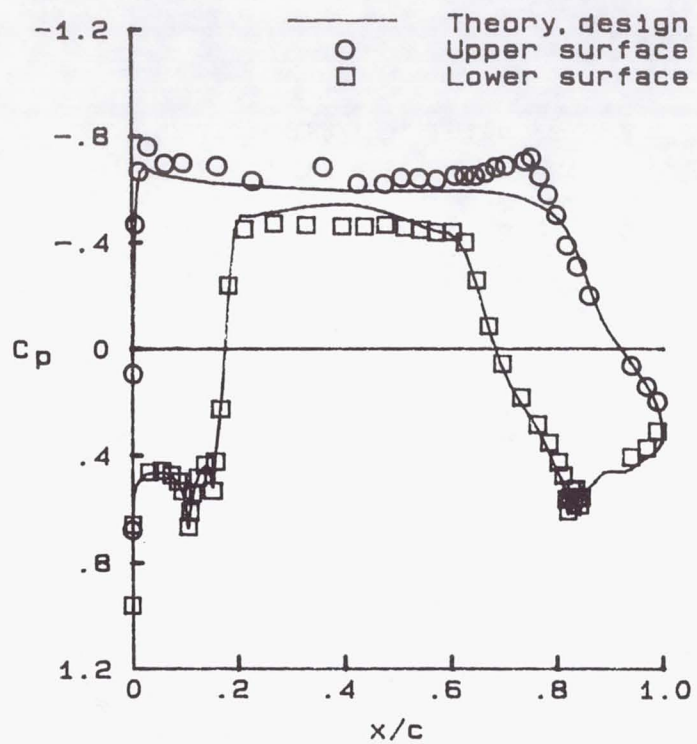
Figure 23. Continued.



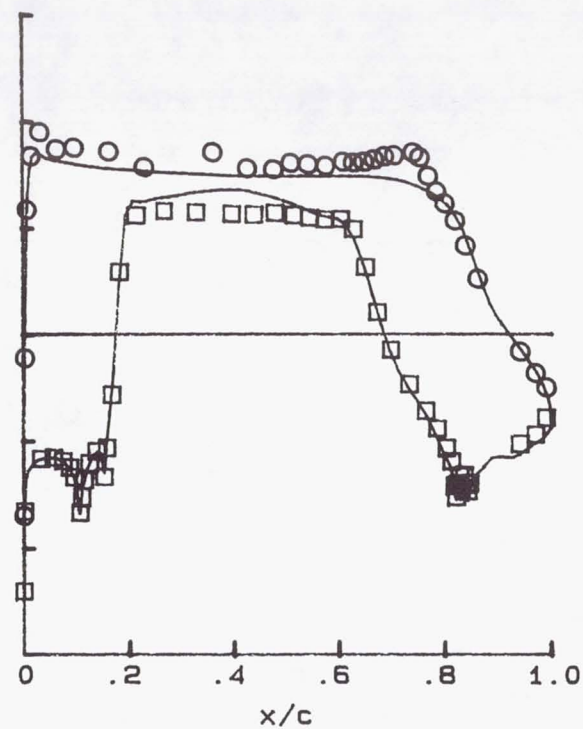
L-82-9339

(d) Photograph of wake rake mounted in test section. Upstream view.

Figure 23. Concluded.

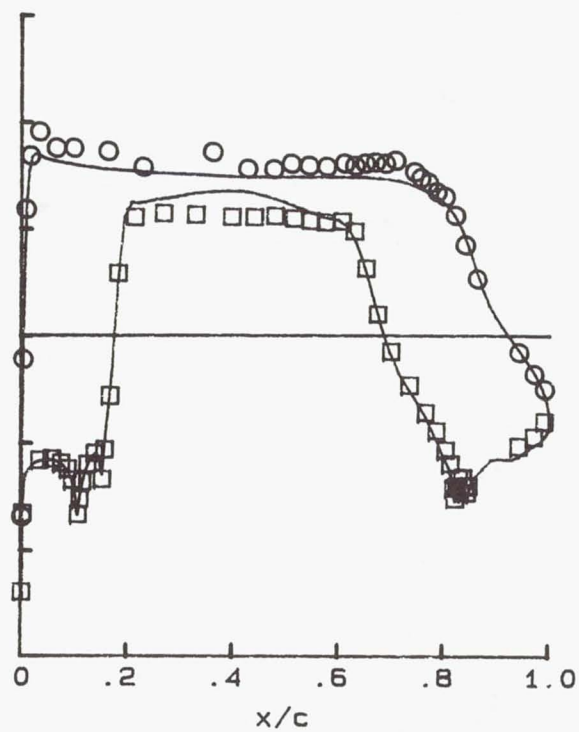


(a) $M_\infty = 0.8225$. $c_l = 0.525$.

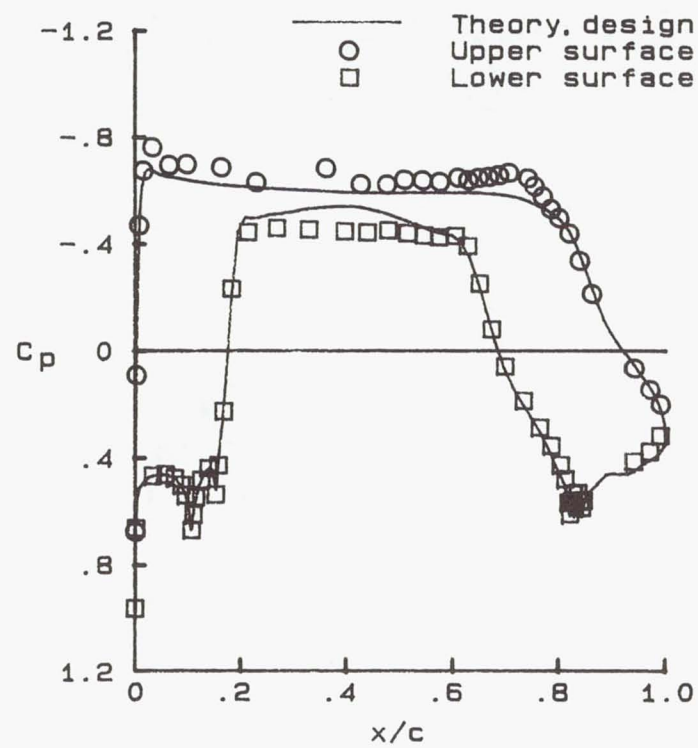


(b) $M_\infty = 0.8221$. $c_l = 0.528$.

Figure 24. Sensitivity of flow near midspan (station 8) to small variations in M_∞ near $M_{\infty, \text{design}}$ at $R_c = 10 \times 10^6$.

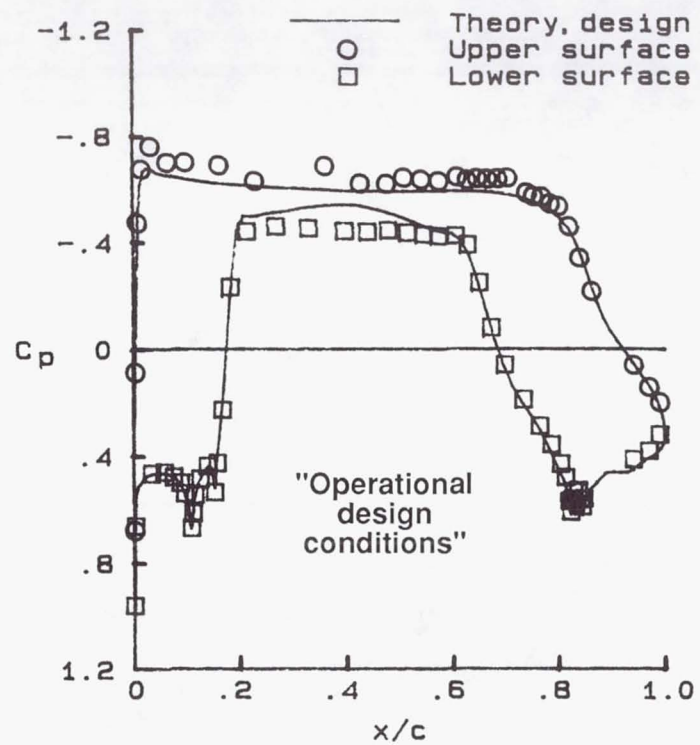


(c) $M_\infty = 0.8220$. $c_l = 0.529$.

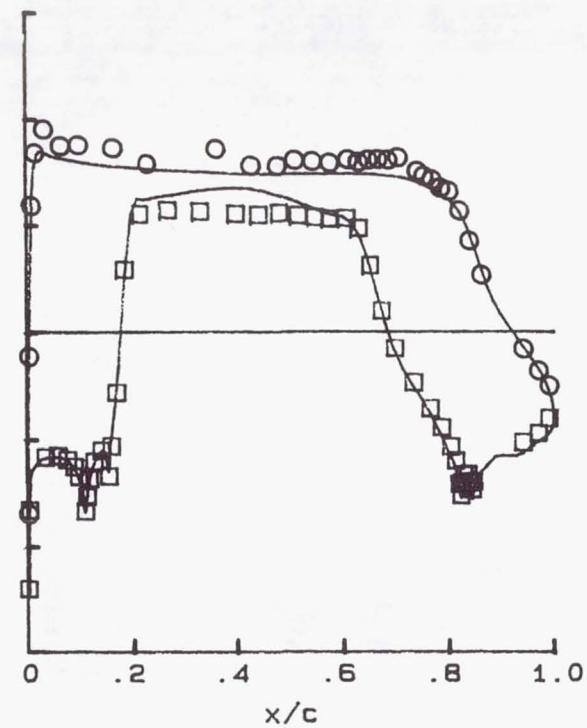


(d) $M_\infty = 0.8217$. $c_l = 0.529$.

Figure 24. Continued.

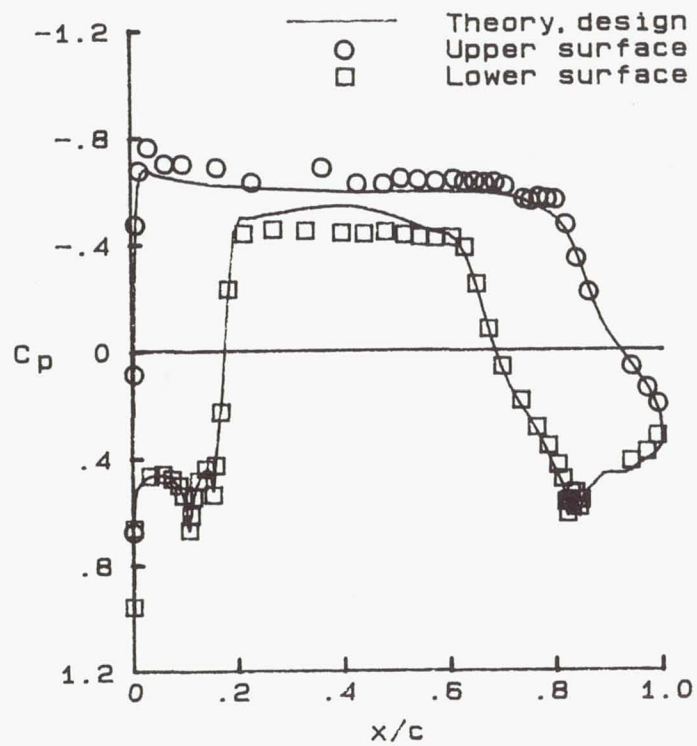


(e) $M_\infty = 0.8216$. $c_l = 0.529$.

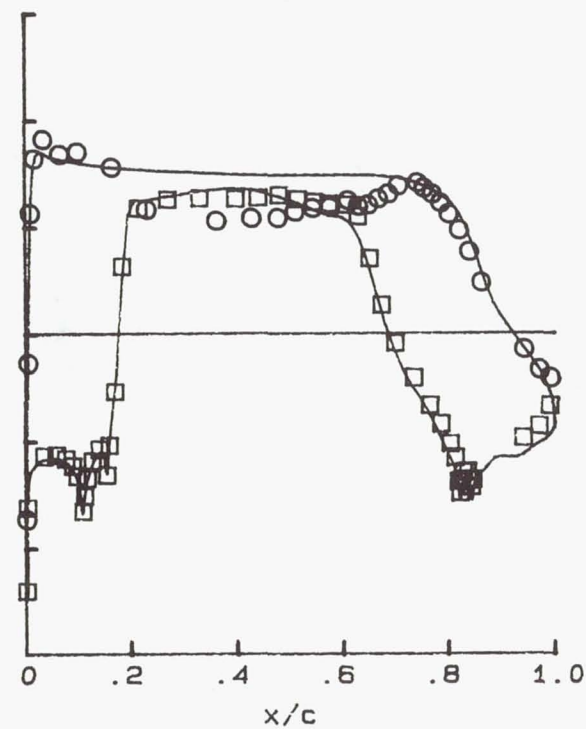


(f) $M_\infty = 0.8215$. $c_l = 0.529$.

Figure 24. Continued.



(g) $M_\infty = 0.8214$. $c_l = 0.529$.



(h) $M_\infty = 0.8207$. $c_l = 0.383$.

Figure 24. Concluded.

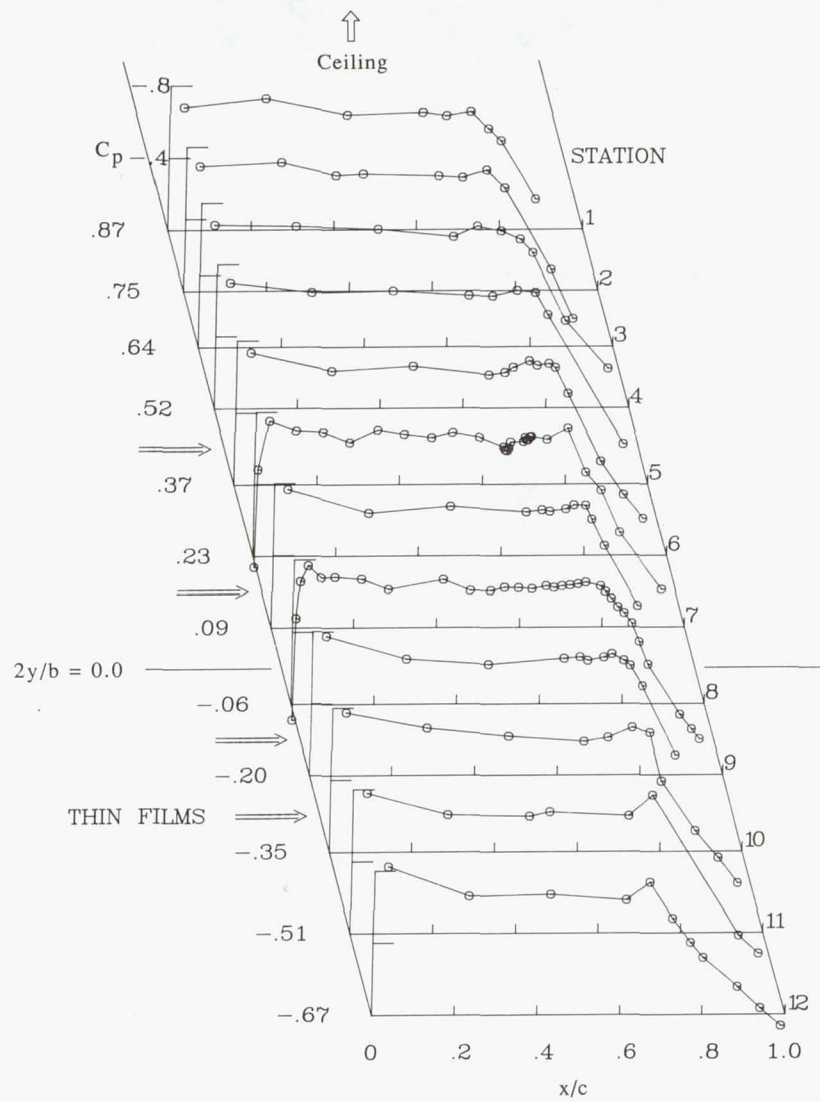
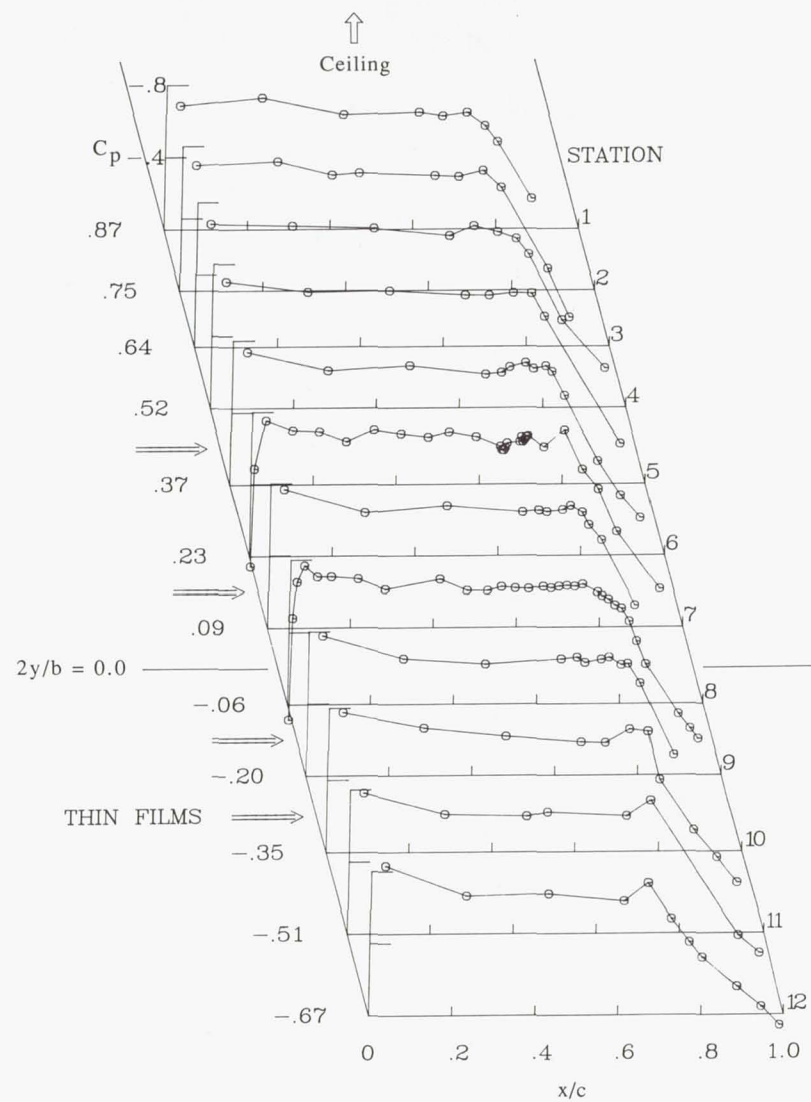
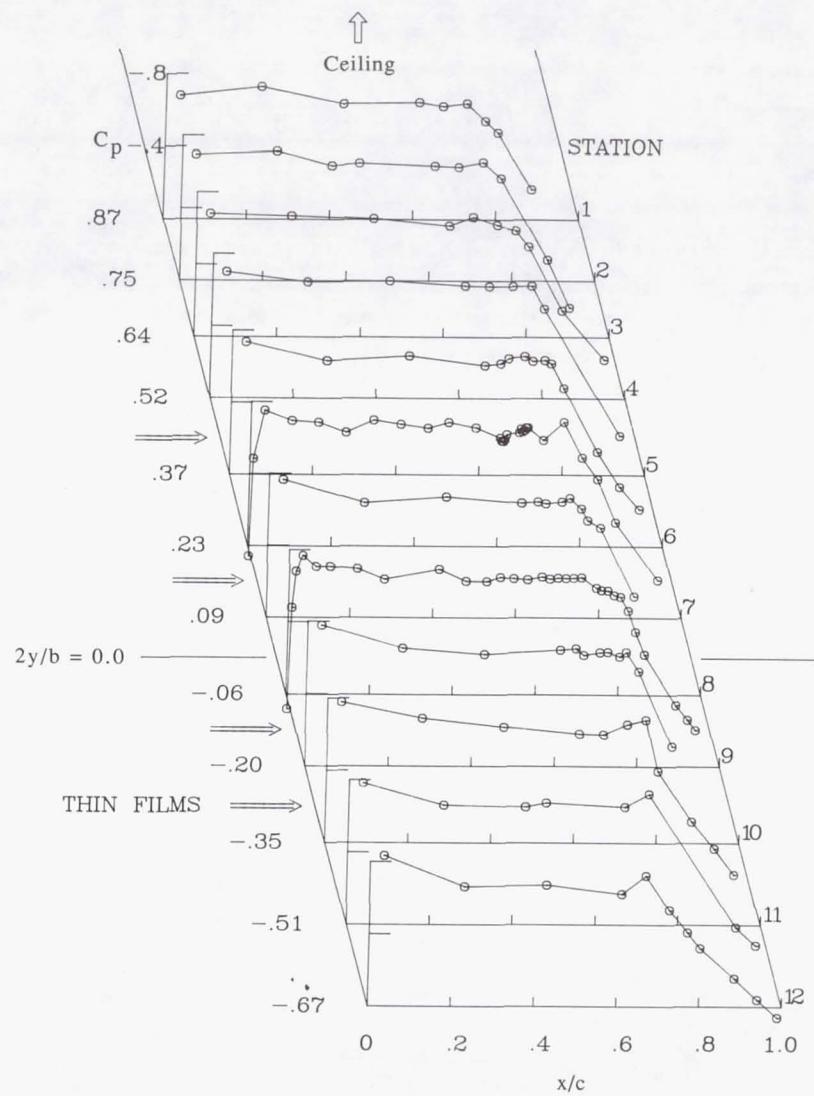
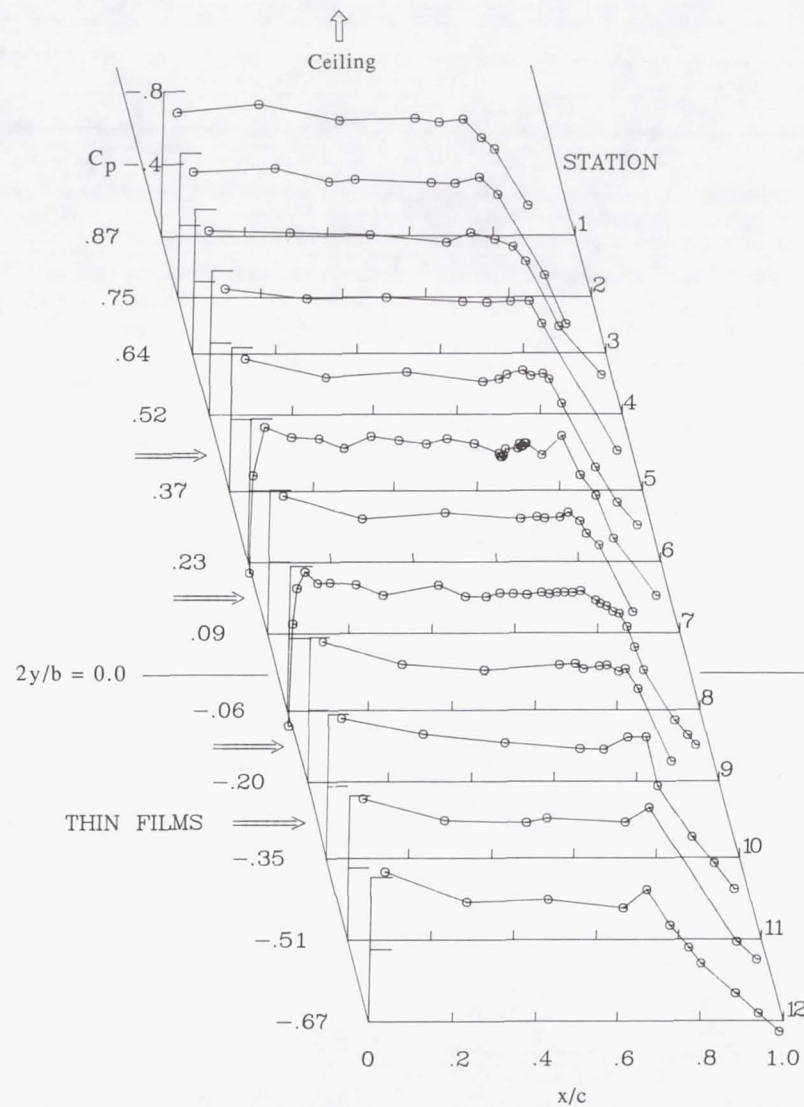
(c) $M_\infty = 0.8220$.(d) $M_\infty = 0.8217$.

Figure 25. Continued.



(e) $M_\infty = 0.8216$.



(f) $M_\infty = 0.8215$.

Figure 25. Continued.

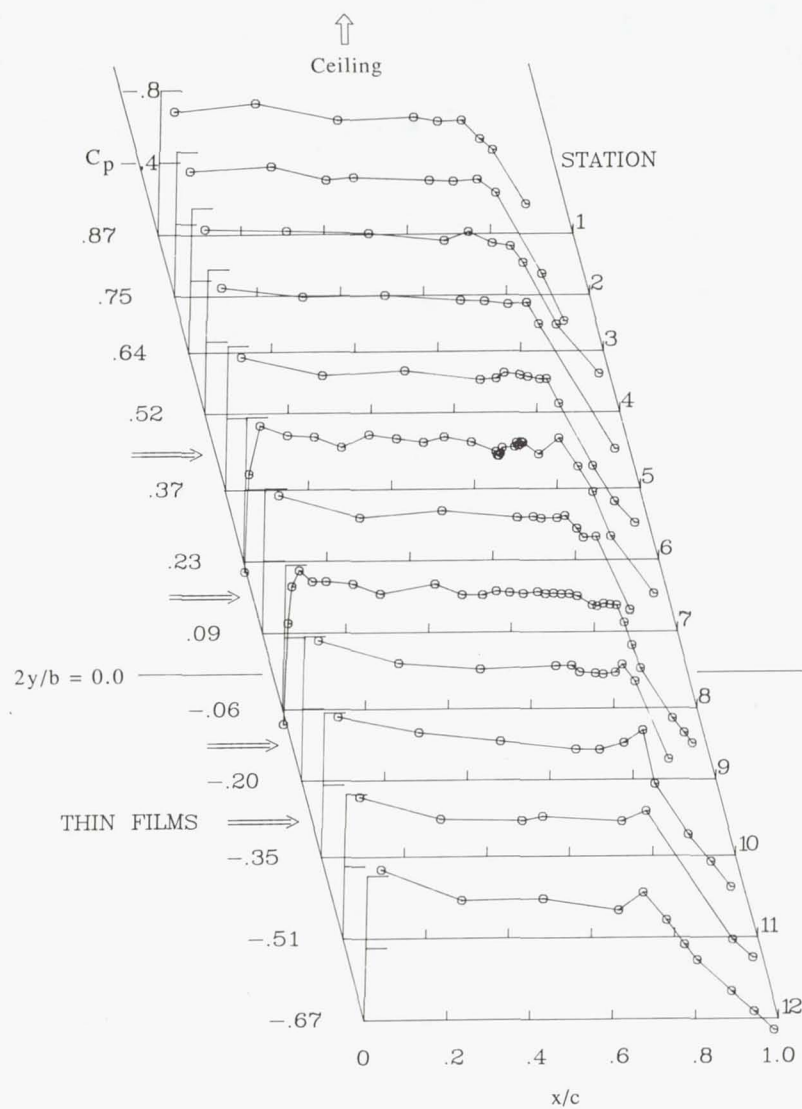
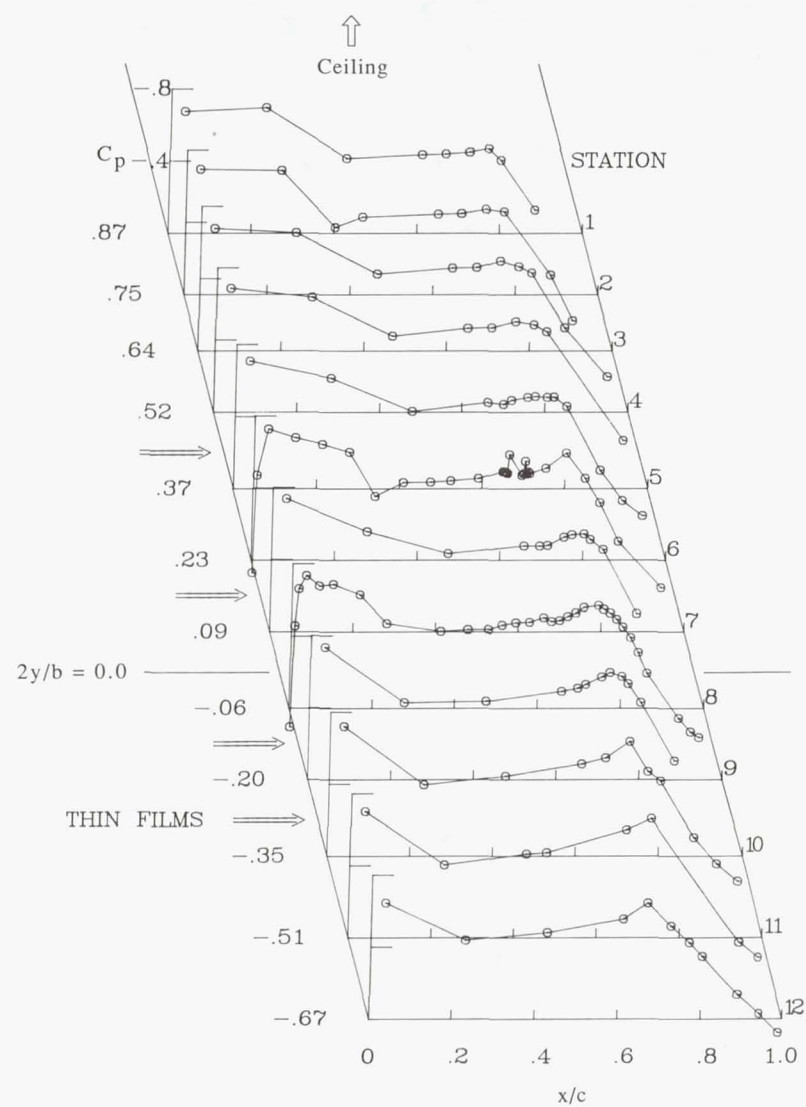
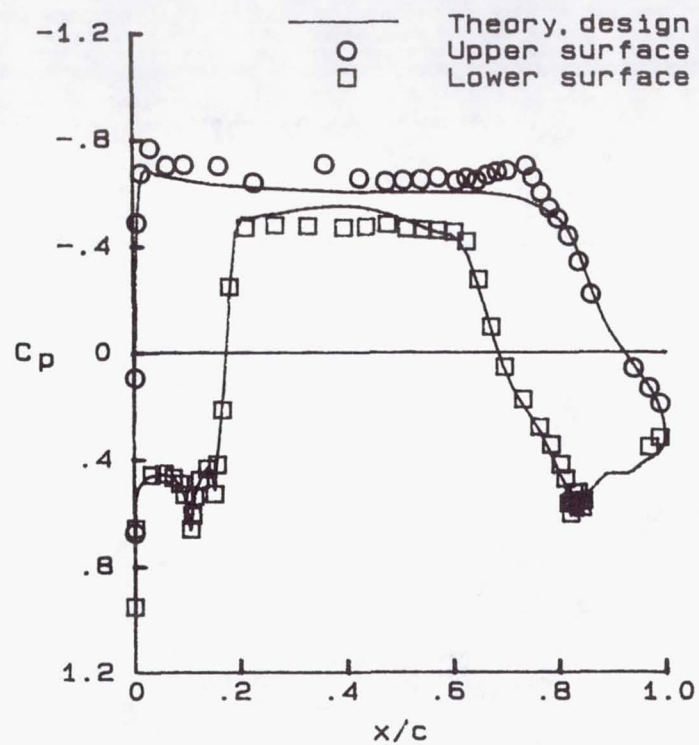
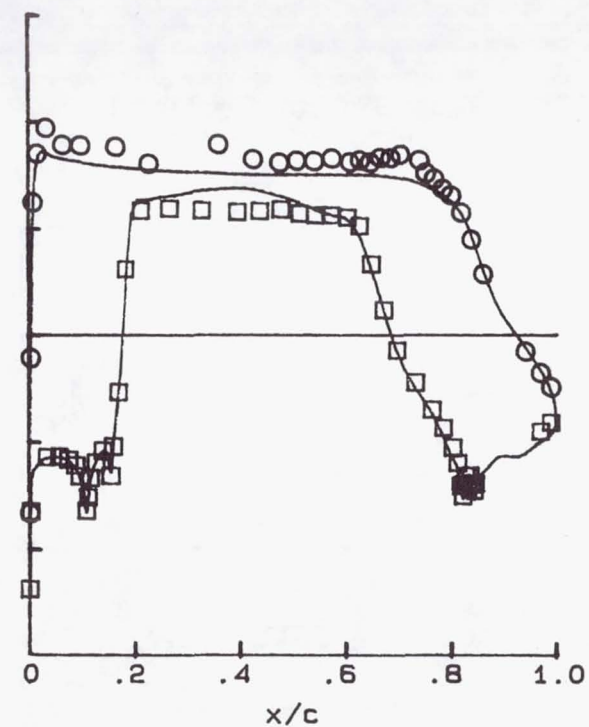
(g) $M_\infty = 0.8214$.(h) $M_\infty = 0.8207$.

Figure 25. Concluded.

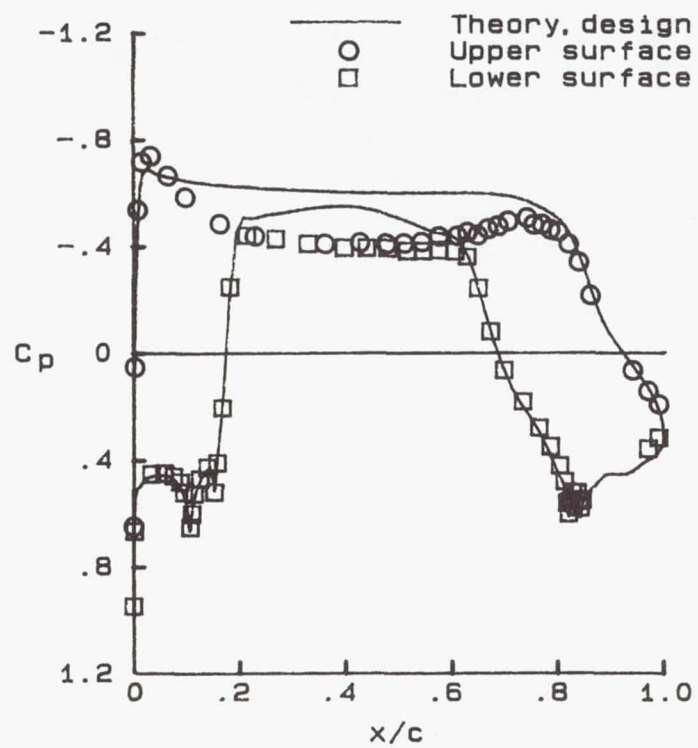


(a) $M_\infty = 0.8226$. $c_l = 0.527$.

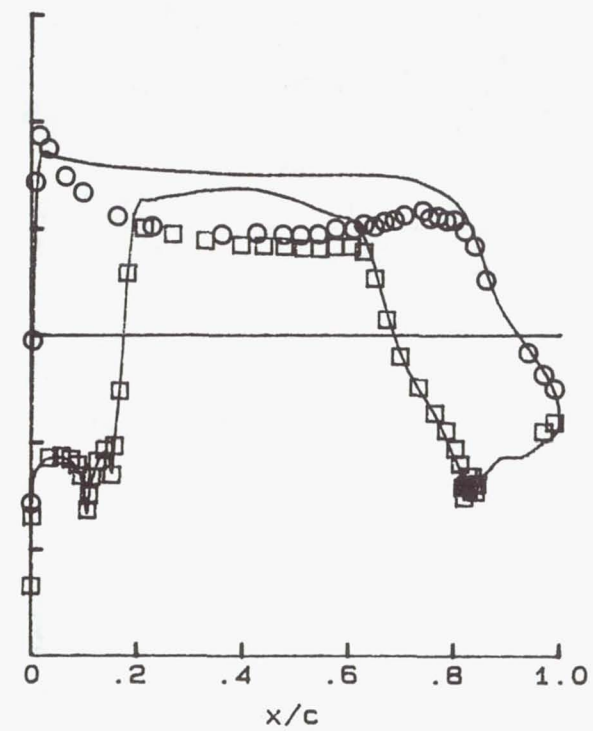


(b) $M_\infty = 0.8219$. $c_l = 0.534$.

Figure 26. Effect on experimental chordwise pressure distribution near midspan (station 8) of varying M_∞ at $R_c = 10 \times 10^6$.

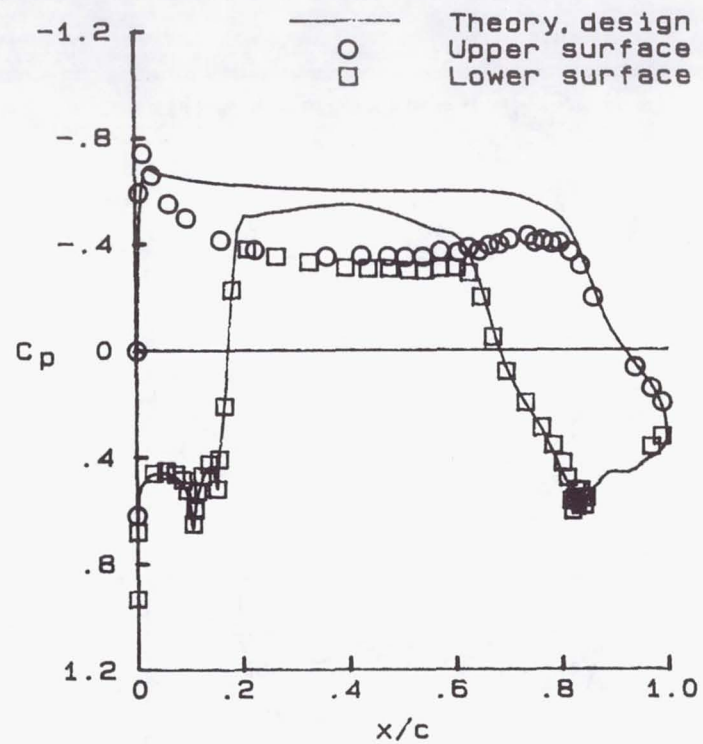


(c) $M_\infty = 0.8005$. $c_l = 0.400$.

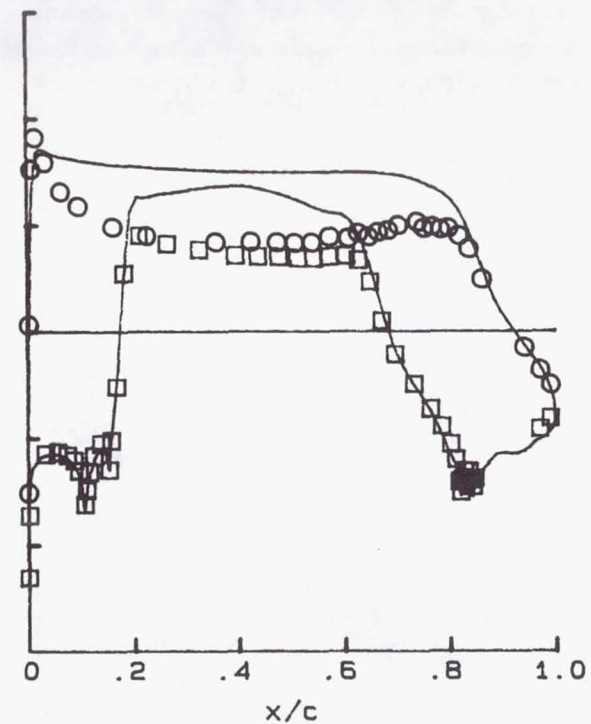


(d) $M_\infty = 0.7807$. $c_l = 0.398$.

Figure 26. Continued.

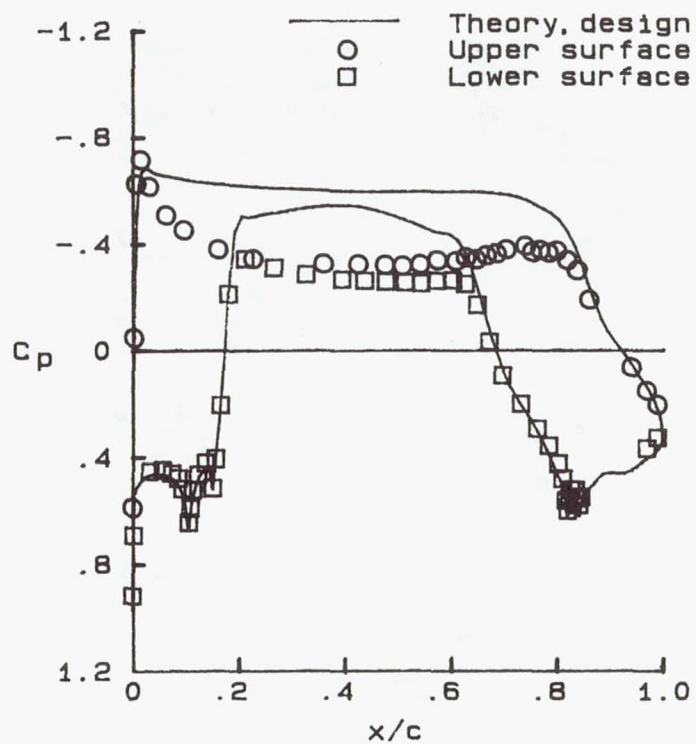


(e) $M_\infty = 0.7617$. $c_l = 0.385$.

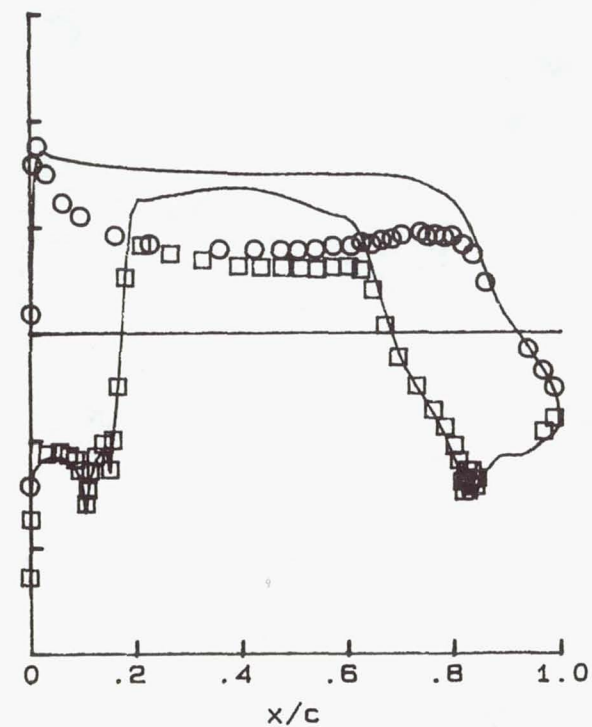


(f) $M_\infty = 0.7417$. $c_l = 0.381$.

Figure 26. Continued.

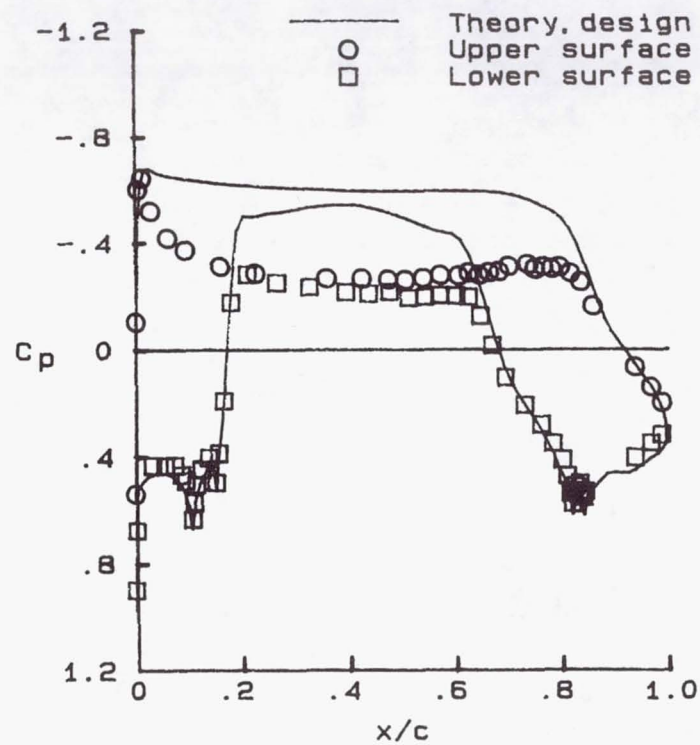


(g) $M_\infty = 0.7218$. $c_l = 0.379$.

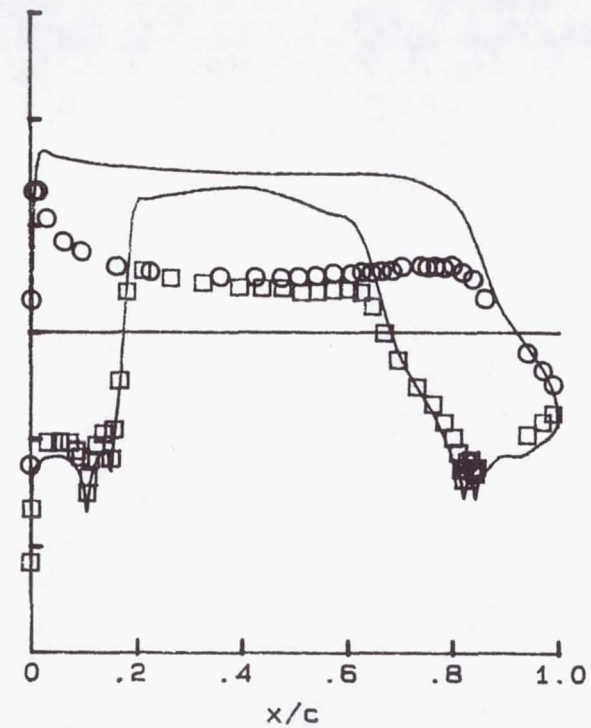


(h) $M_\infty = 0.7014$. $c_l = 0.374$.

Figure 26. Continued.



(i) $M_\infty = 0.6087$. $c_l = 0.345$.



(j) $M_\infty = 0.4019$. $c_l = 0.303$.

Figure 26. Concluded.

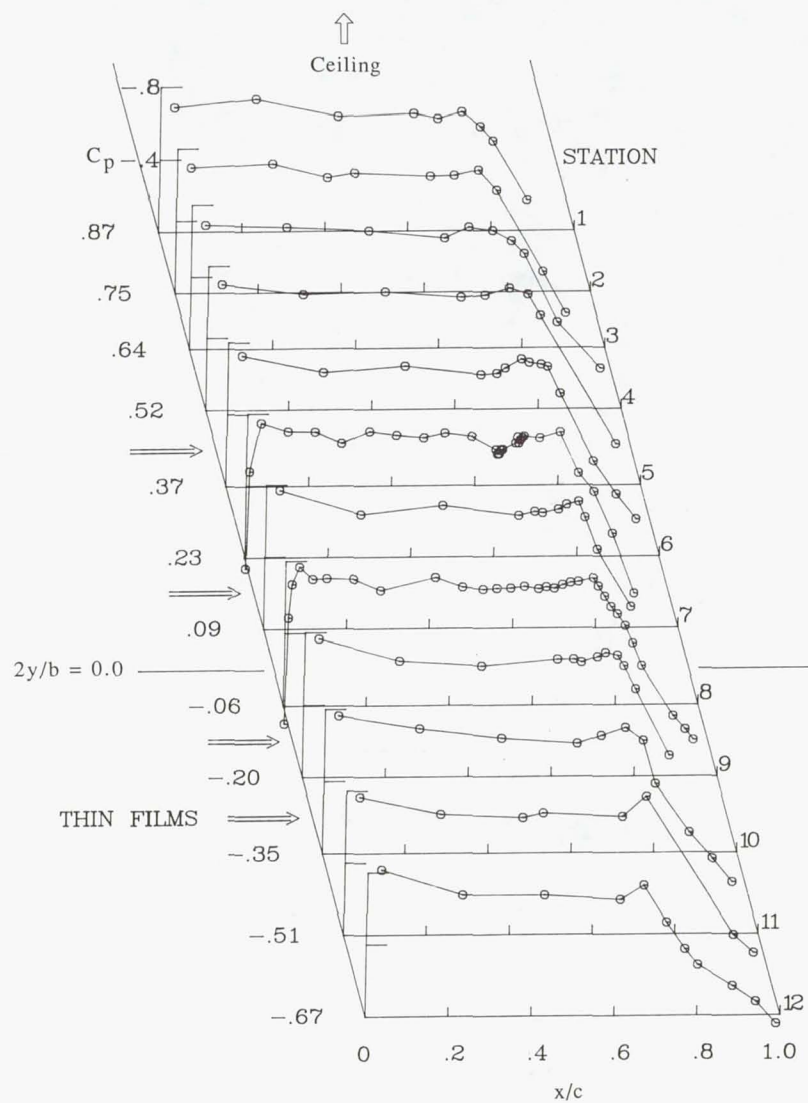
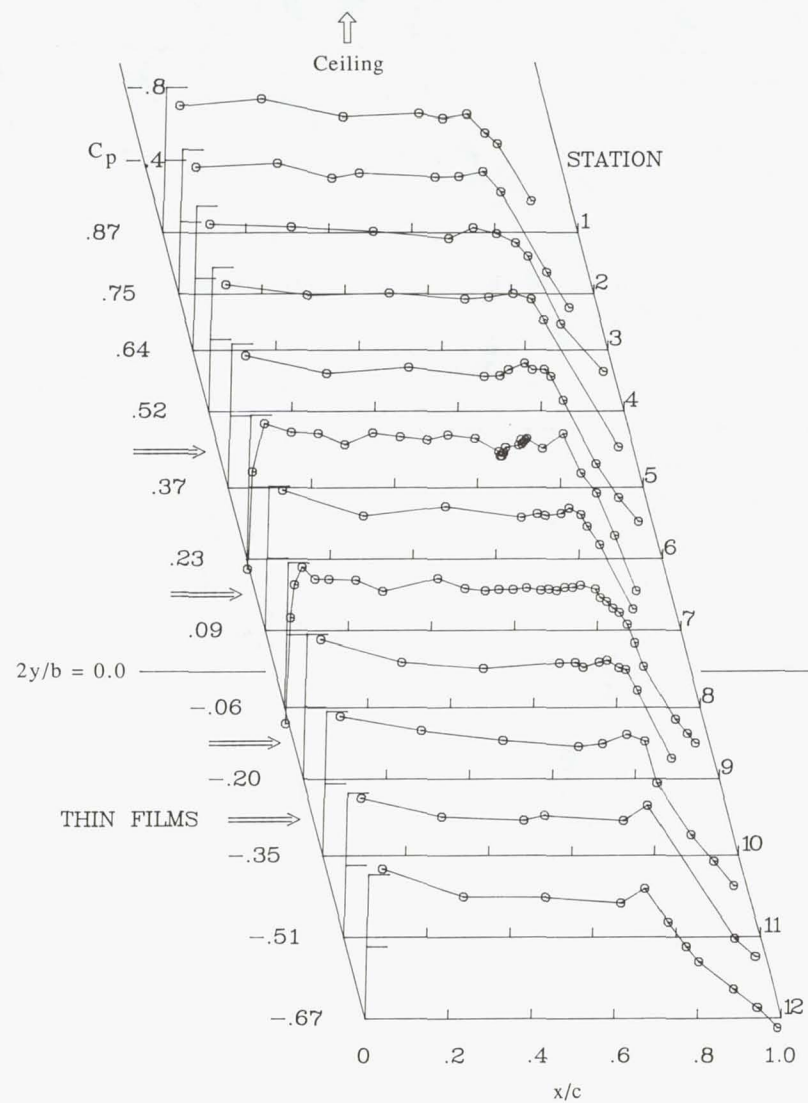
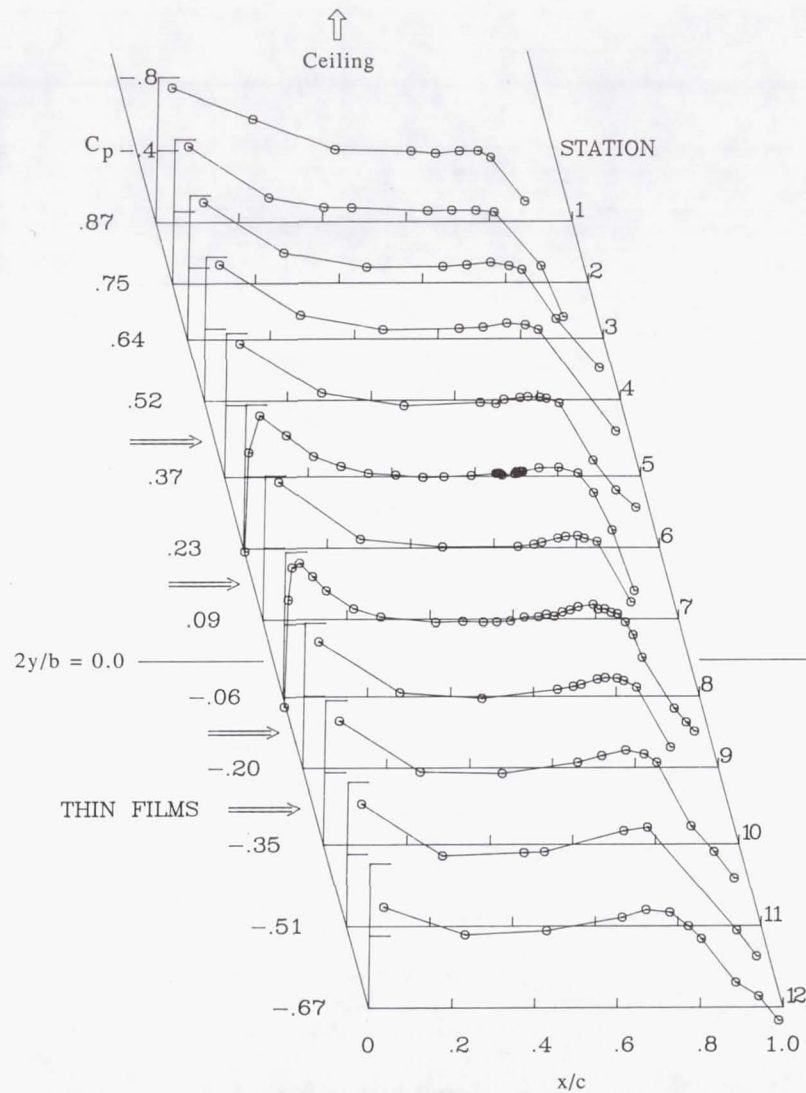
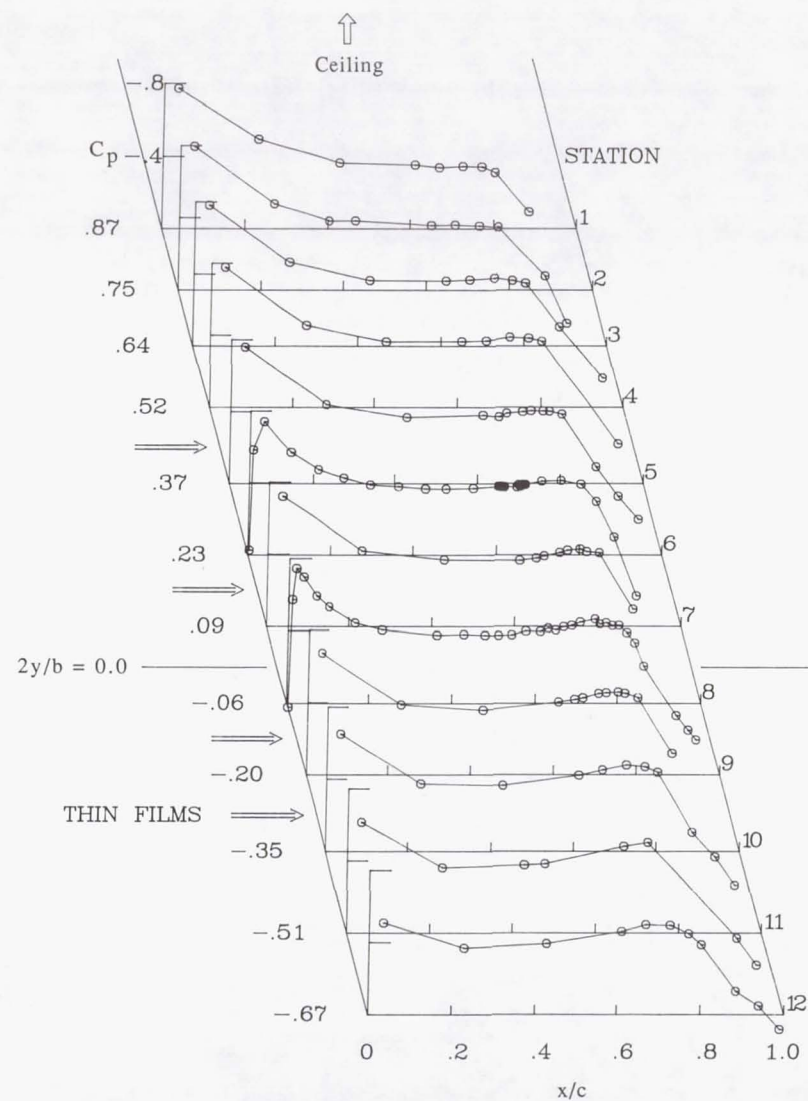
(a) $M_\infty = 0.8226$.(b) $M_\infty = 0.8219$.

Figure 27. Effect on experimental upper-surface spanwise pressure distribution of varying M_∞ at $R_c = 10 \times 10^6$.



(c) $M_\infty = 0.8005$.



(d) $M_\infty = 0.7807$.

Figure 27. Continued.

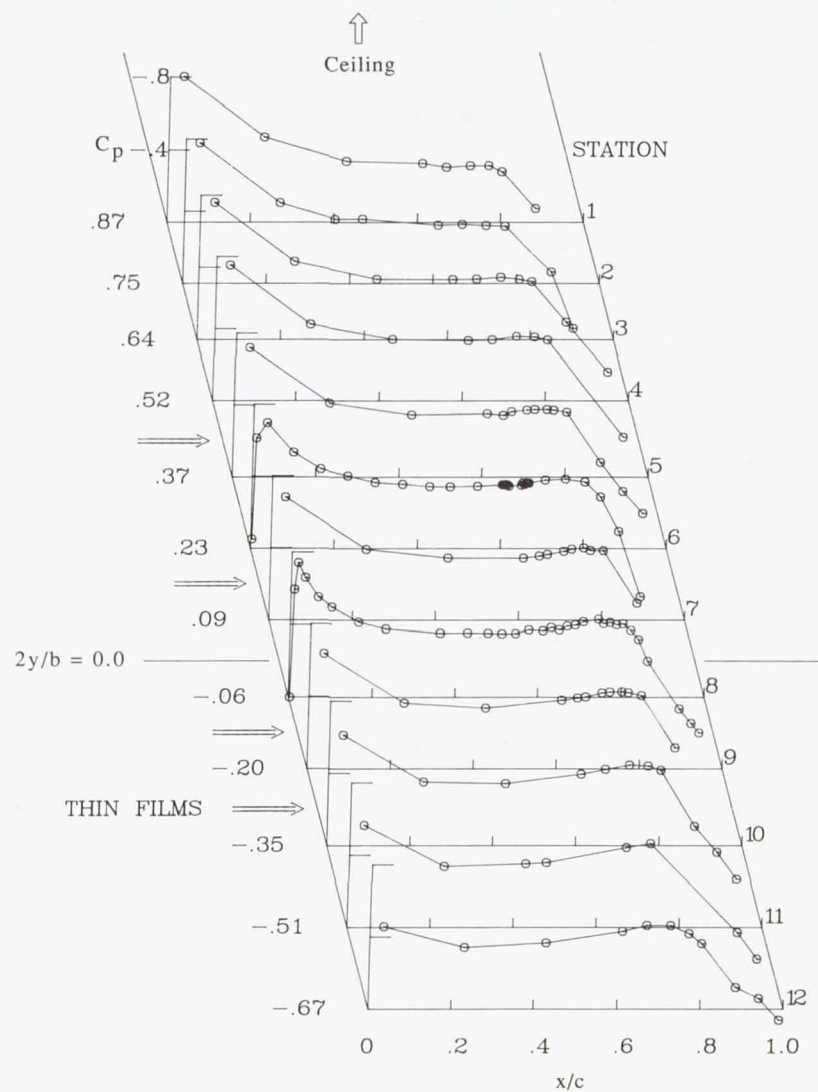
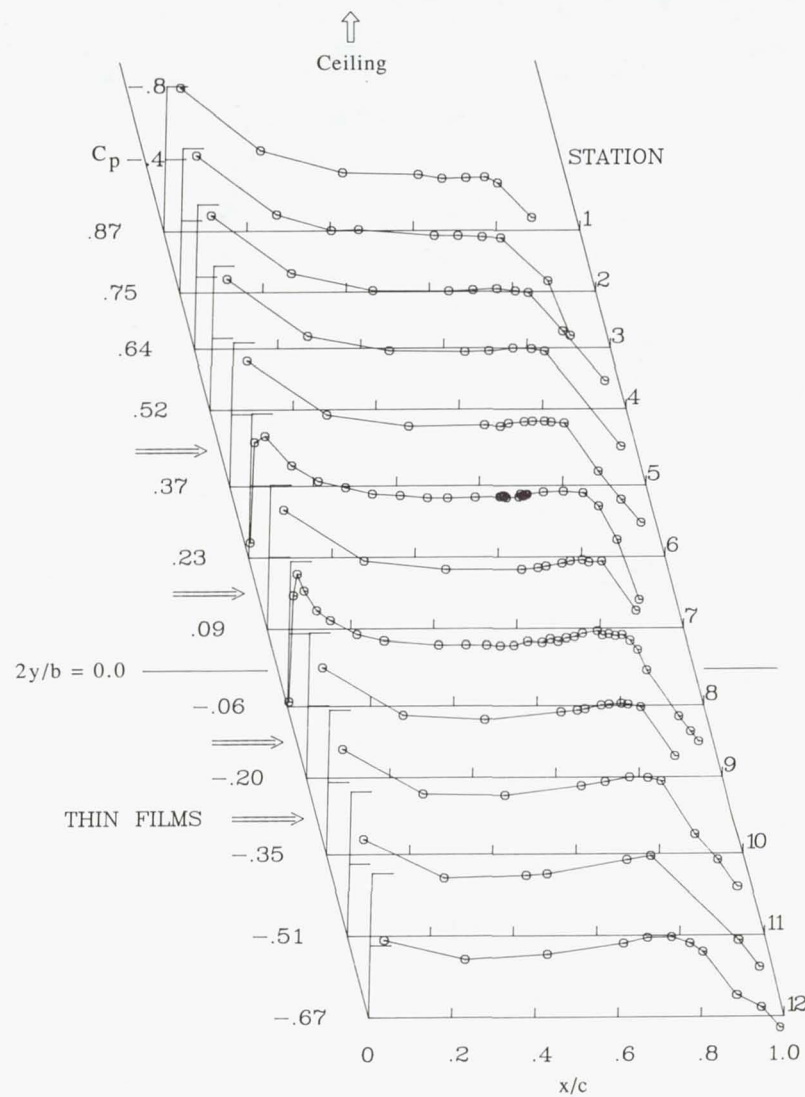
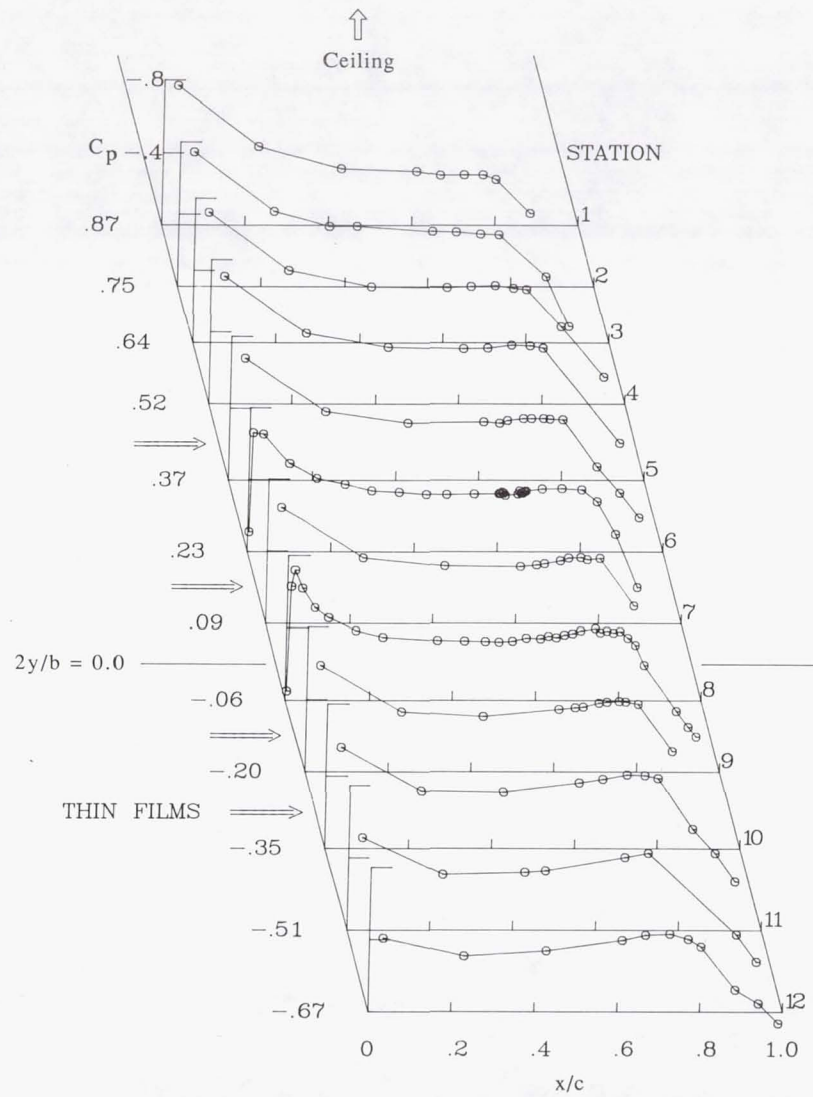
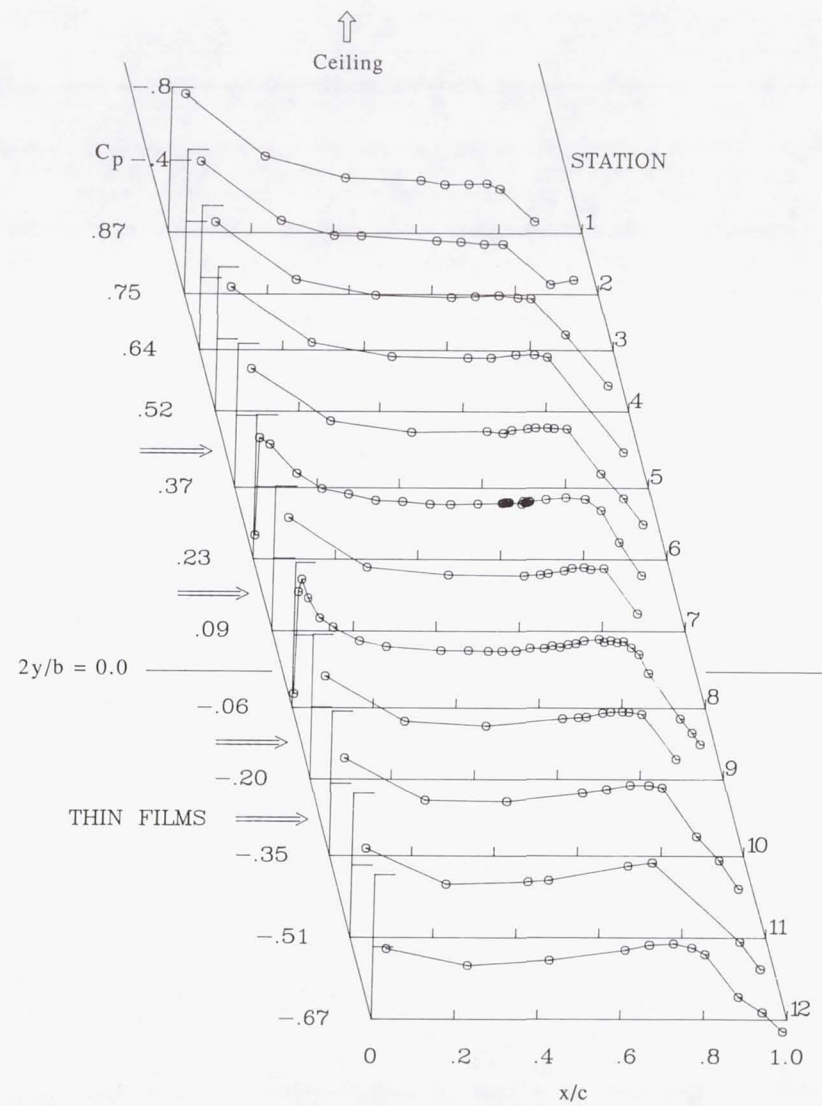
(e) $M_\infty = 0.7617$.(f) $M_\infty = 0.7417$.

Figure 27. Continued.



(g) $M_\infty = 0.7218$.



(h) $M_\infty = 0.7014$.

Figure 27. Continued.

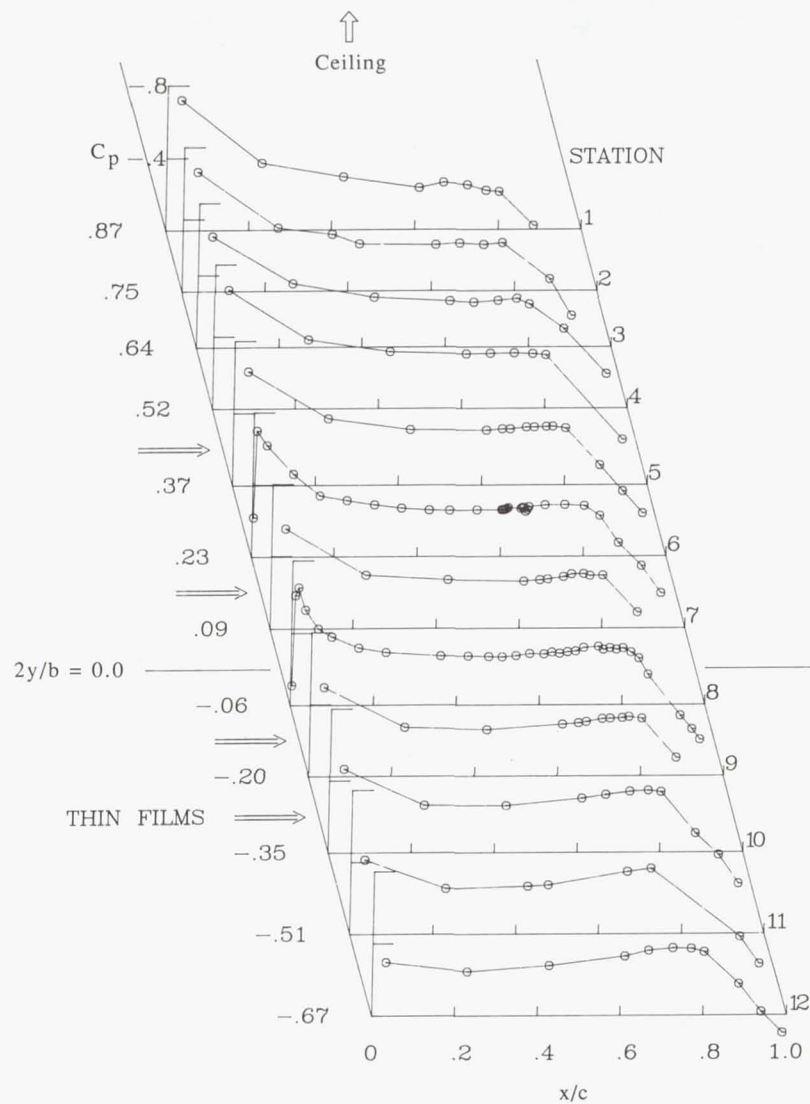
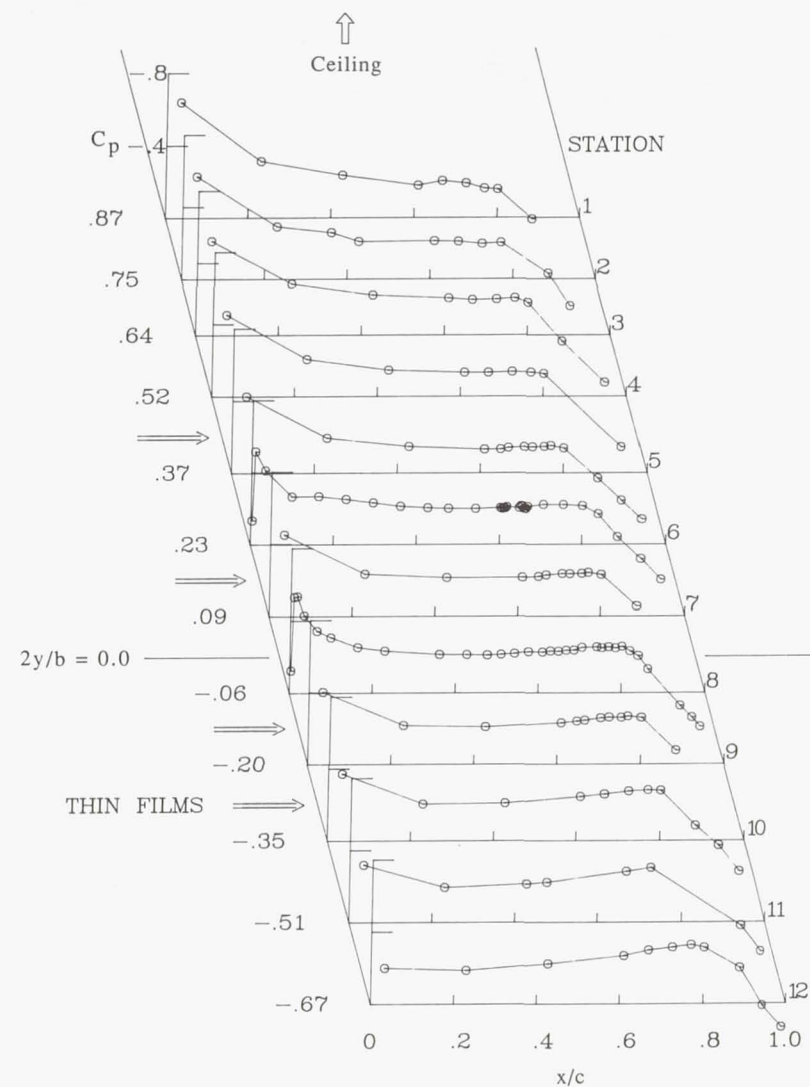
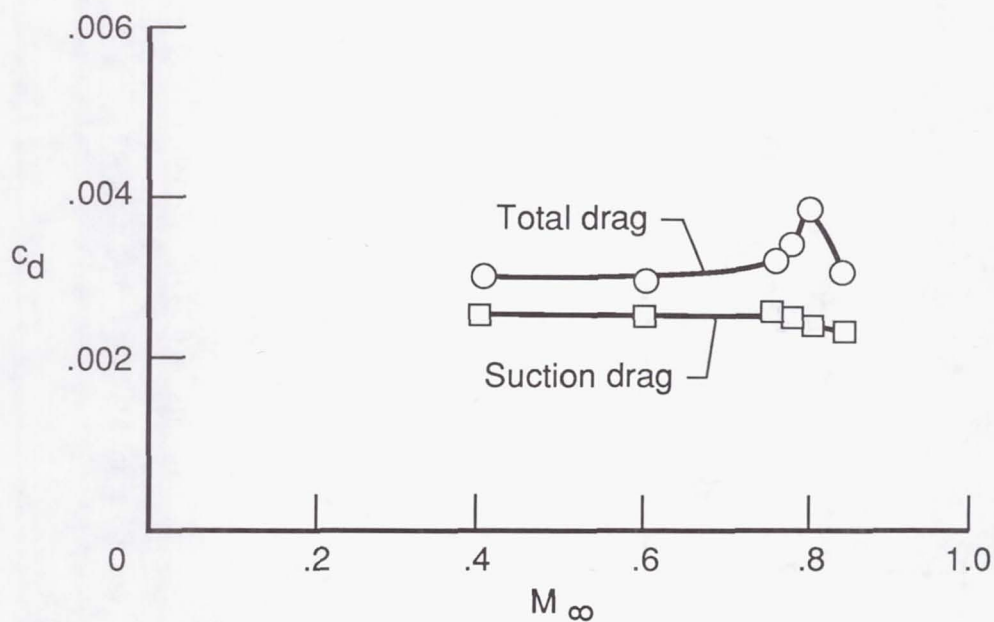
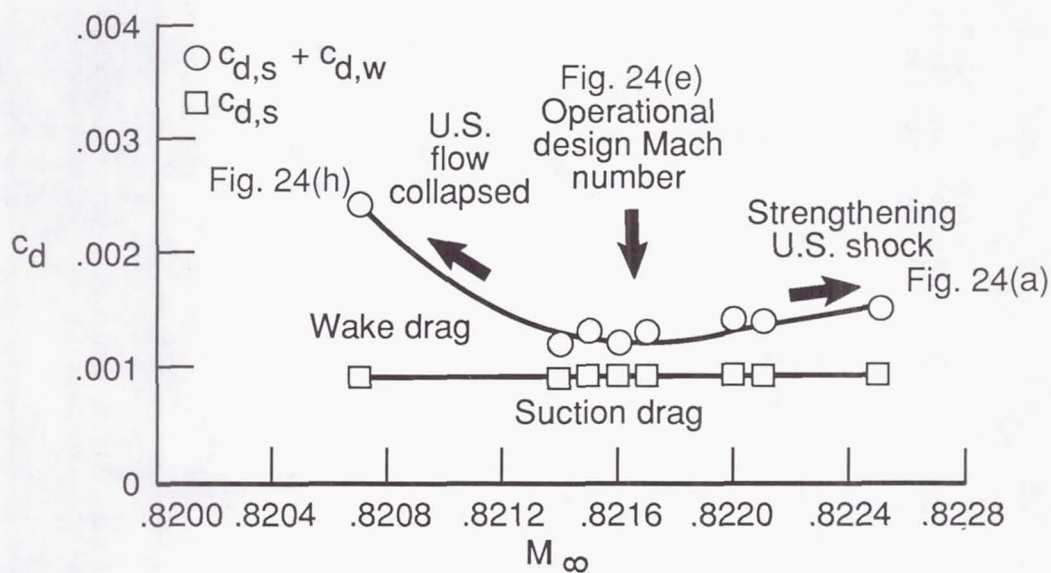
(i) $M_\infty = 0.6087$.(j) $M_\infty = 0.4019$.

Figure 27. Concluded.

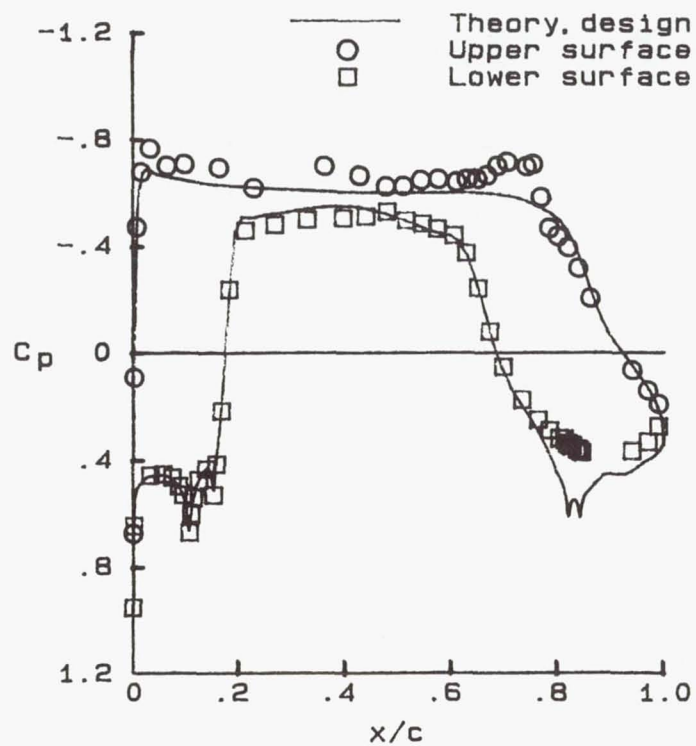


(a) Variation of total drag over wide Mach number range.

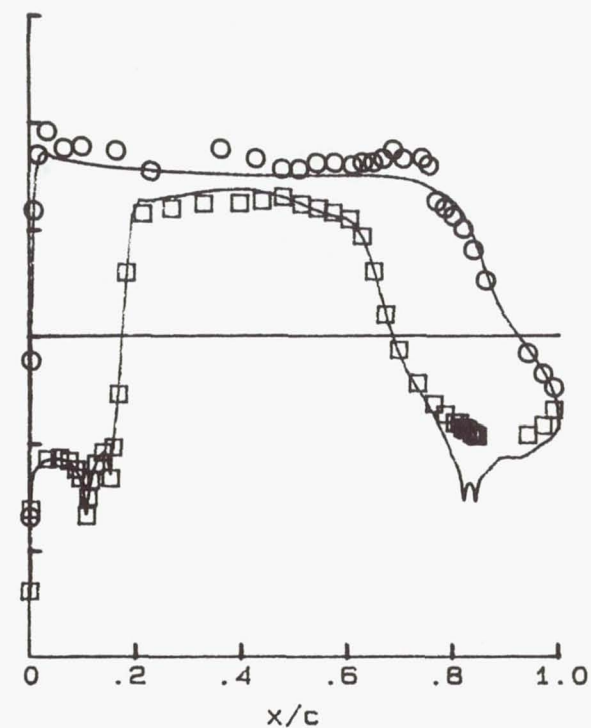


(b) Variation of upper-surface (U.S.) drag near operational design Mach number.

Figure 28. Variation of drag with M_∞ at $R_c = 10 \times 10^6$.

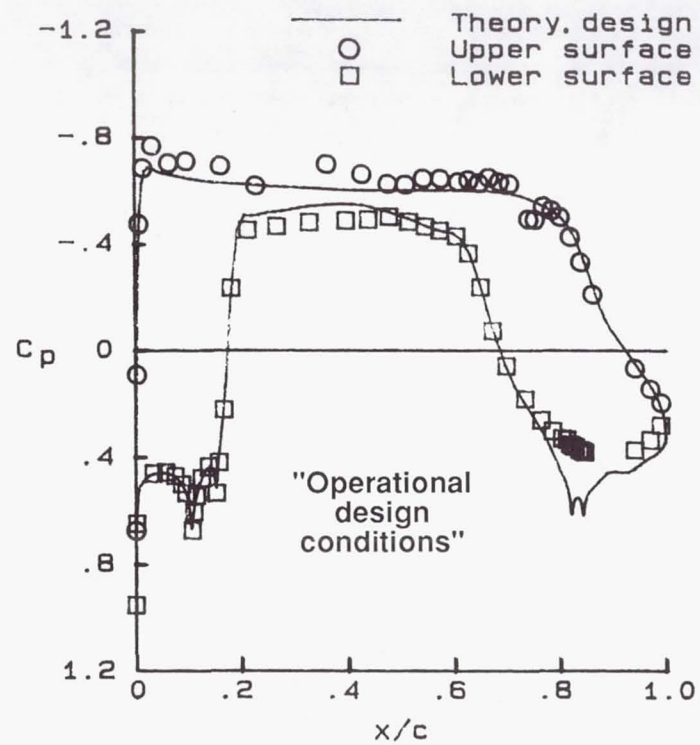


(a) $M_\infty = 0.8234$. $c_l = 0.492$.

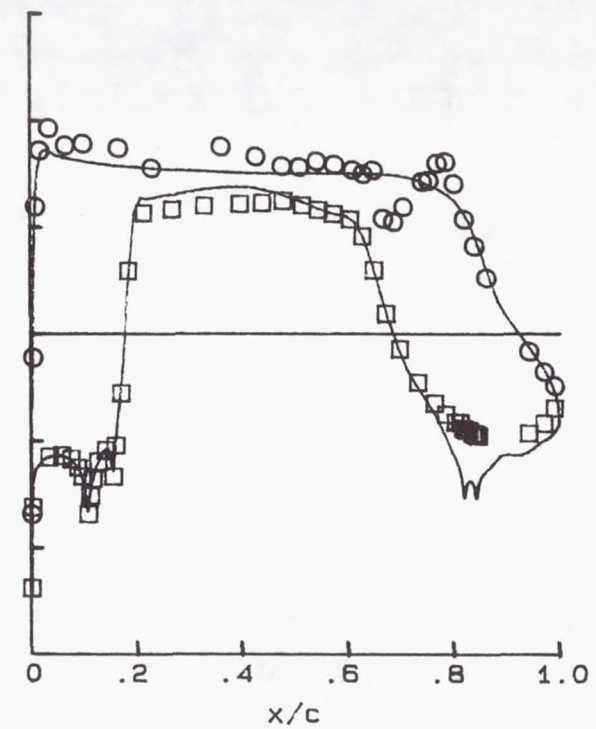


(b) $M_\infty = 0.8231$. $c_l = 0.491$.

Figure 29. Sensitivity of flow near midspan (station 8) to small variations in M_∞ near $M_{\infty, \text{design}}$ at $R_c = 20 \times 10^6$.

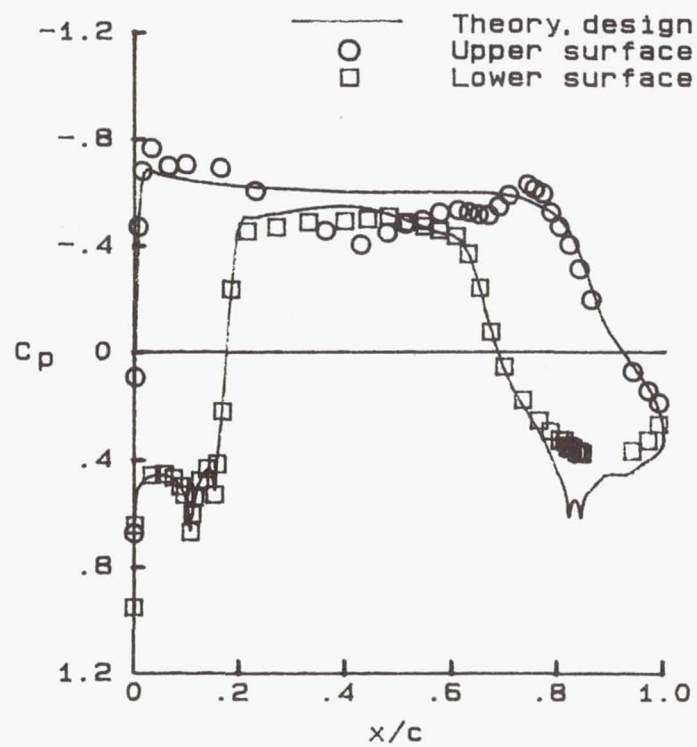


(c) $M_\infty = 0.8226$. $c_l = 0.491$.

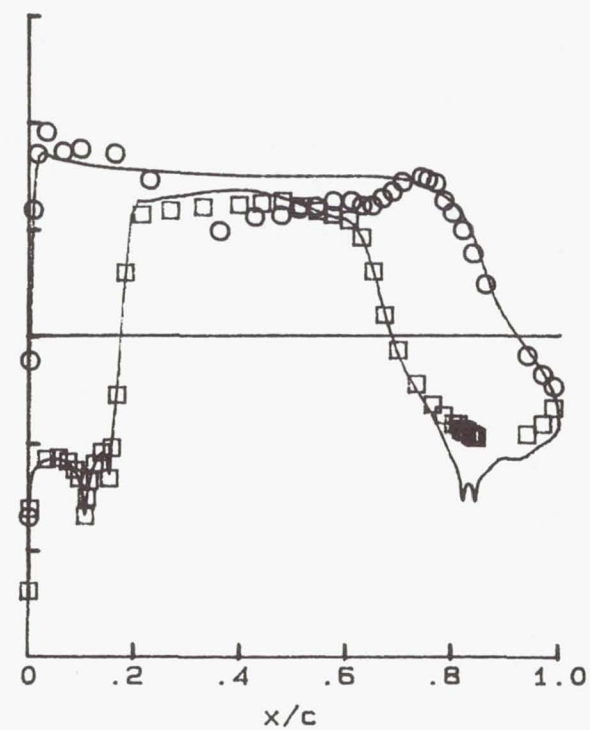


(d) $M_\infty = 0.8225$. $c_l = 0.485$.

Figure 29. Continued.

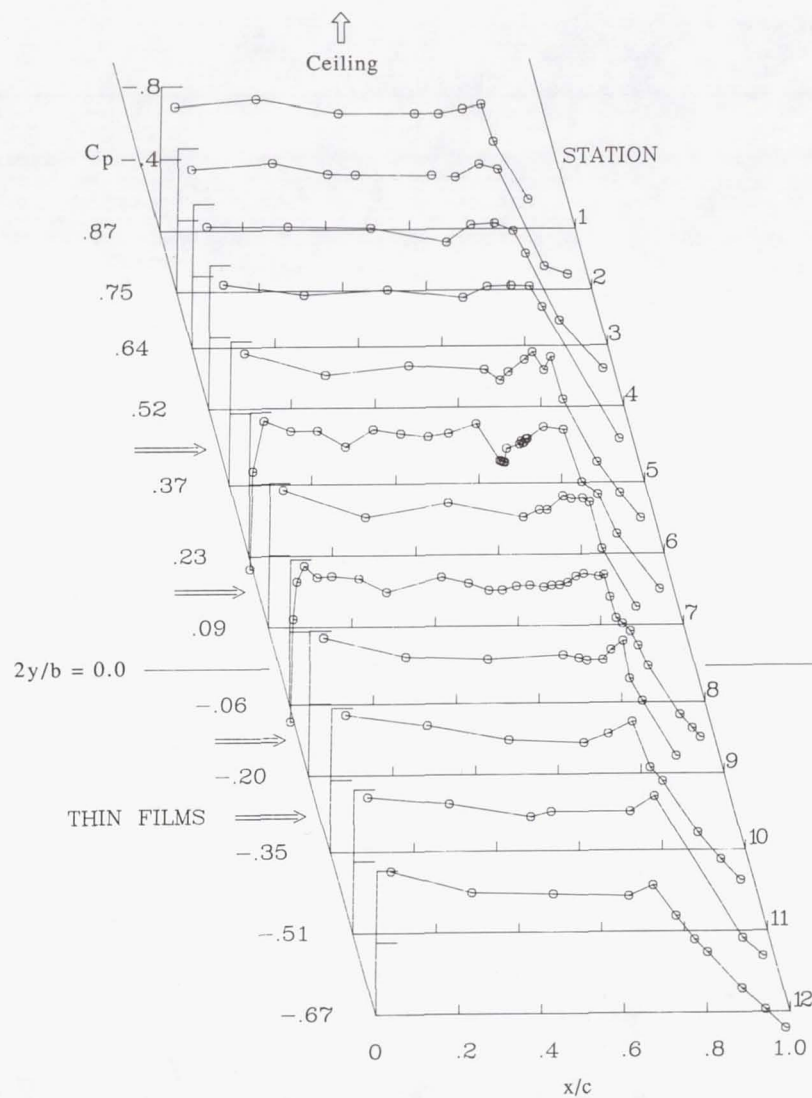


(e) $M_\infty = 0.8223$. $c_l = 0.416$.

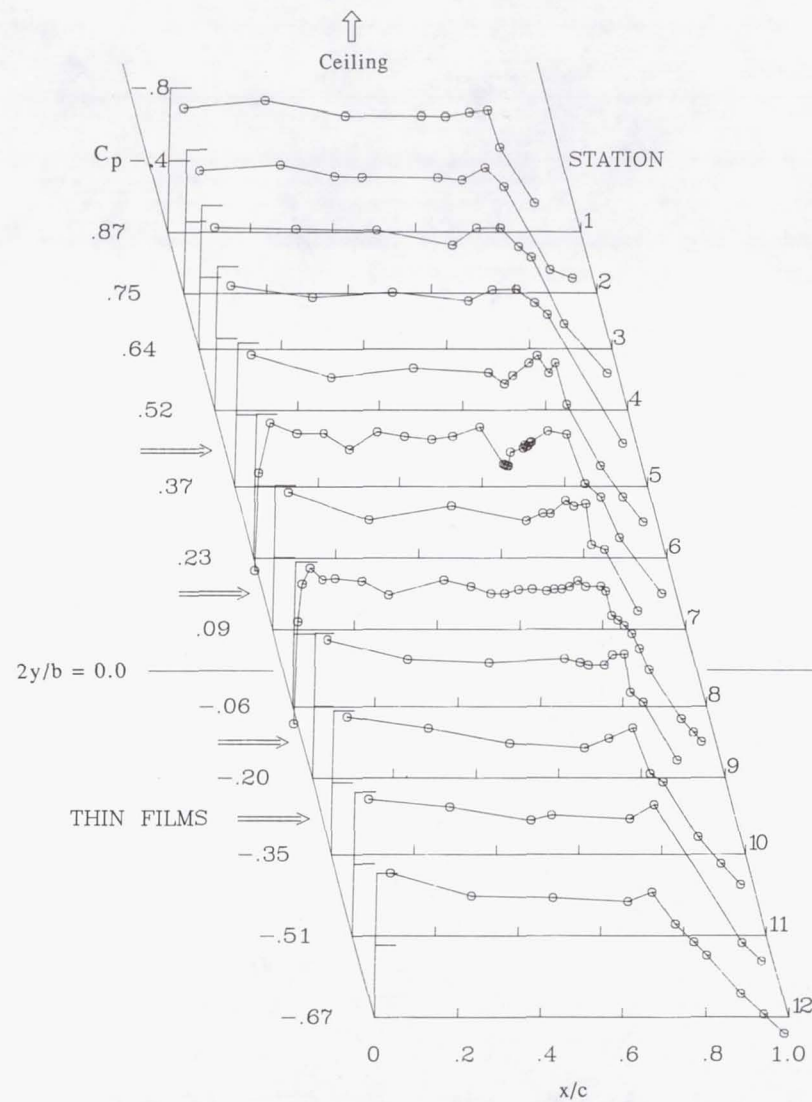


(f) $M_\infty = 0.8214$. $c_l = 0.404$.

Figure 29. Concluded.



(a) $M_{\infty} = 0.8234$.



(b) $M_{\infty} = 0.8231$.

Figure 30. Sensitivity of upper-surface spanwise pressure distribution to small variations in M_{∞} near $M_{\infty, \text{design}}$ at $R_c = 20 \times 10^6$.

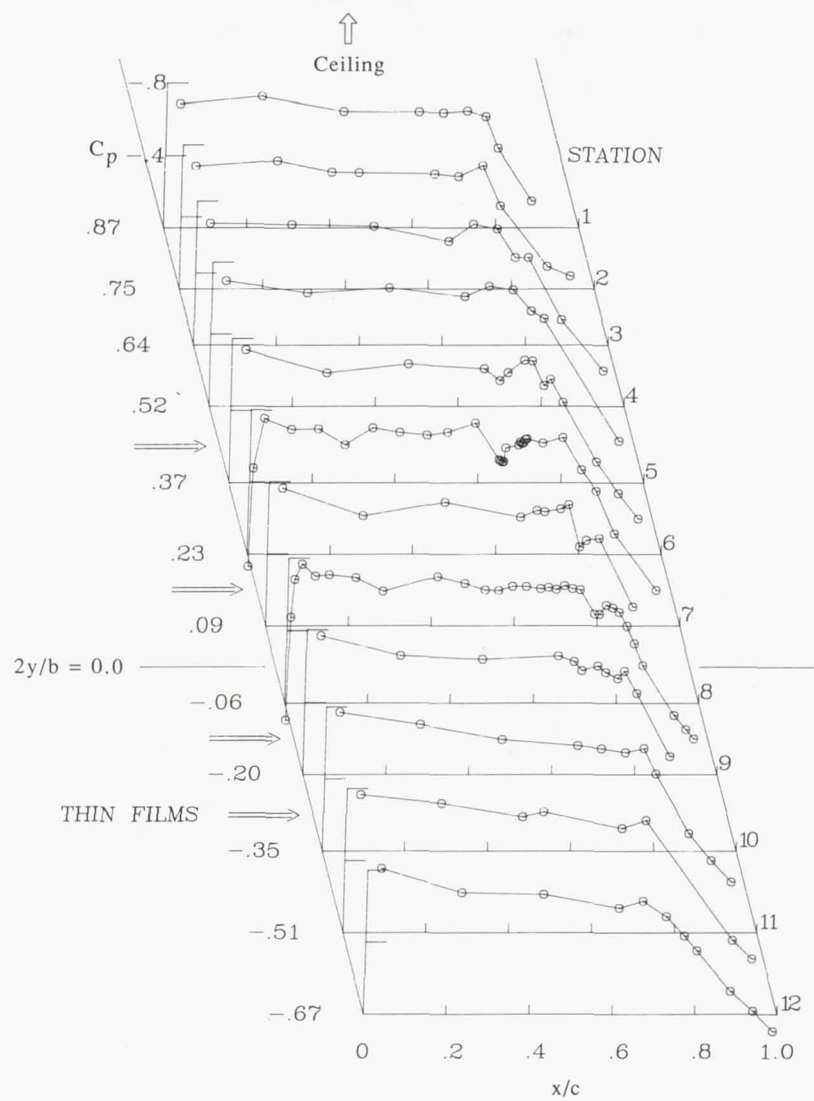
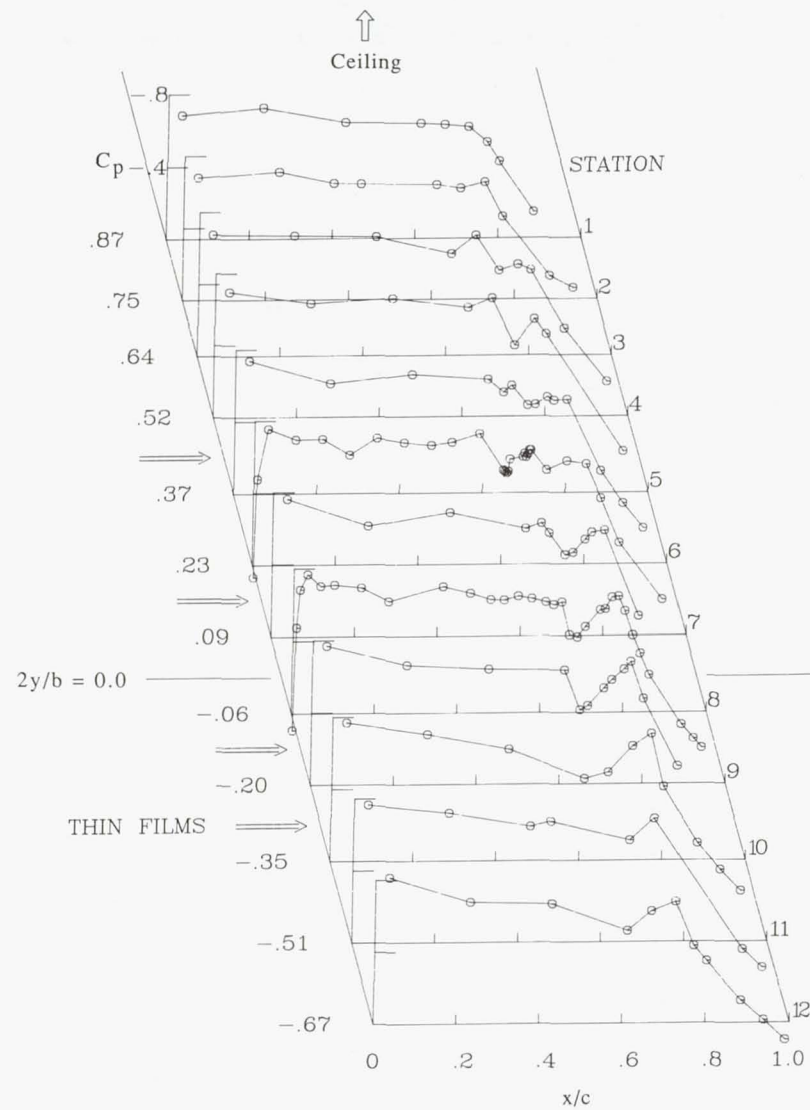
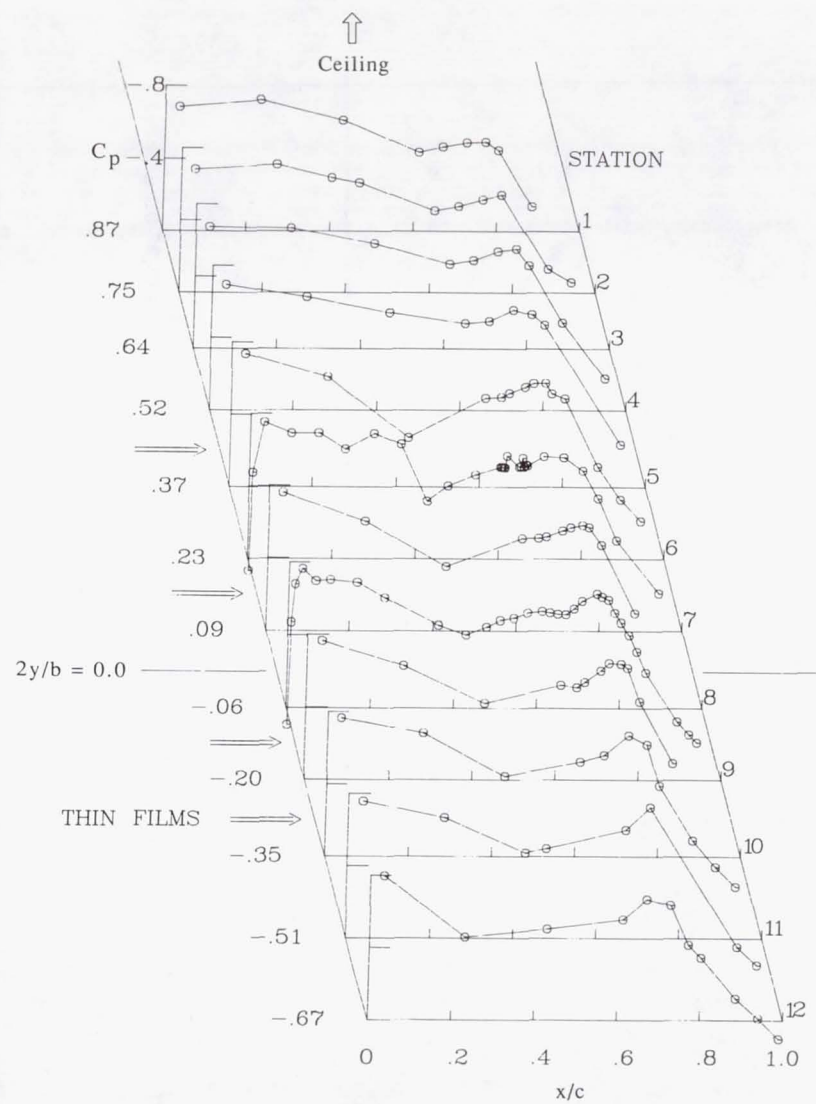
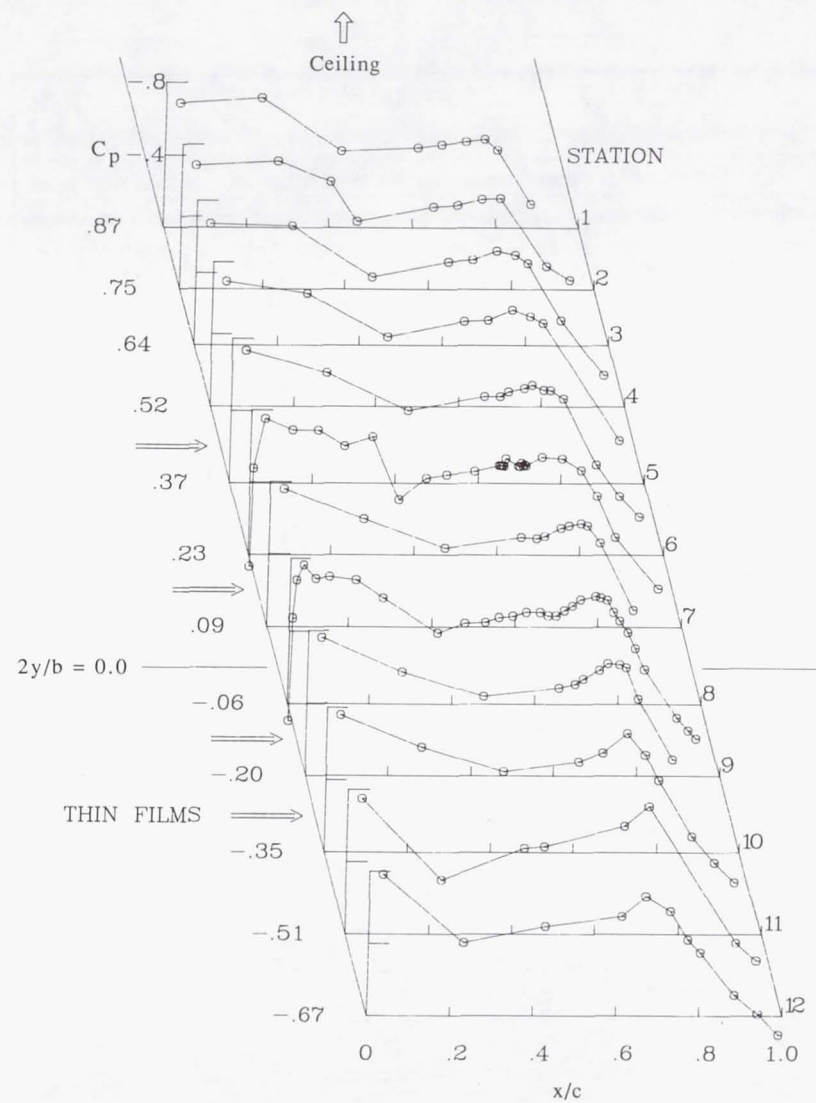
(c) $M_\infty = 0.8226$.(d) $M_\infty = 0.8225$.

Figure 30. Continued.



(e) $M_\infty = 0.8223$.



(f) $M_\infty = 0.8214$.

Figure 30. Concluded.

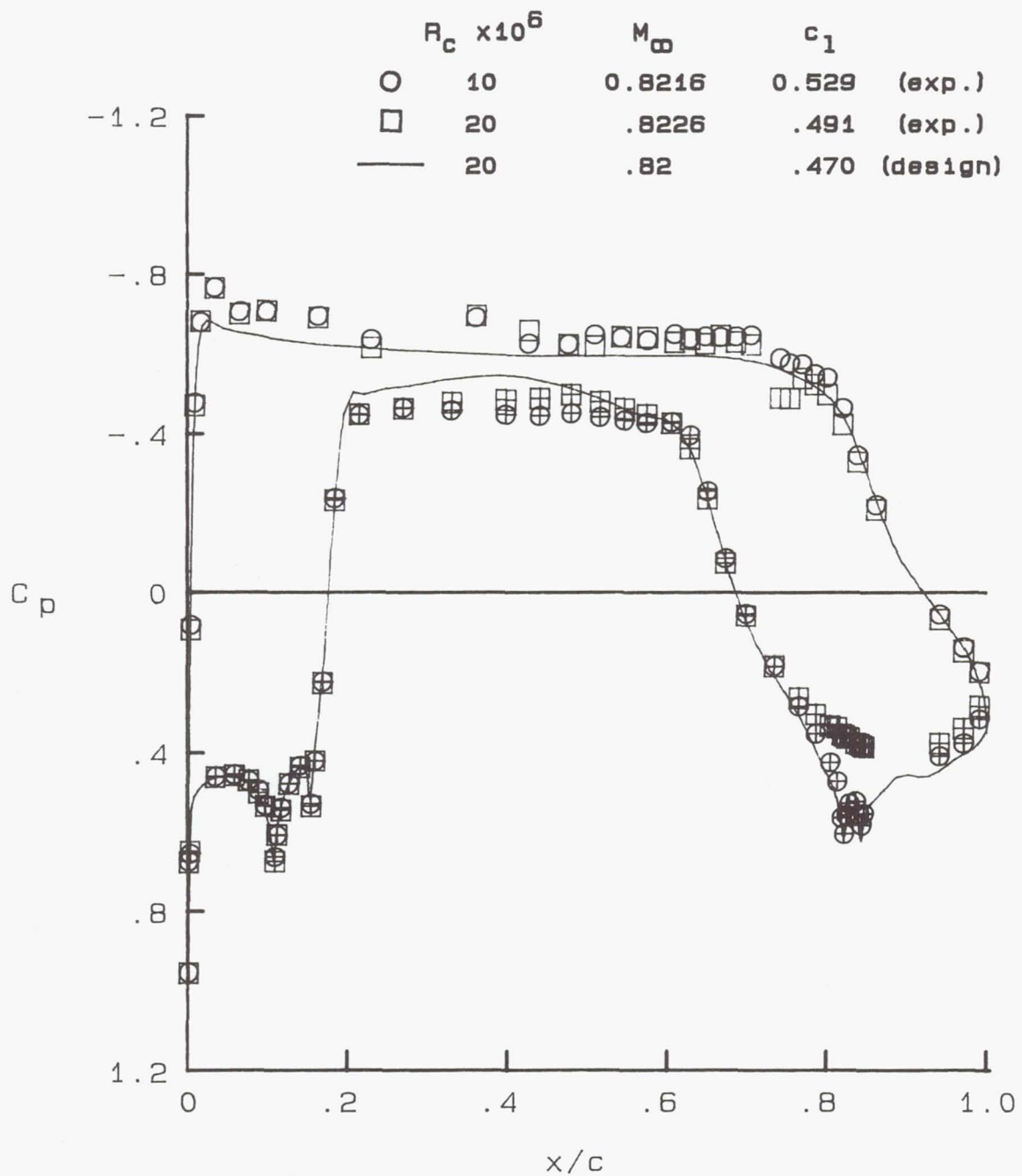
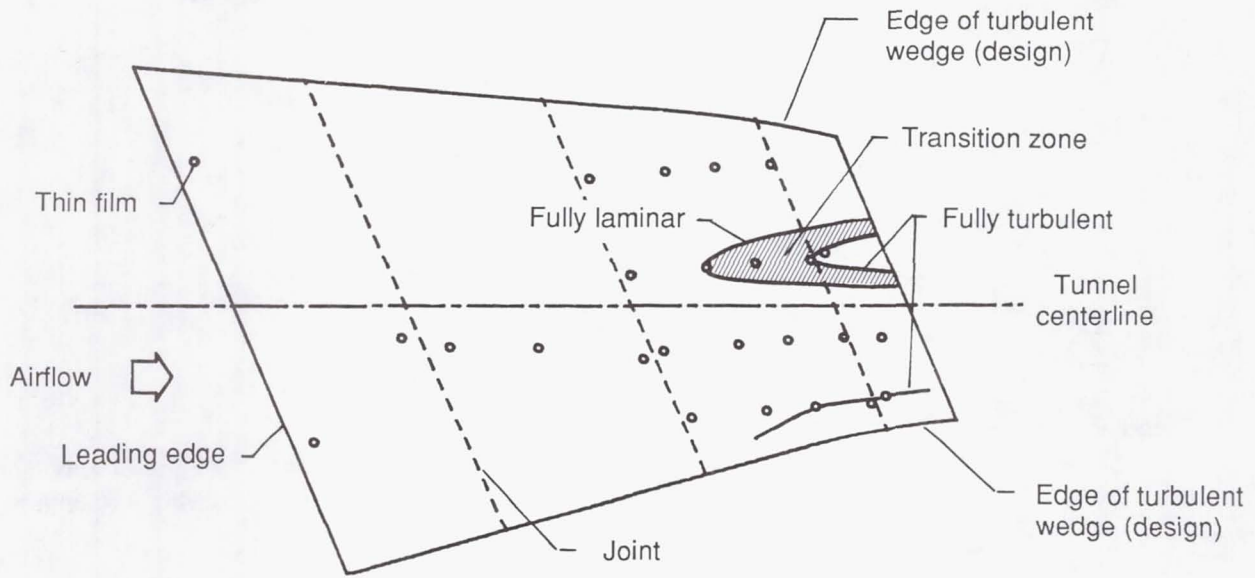
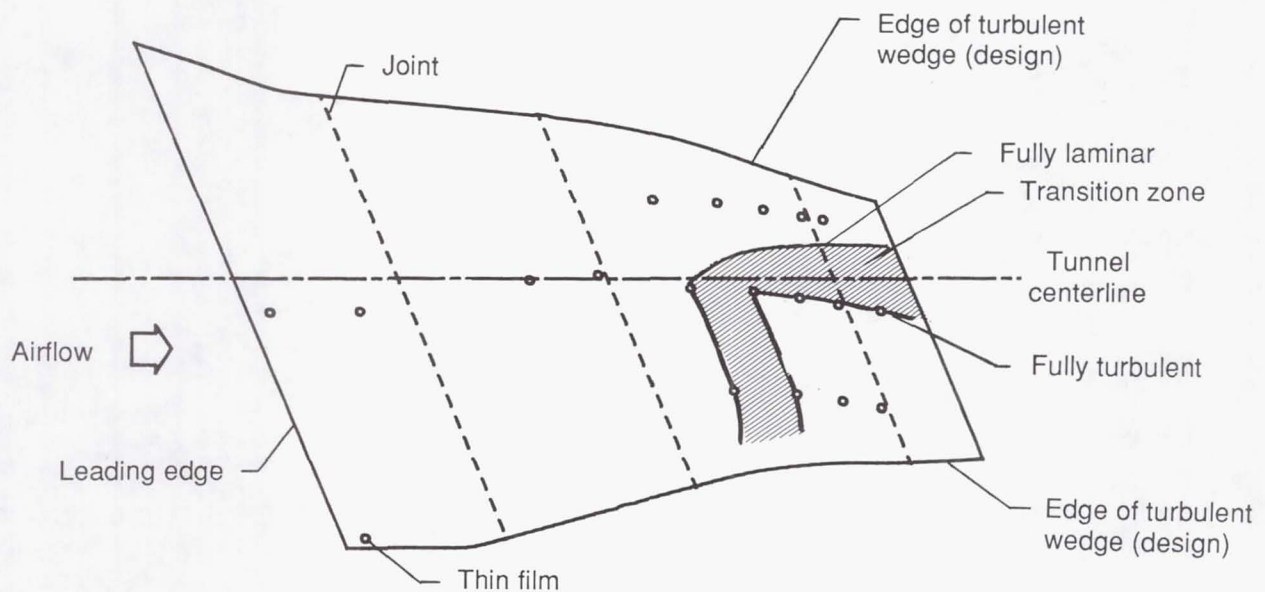


Figure 31. Experimental pressure distributions near midspan (station 8) at operational design conditions. Open symbols denote upper surface.

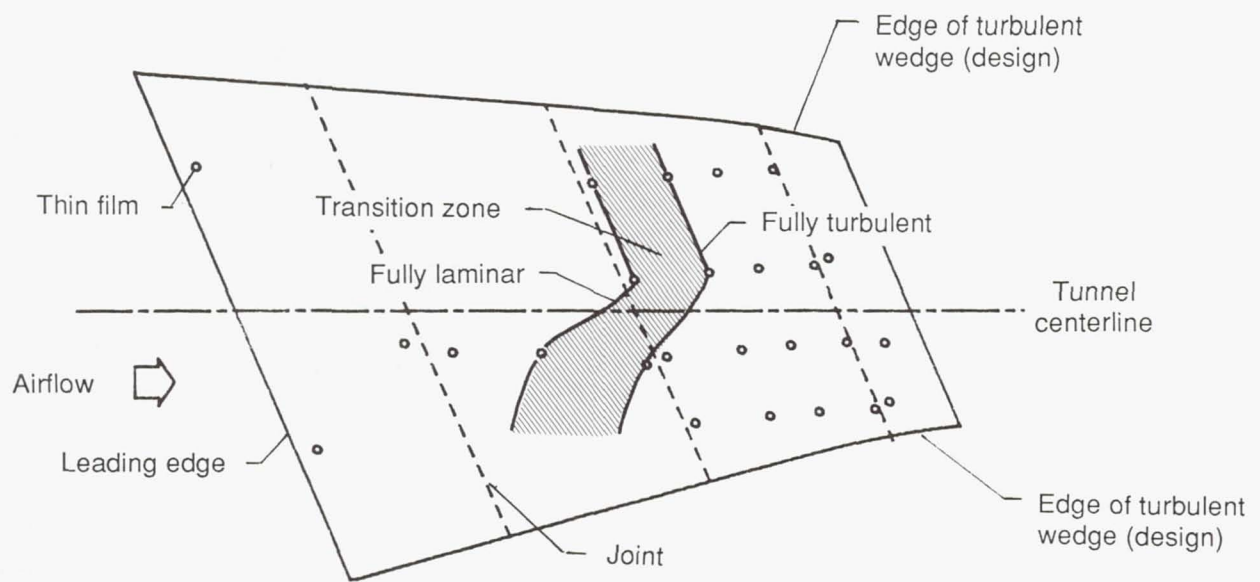


(a) Upper surface. $R_c = 10 \times 10^6$.

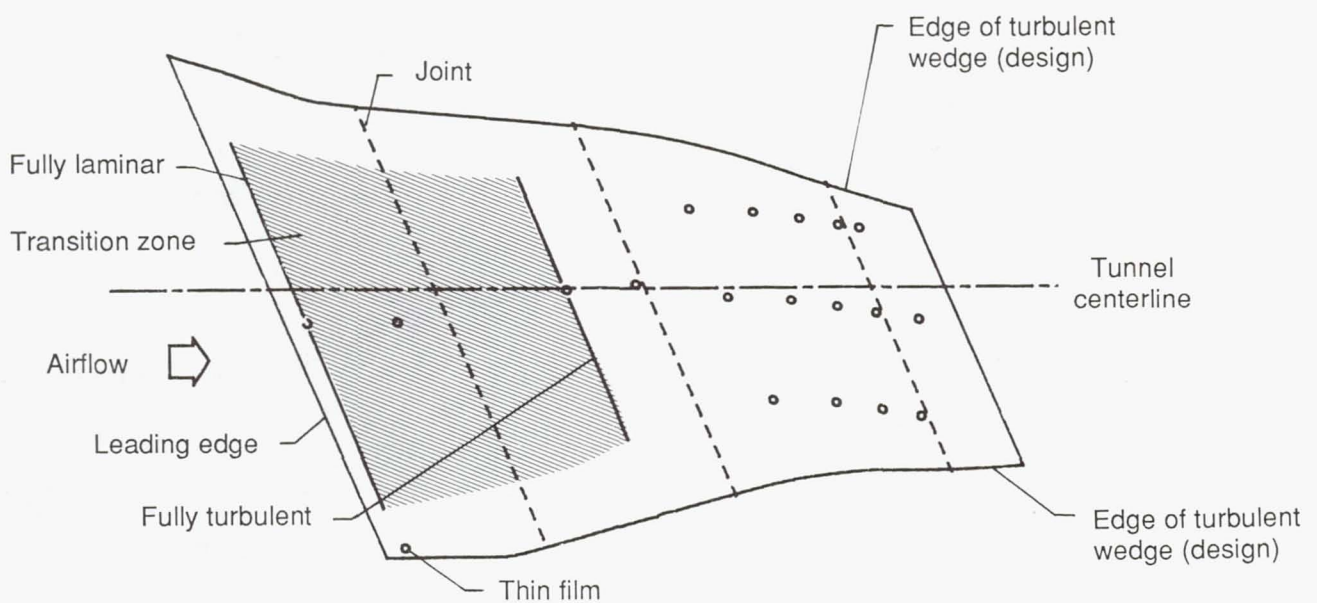


(b) Lower surface. $R_c = 10 \times 10^6$.

Figure 32. Transition patterns at operational design conditions.

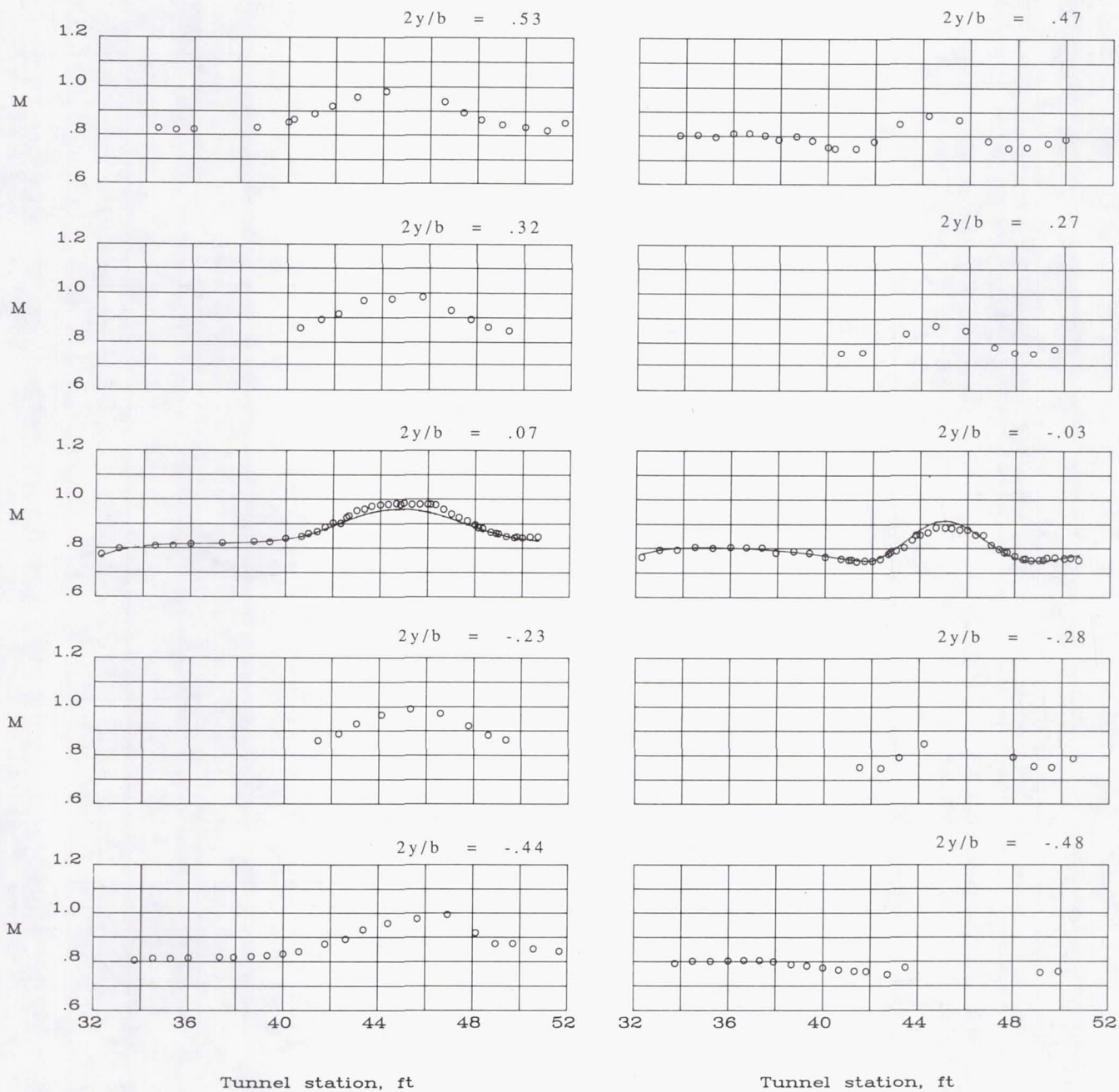


(c) Upper surface. $R_c = 20 \times 10^6$.



(d) Lower surface. $R_c = 20 \times 10^6$.

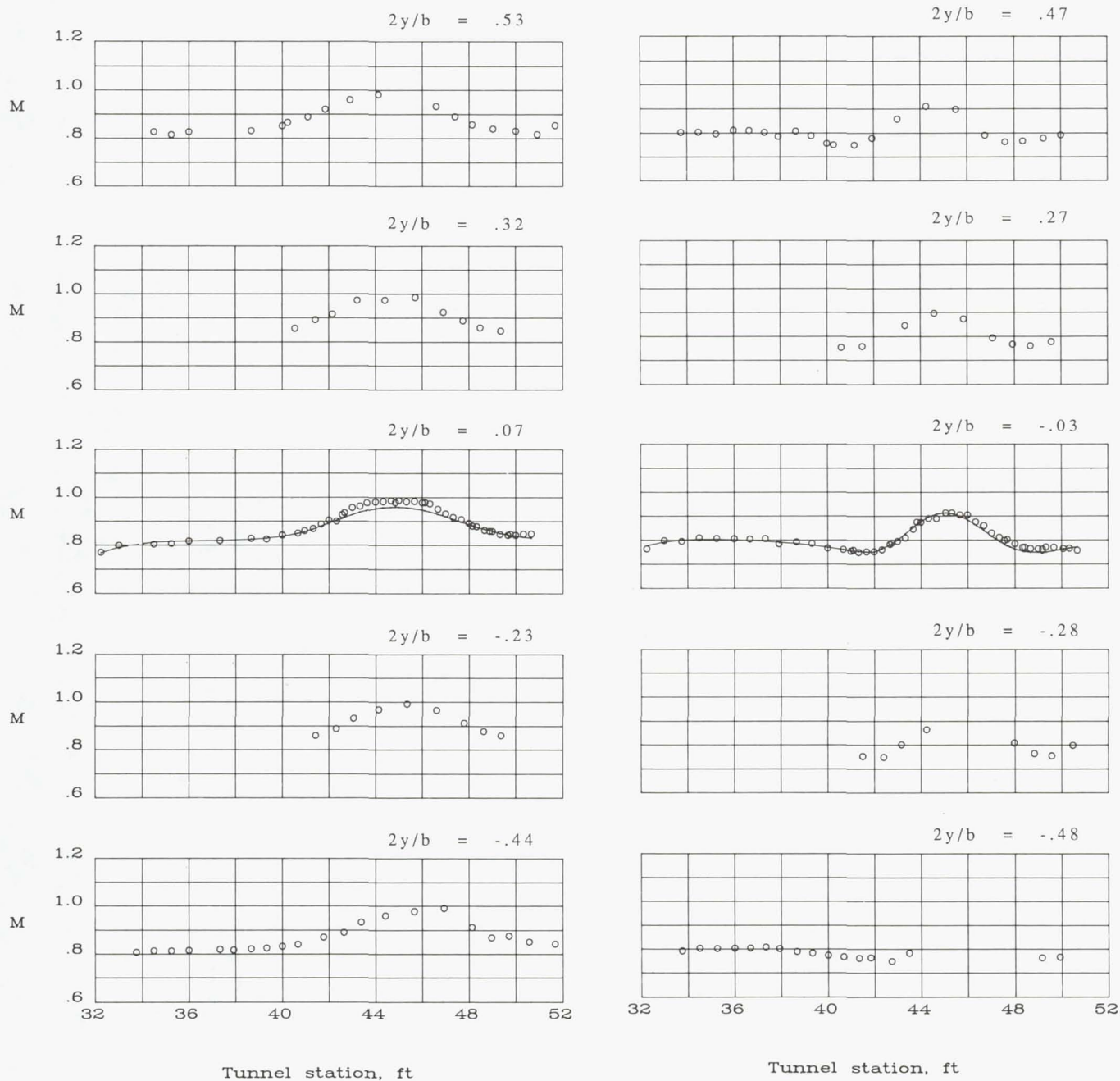
Figure 32. Concluded.



(a) Opposite upper surface.

(b) Opposite lower surface.

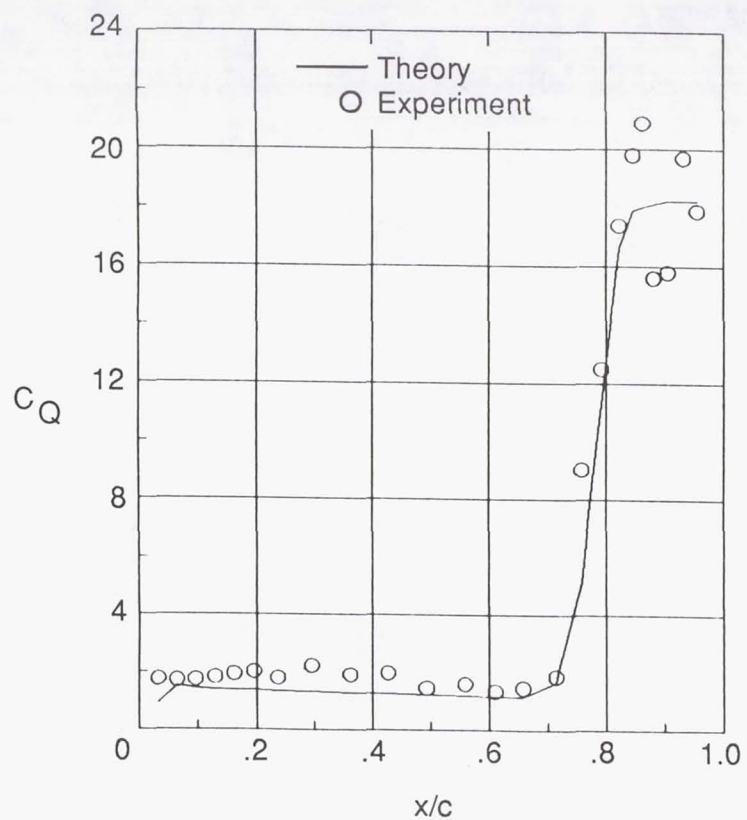
Figure 33. Local Mach number distributions on vertical test section liner walls opposite model upper and lower surfaces. $R_c = 10 \times 10^6$; $M_\infty = 0.8218$; $c_l = 0.529$.



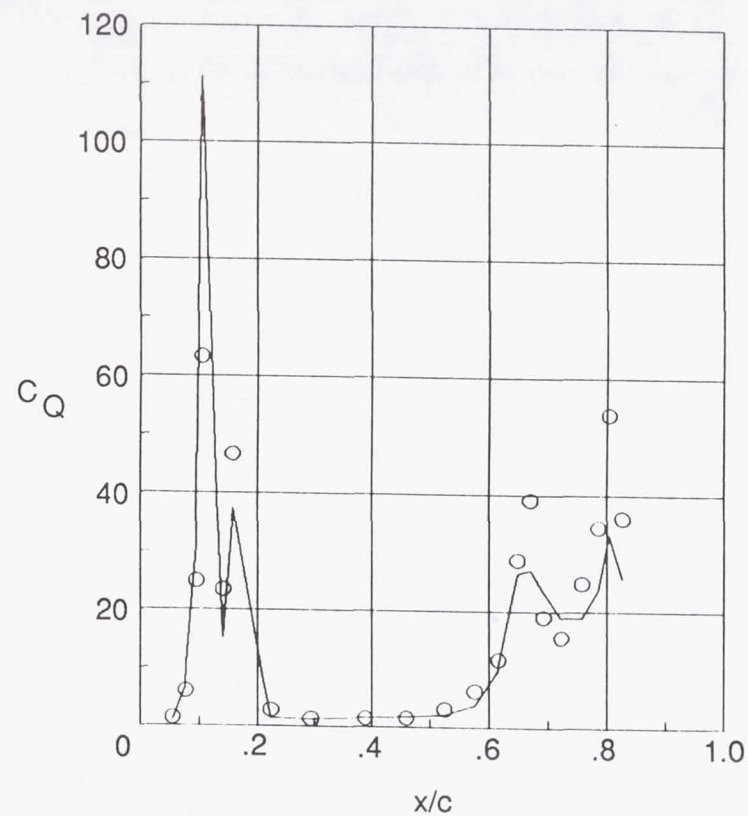
(a) Opposite upper surface.

(b) Opposite lower surface.

Figure 34. Local Mach number distributions on vertical test section liner walls opposite model upper and lower surfaces. $R_c = 20 \times 10^6$; $M_\infty = 0.8232$; $c_l = 0.476$.

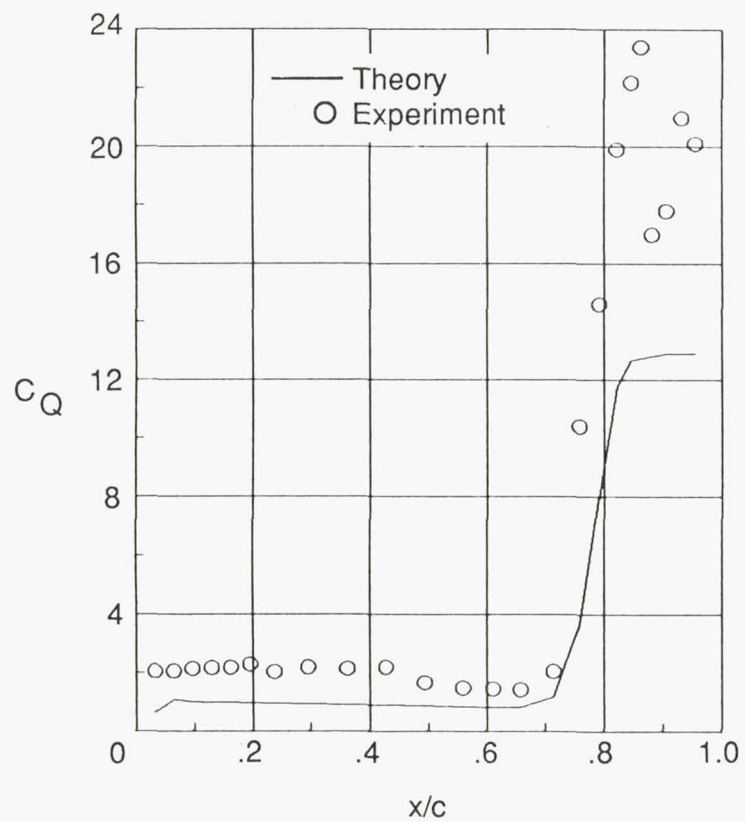


(a) Upper surface. $R_c = 10 \times 10^6$.

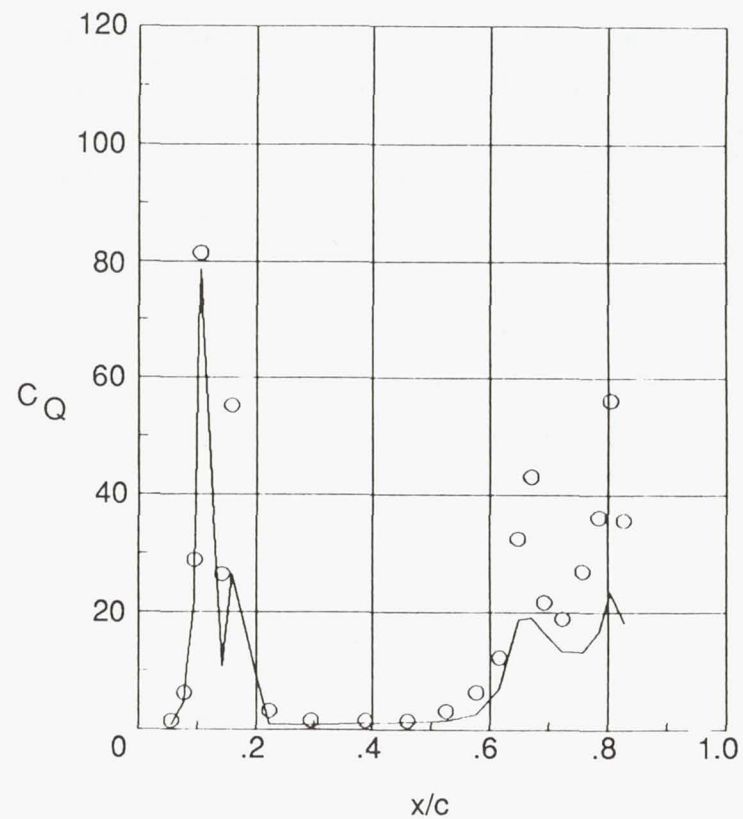


(b) Lower surface. $R_c = 10 \times 10^6$.

Figure 35. Comparison of theoretical and experimental suction distributions at operational design conditions.

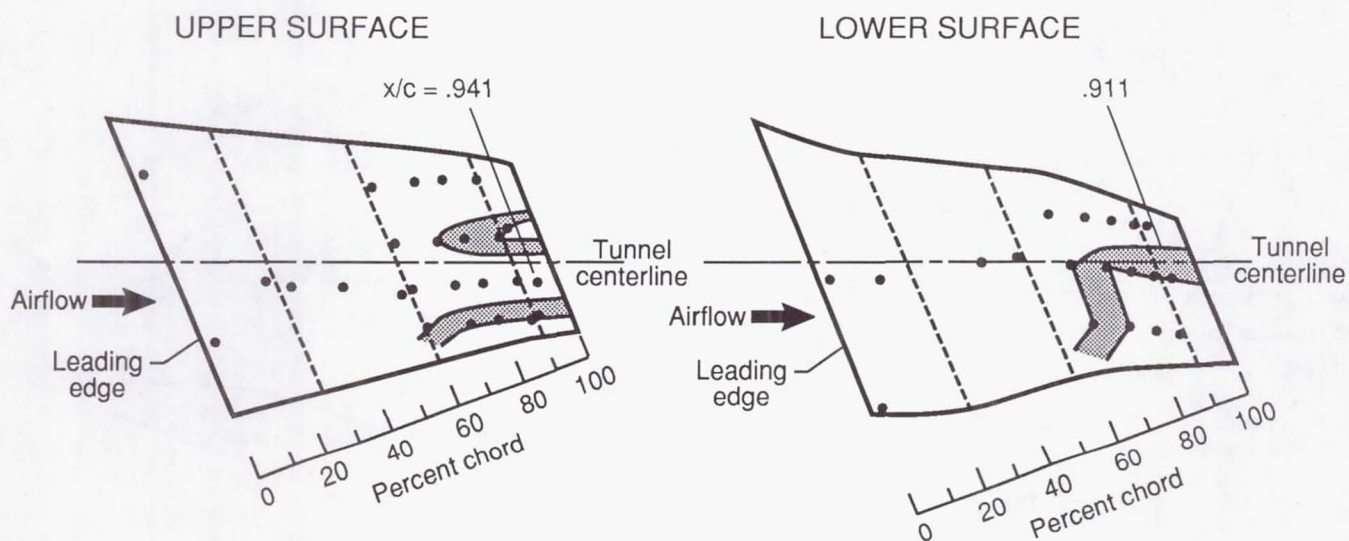


(c) Upper surface. $R_c = 20 \times 10^6$.

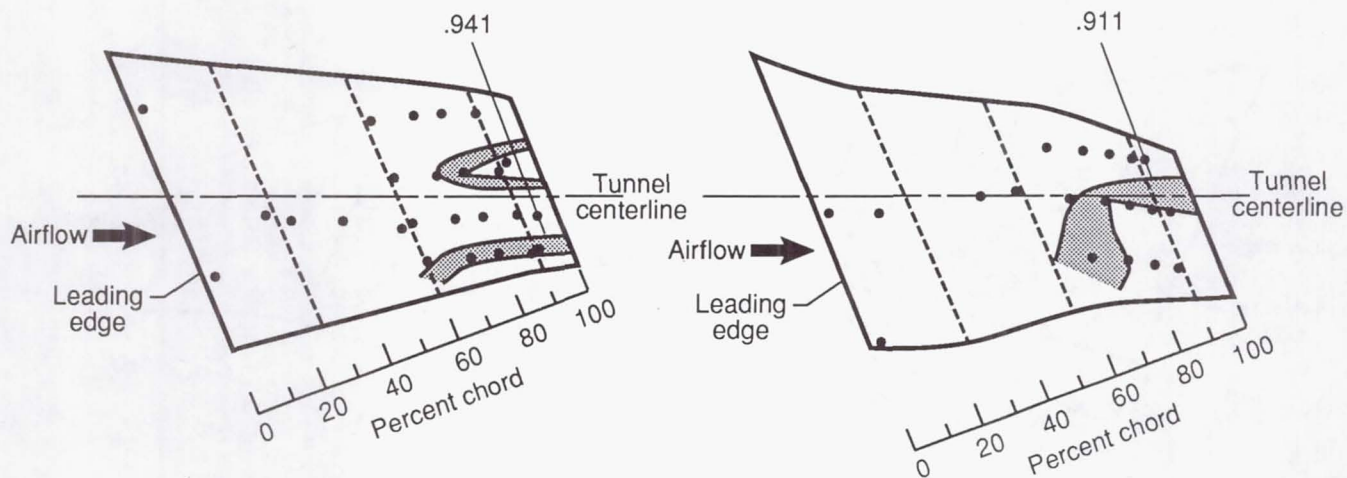


(d) Lower surface. $R_c = 20 \times 10^6$.

Figure 35. Concluded.

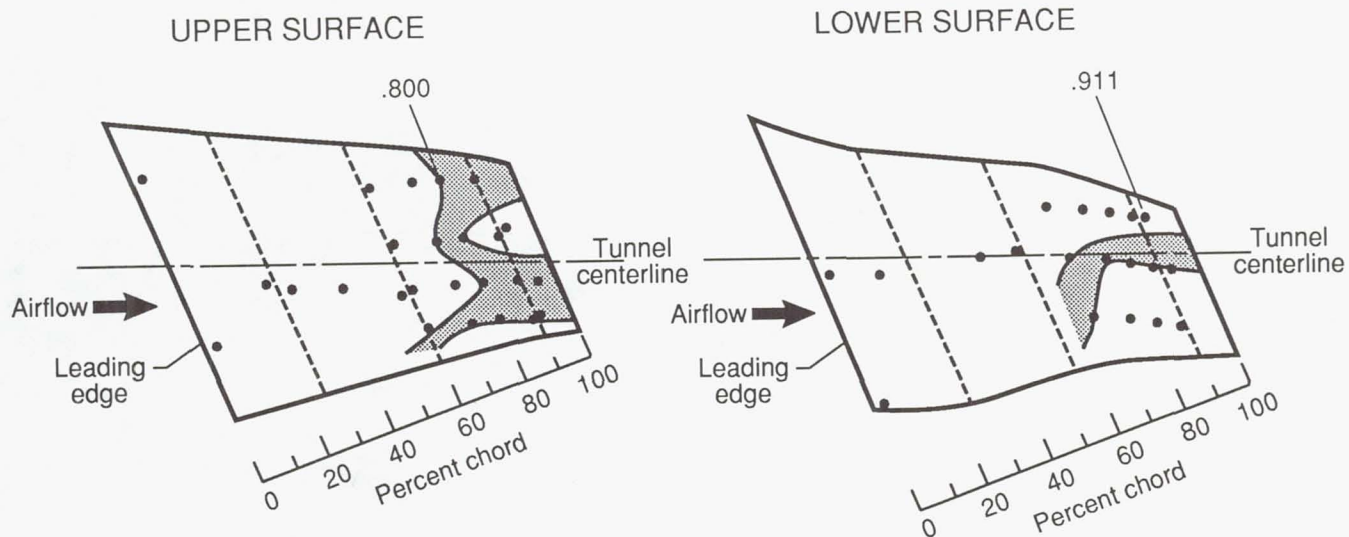


(a) $R_c = 10 \times 10^6$; $M_\infty = 0.8218$; $c_l = 0.529$.

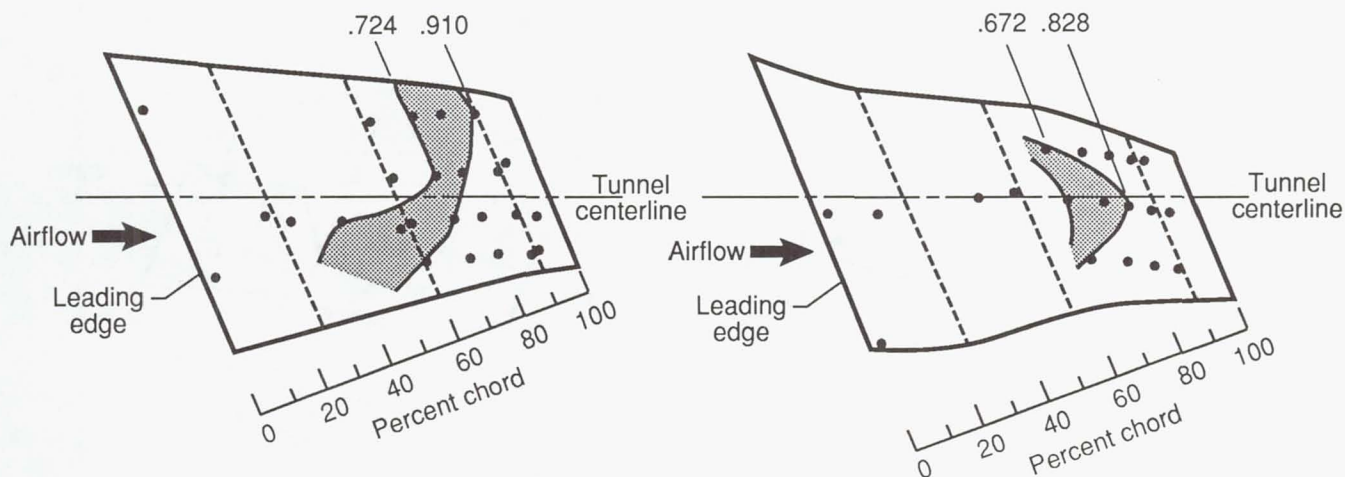


(b) $R_c = 11 \times 10^6$; $M_\infty = 0.8215$; $c_l = 0.534$.

Figure 36. Variation of transition patterns with Reynolds number at operational design Mach number within boundaries of design laminar "test" zones; x/c locations shown are locations of thin-film gauges.

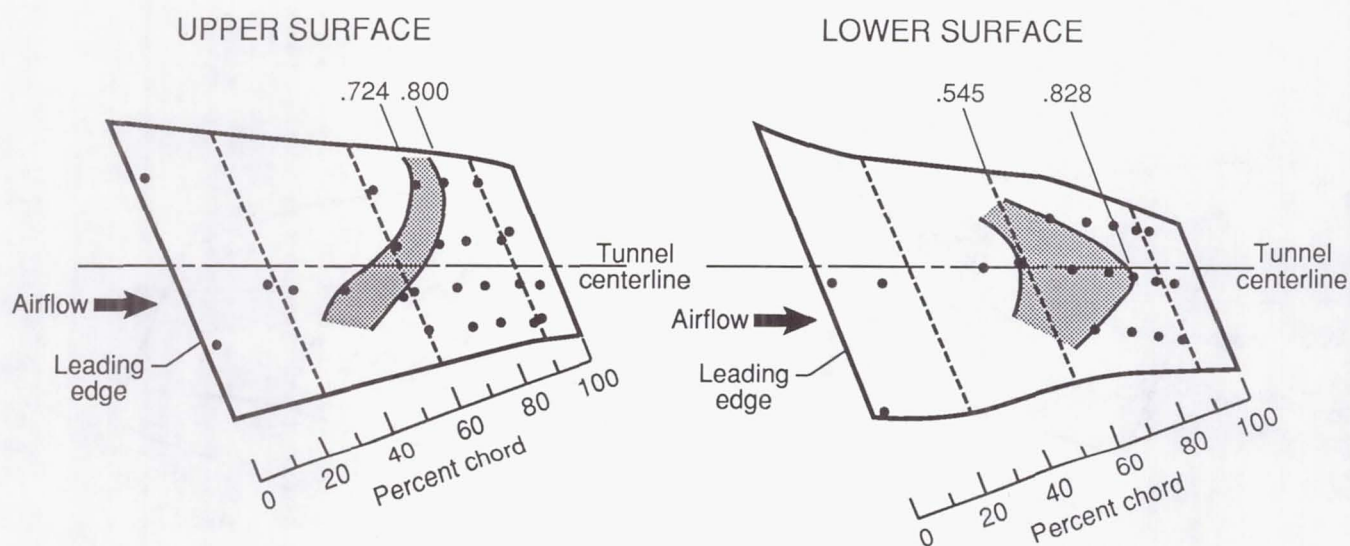


(c) $R_c = 12 \times 10^6$; $M_\infty = 0.8217$; $c_l = 0.532$.

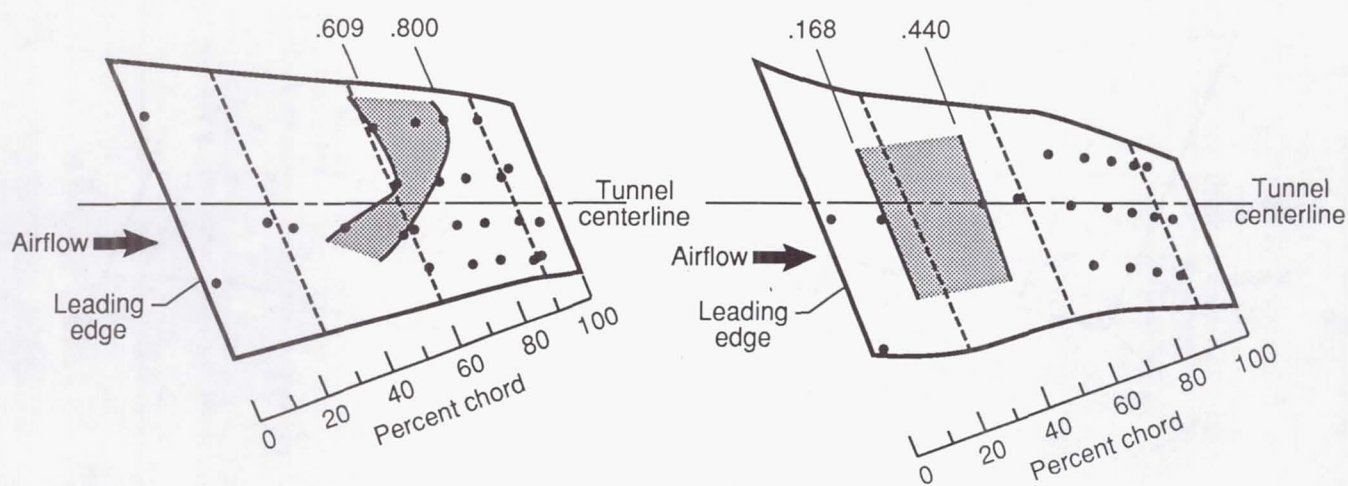


(d) $R_c = 13 \times 10^6$; $M_\infty = 0.8219$; $c_l = 0.523$.

Figure 36. Continued.

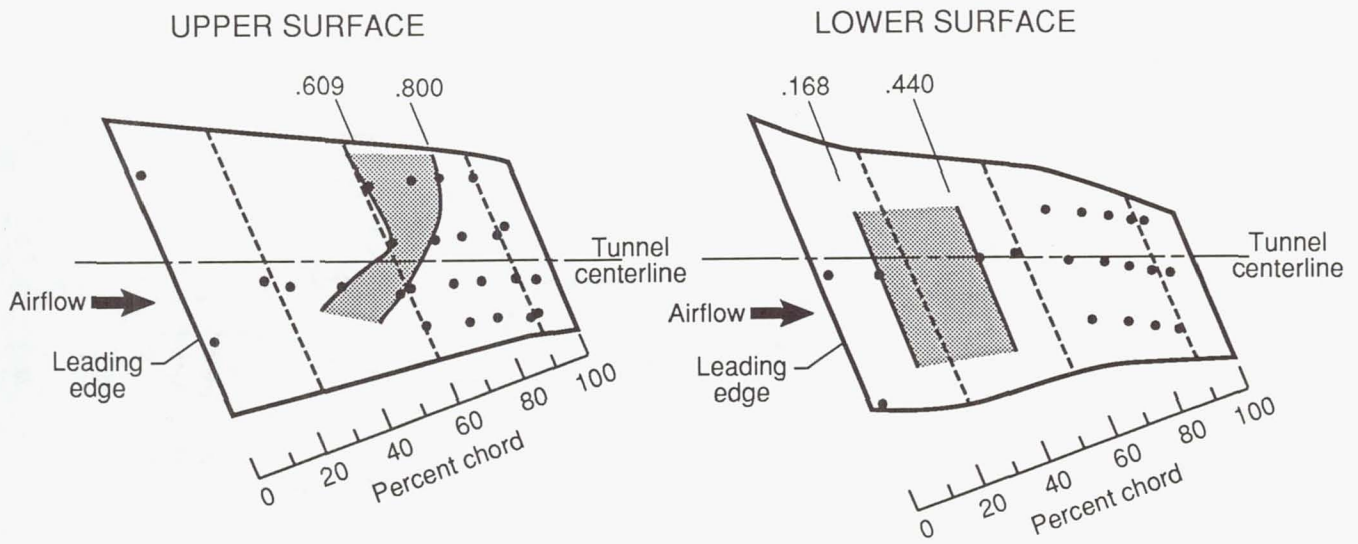


(e) $R_c = 14 \times 10^6$; $M_\infty = 0.8224$; $c_l = 0.517$.

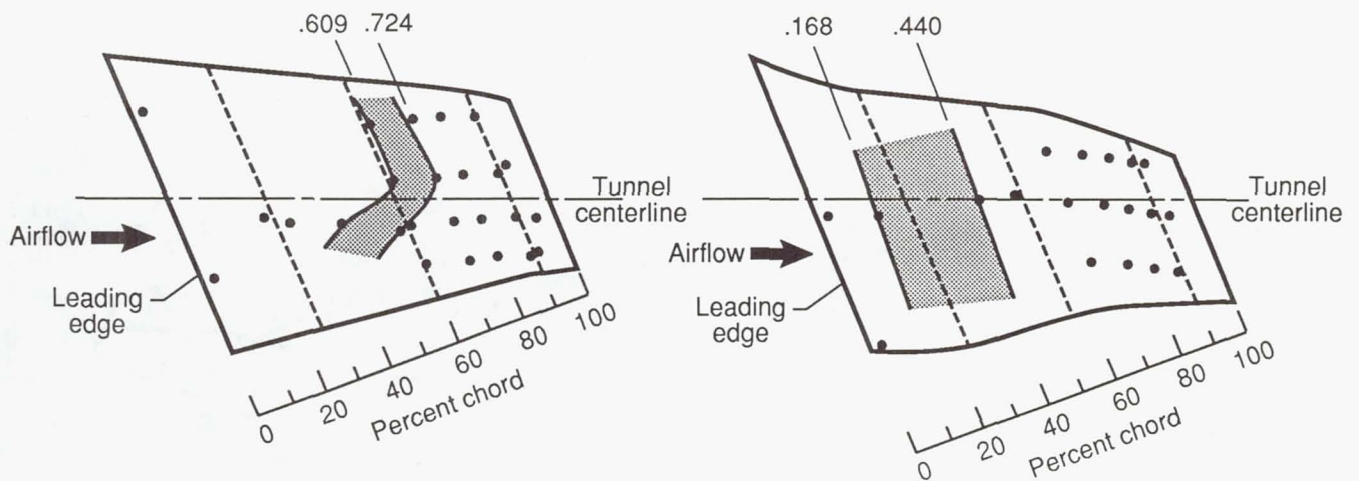


(f) $R_c = 15 \times 10^6$; $M_\infty = 0.8222$; $c_l = 0.503$.

Figure 36. Continued.

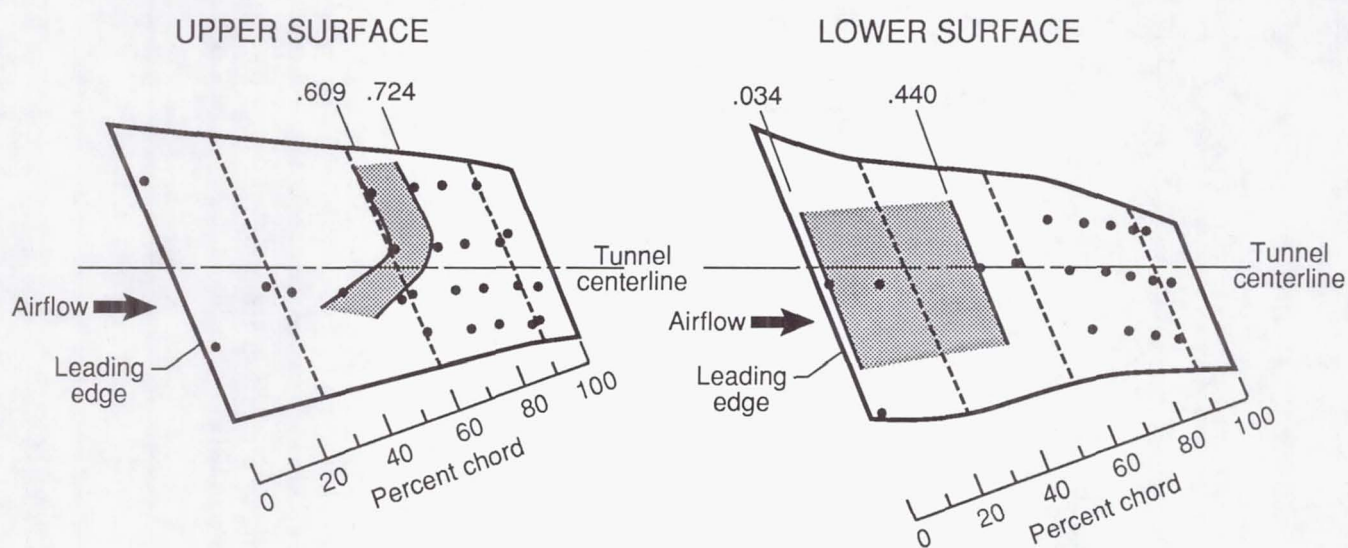


(g) $R_c = 16 \times 10^6$; $M_\infty = 0.8222$; $c_l = 0.499$.



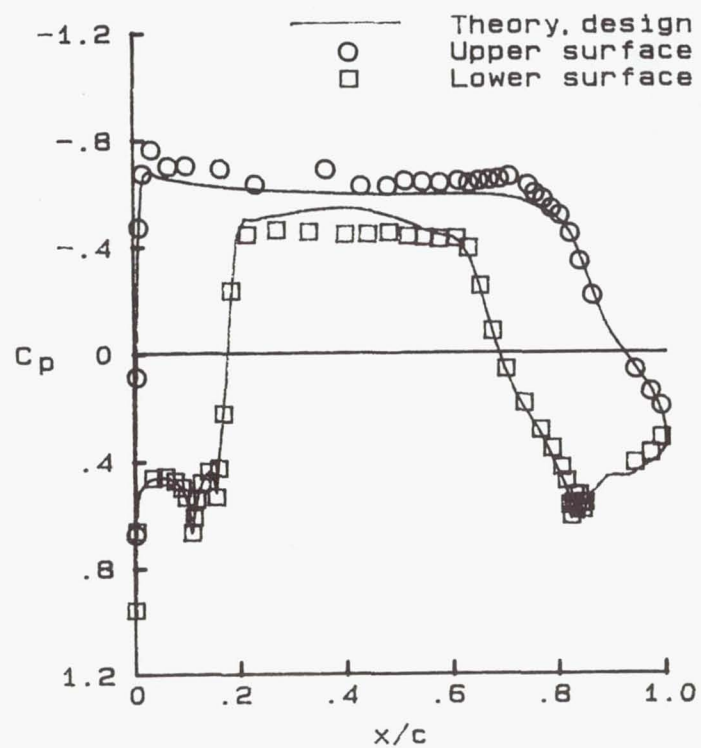
(h) $R_c = 18 \times 10^6$; $M_\infty = 0.8221$; $c_l = 0.498$.

Figure 36. Continued.

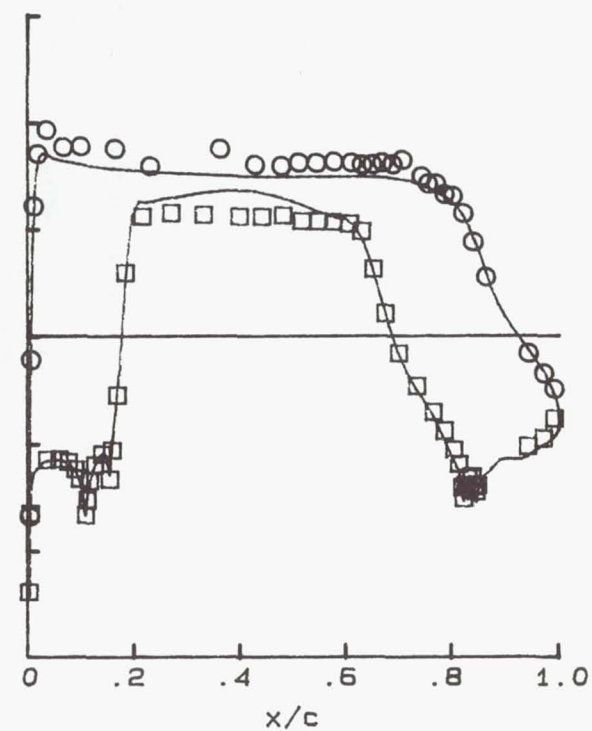


(i) $R_c = 20 \times 10^6$; $M_\infty = 0.8232$; $c_l = 0.476$.

Figure 36. Concluded.

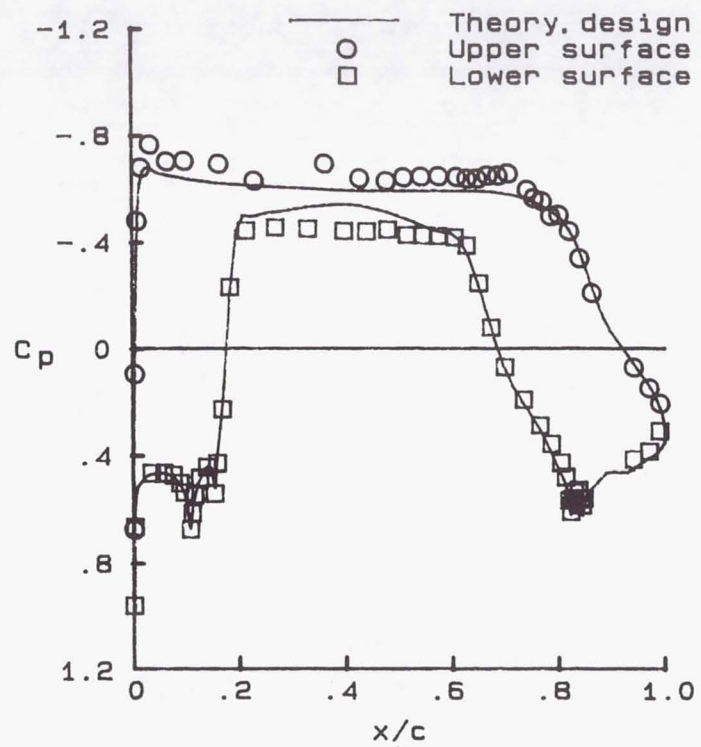


(a) $R_c = 10 \times 10^6$; $M_\infty = 0.8218$; $c_l = 0.529$.

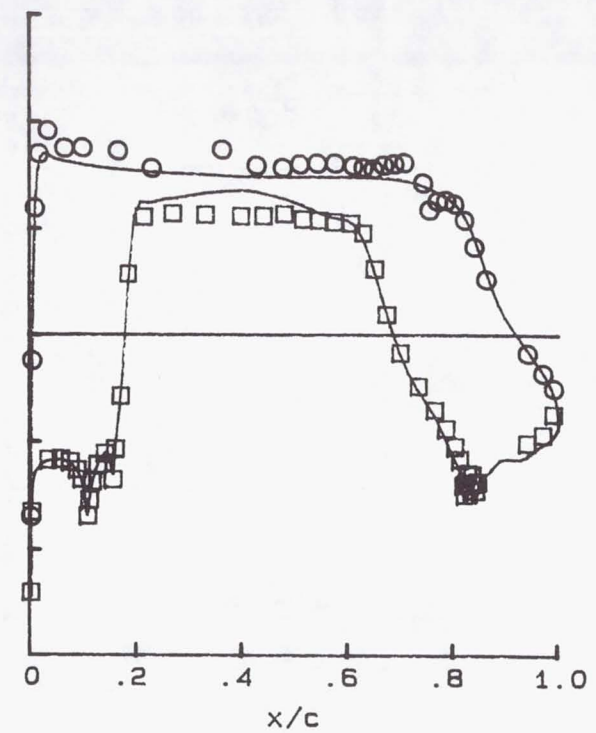


(b) $R_c = 11 \times 10^6$; $M_\infty = 0.8215$; $c_l = 0.534$.

Figure 37. Effect on experimental chordwise pressure distribution near midspan (station 8) of varying Reynolds number at operational design Mach number.

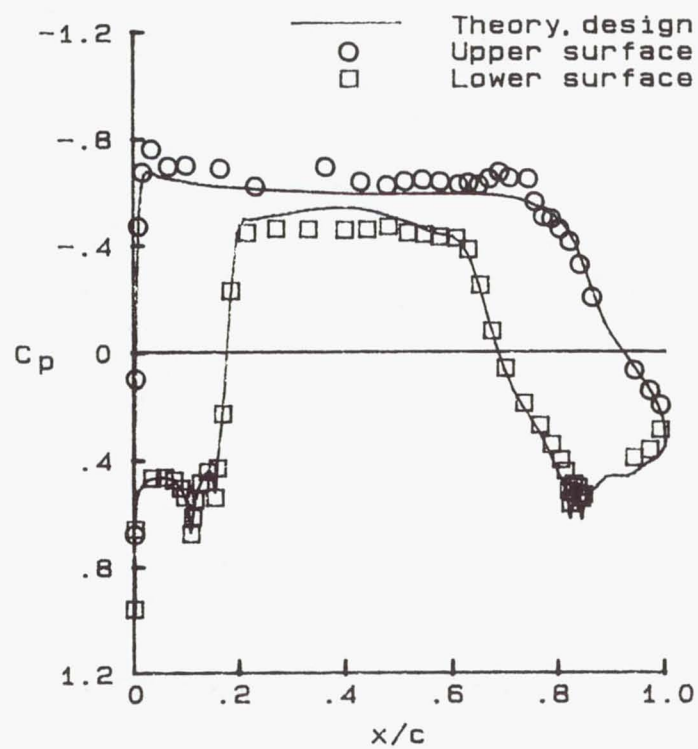


(c) $R_c = 12 \times 10^6$; $M_\infty = 0.8217$; $c_l = 0.532$.



(d) $R_c = 13 \times 10^6$; $M_\infty = 0.8219$; $c_l = 0.523$.

Figure 37. Continued.

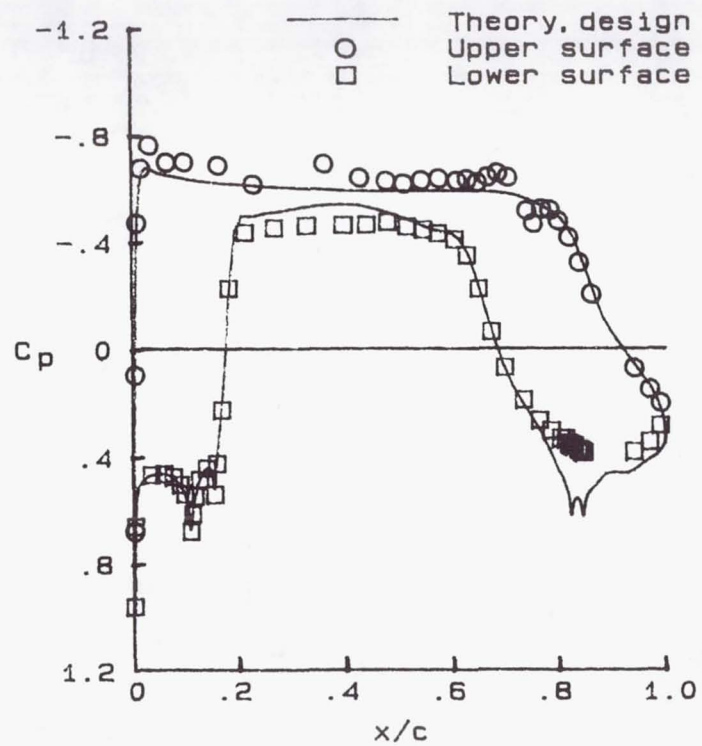


(e) $R_c = 14 \times 10^6$; $M_\infty = 0.8224$; $c_l = 0.517$.

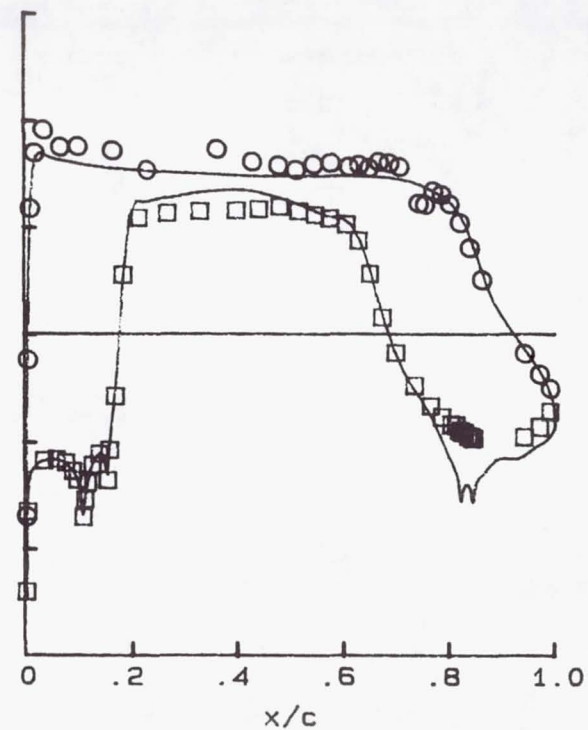


(f) $R_c = 15 \times 10^6$; $M_\infty = 0.8222$; $c_l = 0.503$.

Figure 37. Continued.

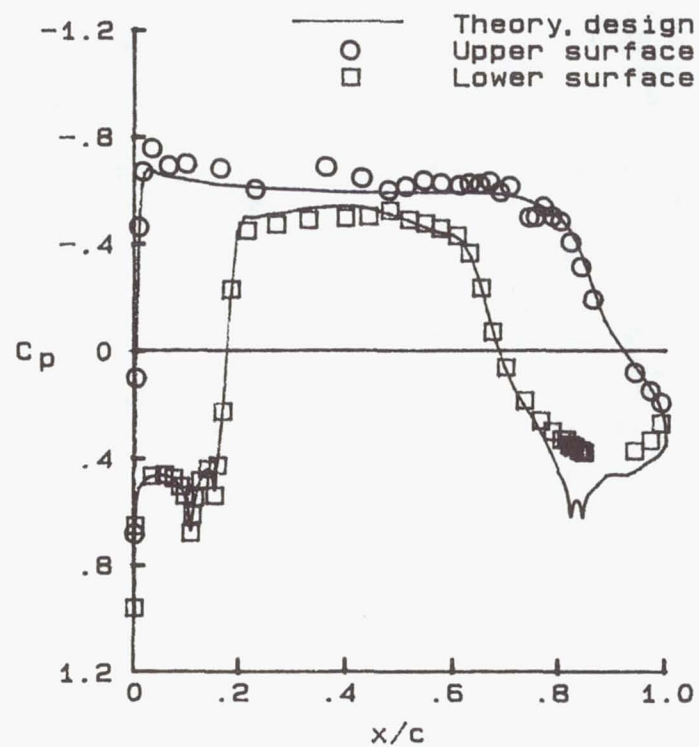


(g) $R_c = 16 \times 10^6$; $M_\infty = 0.8222$; $c_l = 0.499$.



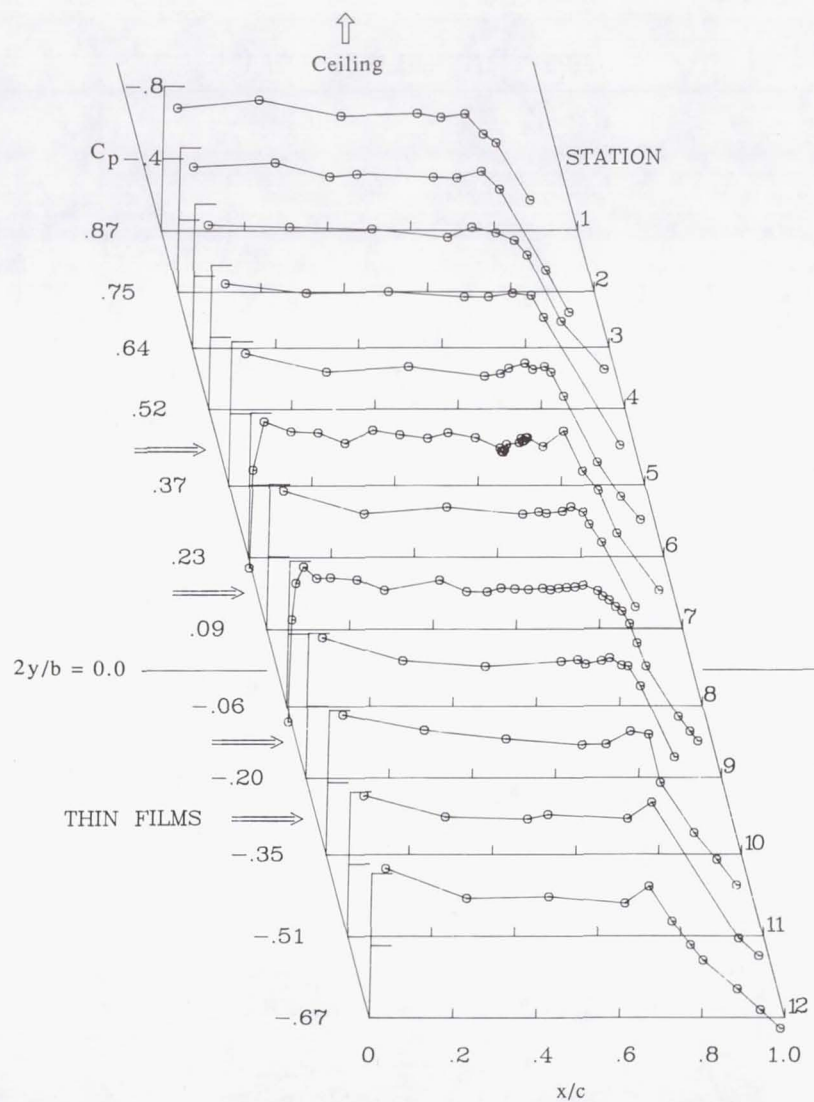
(h) $R_c = 18 \times 10^6$; $M_\infty = 0.8221$; $c_l = 0.498$.

Figure 37. Continued.

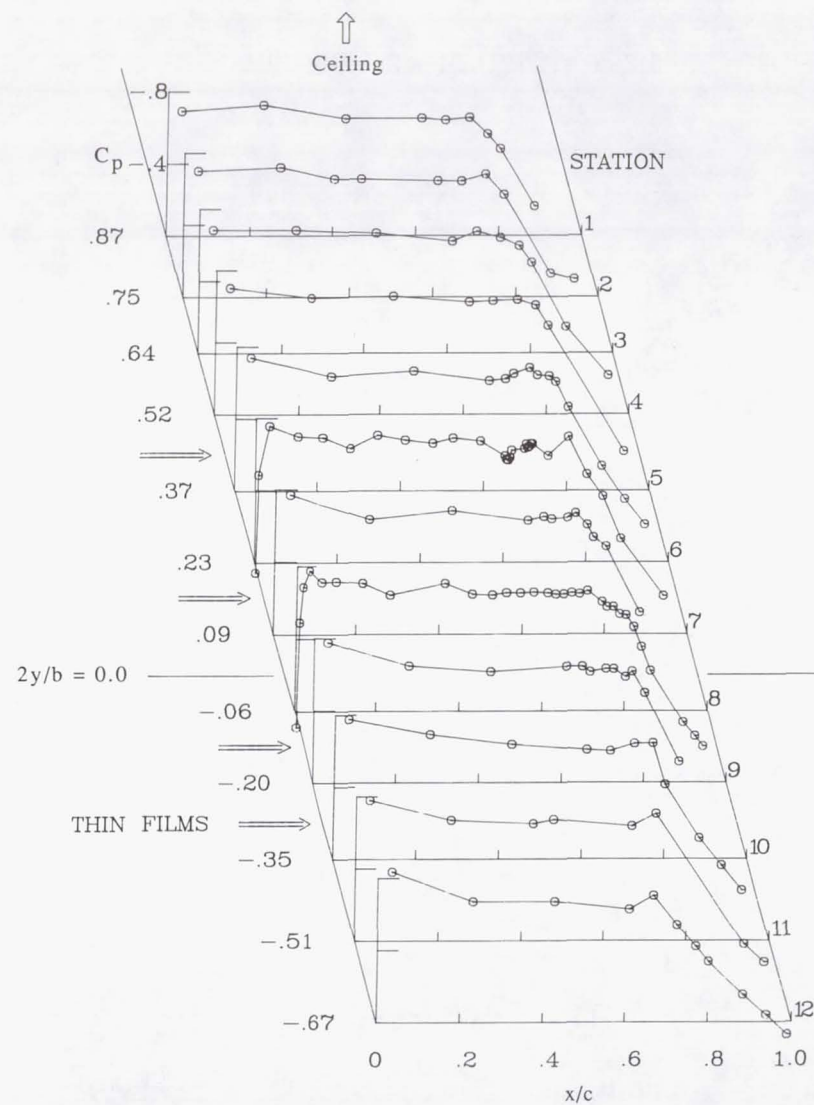


(i) $R_c = 20 \times 10^6$; $M_\infty = 0.8232$; $c_l = 0.476$.

Figure 37. Concluded.



(a) $R_c = 10 \times 10^6$; $M_\infty = 0.8218$.



(b) $R_c = 11 \times 10^6$; $M_\infty = 0.8215$.

Figure 38. Effect on experimental upper-surface spanwise pressure distribution of varying Reynolds number at operational design Mach number.

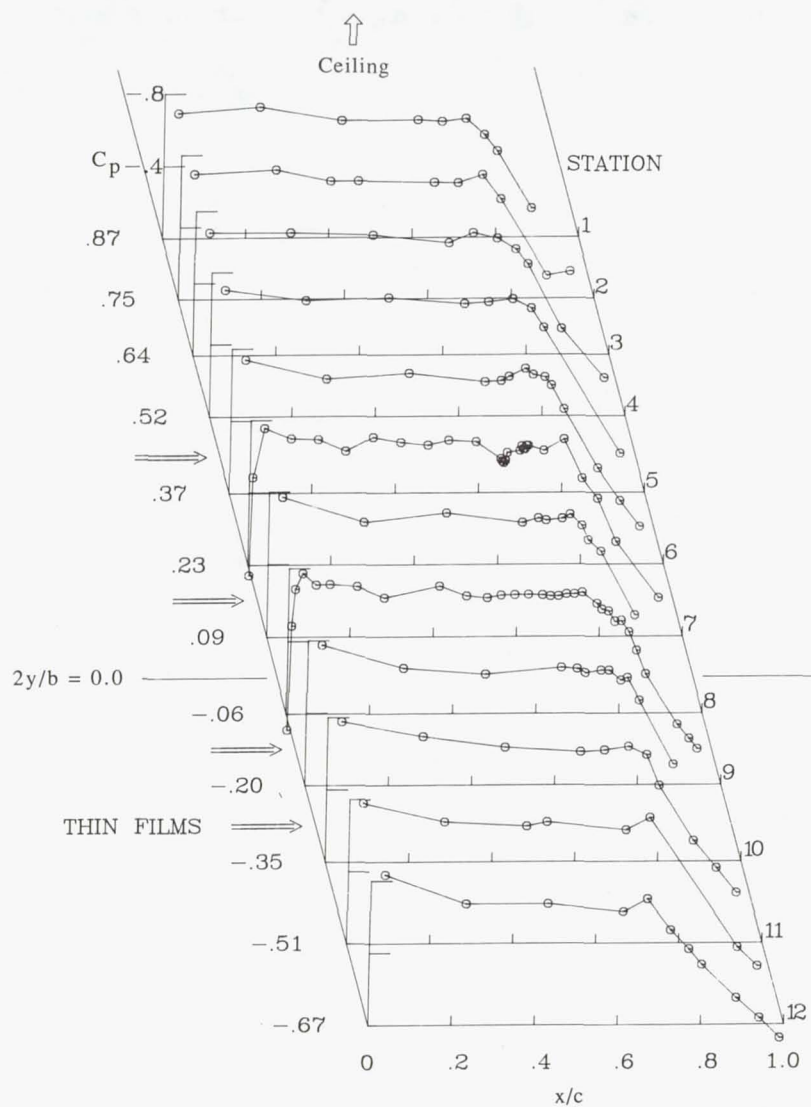
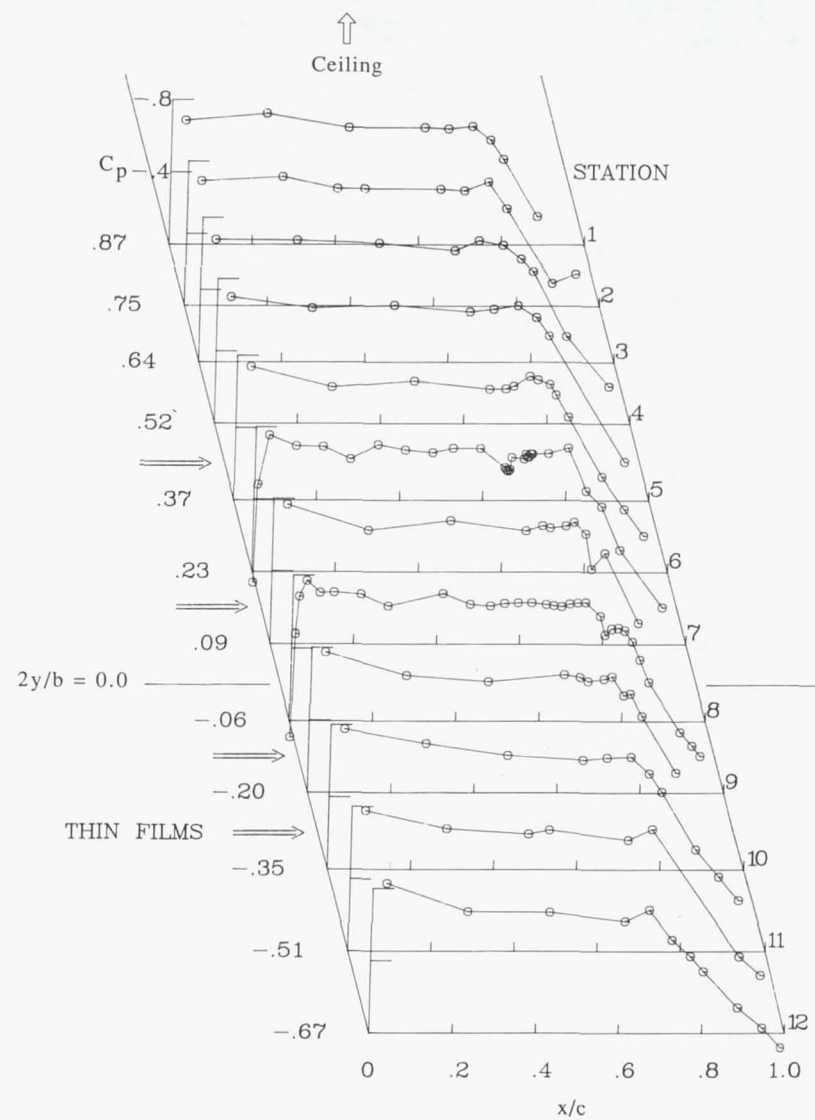
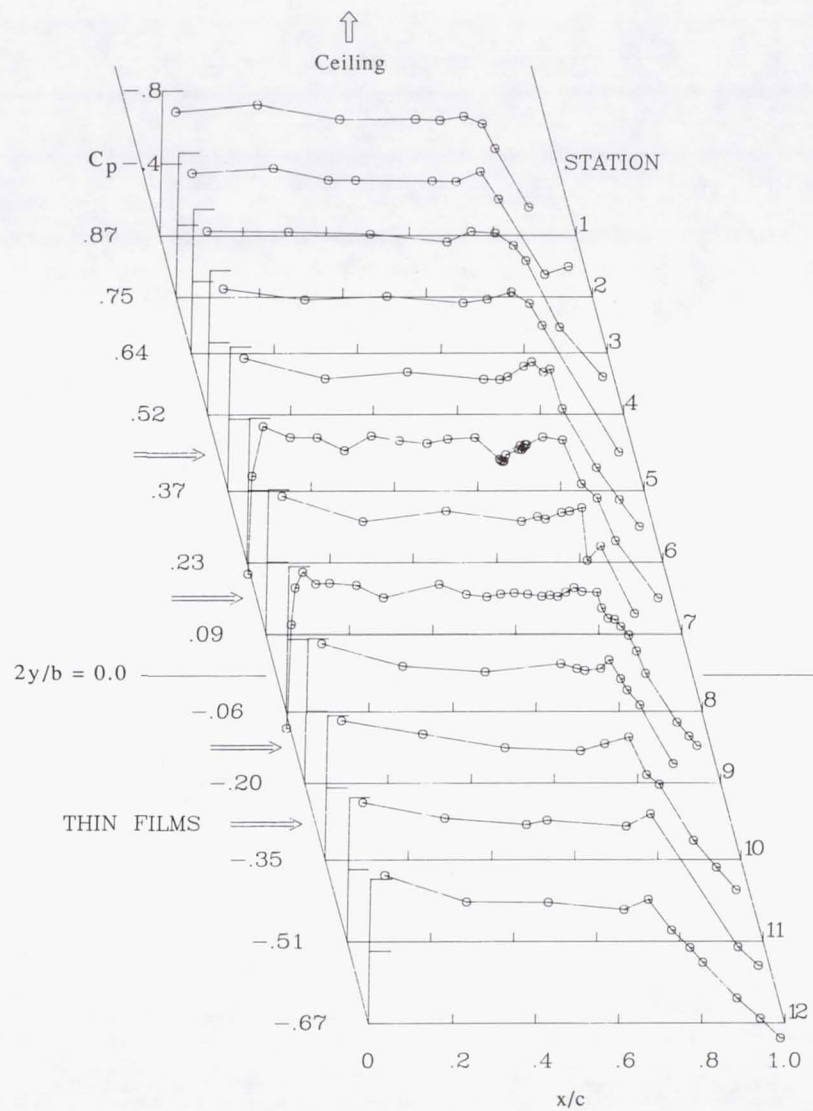
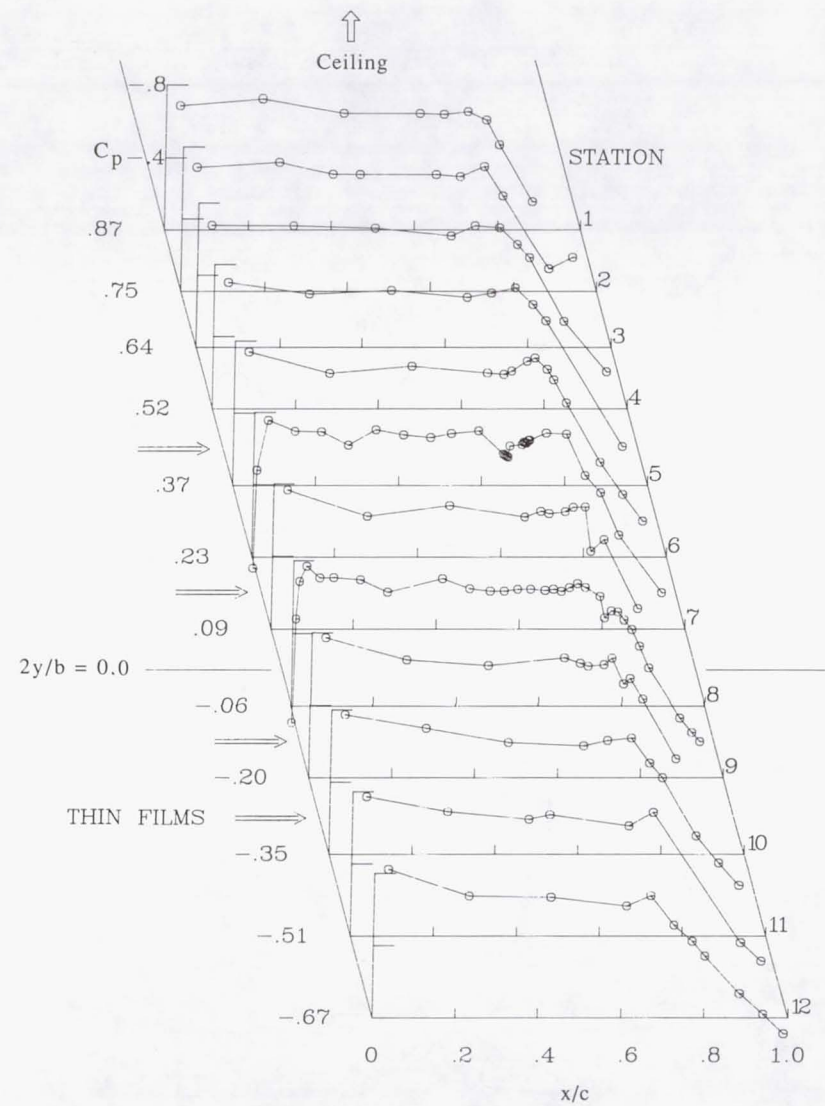
(c) $R_c = 12 \times 10^6$; $M_\infty = 0.8217$.(d) $R_c = 13 \times 10^6$; $M_\infty = 0.8219$.

Figure 38. Continued.



(e) $R_c = 14 \times 10^6$; $M_\infty = 0.8224$.



(f) $R_c = 15 \times 10^6$; $M_\infty = 0.8222$.

Figure 38. Continued.

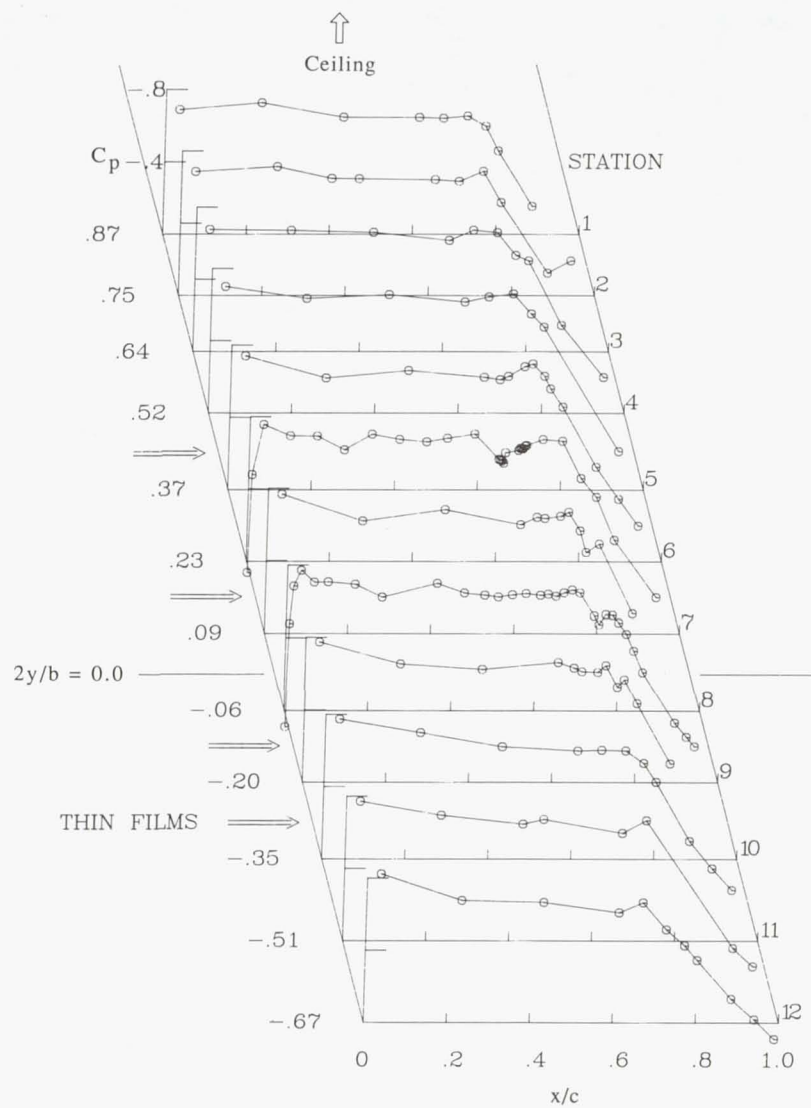
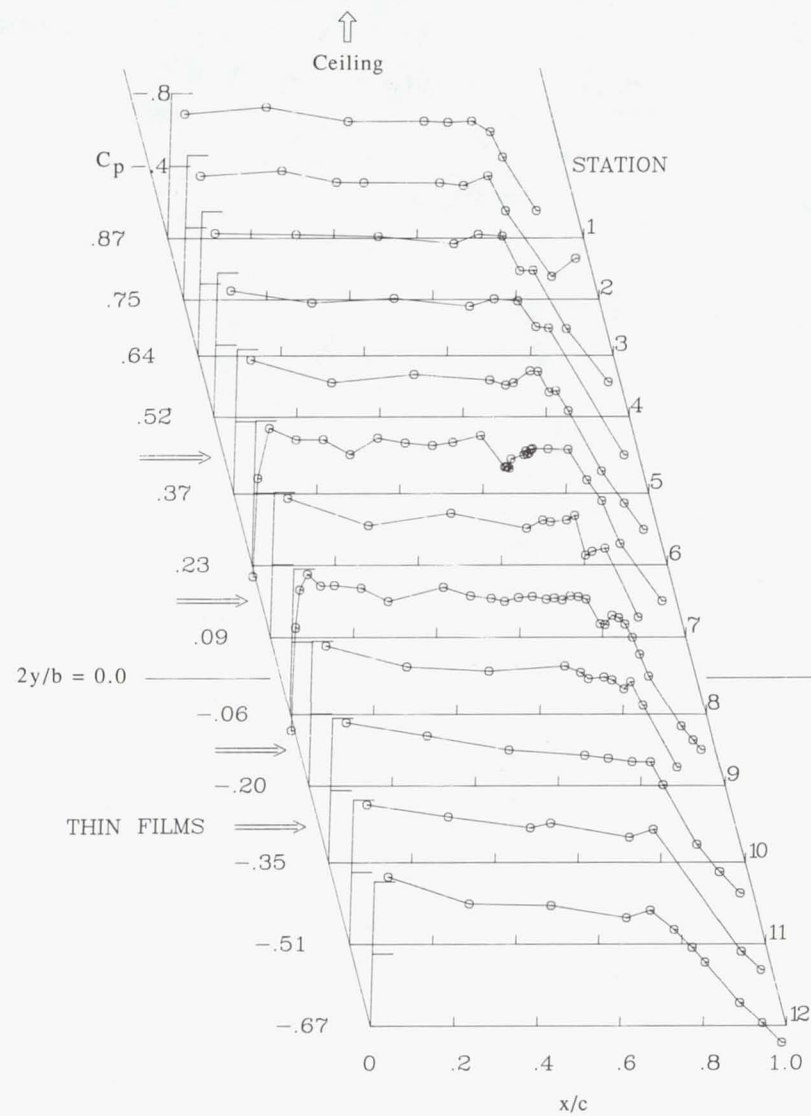
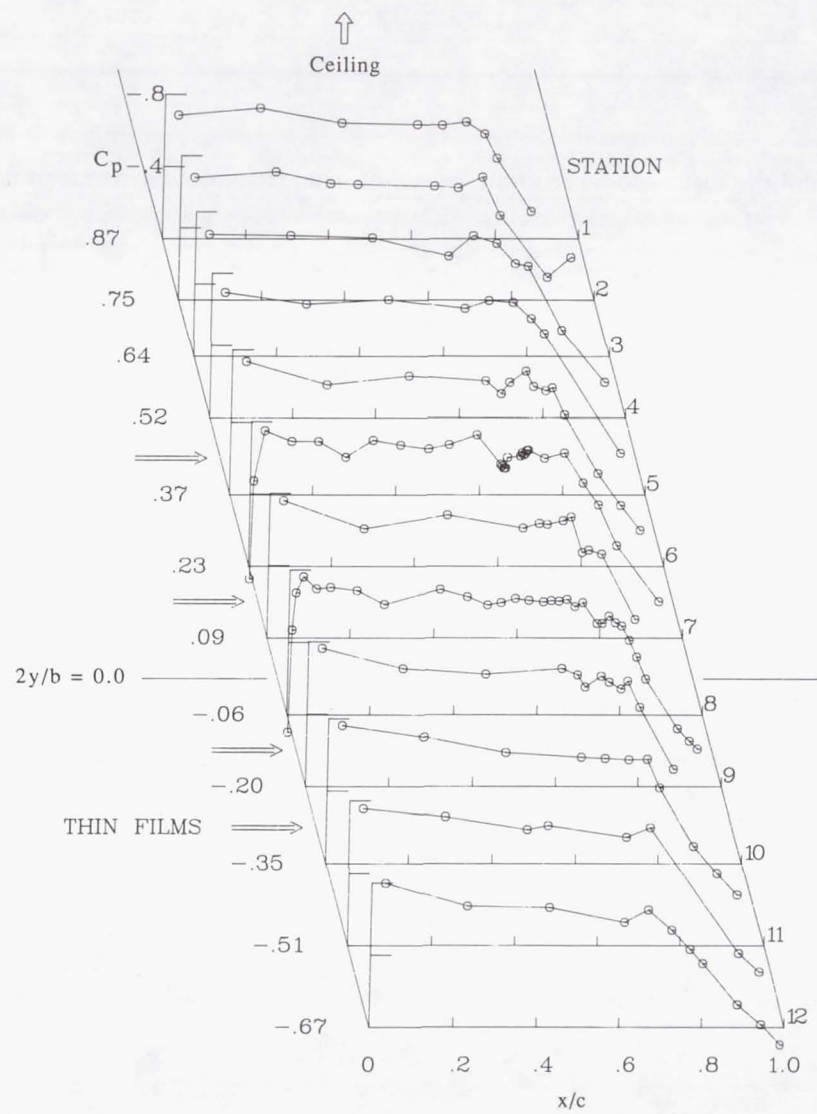
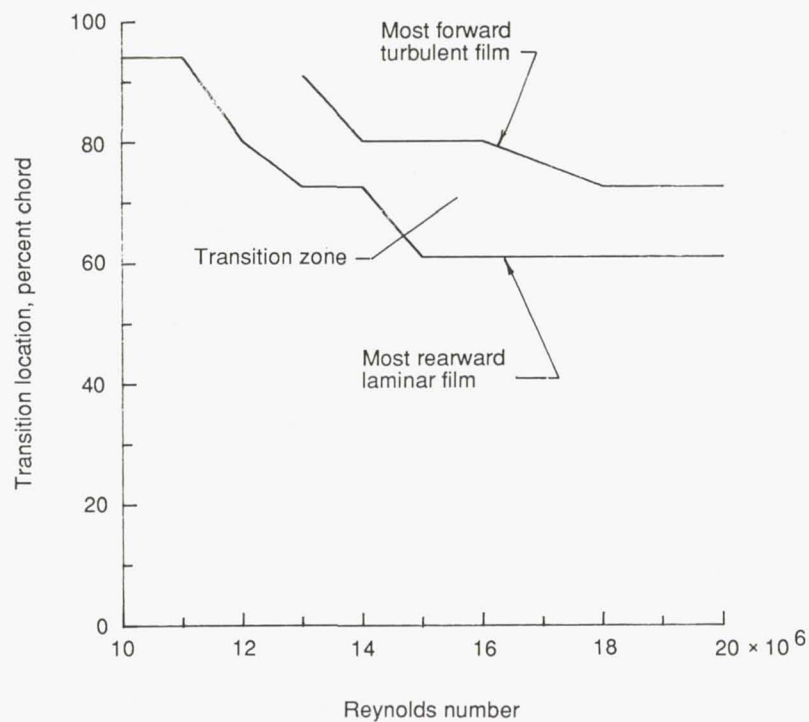
(g) $R_c = 16 \times 10^6$; $M_\infty = 0.8222$.(h) $R_c = 18 \times 10^6$; $M_\infty = 0.8221$.

Figure 38. Continued.

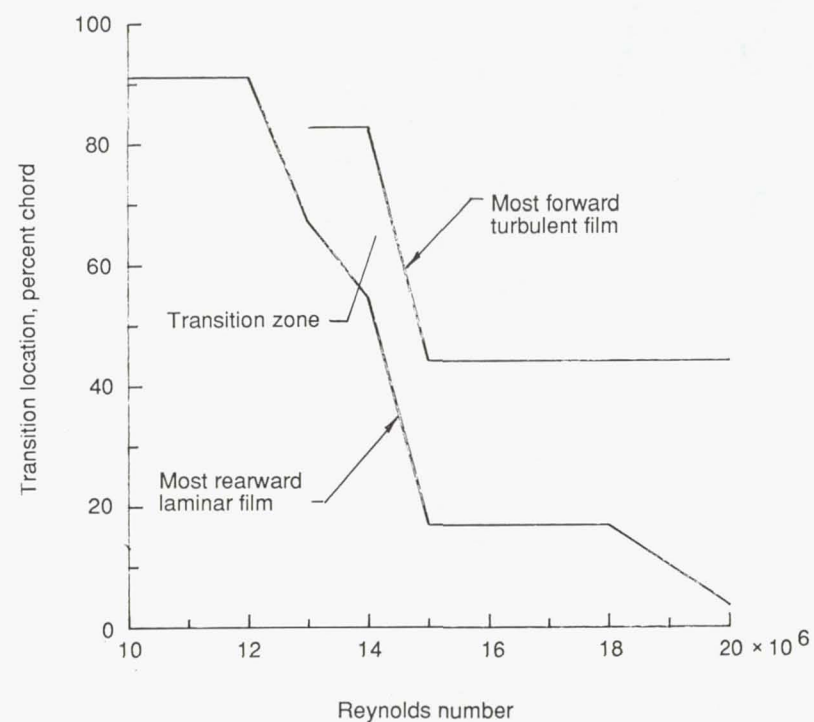


(i) $R_c = 20 \times 10^6$; $M_\infty = 0.8232$.

Figure 38. Concluded.



(a) Upper surface.



(b) Lower surface.

Figure 39. Variation of transition location with Reynolds number at operational design Mach number.

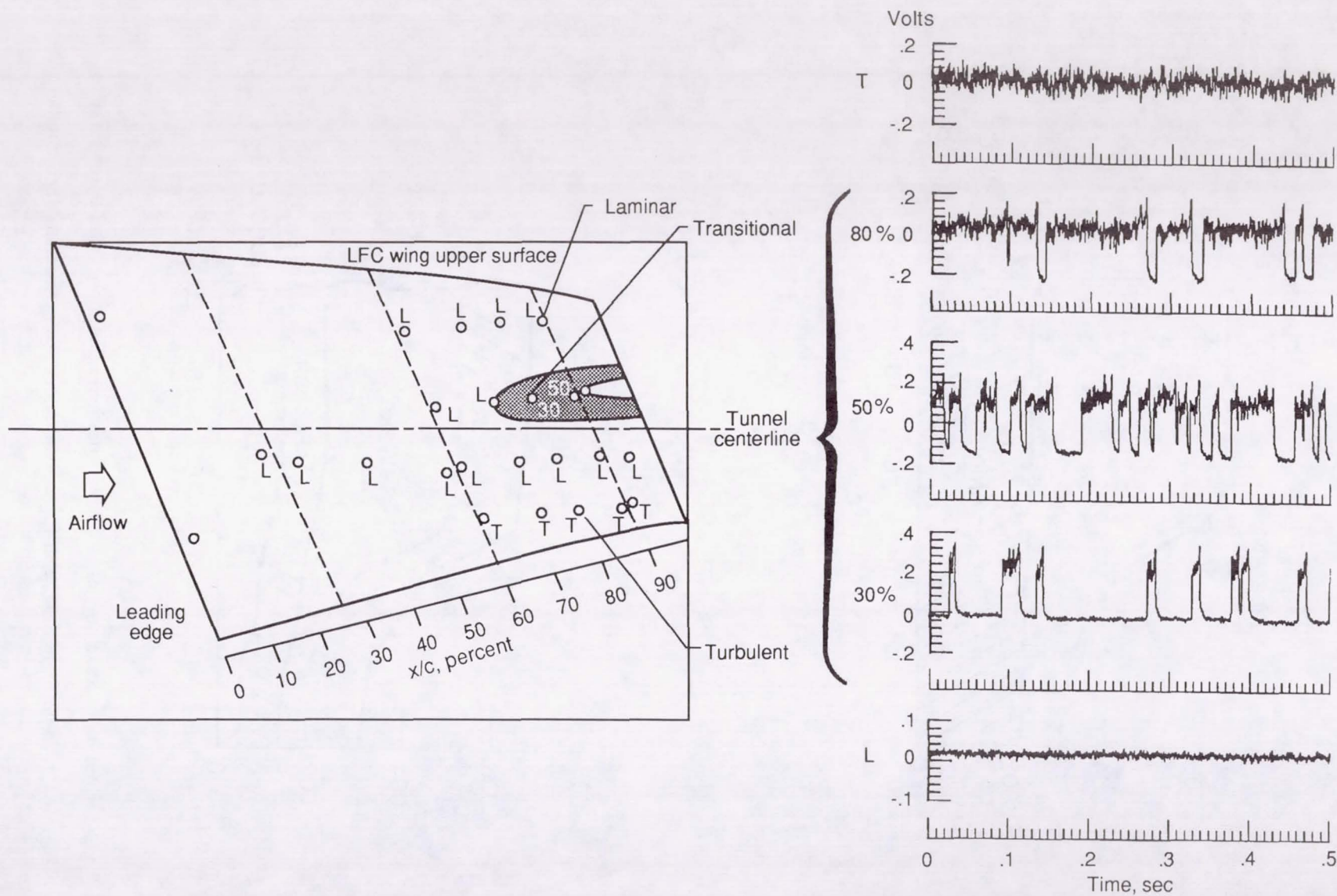
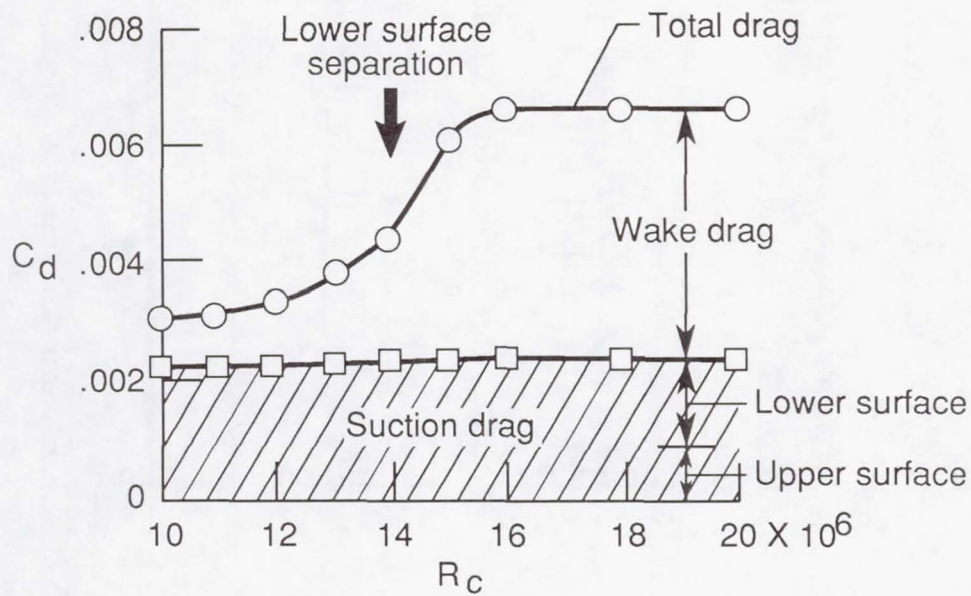
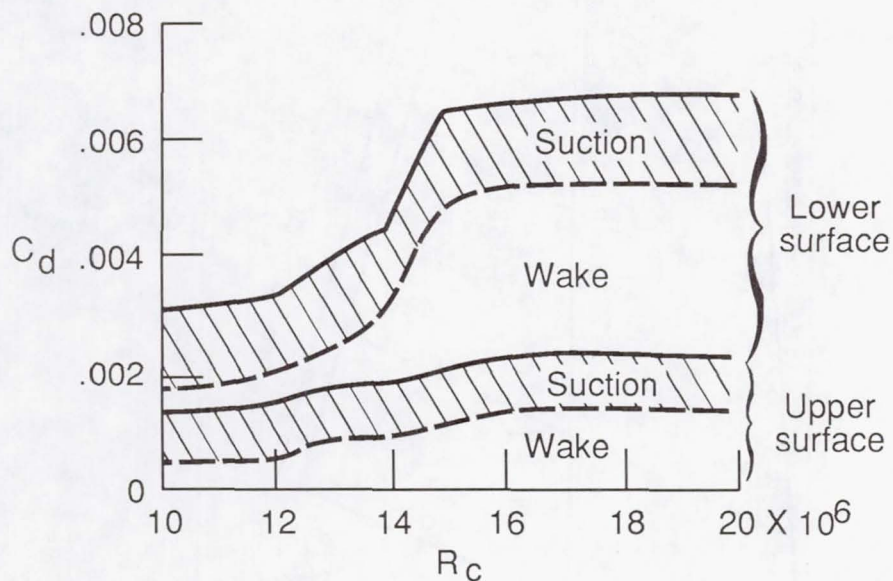


Figure 40. Example thin-film signals and corresponding locations on upper surface.



(a) Variation of wake and suction drag.



(b) Contribution to wake and suction drag from individual upper and lower surfaces.

Figure 41. Variation of drag with Reynolds number at operational Mach number.

Report Documentation Page

1. Report No. NASA TM-4100		2. Government Accession No.		3. Recipient's Catalog No.	
4. Title and Subtitle The NASA Langley Laminar-Flow-Control Experiment on a Swept Supercritical Airfoil <i>Basic Results for Slotted Configuration</i>				5. Report Date June 1989	
				6. Performing Organization Code	
7. Author(s) Charles D. Harris, Cuyler W. Brooks, Jr., Patricia G. Clukey, and John P. Stack				8. Performing Organization Report No. L-16474	
9. Performing Organization Name and Address NASA Langley Research Center Hampton, VA 23665-5225				10. Work Unit No. 505-60-31-03	
				11. Contract or Grant No.	
12. Sponsoring Agency Name and Address National Aeronautics and Space Administration Washington, DC 20546-0001				13. Type of Report and Period Covered Technical Paper	
				14. Sponsoring Agency Code	
15. Supplementary Notes					
16. Abstract The effects of Mach number and Reynolds number on the experimental surface pressure distributions and transition patterns for a large-chord, swept supercritical airfoil incorporating an active laminar-flow-control (LFC) suction system with spanwise slots are presented. The experiment was conducted in the Langley 8-Foot Transonic Pressure Tunnel. Also included is a discussion of the influence of interactions between the model and the tunnel liner on the airfoil pressure distribution. Mach number was varied from 0.40 to 0.82 at two chord Reynolds numbers, 10×10^6 and 20×10^6 , and Reynolds number was varied from 10×10^6 to 20×10^6 at the design Mach number.					
17. Key Words (Suggested by Authors(s)) Laminar flow control Contoured wind tunnel Transonic aerodynamics Supercritical swept wing				18. Distribution Statement Unclassified-Unlimited	
Subject Category 02					
19. Security Classif. (of this report) Unclassified		20. Security Classif. (of this page) Unclassified		21. No. of Pages 119	
				22. Price A06	